IMPERIAL COLLEGE OF SCIENCE TECHNOLOGY AND MEDICINE

University of London

EFFICIENT FINITE ELEMENT MODELLING OF ULTRASOUND WAVES IN ELASTIC MEDIA

by

Mickael Brice Drozdz

A thesis submitted to the University of London for the degree of

Doctor of Philosophy

January 2008

Department of Mechanical Engineering

Imperial College of Science Technology and Medicine

London

SW7 2BX

Ce qui ne tue pas rend plus fort.

Friedrich Nietzsche

Abstract

The aim of the work presented in this thesis is to provide tools to extend modelling capacities and improve quality and reliability of bulk and guided wave propagation models using commercially available finite element (FE) packages.

During the development process of NDT inspection techniques, the knowledge of the interaction of waves with defects is key to the achievement of robust and efficient techniques as well as identifying potential weaknesses. The reflection of ultrasound from cracks and notches of simple geometry and orientation is already well understood, but there are few results for more complex cases. A discrete approach is needed to model how the waves interact with discontinuities, including structural features, cracks, corrosion or other forms of defects. FE methods have been used to model a wide range of bulk and guided waves problems and have successfully provided important information about wave interaction with discontinuities. In these studies, defects were strongly simplified. One reason for this is that initial work is bound to focus on the simplest cases, but many modellers are ready to go on to more complex problems. The reason that so little of that is happening is that, despite rapid growth in computer power, many of the more complex realistic problems are still beyond the capacity of the models. The more complex problems require much larger models than the simplified ones, and so have remained out of reach.

This can be changed by using innovative techniques and improving the quality and reliability of modelling by taking the right decisions during the modelling process.

Perfectly matched layers (PML) and absorbing layers using increasing damping (ALID) enabling a reduction in the model geometric size are implemented in commercially available FE packages. Analytical models are developed in order to facilitate the achievement of high computational efficiency. Demonstrator cases highlight the gains achieved by the use of these techniques.

As the choice of mesh density is crucial in defining the resources necessary to solve a model, a study of the influence of meshing parameters for various element types and numerical schemes on the propagation velocity is performed. This provides information helping modellers to reach the right modelling compromises thanks to an improved understanding of the consequences of the decisions made.

The accuracy of defect modelling is investigated for a range of situations and modelling strategy. The weight of the choice of the right strategies is demonstrated.

The potential implementation of local mesh refinement in commercially available FE packages is considered and discussed in the context of the choices open to the modellers.

The outcome of the use of the techniques and information presented in this thesis is a significant improvement in FE modelling of waves in elastic media.

Acknowledgements

Firstly, I would like to thank my supervisors Professor Mike Lowe and Professor Peter Cawley for their guidance, help and patience during the course of this project. I would also like to express my gratitude for giving me the opportunity to be part of the NDT laboratory at Imperial College.

My thanks extend to all my colleagues in the NDT lab. It was a pleasure to be part of the team.

I would like to thank my family and my wife's family for their support.

Finally, my most sincere thanks go to my beloved wife Hannah who carried me through these years and to my little daughter Delia who has provided me with so much joy in so little time.

This work was funded by the EPSRC and Rolls Royce plc.

Table of contents

Chapter 4
On the influence of mesh parameters on elastic bulk wave velocities

Chapter 7
Conclusions

References

List of figures

List of Tables

Chapter 1

Introduction

1.1. Introduction

During the development process of ultrasonic NDT techniques, the knowledge of the interaction of waves with defects is key to the achievement of robust and efficient procedures as well as identifying potential weaknesses. Any problems such as poor sensitivity to certain shapes and orientation needs to be identified as early as possible. The reflection of ultrasound from cracks and notches of simple geometry and orientation is already well understood, but there are few results for more complex cases, for example from the multiple-crack geometry of stress corrosion cracking, or from realistic profiles of corrosion.

Against this background, experience has shown that, as NDT is developed for increasingly challenging applications, it has become increasingly important to start with careful modelling studies in order to be confident that the procedures which are developed are optimized and robust. Indeed in the particular topic of guided waves it is universally accepted that this is the only viable approach. Whereas various wave models, such as ray models for bulk wave problems or DISPERSE [1] for guided wave problems can predict the properties of waves in continuous uniform structures, a discrete approach is often needed to model how the waves interact with discontinuities, including structural features, cracks, corrosion or other forms of defects. Finite Element (FE) methods have been used to model a wide range of guided waves problems [2, 3, 4, 5, 6, 7] and have successfully provided important information about wave interaction with discontinuities [8, 9, 10, 11, 12, 13]. In these studies, defects were simplified and straight cracks, notches or cylindrical holes were used to represent real defects such as fatigue cracks or corrosion patches. One reason for this is that initial work is bound to focus on the simplest cases, but many modellers are ready to go on to more complex problems. The reason that so little of this is happening is that, despite rapid growth in computer power, many of the more complex realistic problems are still beyond the capacity of the models. The more complex problems require much

larger models than the simplified ones. In a similar way, modelling of bulk wave propagation and scattering has also received a huge amount of interest with many techniques being used but many cases remain out reach.

1.2. Objectives

As engineers involved in developing ultrasound NDT applications, our goal is to find computationally efficient techniques to improve modelling capacity and quality. Commercially available FE packages are chosen from the outset. This decision is based on the fact that they not only offer memory efficient and robust solvers but also remove the highly complex and time consuming necessity of developing and maintaining a specialist FE code. It is worth mentioning that most of the commercial packages have interactive user-friendly pre and post-processing tools which greatly increase their flexibility and ease of use. The choice of commercially available FE packages is also motivated by the fact that they enable new techniques to be quickly transferred to industry where these products are already or could easily be available and where a specific unsupported research code would be difficult to maintain. Two FE packages from a range available on the market are selected and used in this work: ABAQUS [14] and COMSOL Multiphysics [15]. ABAQUS is chosen because it is widely available, well developed and supported. Its level of performance is confirmed by the fact that it is used in many industries. COMSOL Multiphysics (formerly known as FEMLAB) is a relatively new software which gives more control to users. This means that it has an increased flexibility compared to ABAQUS but as it is a "young" package it is not yet so widely available in the industry. At the time of writing, it is noted that COMSOL is generally not as efficient as ABAQUS. The tools available clearly influenced the direction of our research but the findings are not limited to these two packages only as numerous other packages share the same basis to solve problems. In this context, various aspects of the modelling process have the potential to provide users with improved results.

One aspect is that related to the existence of unwanted reflections from the boundaries of a FE model. This has been a limiting factor for FE wave modelling. In time domain solving, it leads to a large increase in the model geometric size (and therefore a large increase in the number of degrees of freedom to be solved) as it is generally desirable

to separate in time the interaction of the waves with defects from unwanted boundary reflections. This point is illustrated in Figure 1.1 where it can be seen that the modelled area is much larger than the area of interest in order to fulfil this. Moreover, in frequency domain solving, removal of unwanted reflections is a requirement in order to correctly represent wave propagation in the system [16].

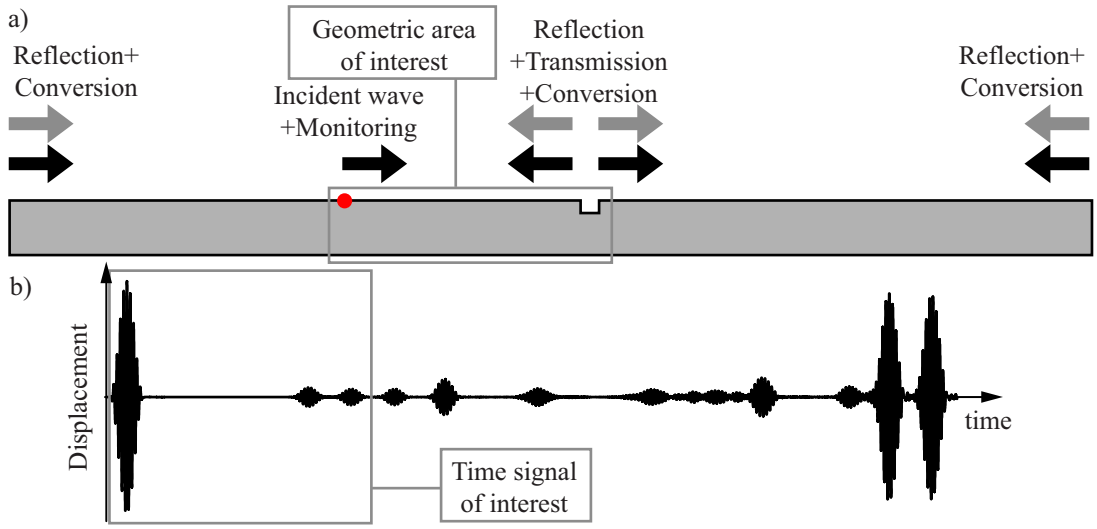

Figure 1.1. a) 2D plane strain model of a plate including a defect, b) Time signal at the monitoring point

Being able to represent total radiation outside the area of study in numerical wave propagation models at a reasonable cost would enable a large increase in computational efficiency. This topic has attracted a vast amount of interest in the last 25 years [17]. Well known techniques include infinite elements [18], boundary integral methods [19], non reflecting boundary conditions (NRBC) [20] and absorbing layer techniques [5, 16, 21, 22, 23, 24].

Another key aspect in the field of NDT is the precise knowledge of wave propagation velocities. The time of flight of a wave packet has been widely used to determine the position of defects in structures in many ultrasound industrial applications. Recently, imaging algorithms [25] and super resolution of defects [26, 27] have been investigated for NDT applications. Research in these techniques is very much active as their use holds promises of improved applications not only in NDT but also in the medical field. In the process of moving from the genesis of a numerical model to its conclusion and the obtention of results enabling a better understanding of a physical phenomenon, a modeller takes a series of design decisions. The choice of the solving

technique, mesh density or time step influences the successful outcome of the exercise but also the level of accuracy with which the phenomenon is represented. Discretization of the space and time leads to a discrepancy between theoretical physical values and their actual values measured in the model. One of the parameters suffering from this is the wave propagation velocity in elastic media. It would be beneficial to provide modellers with information enabling the improvement of not only the quality of their modelling (adequate decision making) but also the quality of the analysis made based on the numerical results (quantitatively taking into account the numerical deviation). There is also an interest in understanding the reasons for mesh scattering where a change in mesh size causes some numerical reflection.

As mentioned above, accurately representing the interaction of a wave with structural features and/or defects is crucial to evaluating the potential of an inspection technique. The degree of accuracy depends on the way the defect and overall model are defined. The space and time are discretized and defects are simplified. Even for the simplest of defects, there are uncertainties about the extent of the discrepancy between the exact and numerical results. NDT researchers have generally favoured the use of regular meshes in order to avoid numerical problems linked to a change in node spacing (numerical scattering). This approach creates problems of its own when it comes to representing defects or features in the regular grid as it generally leads to jagged edges of defects. The investigation of alternative techniques and sound understanding of the factors influencing the numerical errors should lead to increased modelling quality and enable modellers to move forward to more complex cases as efficiently as possible.

Achieving better representation of the interaction of waves with complex defects has led to the development of specialist ways of resolving this interaction. A method generating interest recently is the fictitious domain technique [28, 29, 30]. Investigation of this technique shows that its implementation in a commercially available FE packages is not possible. Instead, in this thesis, the path of local mesh refinement in the context of a regular node grid, is pursued as this could potentially lead to a large increase in model efficiency and improved representation of the defects.

Overall, the knowledge gained from this work should enable modellers to improve the quality of their modelling not only by increasing the computational efficiency of their

models but also by having a better understanding of the quantitative consequences of the decisions taken during the generation of their models.

1.3. Outline of the thesis

Chapter 2 presents the theoretical background necessary to understand the work developed further in the thesis. Bulk and guided wave theory is presented. Numerical implementation of the implicit and explicit solvers used in this work are outlined. The time domain explicit solver of ABAQUS/Explicit [14], the frequency domain direct integration implicit solvers of ABAQUS/Standard [14] and COMSOL Multiphysics [15] are presented.

In Chapter 3, the use of two different absorbing layer techniques for elastodynamic problems is investigated. Implementation of perfectly matched layers [24] (PML) in the frequency domain in COMSOL Multiphysics and absorbing layer using damping [31, 32] (ALID) for time and frequency domain in ABAQUS and COMSOL Multiphysics is devised. Analytical models are developed to enable a quick and accurate determination of adequate layer parameters. Typical example FE models of NDT applications are used to demonstrate the added value of using absorbing layers. The modelling options available to modellers are discussed.

In Chapter 4, the influence of mesh parameters on the propagation velocity is investigated. Both explicit and implicit solvers used with a range of element types are studied. Regular meshes made of square or equilateral triangles are investigated first. These meshes are then distorted in order to understand the influence of element deformation on wave velocities. The general approach is to run a series of FE models. The results of these models enable the identification of simple functions to describe the errors as generally as possible.

The work presented in Chapter 5 aims to provide the foundations to more complex defect modelling. The cases investigated are the reflection of bulk waves from straight edges, straight cracks at an angle and circular holes. For each case, the use of a regular square mesh approach where the defects are defined by removing or disconnecting elements is compared with the use of automatically generated meshes made of

triangular elements. In order to obtain a reference through the convergence of signals, the mesh size with both methods is reduced gradually.

The work is Chapter 6 focuses on local refinement of a regular square mesh using conventional tools available in the commercially available FE package ABAQUS. The method investigated in this part consists of creating 2 separate areas having different mesh densities and tying them together. The effect of the change in element size in a regular mesh of elements is investigated. The knowledge of the propagation velocities gained in Chapter 4 is used. This enables the influence of the way meshes of different size are tied together on reflections at the interface between the 2 meshes to be determined. A range of 1D and 2D FE models are created and studied in order to better understand and quantify the influence of these sources of error. In particular, elastic properties in parts of the models are adjusted in order to minimize the level of reflection. Parametric studies are performed in order to provide modellers with a database of information enabling them to determine the level of reflection which exist in a range of situations.

In Chapter 7, a review of this thesis is presented. Main contributions are summarized and finally consideration is given to suggested further work.

Chapter 2

Theoretical background

2.1. Introduction

This chapter presents the theoretical background to the work presented in this thesis. The theory of wave propagation in elastic media is developed and is followed by a presentation of the FE techniques used in this work.

2.2. Theory of wave propagation in elastic media

The theory of wave propagation in elastic media is presented in this section. Bulk waves and guided waves in a 2D plate are considered. The aim of this section is not only to present the cases which are of interest to us but also to define the notations used in following chapters.

2.2.1 Bulk wave propagation

2.2.1.1 Bulk wave propagation in infinite isotropic elastic media

The propagation of acoustic waves in unbounded isotropic media has been the subject of many studies and its theory is widely available [33, 34]. The general equation of motion relates the particle displacement u in a material of density ρ to the stress field tensor σ by:

$$\rho \frac{\partial^2 u_i}{\partial t^2} = \frac{\partial \sigma_{ij}}{\partial x_j} \tag{2·1}$$

It is well known that Hooke's law links the stress σ and strain ε in an isotropic material:

$$\sigma_{ij} = \lambda \delta_{ij} \varepsilon_{kk} + 2\mu \varepsilon_{ij} \tag{2·2}$$

$$\text{with } \varepsilon_{ij} = \frac{1}{2}\left(\frac{\partial u_i}{\partial x_j} + \frac{\partial u_j}{\partial x_i}\right) \tag{2·3}$$

where λ and μ are the 2 Lamé constants.

The Navier governing equation is derived from equations 2·1, 2·2 and 2·3:

$$\rho\frac{\partial^2 u_i}{\partial t^2} = (\lambda+\mu)\frac{\partial}{\partial x_i}\frac{\partial u_j}{\partial x_j} + \mu\frac{\partial^2 u_i}{\partial x_j^2} \tag{2·4}$$

This can also be expressed in a vectorial form:

$$\rho\ddot{\boldsymbol{u}} = (\lambda+\mu)\nabla(\nabla\cdot\boldsymbol{u}) + \mu\nabla^2\boldsymbol{u} \tag{2·5}$$

The Helmholtz decomposition can be used to derive the displacement $\boldsymbol{u}$ in terms of a compressional scalar potential ϕ, and an equivoluminal vector potential ψ:

$$\boldsymbol{u} = \nabla\phi + \nabla\times\psi \tag{2·6}$$

Using equation 2·6 to substitute the displacement in the Navier equation 2·4, the following relation is obtained:

$$\nabla\left[(\lambda+2\mu)\nabla^2\phi - \rho\left(\frac{\partial^2\phi}{\partial t^2}\right)\right] + \nabla\times\left[\mu\nabla^2\psi - \rho\frac{\partial^2\psi}{\partial t^2}\right] = 0 \tag{2·7}$$

This equation is fulfilled if both terms are zero which can be interpreted as the Helmholtz differential equations:

$$\frac{\partial^2\phi}{\partial t^2} = \frac{(\lambda+2\mu)\nabla^2\phi}{\rho} = c_L^2\nabla^2\phi \tag{2·8}$$

$$\text{and } \nabla^2\psi = \frac{\mu}{\rho}\frac{\partial^2\psi}{\partial t^2} = c_S^2\frac{\partial^2\psi}{\partial t^2} \tag{2·9}$$

c_L and c_S are the velocities of longitudinal (dilatational) and shear (rotational) waves in the infinite isotropic medium and are equal to:

$$c_L = \sqrt{\frac{(\lambda+2\mu)}{\rho}} \text{ and } c_S = \sqrt{\frac{\mu}{\rho}} \tag{2·10}$$

The wave numbers of these waves are defined as:

$$k_L = \frac{\omega}{c_L} \text{ and } k_S = \frac{\omega}{c_S} \tag{2·11}$$

The wavelengths are defined as:

$$\lambda_L = \frac{c_L}{f} = \frac{2\pi c_L}{\omega} = \frac{2\pi}{k_L} \text{ and } \lambda_S = \frac{c_S}{f} = \frac{2\pi c_S}{\omega} = \frac{2\pi}{k_S} \tag{2·12}$$

The solution to the Helmholtz differential equations (2·8) and (2·9) for longitudinal or shear harmonic waves propagating in a given direction is:

$$\phi = \Phi e^{i(\pm k_{Lx}x \pm k_{Ly}y - \omega t)} \text{ and } \psi = \Psi e^{i(\pm k_{Sx}x \pm k_{Sy}y - \omega t)} \tag{2·13}$$

with Φ and Ψ the amplitude of the wave and k_{Lx}, k_{Ly}, k_{Sx} and k_{Sy}, the projection of the wavenumbers of the longitudinal and shear waves on the x and y axes.

2.2.1.2 Bulk propagation in a semi-infinite isotropic elastic medium

Wave propagation in a semi-infinite medium (one interface) is considered in this section. This case is investigated because wave propagation in a multi layered system is modelled in Chapter 3 and will require this theory for its construction.

Let us consider a semi-infinite medium as shown in Figure 2.1. The arrows represent the longitudinal and shear waves that can exist in the material. In this work, positive waves are defined as waves propagating in the positive x direction and negative waves are defined as waves propagating in the negative x direction.

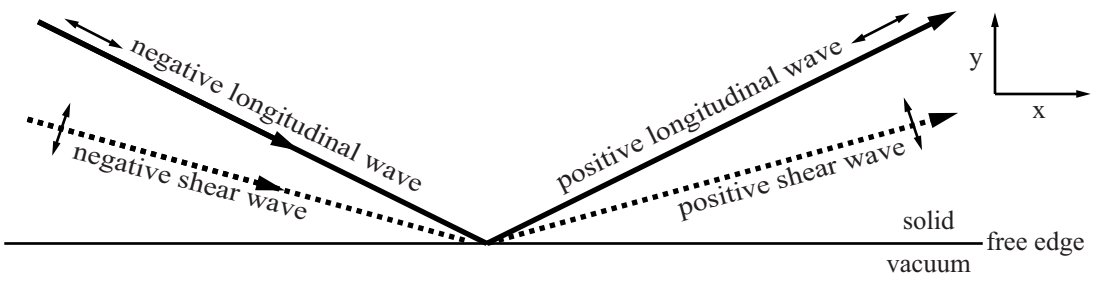

Figure 2.1. Modes considered and their orientation

The wave potentials of each wave type are defined as:

$$\phi_p = \Phi_p e^{i(k_{Ly}y + k_{Lx}x - \omega t)} \tag{2·14}$$

$$\psi_p = \Psi_p e^{i(k_{Sy}y + k_{Sx}x - \omega t)} \tag{2·15}$$

$$\phi_n = \Phi_n e^{i(-k_{Ly}y + k_{Lx}x - \omega t)} \tag{2·16}$$

$$\psi_n = \Psi_n e^{i(-k_{Sy}y + k_{Sx}x - \omega t)} \tag{2·17}$$

It is also considered that these waves are linked by the Descartes-Snell's law. This implies that $k_{Lx}=k_{Sx}=k_x$. The previous expressions can therefore be simplified, omitting the common factor $e^{i(k_x x - \omega t)}$.

$$\phi_p = \Phi_p e^{ik_{Ly}y} \tag{2·18}$$

$$\psi_p = \Psi_p e^{ik_{Sy}y} \tag{2·19}$$

$$\phi_n = \Phi_n e^{-ik_{Ly}y} \tag{2·20}$$

$$\psi_n = \Psi_n e^{-ik_{Sy}y} \tag{2·21}$$

Using equations 2·2, 2·3 and 2·6, the displacements and stresses are derived:

$$u_x = ik_{Lx}\Phi_p e^{ik_{Ly}y} + ik_{Lx}\Phi_n e^{-ik_{Ly}y} + ik_{Sy}\Psi_p e^{ik_{Sy}y} - ik_{Sy}\Psi_n e^{-ik_{Sy}y} \tag{2·22}$$

$$u_y = ik_{Ly}\Phi_p e^{ik_{Ly}y} - ik_{Ly}\Phi_n e^{-ik_{Ly}y} - ik_{Sx}\Psi_p e^{ik_{Sy}y} - ik_{Sx}\Psi_n e^{-ik_{Sy}y} \tag{2·23}$$

$$\begin{aligned}\sigma_{yy} = {} & -((\lambda + 2\mu)k_{Ly}^2 + \lambda k_{Lx}^2)\Phi_p e^{ik_{Ly}y} - ((\lambda + 2\mu)k_{Ly}^2 + \lambda k_{Lx}^2)\Phi_n e^{-ik_{Ly}y} \\ & + 2\mu k_{Sx}k_{Sy}\Psi_p e^{ik_{Sy}y} - 2\mu k_{Sx}k_{Sy}\Psi_n e^{-ik_{Sy}y}\end{aligned} \tag{2·24}$$

$$\begin{aligned}\sigma_{xy} = {} & -2\mu k_{Lx}k_{Ly}\Phi_p e^{ik_{Ly}y} + 2\mu k_{Lx}k_{Ly}\Phi_m e^{-ik_{Ly}y} \\ & -2\mu(k_{Sy}^2 - k_{Sx}^2)\Psi_p e^{ik_{Sy}y} - 2\mu(k_{Sy}^2 - k_{Sx}^2)\Psi_n e^{-ik_{Sy}y}\end{aligned} \tag{2·25}$$

These expressions will be needed in Chapter 3 to model a multi-layered system and can be linked to the potentials in the following way:

$$\begin{bmatrix} u_x \\ u_y \\ \sigma_{yy} \\ \sigma_{xy} \end{bmatrix} = M \begin{bmatrix} \Phi_p \\ \Psi_p \\ \Phi_n \\ \Psi_n \end{bmatrix} \tag{2·26}$$

with M=

$$\begin{bmatrix} ik_{Lx}e^{ik_{Ly}y} & ik_{Sy}e^{ik_{Sy}y} & ik_{Lx}e^{-ik_{Ly}y} & -ik_{Sy}e^{-ik_{Sy}y} \\ ik_{Ly}e^{ik_{Ly}y} & -ik_{Sx}e^{ik_{Sy}y} & -ik_{Ly}e^{-ik_{Ly}y} & -ik_{Sx}e^{-ik_{Sy}y} \\ -(\lambda k^2 + 2\mu k_{Lx}^2)e^{ik_{Ly}y} & 2\mu k_{Sx}k_{Sy}e^{ik_{Sy}y} & -(\lambda k^2 + 2\mu k_{Lx}^2)e^{-ik_{Ly}y} & -2\mu k_{Sx}k_{Sy}e^{-ik_{Sy}y} \\ -2\mu k_{Lx}k_{Ly}e^{ik_{Ly}y} & -2\mu(k_{Sy}^2 - k_{Sx}^2)e^{ik_{Sy}y} & 2\mu k_{Lx}k_{Ly}e^{-ik_{Ly}y} & -2\mu(k_{Sy}^2 - k_{Sx}^2)e^{-ik_{Sy}y} \end{bmatrix} \tag{2·27}$$

This expression enables to link all displacements, stresses and wave potentials and can be used to describe a multi-layered system straightforwardly.

2.2.2 Guided wave propagation in a plate

In this section, the theoretical basis of guided wave propagation in a 2D plate is presented. This case is considered as studies of models of guided waves which are specific to the plate case are done in Chapter 3.

Let us consider the plate represented in Figure 2.2.

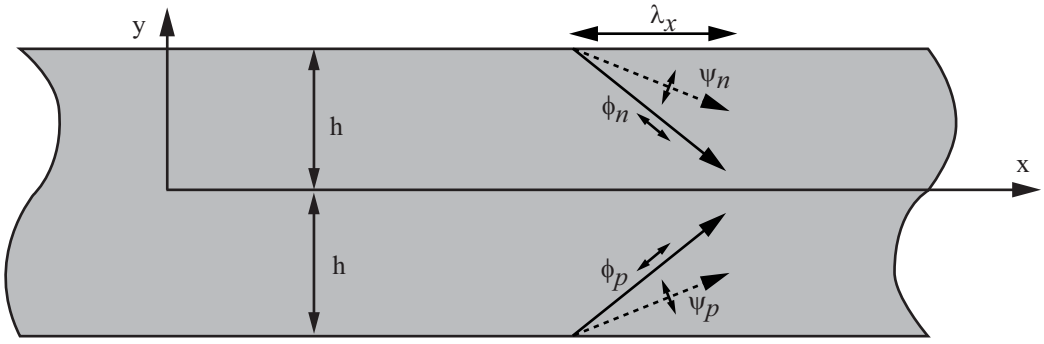

Figure 2.2. Geometry of a 2D plate

Guided waves in plates propagate in the same way as bulk waves in the infinite medium except the fact that the internal longitudinal and shear waves are reflected at the free surfaces. The theory of guided waves is treated in detail in several textbooks [33, 35]. Guided waves result from this interaction of both wave types with the top and bottom surfaces of the plate where Snell's law is satisfied. This implies that both wave types have the same wave number k_x in the x direction. As represented in Figure 2.2, in general there can be up to two shear waves and two longitudinal waves. Following the notation used previously for bulk waves, the field F can be expressed as:

$$F = \phi + \psi = (\phi_y(y) + \psi_y(y))e^{i(k_x x - \omega t)} \tag{2·28}$$

where $$\phi_y(y) = \Phi_p e^{ik_{Ly}y} + \Phi_m e^{-ik_{Ly}y} \tag{2·29}$$

$$\psi_y(y) = \Psi_p e^{ik_{Sy}y} - \Psi_m e^{-ik_{Sy}y} \tag{2·30}$$

It is essential to note that, at this stage, Φ_p, Φ_n, Ψ_p, Ψ_n and k_x are unknown.

The symmetry of the system imposes that the amplitude of waves going up is either equal to or opposite to the amplitude of waves going down:

$$\Phi_p = \Phi_n \text{ and } \Psi_p = \Psi_n \text{ or } \Phi_p = -\Phi_n \text{ and } \Psi_p = -\Psi_n \tag{2·31}$$

This leads to the existence of two types of guided modes: symmetric and anti symmetric modes as represented in Figure 2.3.

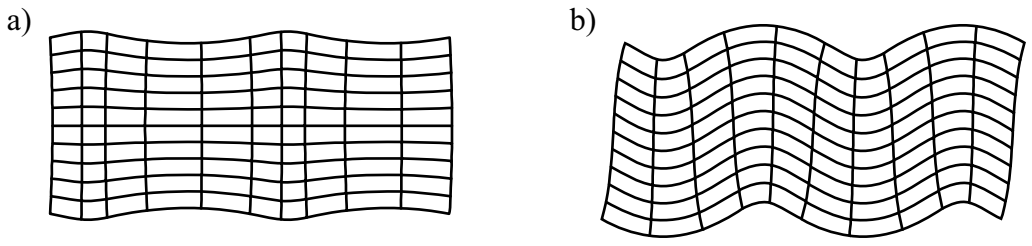

Figure 2.3. Typical deformation caused by symmetric (a) and anti-symmetric (b) modes.

When the amplitudes are equal, symmetric modes exist. The common factor $e^{i(k_x x - \omega t)}$ is omitted and the following expressions are obtained:

$$\phi = \Phi_s \cos(k_{Ly} y) \tag{2·32}$$

$$\psi = \Psi_s \sin(k_{Sy} y) \tag{2·33}$$

Equations 2·2, 2·3 and 2·6 are still valid in this case. The displacements and stresses are derived:

$$u_x = ik_x \Phi_s \cos(k_{Ly} y) - k_{Sy} \Psi_s \cos(k_{Sy} y) = A_s \Phi_s \cos(k_{Ly} y) + B_s \Psi_s \cos(k_{Sy} y) \tag{2·34}$$

$$u_y = -k_{Ly} \Phi_s \sin(k_{Ly} y) + ik_x \Psi_s \sin(k_{Sy} y) = C_s \Phi_s \sin(k_{Ly} y) + D_s \Psi_s \sin(k_{Sy} y) \tag{2·35}$$

$$\sigma_{xx} = -(k_x^2(\lambda + 2\mu) + k_{Ly}^2 \lambda) \Phi_s \cos(k_{Ly} y) - 2\mu i k_x k_{Sy} \Psi_s \cos(k_{Sy} y) \tag{2·36}$$

$$\text{or } \sigma_{xx} = E_s \Phi_s \cos((k_{Ly} y) + F_s \Psi_s \cos(k_{Sy} y)) \tag{2·37}$$

$$\sigma_{xy} = -2\mu i k_x k_{Ly} \Phi_s \sin(k_{Ly} y) + \mu(k_{Sy}^2 - k_x^2) \Psi_s \sin(k_{Sy} y) \tag{2·38}$$

$$\text{or } \sigma_{xy} = G_s \Phi_s \sin(k_{Ly} y) + H_s \Psi_s \sin(k_{Sy} y) \tag{2·39}$$

$$\sigma_{yy} = -((\lambda + 2\mu) k_{Ly}^2 + \lambda k_x^2) \Phi_s \cos(k_{Ly} y) + 2\mu i k_x k_{Sy} \Psi_s \cos(k_{Sy} y) \tag{2·40}$$

$$\text{or } \sigma_{yy} = I_s \Phi_s \cos(k_{Ly} y) + J_s \Psi_s \cos(k_{Sy} y) \tag{2·41}$$

When the amplitudes are opposite, anti symmetric modes exist. The common factor $e^{i(k_x x - \omega t)}$ is omitted and the following expressions are obtained:

$$\phi = \Phi_a \sin(k_{Ly} y) \tag{2·42}$$

$$\psi = \Psi_a \cos(k_{Sy} y) \tag{2·43}$$

$$u_x = ik_x \Phi_a \sin(k_{Ly} y) + k_{Sy} \Psi_a \sin(k_{Sy} y) = A_a \Phi_a \sin(k_{Ly} y) + B_a \Psi_a \sin(k_{Sy} y) \tag{2·44}$$

$$u_y = k_{Ly} \Phi_a \cos(k_{Ly} y) + ik_x \Psi_a \cos(k_{Sy} y) = C_a \Phi_a \cos(k_{Ly} y) + D_a \Psi_a \cos(k_{Sy} y) \tag{2·45}$$

$$\sigma_{xx} = -(k_x^2(\lambda + 2\mu) + k_{Ly}^2\lambda)\Phi_a(\sin(k_{Ly}y) + 2\mu i k_x k_{Sy}\Psi_a \sin(k_{Sy}y)) \quad (2\cdot46)$$

$$\text{or } \sigma_{xx} = E_a\Phi_a \sin((k_{Ly}y) + F_a\Psi_a \sin(k_{Sy}y)) \quad (2\cdot47)$$

$$\sigma_{xy} = 2\mu i k_x k_{Ly}\Phi_a \cos(k_{Ly}y) + \mu(k_{Sy}^2 - k_x^2)\Psi_a \cos(k_{Sy}y) \quad (2\cdot48)$$

$$\text{or } \sigma_{xy} = G_a\Phi_a \cos(k_{Ly}y) + H_a\Psi_a \cos(k_{Sy}y) \quad (2\cdot49)$$

$$\sigma_{yy} = -((\lambda + 2\mu)k_{Ly}^2 + \lambda k_x^2)\Phi_s \sin(k_{Ly}y) - 2\mu i k_x k_{Sy}\Psi_s \sin(k_{Sy}y) \quad (2\cdot50)$$

$$\text{or } \sigma_{yy} = I_a\Phi_a \sin(k_{Ly}y) + J_a\Psi_a \sin(k_{Sy}y) \quad (2\cdot51)$$

Φ_a, Φ_s, Ψ_a, Ψ_s and k_x are unknown. In order to calculate them, the traction-free boundary conditions on the top and bottom surfaces (where $y = \pm h$) are used:

$$\sigma_{yy} = 0 \text{ and } \sigma_{xy} = 0 \quad (2\cdot52)$$

For symmetric modes, this means:

$$I_s\Phi_s \cos(k_{Ly}h) + J_s\Psi_s \cos(k_{Sy}h) = 0 \text{ and}$$
$$G_s\Phi_s \sin(k_{Ly}h) + H_s\Psi_s \sin(k_{Sy}h) = 0 \quad (2\cdot53)$$

Φ_s=1 is taken arbitrarily and leads to:

$$\Psi_s = -\frac{I_s \cos(k_{Ly}h)}{J_s \cos(k_{Sy}h)} \text{ and } \Psi_s = -\frac{G_s \sin(k_{Ly}h)}{H_s \sin(k_{Sy}h)} \quad (2\cdot54)$$

This gives the dispersion equation that enables the calculation of k_x:

$$\frac{I_s \cos(k_{Ly}h)}{J_s \cos(k_{Sy}h)} = \frac{G_s \sin(k_{Ly}h)}{H_s \sin(k_{Sy}h)} \quad (2\cdot55)$$

$$\frac{-((\lambda + 2\mu)k_{Ly}^2 + \lambda k_x^2)\cos(k_{Ly}h)}{2\mu i k_x k_{Sy} \cos(k_{Sy}h)} = \frac{-2\mu i k_x k_{Ly} \sin(k_{Ly}h)}{\mu(k_{Sy}^2 - k_x^2)\sin(k_{Sy}h)} \quad (2\cdot56)$$

$$\text{or } \frac{\tan(k_{Sy}h)}{\tan(k_{Ly}h)} = \frac{4\mu k_x^2 k_{Ly} k_{Sy}}{-((\lambda+2\mu)k_{Ly}^2 + \lambda k_x^2)(k_{Sy}^2 - k_x^2)} \tag{2·57}$$

$$\text{which can be further simplified to: } \frac{\tan(k_{Sy}h)}{\tan(k_{Ly}h)} = -\frac{4k_x^2 k_{Ly} k_{Sy}}{(k_{Sy}^2 - k_x^2)^2} \tag{2·58}$$

For anti symmetric modes, in a similar way, the dispersion equation is:

$$\frac{\tan(k_{Sy}h)}{\tan(k_{Ly}h)} = -\frac{(k_{Sy}^2 - k_x^2)^2}{4k_x^2 k_{Ly} k_{Sy}} \tag{2·59}$$

Equation 2·58 and 2·59 were first published by Lamb [36]. These are solved numerically as there are no analytical solutions to these equations. The solutions give values of k_x which can be either real (propagating mode), imaginary (evanescent mode) or complex (propagating evanescent mode). Figure 2.4 illustrates the deformation of a plate caused by these various types of modes.

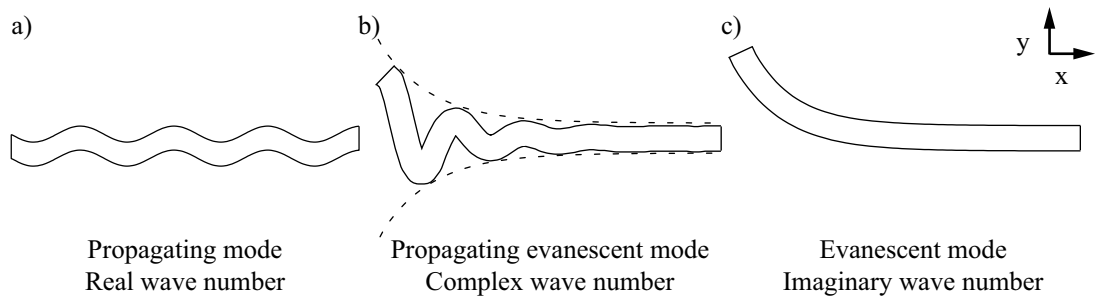

Figure 2.4. Illustration of the deformation of a plate caused by a) propagating, b) propagating evanescent, c) evanescent waves which have a) real, b) complex, c) imaginary wave numbers.

Propagating waves are those which have received the largest amount of research in the field of NDT as they can be used for long range inspection of structures such as rails, plates or pipes. For a given set of properties (plate thickness, bulk wave numbers and frequency), there is a finite number of real and imaginary wave numbers and an infinite number of complex wave numbers. It implies the existence of a finite number of propagating and evanescent waves and an infinite number of propagating evanescent modes. DISPERSE [1, 37], a software tool developed at Imperial College, provides a useful tool to find these solutions. Figure 2.5 shows an example of dispersion curves of propagating modes in a typical engineering structure (3mm thick steel plate).

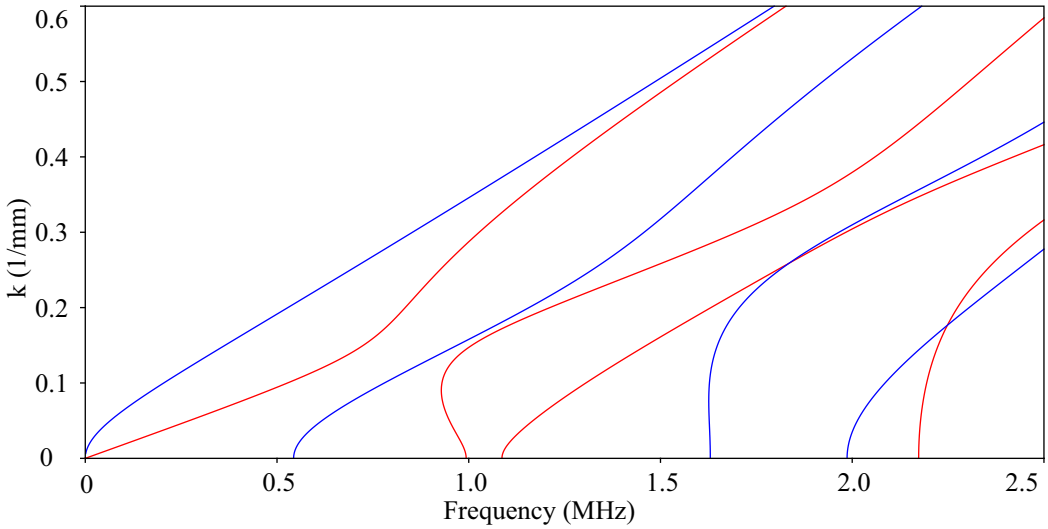

Figure 2.5. Wave number against frequency for a 3mm thick steel plate

These can be presented in many forms but a common form is to represent the phase velocity of the modes against the frequency-thickness product, as shown in Figure 2.6. In this figure, it can be seen that the phase velocities of guided waves in a plate vary with the frequency thickness product. Guided waves in a plate are therefore described as dispersive.

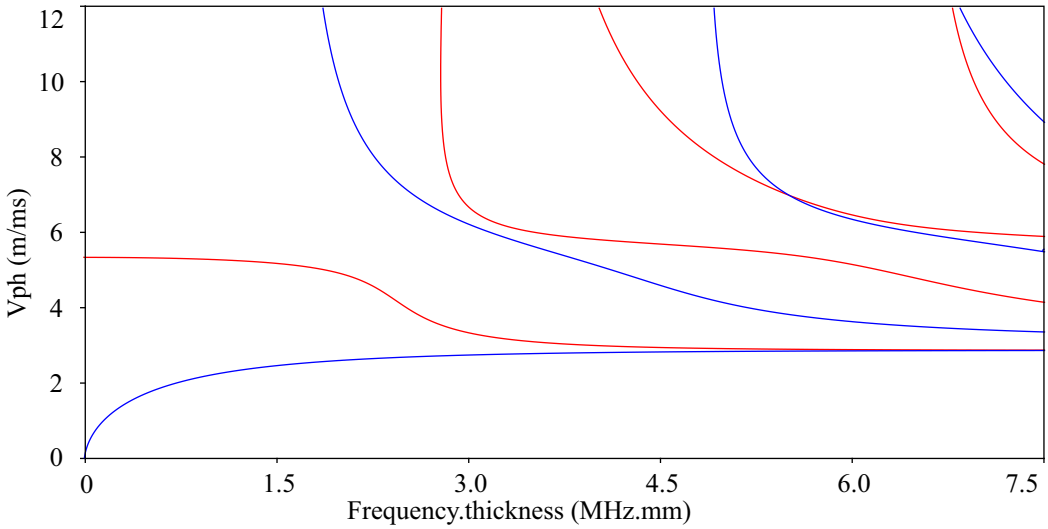

Figure 2.6. Phase velocity against frequency.thickness for a 3mm thick steel plate

In practical NDT, wave packets (often tone bursts) are usually used. Since guided waves are dispersive, the wave packet will not retain its original shape as it travels. In this case, it is convenient to define the velocity of the packet using the group velocity, found from the wave number curves.

The two previous figures illustrate the existence of several guided modes whose existence depends on the frequency and whose velocity varies against the frequency.

In order to identify the modes, each mode is named by a letter and a number. Symmetric modes use 'S' and anti-symmetric modes 'A'. The number is a counter variable starting at 0 used to distinguish modes in their family. S0 is the fundamental symmetric mode, S1, the first symmetric mode to appear as the frequency increases, and so on.

Another aspect of a guided mode is its mode shape. As can be seen from the displacement and stress equations derived previously in this section, the amplitudes of these values vary through the thickness of the plate. Knowledge of the mode shapes is essential to NDT and these are commonly plotted as shown in Figure 2.7.

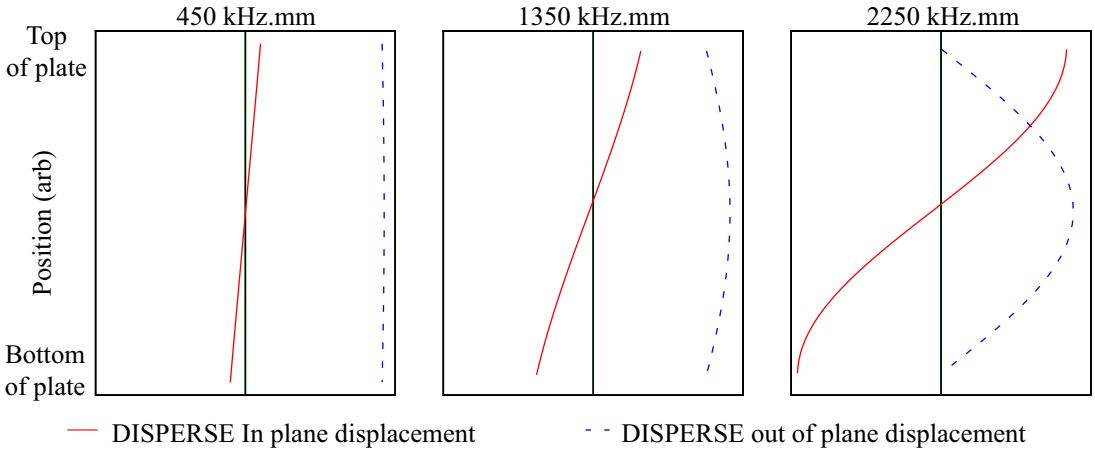

Figure 2.7. Example of A0 mode shapes for a free plate case at different frequencies, shown for a 3mm thick steel plate

2.3. Finite elements modelling of wave propagation

In this work, wave propagation problems are solved using both implicit and explicit solvers. Time domain explicit models are run with ABAQUS/Explicit [14]. For implicit models, ABAQUS/Standard [14] and COMSOL Multiphysics [15] are used. It is important to emphasize that ABAQUS/Explicit and ABAQUS/Standard are two separate programs which are part of the ABAQUS package. This section presents the details of the numerical implementation in these cases.

2.3.1 Explicit method

Explicit dynamic analysis in ABAQUS/Explicit is a direct time stepping method based on the central-difference operator and the use of diagonal element mass matrices [14]. Let us start with the equation of dynamic equilibrium:

$$[M]\ddot{\boldsymbol{u}} + [C]\dot{\boldsymbol{u}} + [K]\boldsymbol{u} = [F_a] \tag{2·60}$$

$\ddot{\boldsymbol{u}}$, $\dot{\boldsymbol{u}}$, $\boldsymbol{u}$ are the acceleration, velocity and displacement respectively. $[M]$ is the diagonal lumped mass matrix whose values are determined by the density of the material used. $[K]$ is the static stiffness matrix whose values are defined by the Young's modulus and Poisson's ratio. $[C]$ is the viscous damping matrix which is determined by the Rayleigh damping. Stiffness or mass proportional damping can be introduced:

$$[C] = C_M[M] + C_K[K] \tag{2·61}$$

where C_M and C_K are the mass and stiffness proportional damping coefficient. $[F_a]$ is the external force.

Wave propagation occurs when the initial equilibrium is disturbed by the application of forces or displacement constraints on nodes. Commonly, these are applied in the form of a tone burst. The central difference operator links the displacement, velocity and acceleration in the following way:

$$\dot{u}^{(i+0.5)} = \dot{u}^{(i-0.5)} + \frac{\Delta t^{(i+1)} + \Delta t^{(i)}}{2}\ddot{u}^{(i)} \tag{2·62}$$

$$u^{(i+1)} = u^{(i)} + \Delta t^{(i+1)}\dot{u}^{(i+0.5)} \tag{2·63}$$

with Δt, the time increment and i, the time increment number.

The procedure is explicit because the process is advanced using known values from the previous time step.

The computational efficiency comes from two aspects of the explicit scheme. Firstly, unlike in the implicit scheme, there is no need to assemble and invert the global mass matrix. Secondly, the diagonal mass matrix is used when calculating the acceleration in the following way:

$$\ddot{u}^{(i)} = [M]^{-1}([F]^{(i)} - [I]^{(i)}) \tag{2·64}$$

where $[F]$ is the applied load vector and $[I]$ is the internal force vector. $[M]^{-1}$ is easily calculated because $[M]$ is diagonal.

This implementation is conditionally stable and the time step Δt has to be smaller than the critical time step Δt_{cr} which in an undamped system depends on the highest frequency in the smallest element [14]:

$$\Delta t \leq \Delta t_{cr} = \frac{2}{\omega_{max}} \tag{2·65}$$

In wave propagation modelling, as small deformations of elements is assumed, an approximation often used is that the critical time step is the transit time of a dilatational wave through the smallest element in the model [38]:

$$\Delta t \leq \Delta t_{cr} = \frac{\Delta L}{c_L} \tag{2·66}$$

where ΔL is the smallest element size and c_L is the velocity of the dilatational wave. Figure 2.8 illustrates the value of ΔL for a linear square element, a linear equilateral-triangular element and a quadratic equilateral-triangular element. It can be noted that this distance corresponds to the shortest distance between 2 nodes for a square element but this is not the case for triangular elements. This will be verified in Section 4.2.3.1.

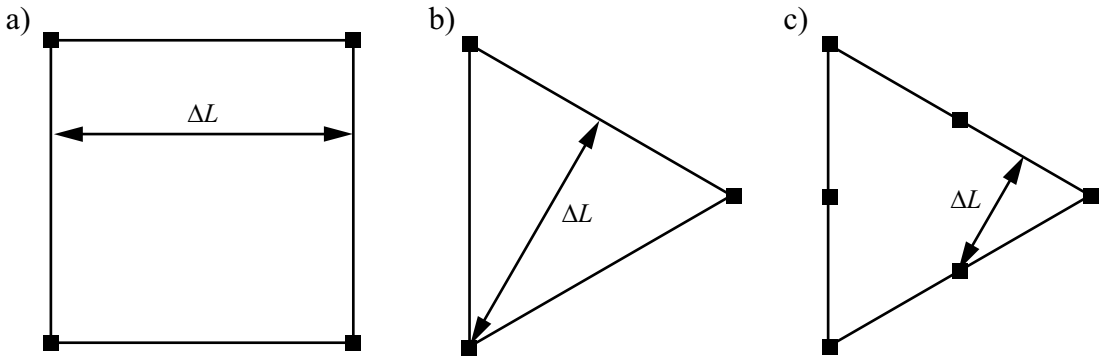

Figure 2.8. Illustration of ΔL for a a) linear square element, b) linear triangle element and c) quadratic triangle element.

The condition in equation 2·66 is referred to as the *CFL* condition after R. Courant, K. Friedrichs, and H. Lewy [39]. The actual time step used in a model can be expressed in terms of its ratio by the critical time step. This ratio is called the Courant (or *CFL*) number:

$$CFL = \frac{\Delta t}{\Delta t_{cr}} \tag{2·67}$$

therefore the time increment is defined as:

$$\Delta t = CFL\Delta t_{cr} = CFL\frac{\Delta L}{c_L} \tag{2·68}$$

Given that the space usually needs to be discretized in such a way that the shortest wavelength in the model is finely discretized (usually, at least 7 nodes per shortest wavelength are used), a large number of increments is required to solve a model. The number of increment in an explicit scheme is larger than the one required with a time domain implicit scheme but, since global mass and stiffness matrices do not need to be formed nor inverted, each increment is computationally inexpensive. This makes the explicit scheme particularly attractive for wave propagation.

2.3.2 Implicit method

Although it is possible to use implicit schemes to solve time domain wave propagation problems, the central difference explicit scheme has proved to be far more efficient than the implicit one. Therefore, in this work, time domain implicit schemes are not investigated and the implicit method is only used to solve wave problems in the

frequency domain (i.e. subjected to continuous harmonic excitation). The steady state response of the model forced by an harmonic excitation (i.e. at a single frequency) is calculated. In this case, it is necessary for waves to radiate out of the area of study in order to model wave propagation. The particular aspect of radiation outside the area of study is the topic of Chapter 3.

This procedure provides frequency domain results which can be used to reconstruct time domain results. The reconstruction procedure is presented in Section 3.5.2.

2.3.2.1 ABAQUS/Standard procedure

The direct steady-state dynamic analysis procedure of ABAQUS/Standard is used to model frequency domain wave propagation. The formulation is based on the dynamic virtual work equation over a small volume V of exterior surface S_t[14]:

$$\int_V \rho \delta \boldsymbol{u} \cdot \ddot{\boldsymbol{u}} dV + \int_V \rho C_M \delta \boldsymbol{u} \cdot \dot{\boldsymbol{u}} dV + \int_V \delta\varepsilon : \sigma dV - \int_{S_t} \delta \boldsymbol{u} \cdot \boldsymbol{t} dS = 0 \qquad (2\cdot69)$$

where σ is the stress, $\boldsymbol{t}$ is the surface traction and $\delta\varepsilon$ is the strain variation compatible with the displacement variation $\delta\boldsymbol{u}$. The : operation means that corresponding conjugate components of the stress and strain rate matrices are multiplied as pairs and the products summed.

The discretized form of this equation is defined as:

$$\delta u^N \{ M^{NM} \ddot{u}^M + C_M M^{NM} \dot{u}^M + I^N - P^N \} = 0 \qquad (2\cdot70)$$

$$\text{with the mass matrix } M^{MN} = \int_V \rho N^N \cdot N^M dV \qquad (2\cdot71)$$

$$\text{the internal load vector } I^N = \int_V \beta^N : \sigma dV \qquad (2\cdot72)$$

$$\text{and the external load vector } P^N = \int_{S_t} N^N \cdot \boldsymbol{t} dS \qquad (2\cdot73)$$

N^N is the shape function of the specified elements and β^N defines the strain variation from the variation of the kinematic variables. The change in internal force vector is:

$$\Delta I^N = \int_V [\Delta\beta^N : \sigma + \beta^N : \Delta\sigma] dV \tag{2·74}$$

The change in stress is:

$$\Delta\sigma = D^{el} : (\Delta\varepsilon + C_K \Delta\dot{\varepsilon}) \tag{2·75}$$

where D^{el} is the elasticity tensor. The strain and strain rate become:

$$\Delta\varepsilon = \beta^M \Delta u^M \text{ and } \Delta\dot{\varepsilon} = \beta^M \Delta\ddot{u}^M \tag{2·76}$$

The stiffness matrix is defined as:

$$K^{NM} = \int_V \beta^N : D^{el} : \beta^M dV \tag{2·77}$$

Therefore equation 2·70 becomes:

$$\delta u^N \{ M^{NM} \ddot{u}^M + (C_M M^{NM} + C_K K^{NM}) \dot{u}^M + K^N u - P^N \} = 0 \tag{2·78}$$

For harmonic excitation and response, we can write:

$$\Delta u^M = (\Re(u^M) + i\Im(u^M)) \exp(i\omega t) \tag{2·79}$$

$$\Delta\dot{u}^M = (-\omega\Im(u^M) + i\omega\Re(u^M)) \exp(i\omega t) \tag{2·80}$$

$$\Delta\ddot{u}^M = -\omega^2 (\Re(u^M) + \Im(u^M)) \exp(i\omega t) \tag{2·81}$$

$$\Delta P^M = (\Re(P^M) + i\Im(P^M)) \exp(i\omega t) \tag{2·82}$$

Therefore Equation 2·78 can be written as:

$$\begin{bmatrix} K^{NM} - \omega^2 M^{NM} & -\omega(C_M M^{NM} + C_K K^{NM}) \\ -\omega(C_M M^{NM} + C_K K^{NM}) & -(K^{NM} - \omega^2 M^{NM}) \end{bmatrix} \begin{bmatrix} \Re(u^M) \\ \Im(u^M) \end{bmatrix} = \begin{bmatrix} \Re(P^M) \\ (-\Im)P^M \end{bmatrix} \quad (2\cdot83)$$

Solving this equation provides the complex response of the system. Provided that radiation out of the area of study occurs, this response describes the wave propagation phenomenon occurring in the model.

2.3.2.2 COMSOL Multiphysics procedure

In COMSOL Multiphysics, it is possible to solve a model by directly defining partial differential equations (PDE) in the following form [15]:

$$\nabla \cdot (-c\nabla \boldsymbol{u}) + a\boldsymbol{u} = 0 \text{ in } \Omega \quad (2\cdot84)$$

$$\boldsymbol{n} \cdot (c\nabla \boldsymbol{u}) = g \text{ in } \partial\Omega \quad (2\cdot85)$$

$$h\boldsymbol{u} = r \quad \text{in } \partial\Omega \quad (2\cdot86)$$

Ω is the computational domain, $\partial\Omega$ is the domain boundary and $\boldsymbol{n}$ is the outward unit normal vector on $\partial\Omega$. $\boldsymbol{u}$ is a dependent variable unknown on the computational domain and can be a scalar or a vector, c, a, g, h and r are constants or matrices depending on the form of $\boldsymbol{u}$.

In a 2D vectorial problem in an orthonormal coordinate system ($\boldsymbol{x}$,$\boldsymbol{y}$), the displacement is defined as:

$$\boldsymbol{u} = u_1\boldsymbol{x} + u_2\boldsymbol{y} \quad (2\cdot87)$$

with u_1 and u_2, two independent scalar variables.

c and a are defined as:

$$c = \begin{bmatrix} \begin{bmatrix} c_{1111} & c_{1112} \\ c_{1121} & c_{1122} \end{bmatrix} & \begin{bmatrix} c_{1211} & c_{1212} \\ c_{1221} & c_{1222} \end{bmatrix} \\ \begin{bmatrix} c_{2111} & c_{2112} \\ c_{2121} & c_{2122} \end{bmatrix} & \begin{bmatrix} c_{2211} & c_{2212} \\ c_{2221} & c_{2222} \end{bmatrix} \end{bmatrix} \tag{2·88}$$

$$a = \begin{bmatrix} a_{11} & a_{12} \\ a_{21} & a_{22} \end{bmatrix} \tag{2·89}$$

In the expanded form, Equation 2·84 gives:

$$-\frac{\partial}{\partial x}\left(c_{1111}\frac{\partial u_1}{\partial x} + c_{1112}\frac{\partial u_1}{\partial y} + c_{1211}\frac{\partial u_2}{\partial x} + c_{1212}\frac{\partial u_2}{\partial y}\right) \tag{2·90}$$

$$-\frac{\partial}{\partial y}\left(c_{1121}\frac{\partial u_1}{\partial x} + c_{1122}\frac{\partial u_1}{\partial y} + c_{1221}\frac{\partial u_2}{\partial x} + c_{1222}\frac{\partial u_2}{\partial y}\right) + a_{11}u_1 + a_{12}u_2 = 0 \tag{2·91}$$

$$-\frac{\partial}{\partial x}\left(c_{2111}\frac{\partial u_1}{\partial x} + c_{2112}\frac{\partial u_1}{\partial y} + c_{2211}\frac{\partial u_2}{\partial x} + c_{2212}\frac{\partial u_2}{\partial y}\right) \tag{2·92}$$

$$-\frac{\partial}{\partial y}\left(c_{2121}\frac{\partial u_1}{\partial x} + c_{2122}\frac{\partial u_1}{\partial y} + c_{2221}\frac{\partial u_2}{\partial x} + c_{2222}\frac{\partial u_2}{\partial y}\right) + a_{21}u_1 + a_{22}u_2 = 0 \tag{2·93}$$

Since the equations of dynamic equilibrium in the frequency domain for a 2D isotropic elastic medium are:

$$\frac{\partial}{\partial x}\left((\lambda + 2\mu)\frac{\partial u_1}{\partial x} + \lambda\frac{\partial u_2}{\partial y}\right) + \frac{\partial}{\partial y}\left(\mu\frac{\partial u_1}{\partial y} + \mu\frac{\partial u_2}{\partial x}\right) + \rho\omega^2 u_1 = 0 \tag{2·94}$$

$$\frac{\partial}{\partial x}\left(\mu\frac{\partial u_1}{\partial y} + \mu\frac{\partial u_2}{\partial x}\right) + \frac{\partial}{\partial y}\left(\lambda\frac{\partial u_1}{\partial x} + (\lambda + 2\mu)\frac{\partial u_2}{\partial y}\right) + \rho\omega^2 u_2 = 0 \tag{2·95}$$

It is therefore possible to solve Equations 2·94 and 2·95 using Equation 2·84 by defining c and a as

$$c = \begin{bmatrix} \begin{bmatrix} \lambda + 2\mu & 0 \\ 0 & \mu \end{bmatrix} \begin{bmatrix} 0 & \lambda \\ \mu & 0 \end{bmatrix} \\ \begin{bmatrix} 0 & \mu \\ \lambda & 0 \end{bmatrix} \begin{bmatrix} \mu & 0 \\ 0 & \lambda + 2\mu \end{bmatrix} \end{bmatrix} \tag{2·96}$$

$$a = \begin{bmatrix} \rho\omega^2 & 0 \\ 0 & \rho\omega^2 \end{bmatrix} \tag{2·97}$$

The model is excited by either applying a force on a boundary with Equation 2·85 or prescribing a displacement using Equation 2·86. The model is solved using one of COMSOL built-in solvers and solutions can be output to be post processed in MATLAB. As with ABAQUS/Standard, provided that radiation out of the area of study exists, the response obtained represents the wave propagation phenomenon occurring in the system.

2.4. Conclusions

In this chapter, the theoretical background necessary to the work presented in this thesis was presented. The theory of wave propagation in elastic media was developed and was followed by a presentation of the FE techniques used in this work.

Chapter 3

Modelling waves in unbounded elastic media using absorbing layers

3.1. Introduction

Unwanted reflections from the boundaries of the system have been a limiting factor for FE modelling of waves. In time domain solving, this leads to a large increase in the model geometric size (and therefore a large increase in the number of degrees of freedom to be solved) as it is generally desirable to separate in time the interaction of the waves with defects from unwanted boundary reflections. This issue is illustrated in Figure 3.1 where it can be seen that the plate had to be extended to achieve separation of the signal of interest and the unwanted reflections. Moreover, in frequency domain solving, removal of unwanted reflections is a requirement in order to correctly represent wave propagation in the system.

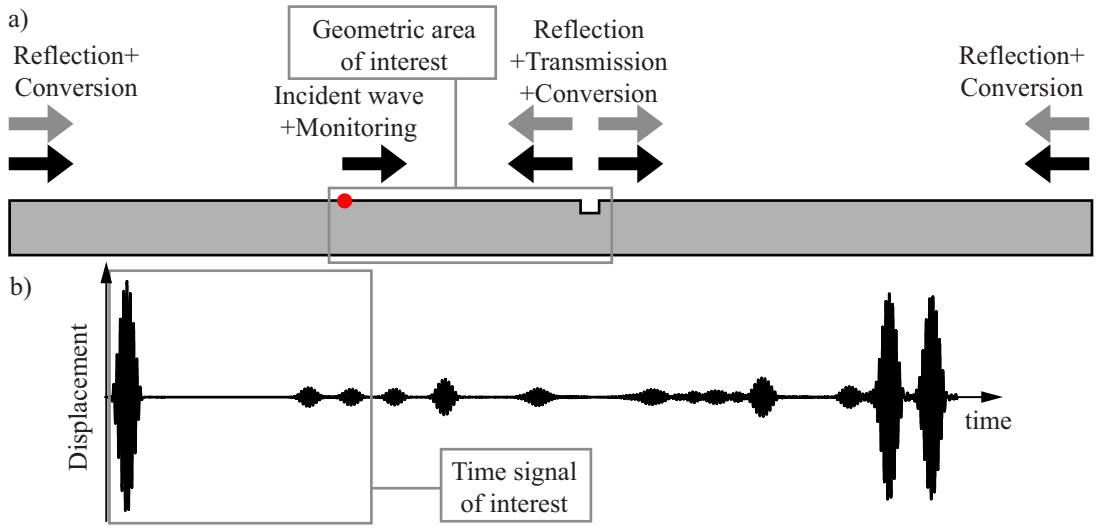

Figure 3.1. a) 2D plane strain model of a plate including a defect, b) Time signal at the monitoring point

Removing unwanted reflections in numerical wave propagation models is equivalent to representing total radiation outside the area of study. This topic has attracted a vast amount of interest in the last 25 years [17]. Well known techniques include infinite elements [18], boundary integral methods [19], non reflecting boundary conditions

(NRBC) [20] and absorbing layer techniques [5, 21, 22, 23, 24]. These various techniques have proved successful in their context but, as engineers involved in developing ultrasound NDT applications, our goal is to find computationally efficient techniques for removing unwanted reflections that can be used with commercial FE packages. Commercial packages were chosen from the outset of the study not only because they offer memory efficient and robust solvers but also because they remove the necessity of developing and maintaining specialist codes. It is key that the technique that achieves the removal of unwanted boundary reflections is easily implementable in the commercial FE packages. It needs to be able to remove the reflections with a high degree of accuracy (typically, in this work, 60dB ≡99.99% of the incident wave amplitude removed) as ultrasound NDT relies on quantitatively evaluating relatively low amplitude signals. A significant reduction in model geometric size compared with the classical technique (i.e. increasing model geometric size) needs to be achieved in order to justify the use of the technique.

In this work, I have focused on two different absorbing layer techniques for elastodynamic problems. I implemented "Perfectly Matched Layers" [24] (PML) in the frequency domain in COMSOL [15] and "Absorbing Layer Using Damping" [31, 32] (ALID) for time and frequency domain in ABAQUS [14] and COMSOL. Optimum definition of the layer parameters is essential to improve modelling capabilities, but it becomes counter efficient to invest a large amount of time to determine the best parameters to use for these layers. This issue is raised in several papers [40,41]. In order to resolve this, we have developed analytical models to enable a quick and accurate determination of adequate layer parameters.

One of the challenges of this chapter is to stimulate interest from fellow researchers, engineers and modellers. To convince them of the advantage of the techniques, two typical examples demonstrate the added value of using absorbing layers.

3.2. Review of non-investigated techniques

As mentioned above, only the use of absorbing layers is investigated in detail as it proved to be the only technique fitting the requirements. In this section, the alternative infinite element and non reflecting boundary condition techniques are summarised. The justification why these are not investigated is given.

3.2.1 Infinite element methods

Infinite elements are a special type of element with modified properties which can be used in conjunction with standard finite elements and which simulate an infinite space. A general presentation of the development of infinite elements can be found in [18]. A single row of infinite elements is positioned outside the boundaries of the area of study as shown in Figure 3.2.

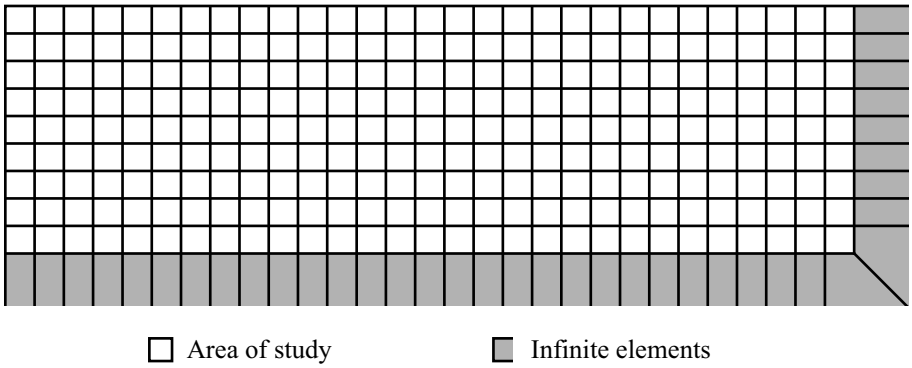

Figure 3.2. Illustration of use of infinite elements

Infinite elements have been proved to work relatively well for static cases as well as in certain domains of wave propagation: electromagnetism, acoustics and elastic bulk waves with incidence at angles close to the normal. It should be noted that elastic wave problems are more complex than acoustic or electromagnetic ones because in 2D two wave types exist in this case. In the general case of wave propagation, the simulation of an infinite expanse of material can be defined using the Sommerfeld radiation condition [42] which defines the condition for total radiation of a wave from a source. Satisfying exactly the radiation condition in the infinite element results in perfect absorption and no reflection from the boundary. For solid media, ABAQUS provides infinite elements based on [43]. A benchmark problem for the use of infinite elements is available in the ABAQUS user manual [14]. This example is similar to the one analysed in [44]. The geometry of the model is presented in Figure 3.3.a. The problem

is an infinite half-space subjected to a vertical pulse line load in the form of a 10MHz raised-cosine function 1-sin(ωt/3)*cos(ωt) with a spatially constant amplitude of 1GPa. The vertical displacement is monitored at point A 2mm below the edge of the load as indicated on Figure 3.3.a. The resulting displacement is plotted on Figure 3.3.b. A comparative model is created. This model has the same properties as the benchmark but does not use infinite elements. Instead, the boundaries of the area of study where the infinite elements were placed are moved away from point A so that the monitored signal at point A does not include any interaction of the waves with these boundaries. This represents an exact reference and the difference between the two models is the reflection from the infinite element boundary. This model is shown in Figure 3.3.c. and the displacement monitored at point A is plotted in Figure 3.3.d.

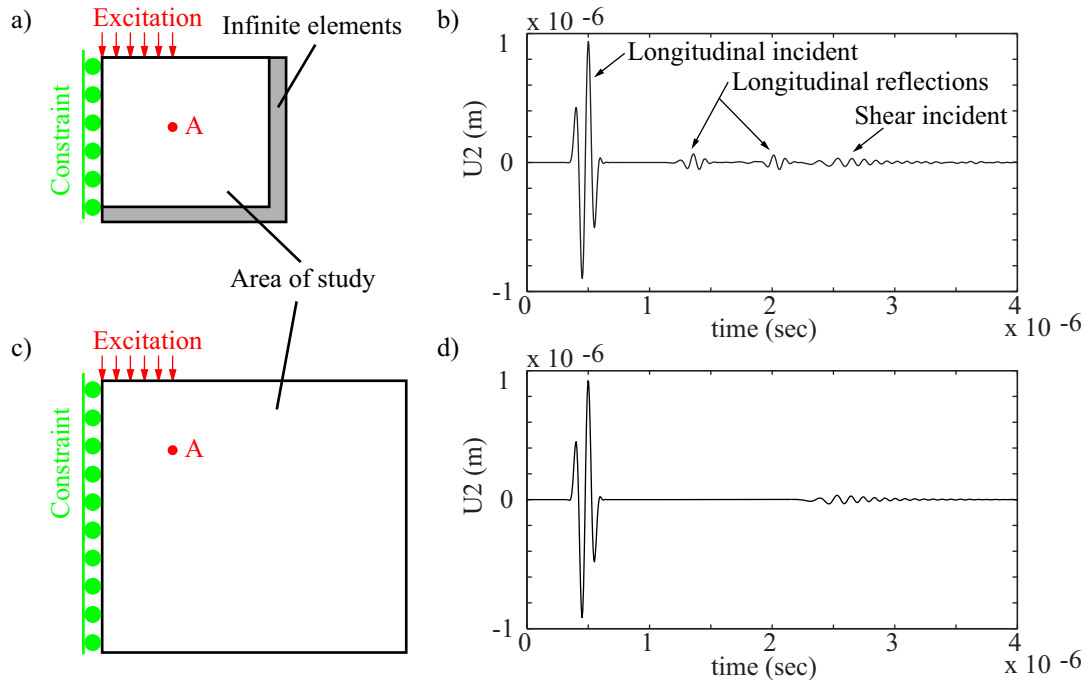

Figure 3.3. ABAQUS benchmark model: a) Model geometry, b) vertical displacement at point A, Extended model (reference): c) Model geometry, d) vertical displacement at point A

There is a clear discrepancy between the 2 monitored signals. This indicates that a noticeable reflection occurs as the wave reaches the infinite elements. This example confirms that infinite elements are not suitable for high accuracy removal of unwanted reflection of bulk waves. Studies [45, 46] have proved that similar conclusions can be drawn for the use of these elements with guided waves. These findings justify why this technique is not investigated further in this chapter.

3.2.2 Non reflecting boundary condition

Non reflecting boundary conditions (NRBC) are special boundary conditions used in FE or finite difference (FD) methods to model wave propagation in unbounded media. The dimensions of the model are the same as the area of study; only the boundary conditions are changed. The modified boundary conditions generally use extra variables in order to approximate the infinite expanse of the medium. Many different methods have been developed for a wide range of fields. Early work in the '70s on NRBC was dominated by the use of the radiation condition given by Sommerfeld [42] but this method had limits as demonstrated in [47]. Other methods were developed such as the Engquist-Majda [48], Bayliss-Turkel [49], and are still widely used today. Exact non-local methods based on the Dirichlet-to-Neumann map [50, 51] or the difference potential method were developed from the late '80s. In the last 10 years, high order local NRBC have been developed for various cases [52]. These techniques were proved to work correctly but, as they require modification of the standard solving procedure, the development of specialist FE codes is required. To the best of the author's knowledge, they cannot be implemented in commercially available FE packages and are therefore not investigated here.

3.3. Absorbing layer theory

3.3.1 Concept

Absorbing layers are finite regions "attached" at the extremities of a model - see Figure 3.4. Their objective is to approximate the case of an unbounded problem by absorbing waves entering them. Small reflections from the absorbing region exist but these can be made acceptably small by correctly defining the layer's parameters.

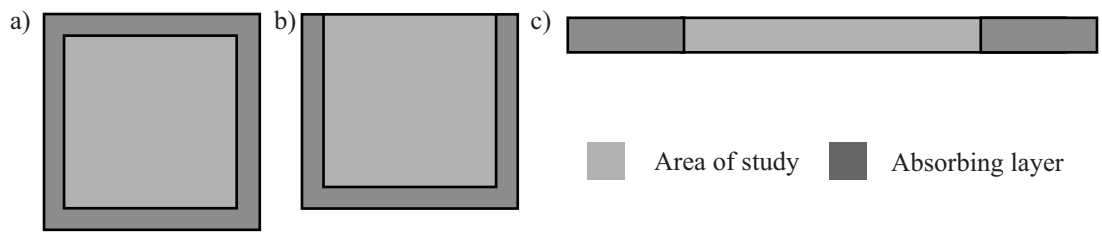

Figure 3.4. Absorbing layer concept for 2D models: a) infinite medium, b) semi infinite medium, c) plate

3.3.2 Perfectly matched layer (PML)

The PML technique was created in 1994 by Berenger for electromagnetism [24] and has been extended to other fields such as acoustics [53, 54, 55] and seismological and other elastic waves [56, 57, 58, 59]. As its name indicates, a PML matches perfectly the impedance of the area of study. This means that, in theory, a wave enters a PML without reflection. Once inside it, the wave decays exponentially. A PML can therefore be used to achieve total radiation of a wave out of the area of study.

In this work, the technique is implemented in the frequency domain for an elastodynamic case without splitting the variables. This implementation was defined in collaboration with Dr Elizabeth Skelton, a mathematician at Imperial College [60]. Let us consider an harmonic wave travelling in the x direction which can be defined by:

$$u(x, y, t) = u_0 e^{-i\omega t} e^{ikx} \tag{3·1}$$

For an elastic isotropic medium in 2D plane strain, the equations of equilibrium are:

$$\frac{\partial}{\partial x}\left((\lambda + 2\mu)\frac{\partial u_x}{\partial x} + \lambda\frac{\partial u_y}{\partial y}\right) + \frac{\partial}{\partial y}\left(\mu\frac{\partial u_x}{\partial y} + \mu\frac{\partial u_y}{\partial x}\right) + \rho\omega^2 u_x = 0 \tag{3·2}$$

$$\frac{\partial}{\partial x}\left(\mu\frac{\partial u_x}{\partial y} + \mu\frac{\partial u_y}{\partial x}\right) + \frac{\partial}{\partial y}\left(\lambda\frac{\partial u_x}{\partial x} + (\lambda + 2\mu)\frac{\partial u_y}{\partial y}\right) + \rho\omega^2 u_y = 0 \tag{3·3}$$

In the PML, we want the wave to decay exponentially and therefore to have the following form.

$$u(x, y, t) = u_0 e^{-i\omega t} e^{ikx - k\alpha_x x} \tag{3·4}$$

The modification from equation 3·1 to equation 3·4 can be achieved by performing a change of variable in the PML.

$$x \to x(1 + i\alpha_x) \tag{3·5}$$

This change of variable can be interpreted as:

$$\frac{\partial}{\partial x} \rightarrow \left(\frac{1}{1+i\alpha_x}\right)\frac{\partial}{\partial x} = S_x\frac{\partial}{\partial x} \tag{3·6}$$

After this change of variable for x and y and some algebra, the equations of equilibrium 3·2 and 3·3 become:

$$\frac{\partial}{\partial x}\left(\frac{S_x}{S_y}(\lambda+2\mu)\frac{\partial u_x}{\partial x}+\lambda\frac{\partial u_y}{\partial y}\right)+\frac{\partial}{\partial y}\left(\frac{S_y}{S_x}\mu\frac{\partial u_x}{\partial y}+\mu\frac{\partial u_y}{\partial x}\right)+\frac{\rho\omega^2}{S_xS_y}u_x = 0 \tag{3·7}$$

$$\frac{\partial}{\partial x}\left(\mu\frac{\partial u_x}{\partial y}+\frac{S_x}{S_y}\mu\frac{\partial u_y}{\partial x}\right)+\frac{\partial}{\partial y}\left(\lambda\frac{\partial u_x}{\partial x}+\frac{S_y}{S_x}(\lambda+2\mu)\frac{\partial u_y}{\partial y}\right)+\frac{\rho\omega^2}{S_xS_y}u_y = 0 \tag{3·8}$$

In the area of study, α_x and α_y are equal to zero, hence S_x and S_y are equal to 1 and equation 3·7 and 3·8 become equation 3·2 and 3·3. In the PML, α_x and α_y are respectively x and y dependent and are defined as illustrated in Figure 3:

$$\alpha_x(x) = A_x \cdot x^p \text{ and } \alpha_y(y) = A_y \cdot y^p \tag{3·9}$$

with A_x and A_y two constants.

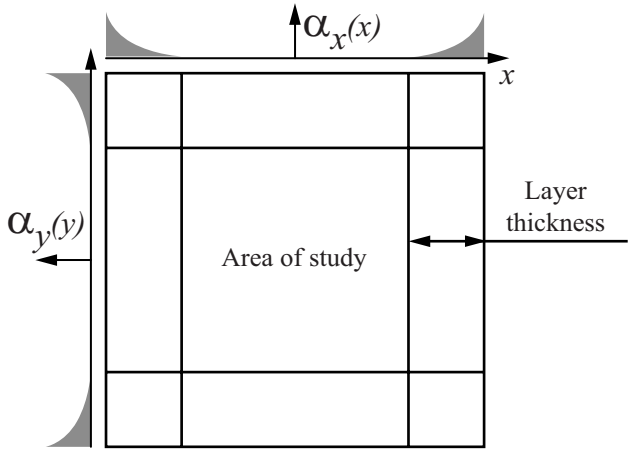

Figure 3.5. Variation of $\alpha_x(x)$ and $\alpha_y(y)$ in a 2D model.

The same approach can be readily extended to 3 dimensional cases by following the same reasoning.

In order to avoid numerical issues due to the discontinuity of the attenuation parameter and its first and second derivatives at the interface between the area of the study and the PML, the attenuation parameters are taken to vary at least quadratically with the distance which implies that p in equation 3·9 has to be superior or equal to 2.

At the end of the PML, the decaying wave is reflected and generally partially mode converted. The reflected waves propagate back toward the area of study while continuing to decay and then re-enter the area of study. The PML has to be defined so that these reflections are negligible.

Correct definition of the PML parameters (thickness of the layer, α and p) is essential to achieve an efficient model. These points are looked at in detail later in this chapter.

Solving of the model is done in the frequency domain but time domain results can be obtained easily by solving the model over a range of frequency and performing an inverse Fourier transform.

3.3.3 Absorbing layer using increasing damping (ALID)

The ALID is an absorbing layer which is made of a material with the same properties as those of the area of study apart from having a gradually increasing damping. The general concept was mentioned in 1980 by Israeli and Orszag in [22] and was recently revived by Liu et al [21] and Castaings et al [16].

Let us start with the equation of equilibrium in the time domain:

$$[M]\ddot{u} + [C]\dot{u} + [K]u = f \tag{3·10}$$

with $[M]$, $[C]$ and $[K]$, the mass, damping and stiffness matrices.

By convention, we consider harmonic waves of the form: $u(x, y, t) = u_0 e^{-i\omega t} e^{ikx}$. We have $\dot{u} \rightarrow -i\omega u$. The equation of equilibrium in the frequency domain is:

$$-[M]\omega^2 u - [C]i\omega u + [K]u = f \tag{3·11}$$

Stiffness or mass proportional damping can be introduced in time or frequency domain models in most FE packages and is generally termed Rayleigh damping. We define:

$$[C] = C_M[M] + C_K[K] \tag{3·12}$$

where C_M and C_K are the mass and stiffness proportional damping coefficients. Equation 3·11 becomes:

$$-[M]\omega^2 u - \left[C_M[M] + C_K[K]\right] i\omega u + [K]u = f \tag{3·13}$$

$$-[M]\left(1 + i\frac{C_M}{\omega}\right)\omega^2 u + [K](1 - i\omega C_K)u = f \tag{3·14}$$

In an ALID with a boundary perpendicular to the x axis, the value of C_M and C_K are gradually increased in the x direction. We set the following formulation:

$$C_M(x) = C_{Mmax} \cdot X(x)^p \quad \text{and} \quad C_K(x) = C_{Kmax} \cdot X(x)^p \tag{3·15}$$

C_{Mmax} and C_{Kmax} are positive real numbers and $X(x)$ varies from 0 at the interface between the ALID and the area of study to 1 at the end of the ALID following a power law whose order is defined by p. In a time domain model, C_{Mmax} and C_{Kmax} are constant and therefore do not vary with the frequency. This leads to a variation of the wave attenuation against the frequency. In a frequency domain model, it can be made constant over the range of frequencies by adjusting C_{Mmax} and C_{Kmax} accordingly with frequency.

The effect of Rayleigh damping can be better understood by using a formulation using complex density and complex stiffness modulus in the ALID:

$$\rho_{ALID} = \rho\left(1 + i\frac{C_M(x)}{\omega}\right) \text{ or } E_{ALID} = E(1 - i\omega C_K(x)) \tag{3·16}$$

The wavenumber is proportional to the square root of the density ρ and inversely proportional to the square root of the Young's modulus, E:

$$k \propto \omega \sqrt{\frac{\rho}{E}} \tag{3·17}$$

From this, we see that, in the ALID, the wave number is complex and the solution to wave equation becomes:

$$u(x, y, t) = u_0 e^{-i\omega t} e^{ik'x - k''x} \tag{3·18}$$

k' and k'' are the real and imaginary parts of the wave number and are both positive numbers for a wave propagating in the positive direction. k'' induces the decay of the wave in the layer. The real part of the wave number in the ALID varies with the damping and does not match perfectly the real part of the wave number in the area of study. This denotes a change in acoustic impedance which will cause reflections at the interface of the ALID as well as inside it. To simulate unboundedness with high accuracy, these reflections need to be negligible. Increasing the damping gradually enables us to achieve this. The technique is not as neat as the PML technique since there is a change of impedance between the area of study and the ALID, and inside the ALID itself, but it has the advantage of being easily implementable in both time and frequency domain solving in most commercially available FE packages.

One important point to note is that the introduction of damping decreases the value of the stable time increment when solving the model with the central difference explicit scheme [14]. The value of the damping at the end of the ALID is usually very large compared to values commonly used in structures. A high value of C_M causes a relatively small decrease in the stable increment whereas one of C_K usually has a very strong effect leading to a great loss in computational efficiency (e.g. time increment divided by a thousand or more). Therefore, it is preferable to avoid using C_K to define ALID with an explicit scheme. For this work, we have only used C_M for time and frequency domain studies:

$$C_M(x) = C_{Mmax} \cdot X(x)^p \text{ and } C_K(x) = 0 \tag{3·19}$$

It is easy to see that correct definition of the layer parameters (length of the layer L, variation of the attenuation parameter C_M and the power law p) is essential to achieve an efficient model.

In FE models, as the space is discretized, the gradual increase of C_M occurs by steps. The ALID is defined as a series of sub layers having the same material properties but different values of C_M. It is preferable to minimize the change in C_M between two adjacent sub layers and therefore it is recommended to have one element thick sub layers.

3.4. Efficient layer parameters' definition

The target when defining layer parameters is to achieve a good approximation of unboundedness in the area of study with the shortest absorbing layer possible. It is essential to determine a sensible acceptability criterion for the approximation of unboundedness. For this work, a layer is considered acceptable when the amplitude of waves reflected from it is smaller than 0.1% (-60dB) of the amplitude of the incident wave entering it. This value was chosen for 2 reasons. The first one is that, given that it is common for NDT applications to monitor reflection as low as 2%, a value of 0.1% gives a good ratio of reflection to signal. The second one is that one aim of this study is to validate the capacity of a technique to achieve highly accurate absorption of the incident wave. When it comes to defining a criterion for a particular model, the key is to have a high ratio between the signal of interest (e.g. reflection from defects or structural features) and the reflection from the absorbing layer. Therefore, in some models, an acceptability criterion can be as high as 5% of the incident wave. Generally, a low percentage criterion (e.g. 0.1%) leads to a thicker absorbing layer than a high percentage one (e.g.5%). Hence, an adequately chosen criterion is the first step towards achieving computational efficiency.

Running FE test cases to determine layer parameters has proved to be highly time consuming and inefficient. It would be beneficial for modellers to be able to use tools to define the layer parameters quickly, reliably and efficiently. Analytical models have therefore been created to evaluate the reflection coefficient of absorbing layers for bulk and guided waves cases. In the following parts, the explanation of what these models

represent and why layers parameters can be defined using them are given. These models guarantee the fulfilment of the acceptability criterion and greatly speed up the correct definition of layer parameters.

All the following models are defined in the frequency domain, as harmonic waves are considered, and they can be extended readily to work in the time domain. For a time domain model, the modeller needs to know the frequency content of its signal and validate the absorbing layer over the range of interest. The parts of the frequency spectrum whose amplitude is smaller than the acceptability criterion can be ignored. The rest of the frequency spectrum defines the frequency range of interest. It is advantageous to take into account the actual frequency spectrum as it relaxes the acceptability criterion for the low amplitude parts of the frequency spectrum.

3.4.1 Analytical model for bulk waves

3.4.1.1 General definition

Analytical models presented in this section have been developed to evaluate the reflection coefficient of harmonic longitudinal and shear plane waves from absorbing layers over a range of frequencies and angles. Although all models in this part are 2 dimensional, they are also valid for 3 dimensional cases. The intention is that these models can be used to validate the acceptability of a given absorbing layer for both longitudinal and shear waves over any desired range of frequencies and angles of incidence. As one considers the geometry of an area of study, it is easy to see that shear and longitudinal waves coming from a range of sources may be incident at the absorbing layers. As will be seen later, knowledge of the range of angles at which these waves are incident at the absorbing layer is one consideration needed to define the absorbing layers. The range of angles of incidence is determined by the geometry of the model and the position of wave sources such as excitation points or scatterers in the model, as illustrated in Figure 3.6.

Frequency domain technique using monochromatic plane waves rather than transient waves generated by point sources are used in the model as this greatly simplifies the approach and provides a conservative value of the reflection from the layer. In the real model, waves decay (beam spread) before reaching the absorbing layer and reflections

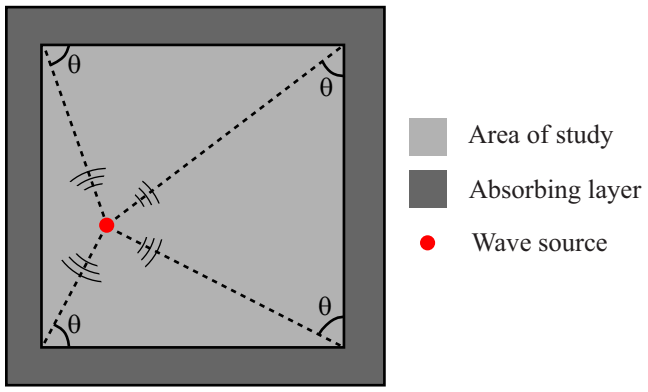

Figure 3.6. Illustration of extreme angles defining the range of angles to consider when dimensionning an absorbing layer.

spread spatially (unless the incidence is purely normal) as the reflection phenomenon will occur at different locations in the layer - see Figure 3.7. In the time domain, the reflection will also be spread in time as a consequence of the previous point.

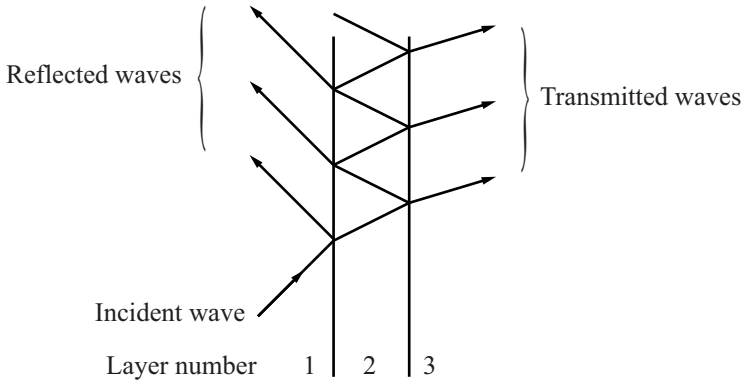

Figure 3.7. Spatial spread of the reflection and transmission for a single layer (no mode conversion shown for simplicity)

To summarize, in order to validate an absorbing layer for a given model against a certain level of reflection defined by the modeller, one can safely use an analytical model that evaluates the reflection coefficient for harmonic plane waves incident at the layer over the range of angles of incidence present in the model and the range of frequencies of interest.

3.4.1.2 Validation procedure

In order to confirm the validity of the analytical models, their results are compared with results from FE models. The challenge is to reproduce exactly the plane wave interaction with the absorbing layers. As, exceptionally in this case, the reflected amplitude from an absorbing layer is the one of interest, it is necessary to use extremely

low (-120dB) reflection ALID referred to below as "ultra" ALID in order to correctly monitor the reflection from the absorbing layer studied.

One model shown in Figure 3.8.a is used for normal incidence. This is a 2D plane strain model where the displacements on the top and bottom surfaces are constrained to zero in the vertical direction to have plane longitudinal wave propagation or in the horizontal direction to have plane shear wave propagation. The excitation is applied uniformly over the thickness of the model on one side of the area of study where an "ultra" ALID is placed. On the other side is the layer studied, either an ALID or a PML. The complex displacement is monitored along a line in the area of study and the amplitude of the incident and reflected signal are determined by performing a spatial FFT [61].

For other angles of incidence, another 2D plane strain model is defined as illustrated in Figure 3.8.b. The area of study is triangular. On one edge is the layer studied. On the other two, "ultra" ALID are placed. The excitation is uniformly applied on one edge. The displacements are monitored along 3 lines aligned with the predicted propagation direction of the incident and reflected waves. Spatial FFTs are performed to obtain reflection coefficients. Models are non-dimensional and the material is defined so that

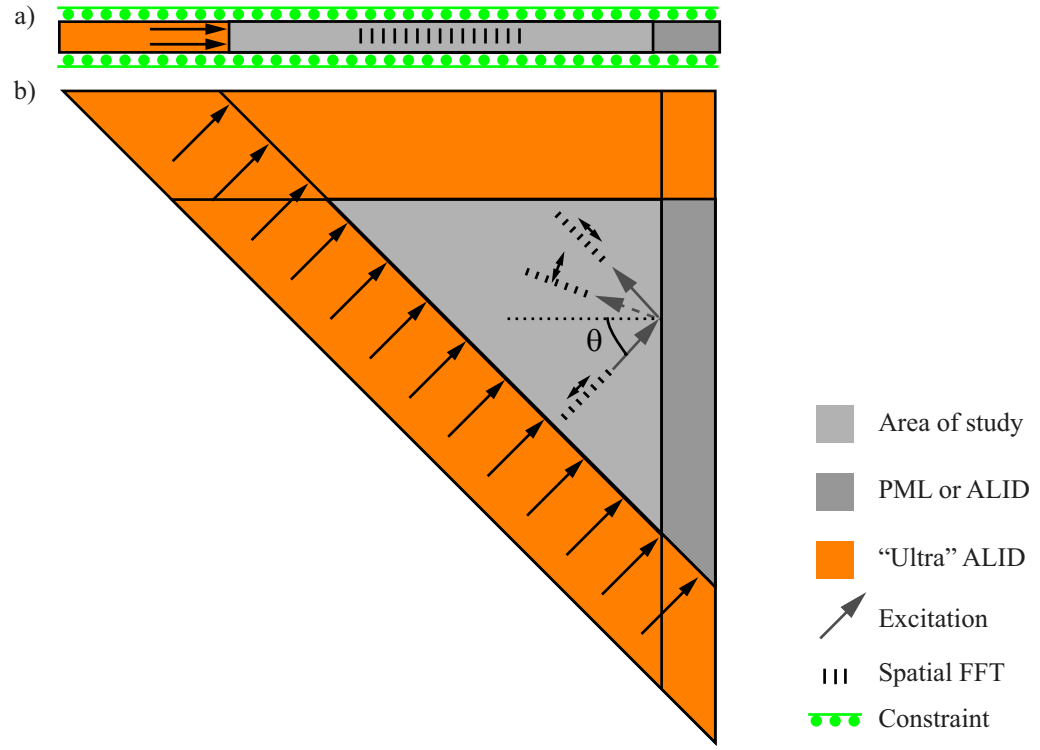

Figure 3.8. FE model used to validate the analytical models a) normal incidence model, b) angled incidence model

the longitudinal and shear wavelengths are 2 and 1 units respectively: Young's modulus is 8/3, Poisson's ratio is 1/3 and density is 1.

Shear and longitudinal wave cases are treated separately. The lengths L of the layers are L=3 for longitudinal wave incidence and L=1.5 for shear wave incidence for PML and ALID. The attenuation parameters as defined previously are A_x=1 and p=3 for PML and C_{Mmax}=10π and p=3.

Performance of the two techniques should not be compared with each other using these examples, as the layers are not optimized.

3.4.1.3 PML analytical model

The PML analytical model for bulk waves is based on the knowledge of wave decay in the PML [60] and the reflection/mode conversion occurring at the end of the PML.

The PML is defined in the x direction and α_x is defined as in equation 3·9. Waves in the PML have the following form:

$$u(x, y, t) = u_0 \exp(-i\omega t) \exp(ik(x\cos\theta + y\sin\theta)) \exp(-A_x k \cos\theta x^p) \qquad (3\cdot20)$$

where θ indicates the angle of incidence of the wave as shown in Figure 3.8. Note that the decay rates of longitudinal and shear waves are unequal as their wave numbers k differ. If the amplitude u_0 of a wave entering the PML is 1, then the amplitude of the wave after travelling the length of the PML is:

$$Amplitude = \exp\left(-A_x k \cos(\theta) \frac{L^{p+1}}{(p+1)}\right) \qquad (3\cdot21)$$

At the free end of the PML, reflection and mode conversion occurs. Calculation of the amplitude of each reflected wave is done using the stress free boundary conditions at the end of the PML:

$$\sigma_{xx} = 0 \text{ and } \sigma_{xy} = 0 \qquad (3\cdot22)$$

The reflected waves exponentially decay again over the length of the PML following equation 3·21. The theoretical reflection coefficient for bulk waves incident at a PML over a range of angles for a given case can therefore be quickly calculated using this method.

As mentioned before, in theory, no reflection should occur at the interface of, or inside, the PML. In practice, numerical experiments have shown that this does occur and is evident in extreme cases when a limited number of elements cannot accurately represent a strong decay of the wave (spatial under-sampling) induced by a large value of A_x. Figure 3.9.a presents the reflection obtained at normal incidence (θ=0) for a case where a PML with a quadratic variation of α is used. A_x is varied from 0 to 50. For low values of A_x the FE reflection coefficient at normal incidence matches the prediction of the theoretical model but as A_x increases a non-negligible numerical reflection occurs. One can see that the numerical reflection grows with A_x and is negligible for low values of A_x where the theoretical reflection is dominant.

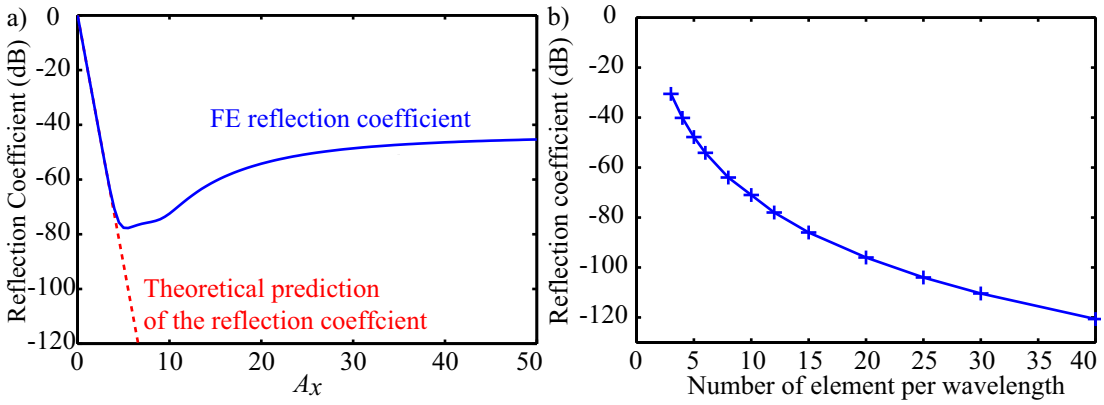

Figure 3.9. a) Reflection coefficient against Ax b) Reflection coefficient against the number of elements per wavelength.

It is also shown that the numerical reflection also depends on the number of elements per wavelength. A series of models are run while only varying the number of elements per wavelength. Results are shown in Figure 3.9.b. As the number of elements per wavelength increases, the numerical reflection decreases. Further studies have shown that the numerical reflection can also be decreased by increasing the polynomial order of the shape function of the element or reducing the decay rate per wavelength. In most cases, the element size and order are given by other parameters of the model and altering them to reduce numerical reflection would decrease computational efficiency.

Unlike the theoretical reflection which is a physical phenomenon, numerical reflection is closely linked to the numerical implementation of the model and is therefore difficult to predict. A simple pragmatic solution is proposed to avoid the problem based on physical data. In a given model, the wave which suffers the most from numerical reflection is the one with the highest wavenumber (and hence the shortest wave length) reflected at normal incidence ($\cos\theta=1$) as it is the most strongly attenuated (i.e. the decay occurs on fewer elements than any other wave).

Starting by taking a layer whose length L_{or} is equal to the shortest wavelength, the reflection coefficient is:

$$RC_{dB} = 20 \cdot \log 10\left(\exp\left(-2A_x k\frac{L^{p+1}}{(p+1)}\right)\right) \tag{3·23}$$

Numerical reflection will be minimum for the lowest value of A_x that satisfies the acceptability criterion RC_{dB}. Experience has shown that for this PML length, the calculation can be based on the theoretical value and the numerical reflection can be confidently neglected. A_x is taken equal to:

$$A_x = -0.5\frac{(p+1)}{k_{max}L_{or}{}^{p+1}}\log\left(10^{\left(\frac{RC_{dB}}{20}\right)}\right) \tag{3·24}$$

Keeping this value of A_x, the modeller can define the length of the PML so that it meets the acceptability criterion over the range of interest by using the theoretical reflection coefficients obtained with the analytical model. Clearly, L_{or} influences the final length of the PML as it limits the value of A_x. Modellers can reduce the value of L_{or} to less than the advised value but should be cautious that numerical reflection does not pollute their results.

A FE model using the parameters defined in Section 3.4.1.2 is used to verify the validity of the analytical model. The comparison of these 2 models is shown in Figure 3.10.

Looking at Figure 3.10, one can see that as expected there is no mode conversion at normal incidence ($\theta=0$). The influence of the angle of incidence is highlighted as the

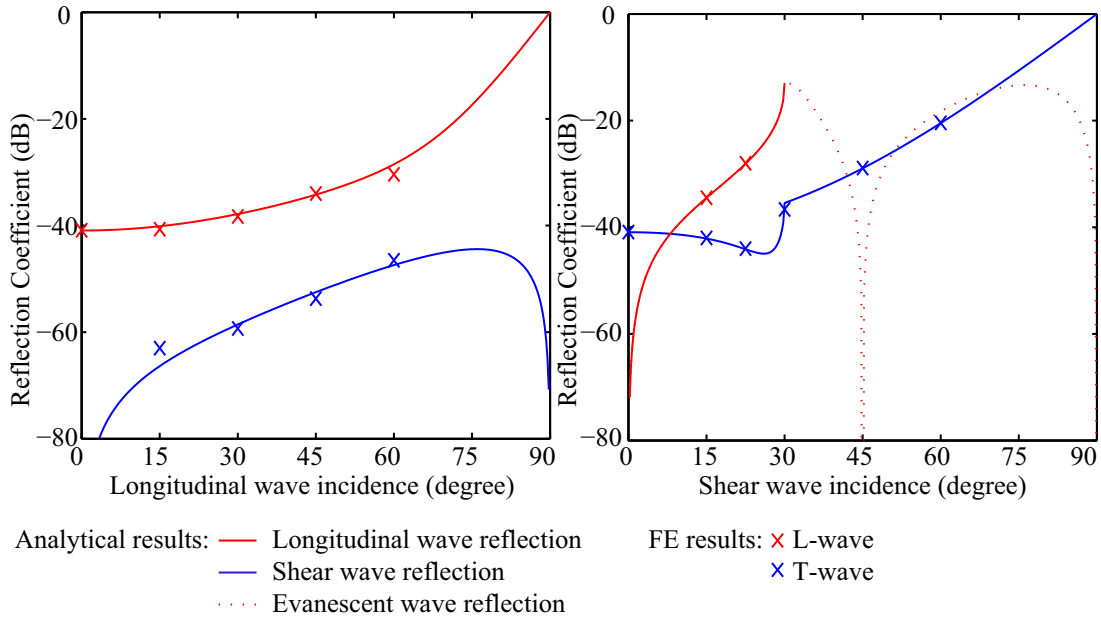

Figure 3.10. Reflection coefficient for a given PML obtained with bulk wave analytical and FE models

non converted reflection of the incident mode smoothly tends towards unity as the angle of incidence tends towards 90 degrees for both wave types. The general shape of these curves for waves at incidence above 60 degrees indicates that PMLs generally cope well with high angle incidence. This confirms that the range of angle of incidence plays a critical role in determining the layer's parameters. One can also note the presence of critical angles indicating that evanescent waves propagating along the back surface of the PML and decaying perpendicularly to the free surface (likely to be a Rayleigh wave) are generated. No reflection of this wave type has been noticed in the area of study. Overall, there is an excellent agreement between the FE model results and the prediction obtained with the analytical model. This confirms that the analytical model can be used to define PML parameters.

This analytical model enables the quick evaluation of the acceptability of a given PML for a particular model. Experience has shown that a small value of p, the variable defining the power dependence, is usually preferable. Combined with previous comments concerning this variable, it is recommended to use: $2 \le p \le 3$. No great gain in model efficiency can be achieved by optimizing p. It is advised to only concentrate on minimising L for the recommended A_x. In the cases where time domain results are required, it is advantageous to take into account the shape of the frequency spectrum.

3.4.1.4 ALID analytical model

The ALID analytical model for bulk waves is based on a multi-layered approach. As space is discretized in a FE model, the ALID is considered as a series of sub layers (referred to as layers in this Section) with increasing damping. The variation of C_M is implemented by changing its value in each of these layers. Using layers one element thick is the thinnest possible and clearly minimizes the change in damping between any 2 consecutive layers. It is of course not a problem to use layers several elements thick, but best results were obtained with the thinnest layer possible. The ALID can be analytically modelled using the continuity of displacements and stresses at the interface of each of these layers. Such an analytical model will enable a modeller to easily optimize the layer parameters.

Let us consider a multi-layered system. We define the displacement and stresses at the front and back with the subscript *f (front)* or *b (back)*. At the front of layer *n*, the following equations are valid:

$$\begin{bmatrix} u_{x[n]f} \\ u_{y[n]f} \\ \sigma_{xx[n]f} \\ \sigma_{xy[n]f} \end{bmatrix} = \begin{bmatrix} u_{[n]f} \\ \sigma_{[n]f} \end{bmatrix} \tag{3·25}$$

$$\begin{bmatrix} \Phi_{p[n]} \\ \Psi_{p[n]} \\ \Phi_{n[n]} \\ \Psi_{n[n]} \end{bmatrix} = \begin{bmatrix} P_{[n]} \\ N_{[n]} \end{bmatrix} \tag{3·26}$$

$$M_{[n]f} = \begin{bmatrix} M_{P[n]f} \, M_{N[n]f} \end{bmatrix} \tag{3·27}$$

$$\text{and} \begin{bmatrix} u_{[n]f} \\ \sigma_{[n]f} \end{bmatrix} = \begin{bmatrix} M_{P[n]f} \, M_{N[n]f} \end{bmatrix} \begin{bmatrix} P_{[n]} \\ N_{[n]} \end{bmatrix} \tag{3·28}$$

At the interface between layer n and n-1, there is continuity of displacements and stresses:

$$\begin{bmatrix} u_{[n-1]b} \\ \sigma_{[n-1]b} \end{bmatrix} = \begin{bmatrix} u_{[n]f} \\ \sigma_{[n]f} \end{bmatrix} \tag{3·29}$$

Several techniques exist to deal with wave propagation through multi-layered systems [37]. The technique used in this section is based on the one used by Pialucha [62]. It does not use a transfer matrix but a global matrix algorithm; amplitudes of the waves are calculated at each interface in the system. The strength of the technique is that instabilities are removed by placing the origin of all waves at their entry point in the layer.

Based on equation 2·26, this leads to:

$$M_{[n]f} = \begin{bmatrix} ik_{Lx} & -ik_{Sy} & -ik_{Lx}e^{ik_{Lx}x} & -ik_{Sy}e^{ik_{Sx}x} \\ ik_{Ly} & ik_{Sx} & ik_{Ly}e^{ik_{Lx}x} & -ik_{Sx}e^{ik_{Sx}x} \\ -(\lambda k^2 + 2\mu k_{Ly}^2) & 2\mu k_{Sx}k_{Sy} & -(\lambda k^2 + 2\mu k_{Ly}^2)e^{ik_{Lx}x} & -2\mu k_{Sx}k_{Sy}e^{ik_{Sx}x} \\ -2\mu k_{Lx}k_{Ly} & -2\mu(k_{Sx}^2 - k_{Sy}^2) & 2\mu k_{Lx}k_{Ly}e^{ik_{Lx}x} & -2\mu(k_{Sx}^2 - k_{Sy}^2)e^{ik_{Sx}x} \end{bmatrix}, \tag{3·30}$$

$$M_{[n]b} = \begin{bmatrix} ik_{Lx}e^{ik_{Lx}x} & -ik_{Sy}e^{ik_{Sx}x} & -ik_{Lx} & -ik_{Sy} \\ ik_{Ly}e^{ik_{Lx}x} & ik_{Sx}e^{ik_{Sx}x} & ik_{Ly} & -ik_{Sx} \\ -(\lambda k^2 + 2\mu k_{Ly}^2)e^{ik_{Lx}x} & 2\mu k_{Sx}k_{Sy}e^{ik_{Sx}x} & -(\lambda k^2 + 2\mu k_{Ly}^2) & -2\mu k_{Sx}k_{Sy} \\ -2\mu k_{Lx}k_{Ly}e^{ik_{Lx}x} & -2\mu(k_{Sx}^2 - k_{Sy}^2)e^{ik_{Sx}x} & 2\mu k_{Lx}k_{Ly} & -2\mu(k_{Sx}^2 - k_{Sy}^2) \end{bmatrix} \tag{3·31}$$

At the back of layer n, displacements and stresses are:

$$\begin{bmatrix} u_{[n]b} \\ \sigma_{[n]b} \end{bmatrix} = M_{[n]b} \begin{bmatrix} P_{[n]} \\ N_{[n]} \end{bmatrix} \tag{3·32}$$

At the front of layer n+1, displacements and stresses are:

$$\begin{bmatrix} u_{[n+1]f} \\ \sigma_{[n+1]f} \end{bmatrix} = M_{[n+1]f} \begin{bmatrix} P_{[n+1]} \\ N_{[n+1]} \end{bmatrix} \tag{3·33}$$

As there is continuity of stresses and displacements - see equation 3·29, the following equation is defined:

$$M_{[n]b} \begin{bmatrix} P_{[n]} \\ N_{[n]} \end{bmatrix} = M_{[n+1]f} \begin{bmatrix} P_{[n+1]} \\ N_{[n+1]} \end{bmatrix} \tag{3·34}$$

$$\text{hence } M_{[n]b} \begin{bmatrix} P_{[n]} \\ N_{[n]} \end{bmatrix} - M_{[n+1]f} \begin{bmatrix} P_{[n+1]} \\ N_{[n+1]} \end{bmatrix} = 0 \tag{3·35}$$

In the layered system, it becomes:

$$M_{[1]b} \begin{bmatrix} P_{[1]} \\ N_{[1]} \end{bmatrix} - M_{[2]f} \begin{bmatrix} P_{[2]} \\ N_{[2]} \end{bmatrix} = 0 \tag{3·36}$$

$$M_{[2]b} \begin{bmatrix} P_{[2]} \\ N_{[2]} \end{bmatrix} - M_{[3]f} \begin{bmatrix} P_{[3]} \\ N_{[3]} \end{bmatrix} = 0 \tag{3·37}$$

and so on...

P[1] is known as it is the model input. Equation 3·32 can be rewritten as:

$$\begin{bmatrix} M_{P[1]b} & M_{N[1]b} \end{bmatrix} \begin{bmatrix} P_{[1]} \\ N_{[1]} \end{bmatrix} - M_{[2]f} \begin{bmatrix} P_{[2]} \\ N_{[2]} \end{bmatrix} = 0 \tag{3·38}$$

$$\begin{bmatrix} M_{N[1]b} \end{bmatrix} \begin{bmatrix} N_{[1]} \end{bmatrix} - M_{[2]f} \begin{bmatrix} P_{[2]} \\ N_{[2]} \end{bmatrix} = - \begin{bmatrix} M_{P[1]b} \end{bmatrix} \begin{bmatrix} P_{[1]} \end{bmatrix} \tag{3·39}$$

At the back of the last layer n:

$$\left[\sigma_{[n]b}\right] = 0 \tag{3·40}$$

$$\text{hence } L_{[n]b}\begin{bmatrix} P_{[n]} \\ N_{[n]} \end{bmatrix} = 0 \tag{3·41}$$

with

$$L_{[n]b} = \begin{bmatrix} -(\lambda k^2 + 2\mu k_{Ly}^2)e^{ik_{Lx}x} & 2\mu k_{Sx}k_{Sy}e^{ik_{Sx}x} & -(\lambda k^2 + 2\mu k_{Ly}^2) & -2\mu k_{Sx}k_{Sy} \\ -2\mu k_{Lx}k_{Ly}e^{ik_{Lx}x} & -2\mu(k_{Sx}^2 - k_{Sy}^2)e^{ik_{Sx}x} & 2\mu k_{Lx}k_{Ly} & -2\mu(k_{Sx}^2 - k_{Sy}^2) \end{bmatrix} \tag{3·42}$$

The complete multi-layered system can be written in a global matrix:

$$\begin{bmatrix} \left[M_{N[1]b}\right] & \left[-M_{[2]f}\right] & 0 & \cdots & 0 \\ 0 & \left[M_{[2]b}\right] & \left[-M_{[3]f}\right] & \cdots & 0 \\ \cdots & \cdots & \cdots & \cdots & 0 \\ 0 & 0 & 0 & \left[M_{[n-1]b}\right] & \left[-M_{[n]f}\right] \\ 0 & 0 & 0 & 0 & \left[L_{[n]b}\right] \end{bmatrix} \begin{bmatrix} \left[N_{[1]}\right] \\ \begin{bmatrix} P_{[2]} \\ N_{[2]} \end{bmatrix} \\ \cdots \\ \begin{bmatrix} P_{[n-1]} \\ N_{[n-1]} \end{bmatrix} \\ \begin{bmatrix} P_{[n]} \\ N_{[n]} \end{bmatrix} \end{bmatrix} = \begin{bmatrix} -\left[M_{P[1]f}\right]\left[P_{[1]}\right] \\ 0 \\ \cdots \\ 0 \\ 0 \end{bmatrix} \tag{3·43}$$

By solving this system, $[N_{[1]}]$ is obtained. It gives the amplitude of the wave potentials reflected into the first layer (the area of study in the FE model). The amplitude of the wave displacements is therefore derived from this data using the expressions defined in Section 2.2.1. Finally, reflection coefficients are deduced from this.

Results for a sample case are compared with the FE models and are presented in Figure 3.11.

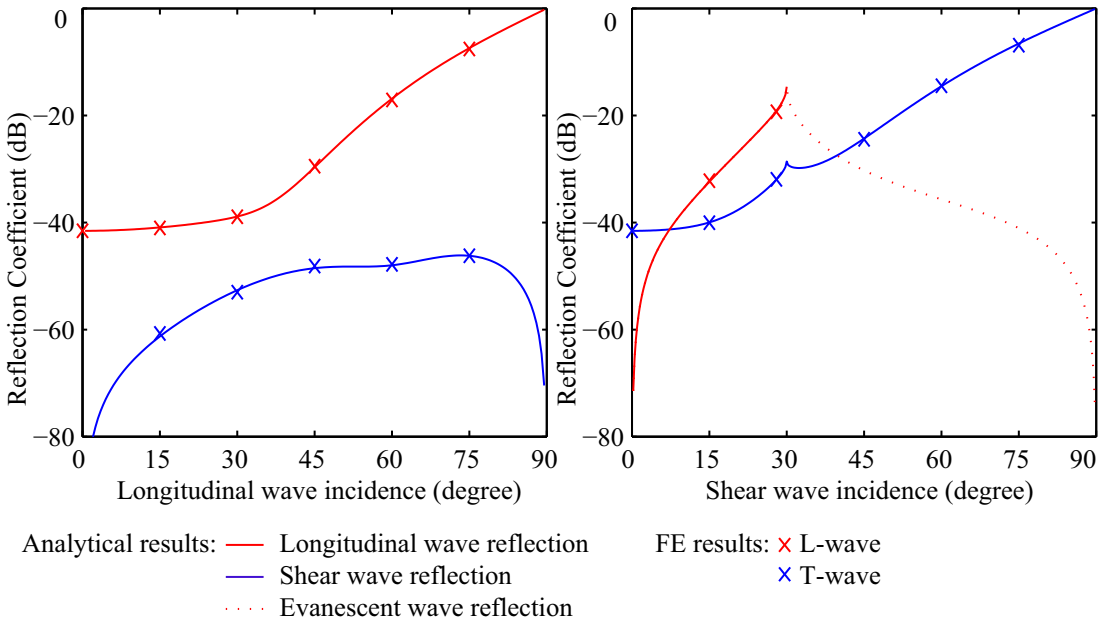

Figure 3.11. Reflection coefficient for a given ALID obtained with bulk wave analytical and FE models

There is an excellent agreement between the FE and analytical results. As for the PML case, one can note the importance of the range of angle of incidence in validating the acceptability criterion. Although the ALID and PML used in this section should not be quantitatively compared, the general shape of the curves in Figure 3.10 and 3.11 at high angles of incidence indicates that the efficiency of absorbing layers for both non mode converted reflected waves deteriorates faster for ALID than PML at these angles. Therefore ALID can be considered as more sensitive to high angles of incidence than PML. The presence of a critical angle for incident shear waves is also noticeable and should be considered when validating the layer.

The excellent agreement between FE and analytical model confirms that the analytical model can be used in the process of quickly determining the ALID parameters. When defining an ALID, we recommended to use a value of p equal to 3 and find the right combination of thickness and C_{Mmax} to minimize the thickness of the ALID.

For time domain models, the frequency spectrum of a signal is not constant. Taking this into account relaxes the constraints to define an acceptable layer and therefore leads to thinner layers.

3.4.2 Analytical model for 2D guided wave cases

The aim of the analytical model for guided wave cases is to evaluate the reflection coefficient of guided waves from a given absorbing layer over a range of frequencies. This part presents the case of guided waves in a 2D plate. The same approach could readily be taken for wave guiding phenomena in pipes or cylinders.

3.4.2.1 Consideration for guided wave PML implementation

In an elastic medium, modes are defined by the following equation:

$$u(x, y, t) = u_x(y)e^{i(k_x x - \omega t)} \tag{3·44}$$

In the PML, this equation becomes:

$$u(x, y, t) = u_x(y)e^{i(k_x x - \omega t)}e^{-A_x k_x \frac{x^p}{L^p}} \tag{3·45}$$

As mentioned above, in an elastic wave guide, k_x can be real, imaginary or complex. When k_x is a real number, the wave behaves in the same way as a bulk wave: the wave enters the PML without reflection and decays inside it.

It is important to mention that PMLs have not been created for evanescent waves (imaginary or complex wavenumber) and do not work well with them [63, 64]. At best, the natural decay of these waves carry on as they propagate in the PML. Let us take the example of a wave with an imaginary wave number k_x=i.k with k a real number. In the PML, the wave is described by:

$$u(x, y, t) = u_x(y)e^{-i\omega t}e^{-k_x x}e^{-iA_x k \frac{x^p}{L^p}} \tag{3·46}$$

The decay is the same as in the elastic area so the wave continues its normal decay in the PML but now there is also a propagating part added to it. This part varies in the PML and leads to a change in impedance. This can also lead to spatial under sampling causing numerical reflection. This confirms that PML is not suited to evanescent modes. A large amount of research has been done regarding this issue in the domain of electromagnetism [65, 66, 67]. Evanescent waves by essence decay and usually do so

rapidly so they are usually very localised in practical cases. A pragmatic approach is therefore to make sure that PML are placed so that only evanescent waves of negligible amplitude (which have sufficiently decayed) reach them or that their potential reflection from the PML will not influence the area of interest in the model.

Another type of guided wave which has proved to be problematic with PML is backwardly propagating modes which in essence are waves whose group and phase velocities are of opposing signs. A backward travelling wave incident at a PML will have a negative wave number k_x=-k with k a real positive number. In the PML, the wave is hence described by:

$$u(x, y, t) = u_x(y) e^{i(-kx - \omega t)} e^{A_x k \frac{x^p}{L^p}} \tag{3·47}$$

It is easy to see that this expression will lead to the wave growing exponentially inside the PML, instead of decaying, which clearly is a problem.

Since these waves only occur over a very limited range of frequencies, which usually is of no practical interest in NDE applications, one way of avoiding the problem is simply to avoid these frequencies. This can be achieved easily in the PML implementation presented here as the models are solved in the frequency domain. A study performed at Imperial College [68] showed that it is possible to fix the problem by performing a modal decomposition using the bi-orthogonality relations of the guided modes [69] and channelling them to separate PMLs defined such that all wave types are absorbed correctly. This is an attractive approach in cases where access to the coding is possible, but is out of reach for the standard packages used in this study. If the frequency range of study includes the possibility of backwardly propagating waves, one pragmatic alternative is to use ALID instead of PML as ALID does not have any difficulty absorbing backwardly propagating waves.

3.4.2.2 Validation procedure

In order to confirm the validity of the analytical models, their results are compared with results from FE models. 2D plane strain models shown in Figure 3.12 are used. As for bulk waves, the use of “ultra” ALID is necessary. The excitation is applied over the

thickness of the model on one side of the area of study where an "ultra" ALID is placed. On the other side is the layer studied, either an ALID or a PML. The displacement is monitored along a line in the area of study and the amplitude of the incident and reflected signal are determined by performing a 2D FFT.

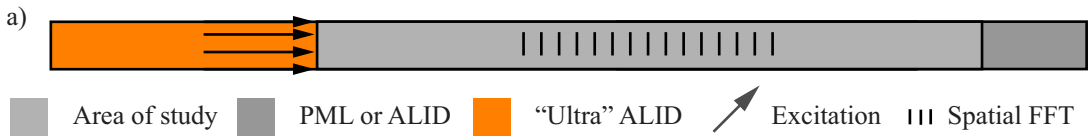

Figure 3.12. FE model used to validate the guided wave analytical models.

The plate is 8mm thick and made of aluminium (ρ=2780kg/m3, E=70GPa, ν=0.33). It is excited at frequencies ranging from 114kHz to 186kHz. At these frequencies, the two fundamental modes, A0 and S0, are studied. For these cases, the PMLs are defined with L= 13.1mm, A_x=2.66e6 and p=3 for S0 and L= 6.55mm, A_x=2.66e6 and p=3 for A0. The ALID are defined with L= 13.1mm, C_{Mmax}=2.66e6 and p=3 for S0 and L= 76.5mm, C_{Mmax}=1e6 and p=3 for A0.

Performance of the two techniques should not be compared using these examples as the layers are not optimized.

3.4.2.3 PML analytical model for guided wave cases

The analytical model used to determine the reflection coefficient of a PML is based on the knowledge of the decay of the mode in the layer and the reflection of modes at the end of the layer.

Propagating modes are treated using a model similar to the PML bulk wave model. One difference is that any mode conversion that may occur at the end of the PML is not taken into account in the analytical model and total reflection is assumed. Each propagating mode is considered independently. The reflection coefficient for each propagating mode is equal to:

$$RC_{dB} = 20 \cdot \log 10 \exp\left(-2A_x k \frac{L^{p+1}}{(p+1)}\right) \qquad (3\cdot48)$$

As for the case of bulk waves, the issue of numerical reflection needs to be taken into account. In a given model, the wave which suffers the most from numerical reflection

is the one with the highest wave number (and hence the shortest wave length) as it is the most strongly attenuated (i.e.: the decay occurs on fewer elements than the other waves).

As a starting point, a layer whose length L_{or} is equal to the shortest wavelength is taken. Numerical reflection will be the lowest for the lowest value of A_x that satisfies the acceptability criterion RC_{dB}. Experience has shown that for this PML length, the calculation can be based on the theoretical value and the numerical reflection can be confidently neglected. A_x is taken equal to:

$$A_x = -0.5\frac{(p+1)}{k_{max}{L_{or}}^{p+1}}\log\left(10^{\left(\frac{RC_{dB}}{20}\right)}\right) \tag{3·49}$$

Keeping this value of A_x, all the other waves will be less strongly attenuated. The wave with the longest wavelength (and so the shortest wave number) will have the slowest decay in the layer. In order to correctly define the PML over the range of wave numbers, the length of the layer for the previously defined A_x is increased to achieve the theoretical reflection criterion using the following formula:

$$L_{PML} = \left(-0.5\frac{(p+1)}{k_{min}A_x}\log\left(10^{\left(\frac{RC_{dB}}{20}\right)}\right)\right)^{\frac{1}{p+1}} \tag{3·50}$$

Using equation 3·49 and 3·50, the length of the PML is:

$$L_{PML} = L_{or}\left(\frac{k_{max}}{k_{min}}\right)^{\frac{1}{p+1}} \tag{3·51}$$

Validating that the reflection coefficient is acceptable for each propagating mode ensures that the PML is correctly defined. As mentioned before, this formula is only valid for propagating modes. Evanescent and backwardly propagating modes need to be dealt with separately.

Clearly, L_{or} directly influences the final length of the PML but this can be reduced to less than the advised value if required although caution is necessary in this case. The

formula also highlights that the final length of the PMLs depends on the ratio of the extreme wave numbers. High ratios typically occur at frequencies just above cut-off and lead to potentially long PMLs.

As shown previously, evanescent waves are not correctly dealt with by PMLs and it is necessary to make sure they do not have a significant impact on the displacement field of the area of study. The evanescent wave with the smallest imaginary part k''_{min} (which has the lowest decay rate) is considered. Its amplitude is conservatively taken equal to 1 at any feature which can generate evanescent waves (e.g. defect, source). It is also conservatively considered that an evanescent wave incident at a PML would be totally reflected. In order to have an acceptable displacement field between the PML and the feature, the wave needs to have decayed sufficiently (i.e. its amplitude is equal to RC_{dB}) when it reaches the PML.

The distance between the feature and the PML needs to be:

$$L = -\frac{1}{k''_{min}} \log\left(10^{\left(\frac{RC_{dB}}{20}\right)}\right) \tag{3·52}$$

In cases where the displacement field between the PML and the feature is not monitored, one can use:

$$L = -\frac{1}{2k''_{min}} \log\left(10^{\left(\frac{RC_{dB}}{20}\right)}\right) \tag{3·53}$$

In these cases, the wave amplitude is equal to RC_{dB} as it reaches the feature after being reflected and is therefore acceptable.

Results from the analytical model are compared with FE results obtained for the first fundamental propagating modes A0 and S0 with the parameters defined in Section 3.4.2.2. Figure 3.13 shows that there is an excellent agreement between both sets of results and validates the use of the analytical approach to dimension PMLs for guided waves.

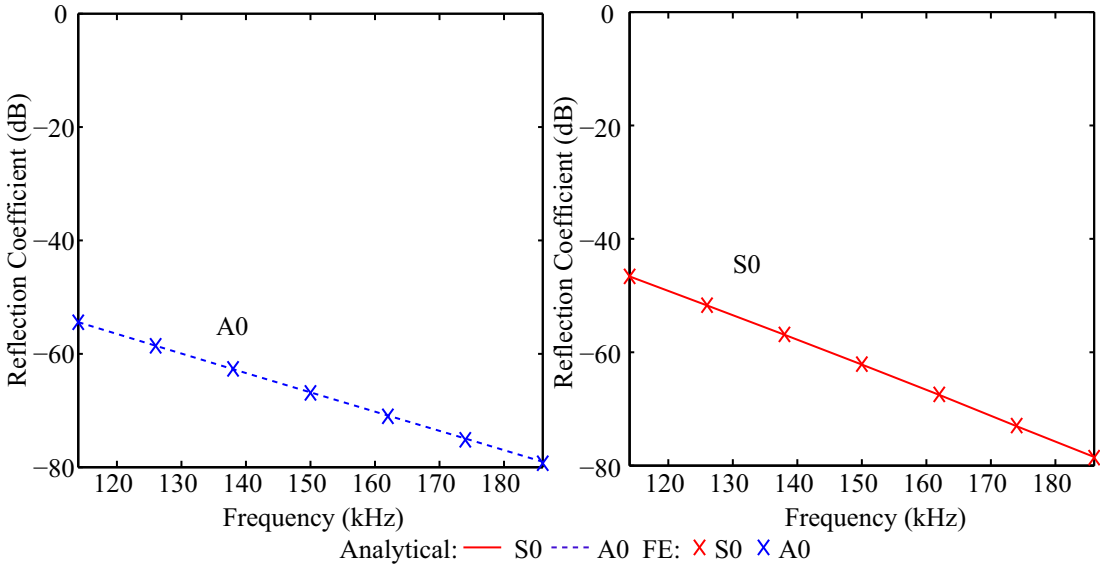

Figure 3.13. Reflection coefficient for a given PML obtained with guided wave analytical and FE models

3.4.2.4 ALID analytical model

The following analytical model determines the reflection coefficient of ALID for guided waves in plates modelled in 2D plane strain. It is based on a multi-layered approach and makes use of an impedance matrix.

An infinity of modes can exist in a given guided wave system. A finite number of modes are selected. This selection is based on the characteristics of the wave number of the mode in the elastic part of the model. All real (propagating) and imaginary (evanescent) modes and a finite number of complex modes (inhomegeneous) are included in the model. As explained before, each layer in the ALID has the same elastic properties as the area of study save for having a gradually increasing damping. As for bulk waves, the damping causes the properties of the waves to vary as they propagate through the ALID. The actual properties of modes existing in each layer inside an ALID need to be calculated by solving the Rayleigh equation using the properties of each layer. All modes have a complex wave number in the ALID. As for bulk waves, the real part of the wave number varies as the damping is increased, leading to a change of acoustic impedance inside the layer and therefore causing reflection. Contrary to the PML, due to the physical properties of the ALID materials, all modes including backwardly propagating modes decay in the ALID [31].

In guided wave cases as in bulk wave cases, ALID can be seen as a series of finite layers with varying properties. In 2D, the symmetric and anti-symmetric modes can be treated independently as ALID are symmetric with respect to the mid plane of the plate.

The model defined in this section is a development of a model by Pagneux [70]. The idea is to define a global impedance matrix of the ALID that can be used to determine reflection coefficients. The matrix is defined starting from the end of the ALID and propagated through each layer and each interface between these layers until the area of study. Let us consider a multi layered system as represented in Figure 3.14 where layer 1 represents the area of study.

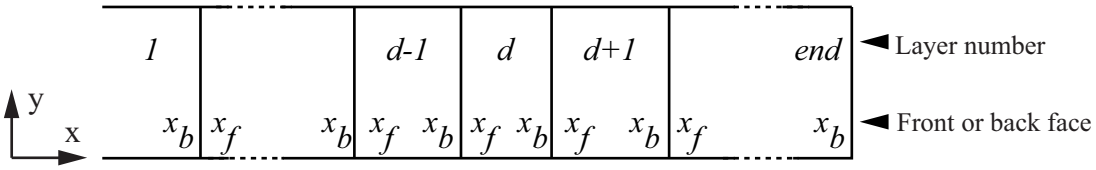

Figure 3.14. Definition of the multi layered system

One starts by noting that at any point in the plate and ALID the total displacements and stresses (subscript *tot*) are equal to the sum of the displacement and stresses of the modes travelling in the positive (*po*) and the negative (*ne*) *x*-direction. Combining this with the symmetry properties of the Lamb wave mode shape, we have:

$$\begin{bmatrix} u_{x(tot)}(x,y) \\ u_{y(tot)}(x,y) \\ \sigma_{xx(tot)}(x,y) \\ \sigma_{xy(tot)}(x,y) \end{bmatrix} = \begin{bmatrix} u_{x(po)}(x,y) \\ u_{y(po)}(x,y) \\ \sigma_{xx(po)}(x,y) \\ \sigma_{xy(po)}(x,y) \end{bmatrix} + \begin{bmatrix} u_{x(ne)}(x,y) \\ u_{y(ne)}(x,y) \\ \sigma_{xx(ne)}(x,y) \\ \sigma_{xy(ne)}(x,y) \end{bmatrix} \tag{3·54}$$

$$\text{with} \begin{bmatrix} u_{x(po)}(x,y) \\ u_{y(po)}(x,y) \\ \sigma_{xx(po)}(x,y) \\ \sigma_{xy(po)}(x,y) \end{bmatrix} = \sum_{1}^{n} A_n(x) \begin{bmatrix} u_x^n(y) \\ u_y^n(y) \\ \sigma_{xx}^n(y) \\ \sigma_{xy}^n(y) \end{bmatrix} \tag{3·55}$$

$$\text{and} \begin{bmatrix} u_{x(ne)}(x,y) \\ u_{y(ne)}(x,y) \\ \sigma_{xx(ne)}(x,y) \\ \sigma_{xy(ne)}(x,y) \end{bmatrix} = \sum_{1}^{n} B_n(x) \begin{bmatrix} -u_x^n(y) \\ u_y^n(y) \\ \sigma_{xx}^n(y) \\ -\sigma_{xy}^n(y) \end{bmatrix} \tag{3·56}$$

One defines $a_n(x) = A_n(x) - B_n(x)$ and $b_n(x) = A_n(x) + B_n(x)$, so equation 3·54 can be expressed by:

$$\begin{bmatrix} u_{x(tot)}(x,y) \\ \sigma_{xx(tot)}(x,y) \end{bmatrix} = \sum_{1}^{n} a_n(x) \begin{bmatrix} u_x^n(y) \\ \sigma_{xx}^n(y) \end{bmatrix} \text{and} \begin{bmatrix} u_{y(tot)}(x,y) \\ \sigma_{xy(tot)}(x,y) \end{bmatrix} = \sum_{1}^{n} b_n(x) \begin{bmatrix} u_y^n(y) \\ \sigma_{xy}^n(y) \end{bmatrix} \tag{3·57}$$

One defines $a(x) = \begin{bmatrix} a_1(x) & \dots & a_n(x) \end{bmatrix}^T$ and $b(x) = \begin{bmatrix} b_1(x) & \dots & b_n(x) \end{bmatrix}^T$ and the impedance matrix as:

$$a(x) = Z(x)b(x) \tag{3·58}$$

Inside a layer, the impedance matrix can be propagated between the back (*b*) and the front (*f*) of a layer *d*. One has:

$$A_n^d(x_f) = A_n^d(x_b)\exp(ik_n(x_f - x_b)) \text{ and } B_n^d(x_f) = B_n^d(x_b)\exp(ik_n(x_f - x_b)) \tag{3·59}$$

therefore:

$$\begin{bmatrix} a^d(x_f) \\ b^d(x_f) \end{bmatrix} = \begin{bmatrix} C & iS \\ iS & C \end{bmatrix} \begin{bmatrix} a^d(x_b) \\ b^d(x_b) \end{bmatrix} \tag{3·60}$$

with *C* and *S*, diagonal matrices made of $\cos(k_n(x_f - x_b))$ and $\sin(k_n(x_f - x_b))$ elements respectively.

The link between $Z^d(x_f)$ and $Z^d(x_b)$ is:

$$Z^d(x_f) = \left[iS + CZ^d(x_b)\right]\left[C + iSZ^d(x_b)\right]^{-1} \tag{3·61}$$

This formulation shows instabilities [70] and the following equation is a better alternative:

$$Z^d(x_f) = -iT^{-1} + S^{-1}\left[Z^d(x_b) - iT^{-1}\right]^{-1} S^{-1} \tag{3·62}$$

with T, a diagonal matrix made of $\tan(k_n(x_f - x_b))$ elements.

At the boundary between the back face of layer d and the front face of layer d+1, one has:

$$\sum_1^n a_n^d(x_b)\begin{bmatrix} u_x^{n,d}(y) \\ \sigma_{xx}^{n,d}(y) \end{bmatrix} = \sum_1^n a_n^{d+1}(x_f)\begin{bmatrix} u_x^{n,d+1}(y) \\ \sigma_{xx}^{n,d+1}(y) \end{bmatrix} \tag{3·63}$$

$$\sum_1^n b_n^d(x_b)\begin{bmatrix} -\sigma_{xy}^{n,d}(y) \\ u_y^{n,d}(y) \end{bmatrix} = \sum_1^n b_n^{d+1}(x_f)\begin{bmatrix} -\sigma_{xy}^{n,d+1}(y) \\ u_y^{n,d+1}(y) \end{bmatrix} \tag{3·64}$$

These expressions are multiplied by $\left[-\sigma_{xy}^{m,d}(y)\ u_y^{m,d}(y)\right]^T$ and $\left[u_x^{m,d+1}(y)\ \sigma_{xx}^{m,d+1}(y)\right]^T$ respectively and integrated over the thickness of the plate:

$$\sum_1^n a_n^d(x_b)\int_{-h}^{h}\begin{bmatrix} u_x^{n,d}(y) \\ \sigma_{xx}^{n,d}(y) \end{bmatrix}\cdot\begin{bmatrix} -\sigma_{xy}^{m,d}(y) \\ u_y^{m,d}(y) \end{bmatrix} dy = \sum_1^n a_n^{d+1}(x_f)\int_{-h}^{h}\begin{bmatrix} u_x^{n,d+1}(y) \\ \sigma_{xx}^{n,d+1}(y) \end{bmatrix}\cdot\begin{bmatrix} -\sigma_{xy}^{m,d}(y) \\ u_y^{m,d}(y) \end{bmatrix} dy \tag{3·65}$$

$$\sum_1^n b_n^d(x_b)\int_{-h}^{h}\begin{bmatrix} u_x^{m,d+1}(y) \\ \sigma_{xx}^{m,d+1}(y) \end{bmatrix}\cdot\begin{bmatrix} -\sigma_{xy}^{n,d}(y) \\ u_y^{n,d}(y) \end{bmatrix} dy = \sum_1^n b_n^{d+1}(x_f)\int_{-h}^{h}\begin{bmatrix} u_x^{m,d+1}(y) \\ \sigma_{xx}^{m,d+1}(y) \end{bmatrix}\cdot\begin{bmatrix} -\sigma_{xy}^{n,d+1}(y) \\ u_y^{n,d+1}(y) \end{bmatrix} dy \tag{3·66}$$

One has:

$$a^d(x_b)J_{n,m}^{d,d} = a^{d+1}(x_f)J_{n,m}^{d,d+1} \tag{3·67}$$

$$b^d(x_b)J_{m,n}^{d+1,d} = b^{d+1}(x_f)J_{m,n}^{d+1,d+1} \tag{3·68}$$

The analytical expression of the matrices coefficients is calculated analytically as the stresses and displacements in the plate are known. Using the last two equations, the impedance matrices of layer d and d+1 are linked:

$$\left[a^{d}(x_b)\right] = \left[a^{d+1}(x_f)\right]\left[J^{d,\,d+1}_{n,\,m}\right]\left[J^{d,\,d}_{n,\,m}\right]^{-1} \tag{3·69}$$

$$\left[b^{d}(x_b)\right]^{-1} = \left[b^{d+1}(x_f)\right]^{-1}\left[J^{d+1,\,d+1}_{m,\,n}\right]^{-1}\left[J^{d,\,d+1}_{m,\,n}\right] \tag{3·70}$$

$$Z^{d}(x_b) = \left[a^{d}(x_b)\right]\left[b^{d}(x_b)\right]^{-1} = Z^{d+1}(x_f)\left[J^{d,\,d+1}_{n,\,m}\right]\left[J^{d,\,d}_{n,\,m}\right]^{-1}\left[J^{d+1,\,d+1}_{m,\,n}\right]^{-1}\left[J^{d+1,\,d}_{m,\,n}\right] \tag{3·71}$$

The bi-orthogonality relation [69, 71] leads to:

$$J^{d,\,d}_{n,\,m} = J^{d,\,d}_{n,\,m}\delta_{n,\,m} \tag{3·72}$$

The final missing part to describe an ALID is the determination of the behaviour at the end of the last layer. At this point, there is a stress free condition:

$$\sigma^{end}_{xx(tot)}(x_b) = 0 \text{ and } \sigma^{end}_{xy(tot)}(x_b) = 0 \tag{3·73}$$

$$\begin{bmatrix}\sigma^{end}_{xx(tot)}(x_b, y)\\ \sigma^{end}_{xy(tot)}(x_b, y)\end{bmatrix} = \begin{bmatrix}\sigma^{end}_{xx(po)}(x_b, y)\\ \sigma^{end}_{xy(po)}(x_b, y)\end{bmatrix} + \begin{bmatrix}\sigma^{end}_{xx(ne)}(x_b, y)\\ \sigma^{end}_{xy(ne)}(x_b, y)\end{bmatrix} = 0 \tag{3·74}$$

$$\sum_{1}^{n} A^{end}_{n}(x_b)\begin{bmatrix}\sigma^{n,\,end}_{xx}(y)\\ \sigma^{n,\,end}_{xy}(y)\end{bmatrix} + \sum_{1}^{n} B^{end}_{n}(x_b)\begin{bmatrix}\sigma^{n,\,end}_{xx}(y)\\ -\sigma^{n,\,end}_{xy}(y)\end{bmatrix} = 0 \tag{3·75}$$

$$\sum_{1}^{n} a^{end}_{n}(x_b)\begin{bmatrix}0\\ \sigma^{n,\,end}_{xy}(y)\end{bmatrix} + \sum_{1}^{n} b^{end}_{n}(x_b)\begin{bmatrix}\sigma^{n,\,end}_{xx}(y)\\ 0\end{bmatrix} = 0 \tag{3·76}$$

One multiplies equation 3·76 by: $\left[u_x^{m,\,end}(y)\;\; u_y^{m,\,end}(y)\right]^T$ and integrates through the thickness

$$\sum_1^n a_n^{end}(x_b)\int_{-h}^{h}\begin{bmatrix}0\\ \sigma_{xy}^{n,\,end}(y)\end{bmatrix}\cdot\begin{bmatrix}u_x^{m,\,end}(y)\\ u_y^{m,\,end}(y)\end{bmatrix}dy+\sum_1^n b_n^{end}(x_b)\int_{-h}^{h}\begin{bmatrix}\sigma_{xx}^{n,\,end}(y)\\ 0\end{bmatrix}\cdot\begin{bmatrix}u_x^{m,\,end}(y)\\ u_y^{m,\,end}(y)\end{bmatrix}dy\;=\;0 \tag{3·77}$$

$$a^{end}(x_b)G_{n,\,m}+b^{end}(x_b)H_{n,\,m}\;=\;0 \tag{3·78}$$

So the impedance at the end of ALID is:

$$Z^{end}(x_b)\;=\;-\left[H_{n,\,m}\right]\left[G_{n,\,m}\right]^{-1} \tag{3·79}$$

$Z^{end}(x_b)$ is used in equation 3·62 to obtain $Z^{end}(x_f)$ which is used to obtain $Z^{end-1}(x_b)$ with equation 3·71 and so on until $Z^{1}(x_b)=Z_{ALID,}$ which represents the total impedance of the ALID.

The following expressions are defined: $A^1(x_b)\;=\;\left[A_1(x_b)\;\ldots\;A_n(x_b)\right]^T$ and $B^1(x_b)\;=\;\left[B_1(x_b)\;\ldots\;B_n(x_b)\right]^T$. At the entrance of the ALID, $A^1(x_b)$ is proportional to the amplitude of the modes incident to the ALID and $B^1(x_b)$ to the reflected modes:

$$\left[B^1(x_b)\right]\;=\;\left[I-Z_{ALID}\right]\left[I+Z_{ALID}\right]^{-1}\left[A^1(x_b)\right]\;=\;\left[RC\right]\left[A^1(x_b)\right] \tag{3·80}$$

In order not to over-complicate the model, each mode is studied separately and it is conservatively assumed that each mode has a unit amplitude as it reaches the ALID. The diagonal of matrix [*RC*] gives the ratio of the reflected to incident amplitude for each mode (propagating and evanescent). This value is used to evaluate the compliance of all modes with the acceptability criterion. As all modes are considered, the ALID can be placed very close to any feature (e.g. defect, source) in the model.

Results obtained with this analytical model are compared with FE models with the parameters defined in Section 3.4.2.2. Results for propagating modes are presented in Figure 3.15. There is an excellent agreement between both techniques so the analytical models can be confidently used to determine parameters of the ALID.

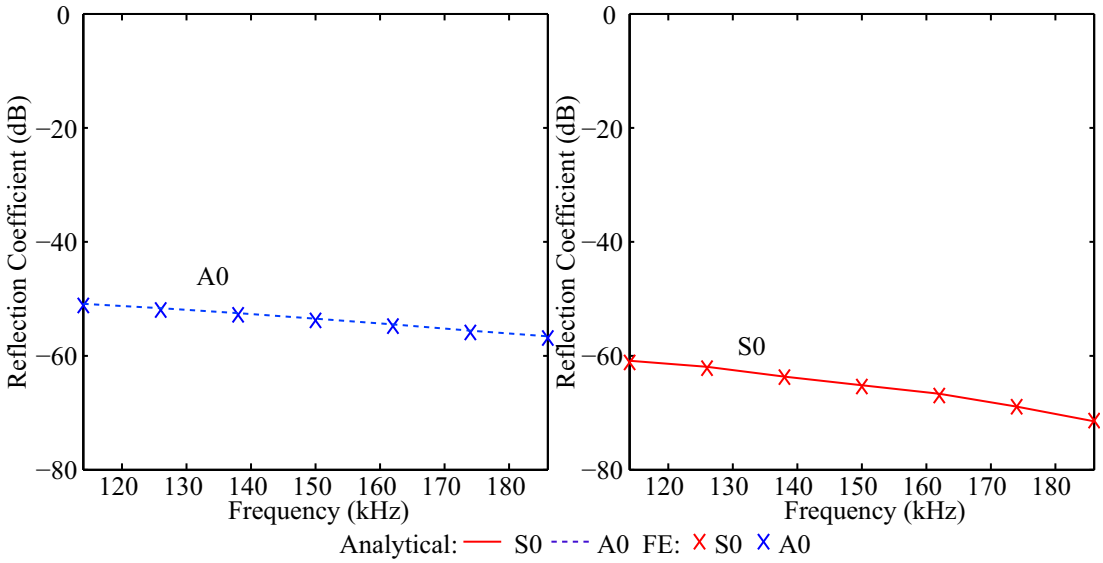

Figure 3.15. Reflection coefficient for a given ALID obtained with guided wave analytical and FE models

3.5. Demonstrators

These demonstrators show the possibilities and gains that can be achieved using absorbing layers.

3.5.1 Computational efficiency

These models demonstrate that a significant gain in computational efficiency can be achieved by implementing the 2 absorbing layer techniques presented in this chapter in real life cases. The parameters of the layers used in this part were obtained using the analytical models defined previously.

3.5.1.1 Bulk wave model

This model is a realistic simplified practical bulk wave case represented in Figure 3.16.a. The material used is steel (ρ=7800kg/m3, *E*=200Gpa, ν=0.33). The model is excited by a point force on the top free surface acting at 45 degrees to the normal (in order to extend the generality of the model). It is applied in the form of a 2MHz 5 cycles tone burst (Blackman Harris 3 terms). A simplified horizontal 4.5mm crack is located 30mm under and to the right of the excitation point. The aim of this is to monitor the interaction of the waves with the free surface and the defect by monitoring the displacement at a chosen point. In this example, the monitoring point is located at the excitation point.

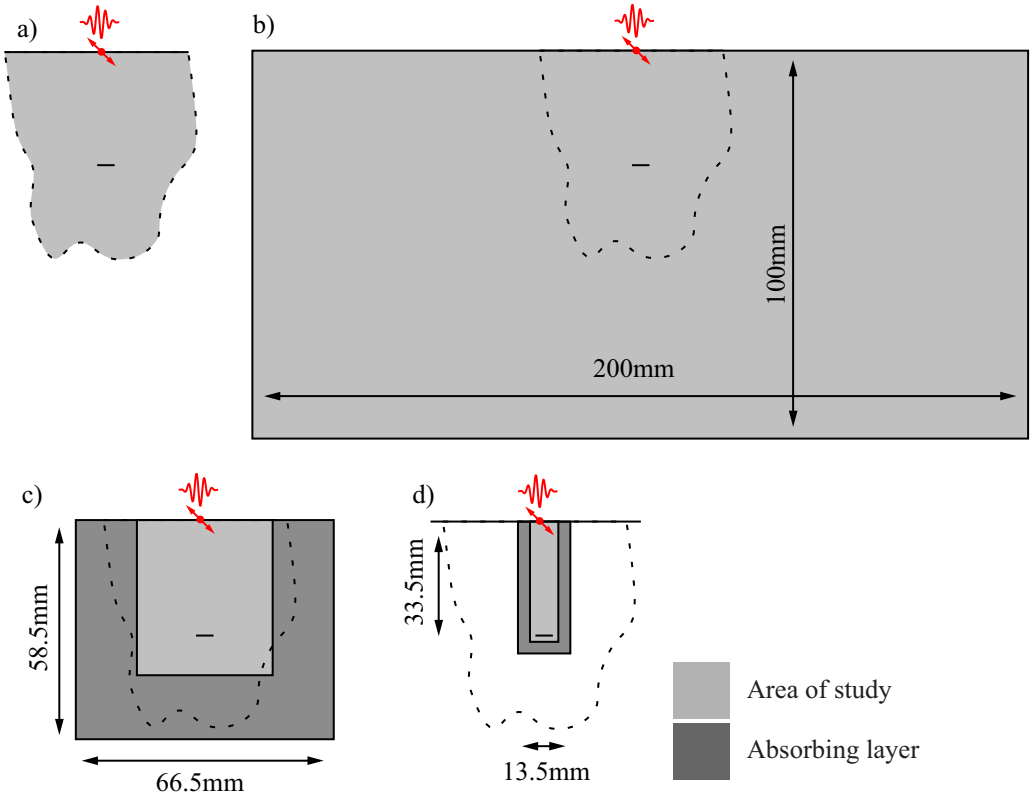

Figure 3.16. a) bulk wave demonstrator, FE model: b) without absorbing layer, c) with ALID, d) with PML.

Without using absorbing layers, the model needs to be 100mm by 200mm (Figure 3.16.b) in order to achieve separation of the first reflections from the defect and the unwanted reflections at the monitoring point.

For models using absorbing layers, the acceptability criterion is set at -60dB meaning that the maximum reflection from the absorbing layers will be smaller than 0.1% of the maximum displacement of the excitation point. Using the models described previously in this chapter to define the required PML or ALID and taking into account the frequency spectrum of the excitation, the model size can be reduced to 66.5mm by 56mm (Figure 3.16.c) using ALID and 33.5mm by 13.5mm (Figure 3.16.d) using PML. The thickness of the ALID is 16mm, C_{Mmax} is 11e6 and p is 3. The PML is 3mm thick, A_{max} is equal to 2.3e9 and p is 3. The thickness of the PML is smaller than the ALID one because of the perfectly matched impedance. It should also be noted that the area of study is smaller for the PML case than for the ALID case because ALID is more sensitive than PML to waves incident at high angles. The geometric size of the 2D model is divided by 5.35 with ALID and 44 with PML compared with the classical

technique. This reasoning can be extended to a 3D model of the same case where the model size would be divided by 15 and 655 respectively.

An added benefit of models using absorbing layers is that the complete area of study is clean of any unwanted reflection. This can help a better understanding of the physical phenomena occurring in the model. Figure 3.17 shows the displacement field obtained for the ALID case described above. The absolute value of the displacement is represented and, in order to highlight low amplitude reflection, the colour scale only spans up to 0.1% of the maximum absolute displacement in the model. These figures show that there is no visible reflection coming back from the ALID into the area of study. This confirms the correct dimensioning obtained using the analytical model.

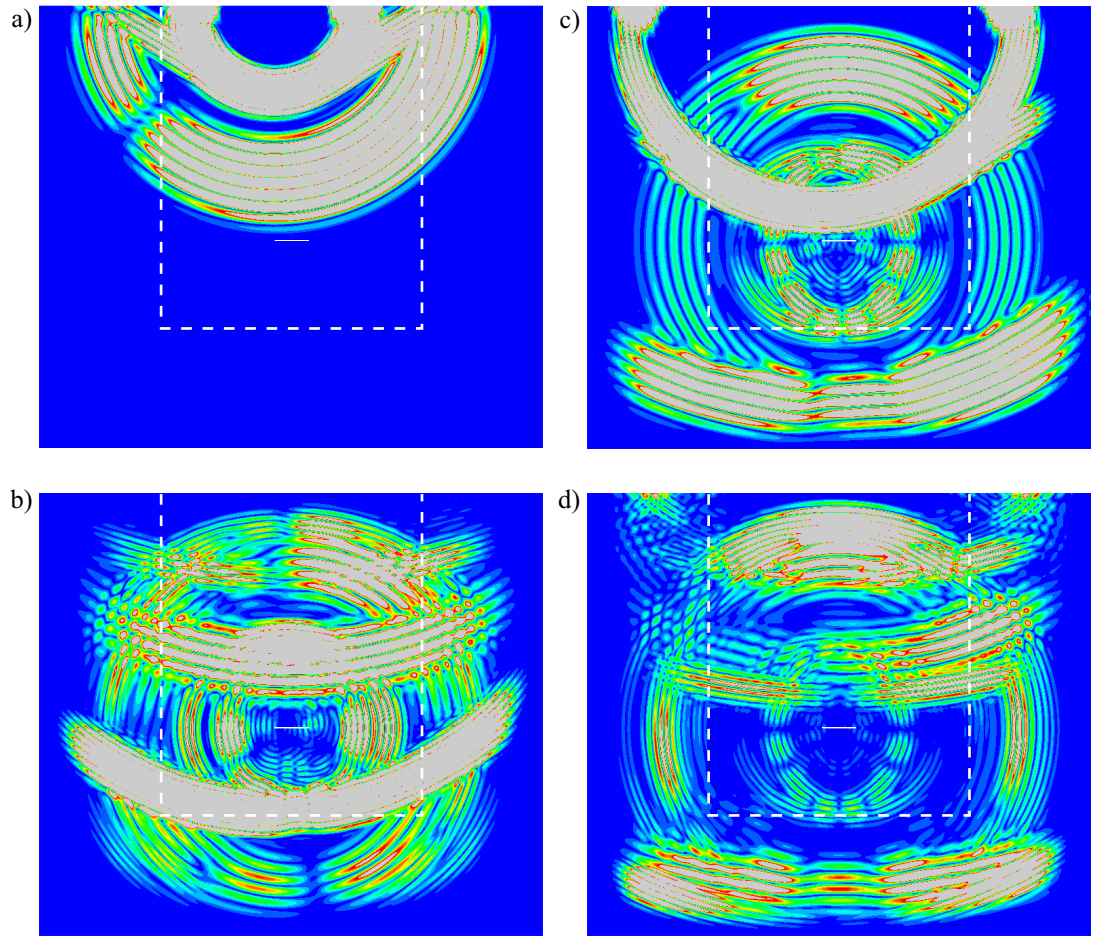

Figure 3.17. Absolute displacement field for the bulk demonstrator with ALID at time: a)5µsec b)10µsec c)15µsec d)20µsec. Colour scale extends from 0 (blue) to 0.1% (red) of the maximum absolute displacement. Grey indicates out of scale (0.1% to 100%). White dashed line indicates the boundary between area of study and ALID

3.5.1.2 Guided wave model

The guided wave model represented in Figure 3.18.a is a simplified practical case which has been used extensively in guided wave research. An 8mm thick aluminium (ρ=2780kg/m3, *E*=70Gpa, ν=0.33) plate is excited by a 150kHz 12 cycles tone burst (Blackman Harris 3 terms) with a point force at 45 degrees in order to strongly excite both fundamental modes. Over the frequency range excited, the fundamental symmetric and anti-symmetric modes can propagate in the medium. The plate contains a 2mm by 2mm slit located 700mm from the excitation. If the first reflections from the defect were studied without using absorbing layers, the model would need to be 2700mm long (Figure 3.18.b) to avoid the presence of unwanted reflections reaching the monitoring point before the reflections from the slit.

Using the analytical models devised above and taking into account the frequency spectrum, an optimized ALID is 80mm thick. In this case, C_{Mmax} is 2.1e6 and C_M varies following a cubic law. The left hand side ALID starts at the excitation point and the right hand side ALID 3mm behind the slit. The model size is divided by 3.12 (Figure 3.18.c).

Using the analytical model, an optimized PML is 18.5mm thick. A_{max} is 8.36e5 and α varies following a cubic law. As only the field between the slit and the excitation point is of interest, it is calculated (taking advantage of the shape of the frequency spectrum) that the PML needs to be located 29mm away from these features. The model size is hence divided by 3.38 with PML (Figure 3.18.d).

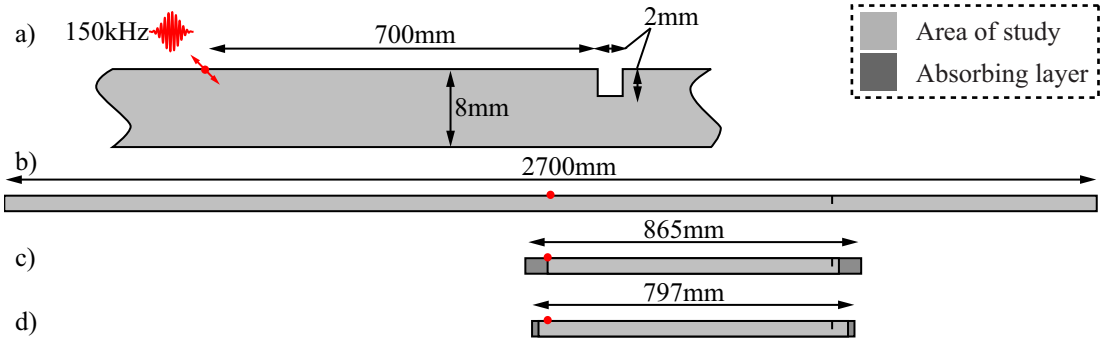

Figure 3.18. a) guided wave demonstrator, FE model: b) without absorbing layer, c) with ALID, d) with PML.

Figure 3.19 shows the displacement field for the ALID case described above. A scale factor of 10 is applied in the vertical direction in order to improve the visibility. The

colour scale is adjusted to highlight the low amplitude part of the absolute displacement field. Figure 3.19.a shows the 2 modes propagating in the plate. On Figure 3.19.b one can see the reflection of these 2 modes from the defect. As mode conversion occurs at the defect, 4 wave packets exist. On Figure 3.19.c the last wave packet is about to enter the ALID and the absence of any other visible wave packets reflected from the ALID can be noted, although some numerical noise in the form of low amplitude long wavelength waves can be observed. Other models were run and confirmed that this noise is not related to the ALID. Finally, Figure 3.19.d shows that all modes have been correctly absorbed indicating that the ALID worked correctly.

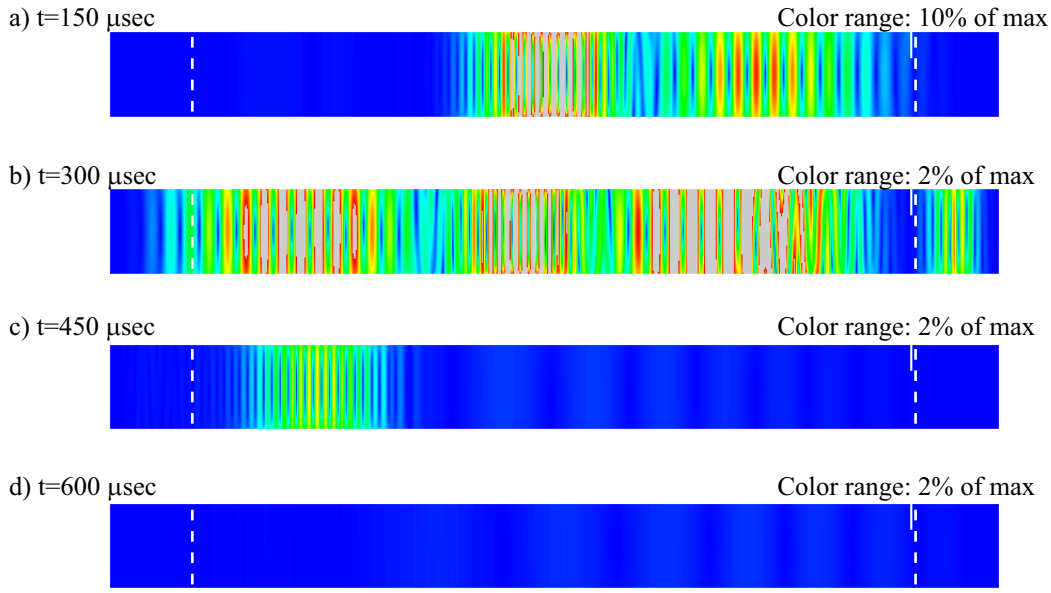

Figure 3.19. Absolute displacement field for the guided demonstrator with ALID at time: a)150µsec b)300µsec c)450µsec d)600µsec. Colour scale is varied and extends from 0 (blue) to 2% or 10% (red) of the maximum absolute displacement as indicated on the figure. Grey indicates out of scale (2% or 10% to 100%). White dashed line indicates the boundary between area of study and ALID.

3.5.2 Time reconstruction

As mentioned in the introduction, our implementation of the PML can only be used in the frequency domain. Wave propagation time domain results can be obtained by using absorbing layers (either ALID or PML) and running the model in the frequency domain. Results are then processed with an inverse Fourier transform. The aim of this case is to describe the method used to do this, using an example of modelling of guided waves. This case was developed with Ludovic Moreau and formed part of a publication [31].

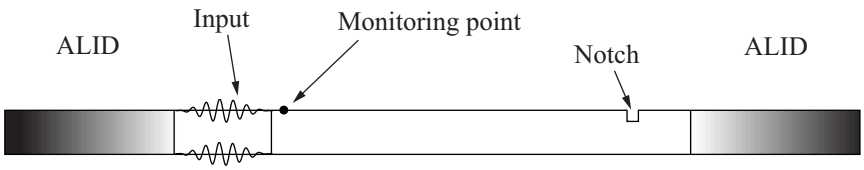

Figure 3.20. Model geometry for time reconstruction case

In this case, the first anti-symmetric mode A0 is generated in an 8mm thick aluminium plate with a 2mm by 2mm rectangular notch as shown in Figure 3.20. The excitation time signal desired is a 150kHz 10 cycle tone burst applied in the normal direction to the plate. Frequency domain input data is defined by FFT of the time excitation shown in Figure 3.21. Most of the energy is concentrated between 120kHz and 180kHz. Only frequencies located in this range will be used to solve the model.

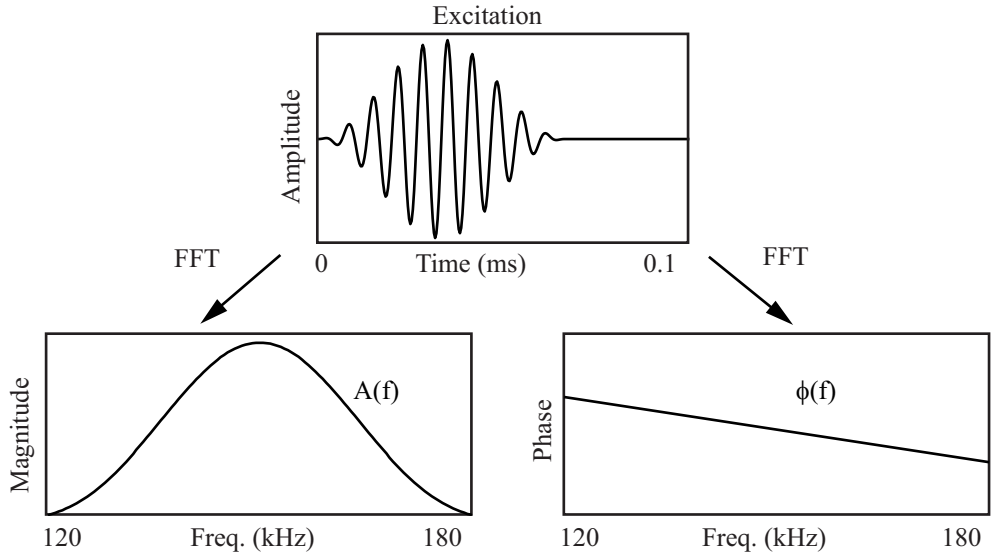

Figure 3.21. Input preprocessing

A0 mode generation is achieved by applying the input data as a force in the normal direction over a region on the top and bottom surfaces of the plate, in a spatially windowed sine wave whose wavelength matches the wavelength (obtained using DISPERSE for example) of the desired mode. This is shown in Figure 3.22. For this case, ALIDs are used to absorb incident waves but PMLs could have been used similarly. The complex normal displacements for each frequency are monitored 700mm away from the defect and an inverse FFT is applied to this complex spectrum. The real part of the inverse FFT result gives the time traces. In order to validate the method, they are compared with time traces obtained with a classical time domain model.

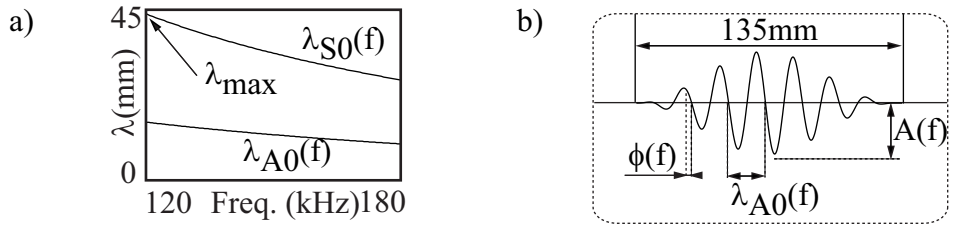

Figure 3.22. a) dispersion curve data used for input definition, b) input definition

Results are presented in Figure 3.23. At the monitoring point, results from the different models agree with high accuracy in terms of propagation velocities and relative amplitudes. Differences on both of these parameters are smaller than 1%. This confirms that it is possible to obtain wave propagation time domain results by using absorbing layers and solving the model in the frequency domain.

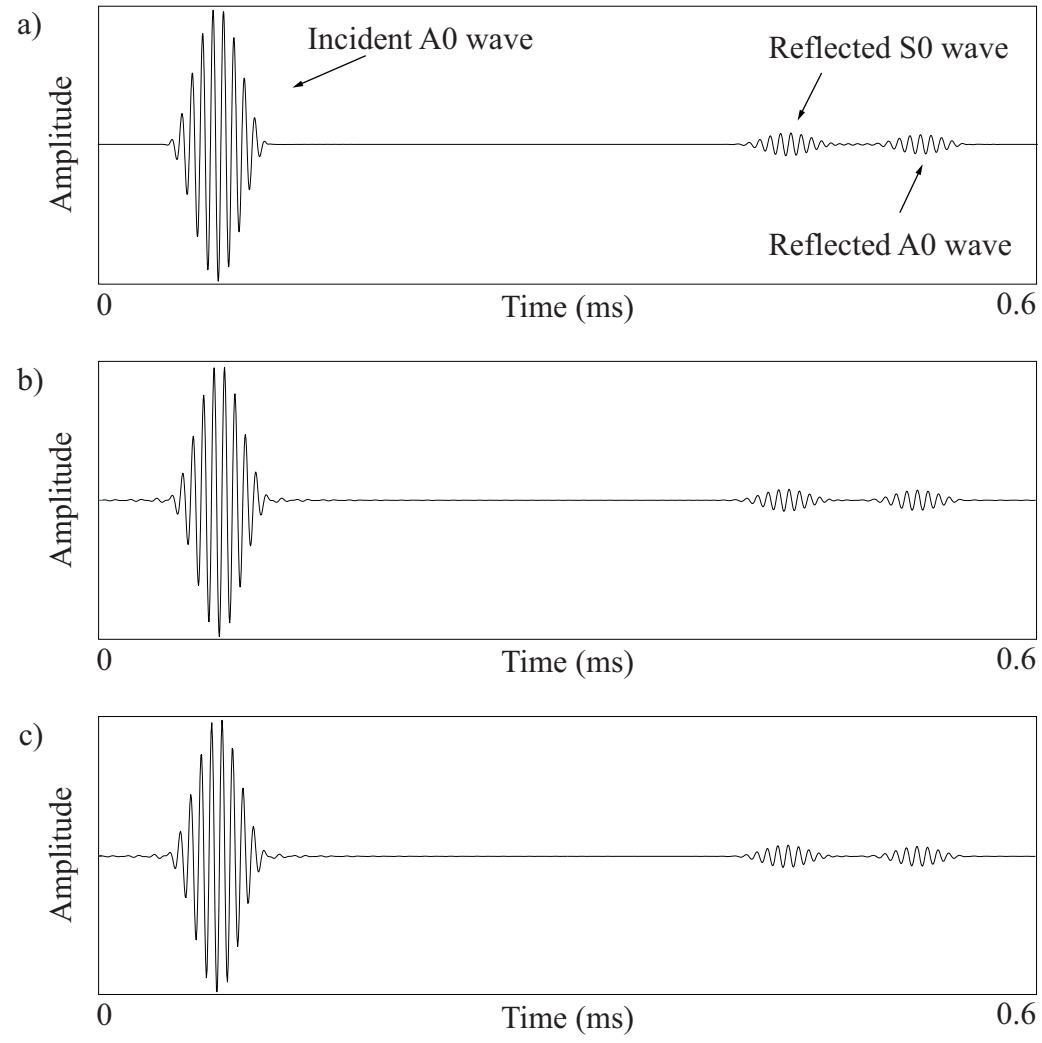

Figure 3.23. Normal displacement monitored 700mm away from the defect. a) Classical time domain analysis with ABAQUS, b) Frequency domain analysis with ABAQUS, c) Frequency domain analysis with COMSOL

3.5.3 Wave scattering

Using absorbing layers in models designed to study wave scattering can greatly simplify them in addition to reducing their size compared to classical models.

3.5.3.1 Single-mode reflection coefficient

The model used in this section is similar to the one used in [72]. The plate used is 3mm thick and made of steel as defined in the published paper [72]. A notch 0.5mm deep is positioned 1m away from the excitation. The width of the notch is varied from 0.5mm to 5mm in separate analyses. The COMSOL FE model is represented in Figure 3.24. It is excited by an harmonic normal force whose amplitude is constant through the thickness of the plate. The frequency of the harmonic excitation is varied from 400kHz to 500kHz. ALID are placed on each side of the area of study to absorb any incoming wave.

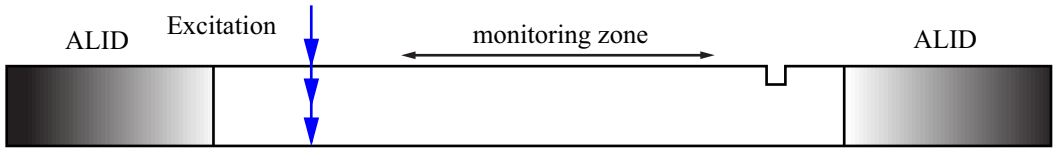

Figure 3.24. Representation of model used for guided wave scattering validation

The complex out-of-plane displacements are monitored mid-plane between 0m and 1m away from the excitation. This data is used to perform a spatial FFT [61] which yields the amplitude of the incident wave $A0_{inc}$ and the reflected waves: $A0_{ref}$ as shown in Figure 3.25. It should be noted that the position of the peaks indicates the wave numbers of the modes.

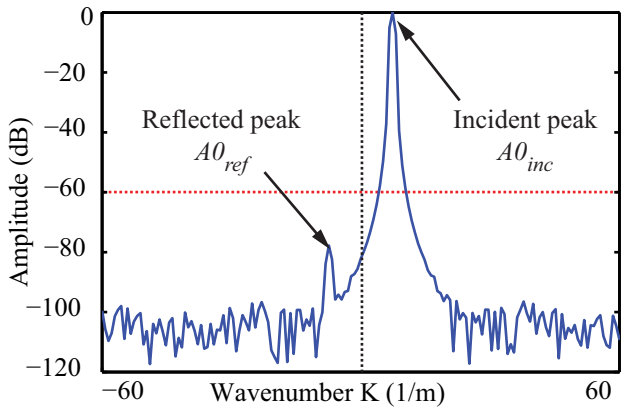

Figure 3.25. Example of a typical spatial FFT curve

The reflection coefficient *RC* is evaluated in the following way:

$$RC = \frac{A0_{ref}}{A0_{inc}} \tag{3·81}$$

The notch width varies from 0.5 to 5mm and the wavelength from 5.17mm to 6.16mm. The notch width is therefore varied from 8.1% to 96.7% of the wavelength. In Figure 3.26, the reflection is plotted against the notch width. Results from the COMSOL models are compared with the published experiments and published finite element models (FINEL [73]).

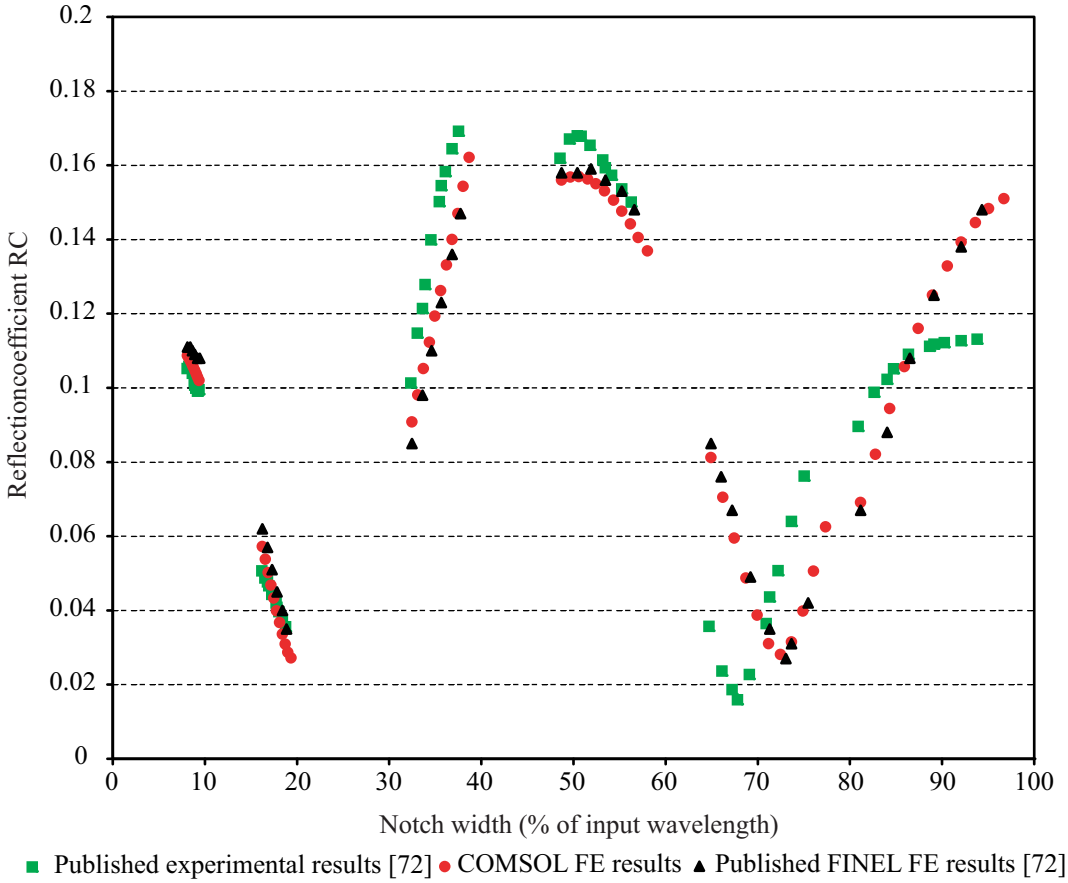

Figure 3.26. Reflection coefficient against notch width

It can be seen that results obtained from time domain modelling with FINEL and frequency domain modelling with COMSOL agree very well. Incidentally, the agreement of the COMSOL results with experimental ones is similar to the agreement of FINEL results with experimental ones.

3.5.3.2 Multi-mode reflection coefficient

The aim of this case is to show that multi-mode reflection coefficients from a scatterer can be easily obtained using frequency domain analysis and absorbing regions. This case was developed with Ludovic Moreau and formed part of a publication [31].

The model set up is similar to the previous case although the dimensions are changed and the excitation is defined so that only the fundamental anti symmetric mode is excited as was done in section 3.5.2. The plate is an 8mm thick aluminium plate with a 2mm by 2mm notch. The excitation frequency is varied from 140kHz to 500kHz by steps of 15kHz. ALID are placed on each side of the area of study. The normal displacement is monitored on the top surface of the plate over a region whose length is equal to 3 times the longest wavelength in the model. It is used to perform a spatial FFT [61] which gives the relative amplitude of the normal displacements for each mode. As the mode shapes of each mode is different, it is necessary to use power-normalized mode shapes in order to obtain the reflection coefficients in terms of energy.

For a particular mode, the value of the energy E_i carried by each mode [33]:

$$E_i = \left(\frac{A_i}{M_i}\right)^2 \tag{3·82}$$

with A_i, the amplitude of the displacement in a given direction at a through thickness position given by the spatial FFT and M_i, the value of the displacement in the same through thickness position and direction of the power normalized mode shape of the mode of interest. In this way, it is possible to verify that the summation of the energies carried by the different modes reflected and transmitted from a defect is equal to the energy of the incident mode. Reflection coefficients are calculated by dividing the value of the energy carried by each mode by the value of the energy carried by the incident mode (A0 in this case).

Results obtained with ABAQUS and COMSOL (both using ALID) are shown in Figure 3.27. The evolution of the reflection coefficient from an A0 incident mode for frequencies ranging from 140kHz to 500kHz is presented for each possible mode. They agree well, showing the same patterns, the maximum difference over the range of

values being 3.2%. Similar results were obtained for transmission coefficients calculation.

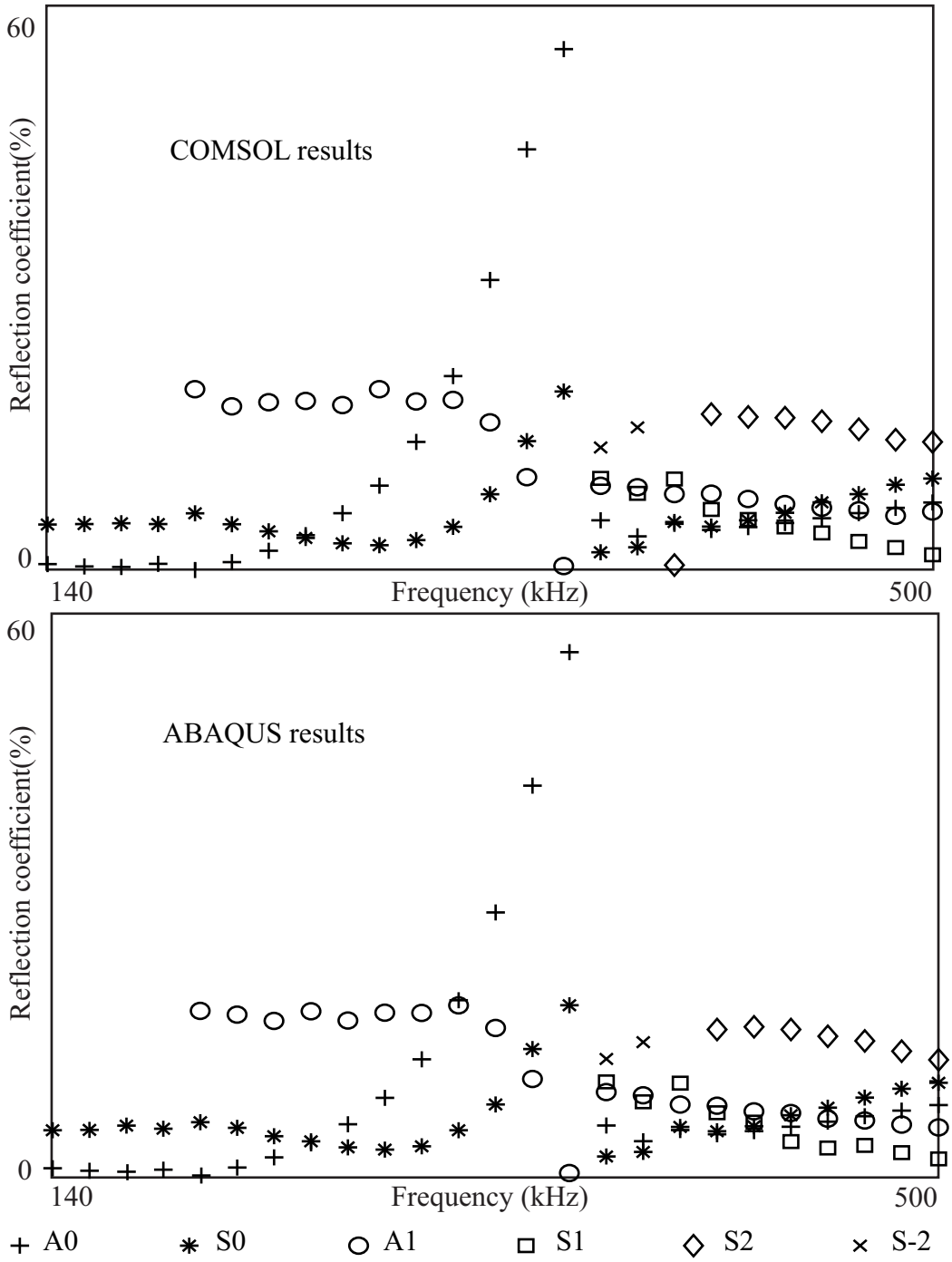

Figure 3.27. Energy reflection coefficient for A0 incident on a 2mm square notch in an 8mm thick aluminium plate from 140kHz to 500kHz

In this case, as several modes having a large range of velocities are present, the use of absorbing regions greatly simplifies the obtention of the reflection curves.

3.6. Discussion

The previous demonstrators have highlighted the gains obtained by using ALID or PML and have also shown that PML generally achieves smaller model size than ALID. This can be explained by the fact that with PML the layer matches the impedance of the area of study perfectly whereas for the ALID the strength of the decay is limited by the impedance change it causes. As a consequence, for a given case, ALID is generally thicker than PML. It is also more sensitive to waves incident at high angles leading to a necessary increase of the area of study in order to minimize the model size. In short, PML is superior to ALID from a theoretical point of view for all wave types except evanescent and backwardly ones. As the aim is to improve modelling capabilities, this gives an advantage to the PML technique but it has to be balanced by the fact that, to our knowledge at the time of writing, COMSOL is the only mainstream FE package that allows implementation of PML. The implementation is limited to frequency domain solving with implicit solvers whereas ALID can be implemented to be used with any FE package which allows Rayleigh damping. The actual performance comparison depends on the type of result required.

A user wishing to obtain frequency domain results such as the reflection coefficient from a defect has a choice of directly using either PML or ALID. The two best combinations investigated are ABAQUS with ALID and COMSOL with PML. ABAQUS models were solved using the "Direct-solution steady-state dynamic analysis" procedure of ABAQUS/Standard which uses a direct implicit solver. COMSOL offers a range of direct and iterative implicit solvers. Direct solvers have proved to be robust and efficient but limited in terms of the number of degrees of freedom that can be solved. Iterative solvers showed improvement in terms of speed and memory but convergence proved difficult. Overall, in our experience, using COMSOL 3.2 and ABAQUS 6.6, COMSOL did not match the performance of ABAQUS for a given number of degrees of freedom. Given these two combinations it is therefore not possible to clearly recommend one of them, as the best solution depends on the specific details of the model considered.

For time domain results, the most straightforward approach is to use ABAQUS/ Explicit with ALID. The explicit solver of ABAQUS uses the central difference

algorithm. It is particularly attractive for large models as it is faster and more memory efficient than an implicit solver. This technique is recommended for most cases where time domain results are required. An alternative is to solve the model in the frequency domain and reconstruct the time domain results by performing an inverse fourier transform.

3.7. Conclusion

In this chapter, 2 techniques to remove unwanted reflections from the boundaries of FE models were investigated: ALID and PML. The principles of these techniques were described. Analytical models to facilitate the efficient and reliable design of FE models to exploit them were developed. Using demonstrator cases, it was shown that both techniques enable a significant reduction in model size which justifies their use. The discussion explained the wider considerations to assist the choice of technique for practical cases. Given the pace of recent developments in computer technology and software packages in the last few years, the constant improvement of modelling capabilities was witnessed and it was also realized that modellers constantly test the modelling capabilities to their limits. The use of absorbing layers presented in this chapter clearly aims at pushing these limits further and the analytical models devised enable to streamline the achievement of an efficient model using these techniques.

Chapter 4

On the influence of mesh parameters on elastic bulk wave velocities

4.1. Introduction

In the process of moving from the genesis of a numerical model to its conclusion and the obtention of results enabling a better understanding of a physical phenomenon, a modeller takes a series of design decisions. In the context of wave propagation modelling, the choice of the solving technique, mesh density or time step influences the successful outcome of the exercise but also the level of accuracy with which the phenomenon is represented. Approximation by discretization of the space and time leads to a discrepancy between theoretical physical values and their actual values in the model. One of the parameters suffering from this is the propagation velocity of bulk waves in elastic media. This study looks into how this is influenced by design decisions and aims to provide modellers with information enabling them to improve not only the quality of their modelling (adequate decision making) but also the quality of the analysis made based on the numerical results (quantitatively taking into account the numerical deviation). There is also an interest in understanding the reasons for mesh scattering where a change in mesh size causes some numerical reflection. This is an important point as a better understanding of this could lead to vast increase of modelling capabilities by enabling local mesh refinement to be implemented.

In this chapter, both explicit and implicit solvers used with a range of element types are studied. Regular meshes made of square or equilateral triangles are investigated first. These meshes are then distorted in order to understand the influence of element deformation on wave velocities. The general approach is to run a series of FE models. The results of these models enables the identification of simple functions to describe the errors as generally as possible and enable users to establish guidelines to suit their modelling requirements.

Details from all the studies performed are presented in this chapter. This is done in complete details in order to provide a useful general reference to users for future use. Being aware that providing such a level of details for all cases studied does not help with the flow of the chapter, it is suggested for users interested in a particular case to investigate findings for this particular case and then to proceed to general discussion and conclusions. Users interested in the principles will find them described in the following sections: 4.2.1 (explicit solving), 4.3.1 (implicit solving), 4.2.2.1 (square elements) and 4.2.3.1 (equilateral triangle elements).

4.2. Explicit solving

4.2.1 Introduction

For time domain models solved with an explicit scheme (ABAQUS/Explicit), we investigate the influence of the time step, mesh density and angle of incidence for linear quadrilateral elements (CPE4R), linear triangular elements (CPE3) and modified quadratic triangular elements (CPE6M) for both longitudinal and shear waves.

FE models are run for each case and post processing leads to the obtention of a precise value of actual propagation velocity in the model. For simplicity, all models are non-dimensional: density ρ=1, frequency f=1, Young's modulus E=8/3, Poisson's ratio η=1/3 so that we have a longitudinal velocity c_L=2 and shear velocity c_S=1. Models are made with a regular mesh of elements and represent an area covering at least 20 wavelengths away from the excitation point (different model sizes were taken for longitudinal and shear waves) as shown in Figure 4.1.

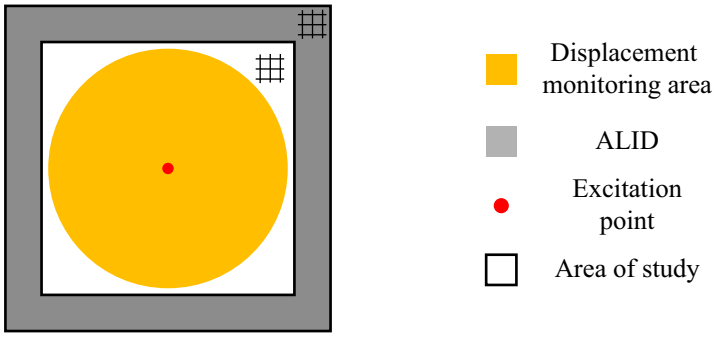

Figure 4.1. Definition of the main feature of the model

Models are 2D plane strain. Both shear and longitudinal wave generations are considered, as models are excited by nodal forces being applied on four elements as

shown on Figure 4.2. This generates an almost pure wave - shear or longitudinal - and as the size of the source is only a fraction of a wavelength, it is close to a point source. The point located at the centre of the four elements is referred to as the excitation point.

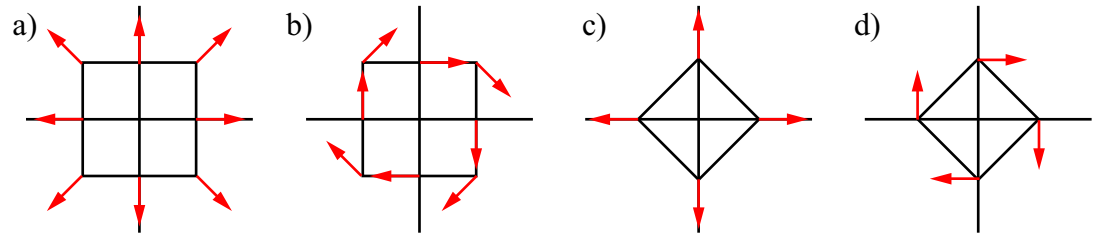

Figure 4.2. a) Longitudinal and b) shear wave excitation for a square element mesh and c) longitudinal and d) shear excitation for a triangular elements mesh

The time domain excitation signal is a sine function of unit frequency. Displacements are monitored over a disc area centred on the excitation point of 18 wavelengths radius. Spatial FFTs are performed on the displacements over a range of radii at different angles in a similar way to the example presented in Section 3.5.3.1. On these radii, only the displacements from 3 to 18 wavelength from the centre are used. The signals used for the spatial FFTs are Hanning windowed and padded in order to improve the velocity precision. As some coarse meshes are used, cubic interpolation is performed in order to increase the ability to look correctly at the influence of the direction of propagation.

ALID are placed outside the area of study in order to absorb incoming waves.

4.2.2 Linear quadrilateral elements

This section investigates models made of linear quadrilateral elements. In ABAQUS/ Explicit, the only element of this type is a 4 node linear quadrilateral element with reduced integration referred to as CPE4R [14]. It should be noted that this element is the most commonly used quadrilateral element type. Meshes made of squares, rectangles, rhombi and parallelograms are investigated.

4.2.2.1 Square elements

This study looks into the velocity error for models made with square elements. The side of the square element is $L=L0=L90$ as shown in Figure 4.3.

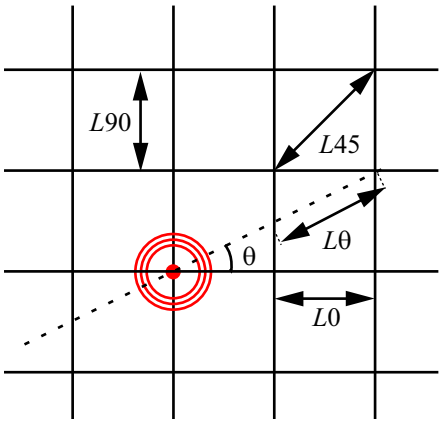

Figure 4.3. Schematic defining $L0$, $L90$, $L45$ and $L\theta$ in a mesh of square elements.

The mesh density N is expressed in term of nodes per wavelength and is varied from 6 to 30 along the side of the element:

$$N = N0 = \frac{\lambda}{L0} = N90 = \frac{\lambda}{L90} \tag{4·1}$$

In this chapter, the mesh density is defined relative to the considered wave. As the longitudinal wavelength is twice the shear one, for a given mesh density, the element size for longitudinal waves is twice that of shear ones.

In the first series of models run, the Courant number CFL as defined in Section 2.3.1 is varied between 1 and 0.05. Figure 4.4.a and 4.4.b represent the variation of the error on the longitudinal velocity Ec_L and shear velocity Ec_S along the element side (at 0 degrees) against CFL for various mesh densities N. Some shear wave models did not complete when run at the stability limit (CFL=1). The maximum CFL used for shear waves is 0.98.

On Figure 4.4.a, it can be seen that the error on the longitudinal wave Ec_L is nil when the CFL is equal to 1. This is mentioned in [38] and can be explained by the fact that, in this case at 0 and 90 degrees, there is a match between the time stepping frequency and the highest frequency of a single element:

$$\Delta t = \frac{\Delta L}{c_L} = \frac{2}{\omega_n} \tag{4·2}$$

$$\text{hence } \omega_n = \frac{2c_L}{\Delta L} = \omega_{max} \tag{4·3}$$

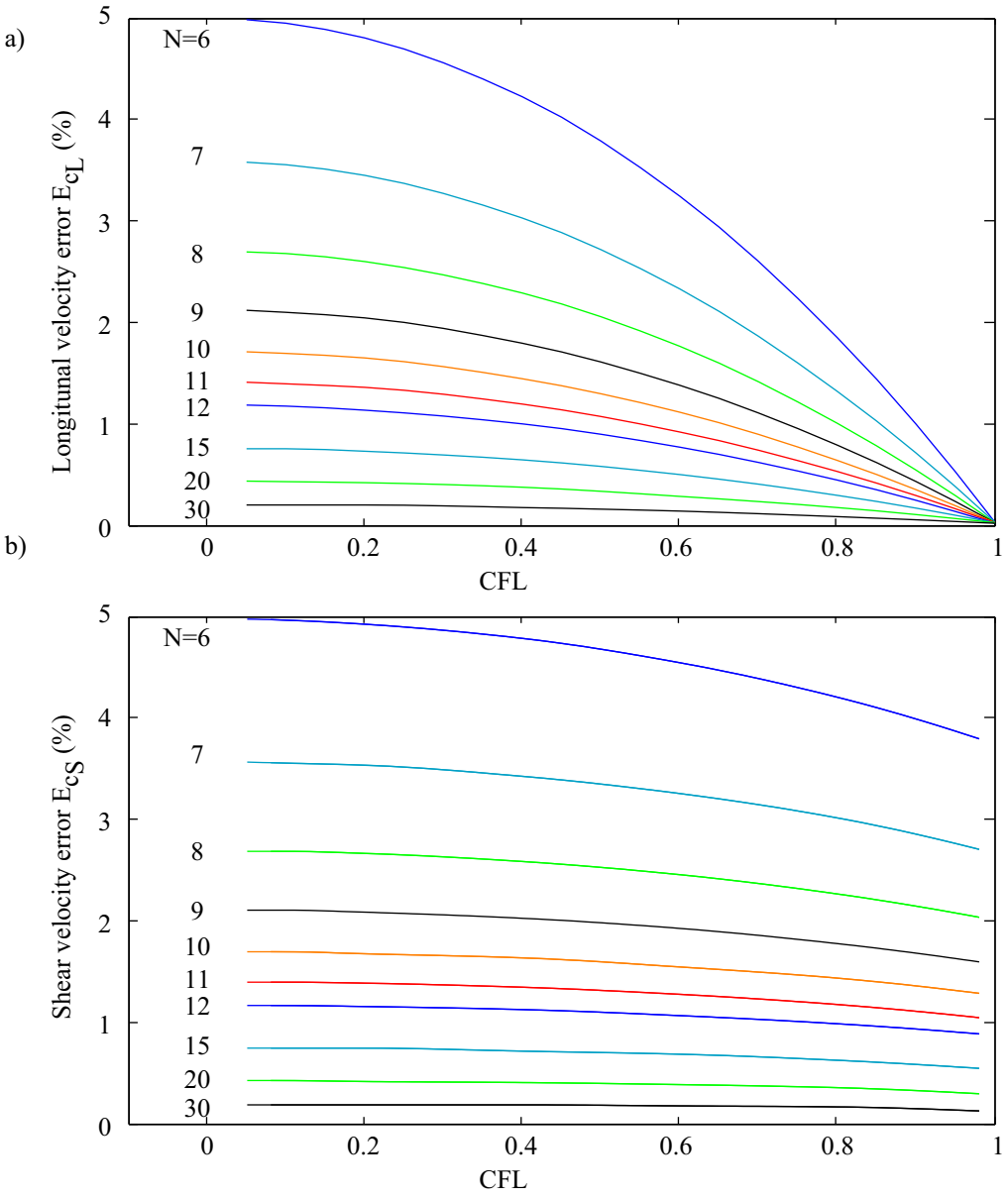

Figure 4.4. a) Longitudinal and b) shear velocity errors against *CFL* for various mesh densities at 0 degrees.

As *CFL* is reduced, the error increases and seems to reach an asymptote.

On Figure 4.4.b, a similar phenomenon is observed although the error does not tend towards zero as *CFL* tends towards 1. This can be explained by the fact that the highest frequency of elements is determined by the (faster) longitudinal wave and not the (slower) shear wave (see equation 2·67). For *CFL*=1, the time stepping frequency does not match the highest frequency for a shear wave. This explains why the error is not zero for shear waves.

Let us consider a hypothetical critical time step for a shear wave at 0 degrees, Δt_{S0}, which would correspond to the maximum frequency for this wave, $\omega_{max,S0}$, such as:

$$\Delta t_{s0} = \frac{L0}{c_S} = \frac{2}{\omega_{max,\,L0}} = \frac{c_L}{c_S}\Delta t_{cr} \tag{4·4}$$

Δt_{s0} is larger than Δt_{cr}, so the model could not be run as it would be unstable. We define M_{S0} as the ratio between Δt_{S0} and Δt_{cr}:

$$M_{S0} = \frac{\Delta t_{cr}}{\Delta t_{S0}} \tag{4·5}$$

This leads to the following relation:

$$\Delta t = CFL\Delta t_{cr} = M_{S0} \cdot CFL\Delta t_{S0} \tag{4·6}$$

For completeness, we define Δt_{L0} and M_{L0} as:

$$\Delta t_{L0} = \frac{L0}{c_L} = \frac{2}{\omega_{max,\,L0}} = \Delta t_{cr} \tag{4·7}$$

$$\text{and } M_{L0} = \frac{\Delta t_{cr}}{\Delta t_{L0}} = 1 \tag{4·8}$$

We also define:

$$CFL_X = M_{L0}CFL = M_{S0}CFL \tag{4·9}$$

Plotting the curves of Figure 4.4.a and 4.4.b against CFL_X leads to a good agreement as shown on Figure 4.5.

This confirms that the amplitude of the velocity errors on both waves are subject to the same mechanism. A general analytical function of CFL_X fitting these curves is:

$$E_c(N, CFL_X) = E_c(N)_{(CFL_X \to 0)} \cdot (1 - CFL_X{}^2) \tag{4·10}$$

where $E_c(N)_{(CFL_X \to 0)}$ is the value of the velocity error when CFL_X tends to zero. This value is dependent on the mesh density and can rightly be considered as the worst

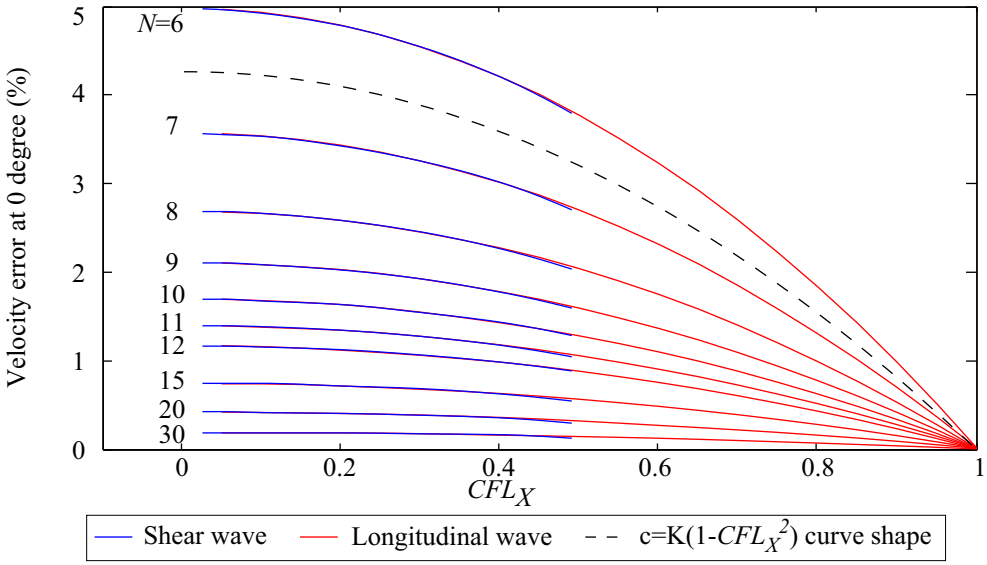

Figure 4.5. Velocity errors against CFL_X for various mesh densities at 0 degrees.

possible error for a given mesh density. In order to establish the dependency, the velocity error for both the longitudinal and shear waves at 0 degrees are plotted against the mesh density N in Figure 4.6. For these cases, CFL is taken equal to 0.025. Following equation 4·10, for this value of CFL, the velocity error is less than 0.1% away from $E_c(N)_{(CFL_X \to 0)}$.

Figure 4.6 highlights the strong influence of the mesh density on the velocity error. The shape of the curve is hyperbolic and shows how the error varies from a value of about 5% for N=6 to a value of less than 0.2% for N=30.

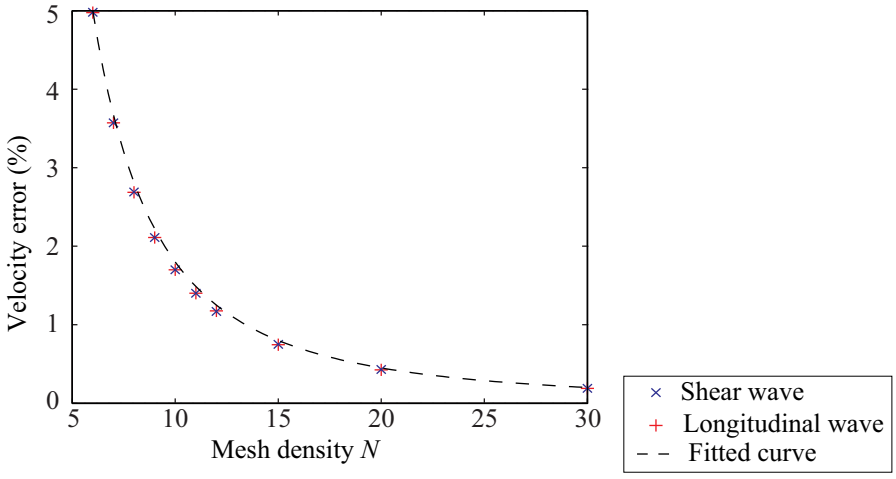

Figure 4.6. Velocity error against mesh density for shear and longitudinal waves at 0 degree with a CFL of 0.025.

As mentioned previously, the mesh density value has a great impact on the computational model size and therefore the amount of memory required to solve a model. For example, in 3D, a model with N=30 would require 125 times more memory than a model with N=6. It would also take much longer to solve as the number of time steps would be multiplied by 5, and each time step would take longer to solve. This illustrates the importance of carefully choosing N to match the accuracy required.

In order to facilitate the choice of N, the error variation can be fitted to the following analytical expression:

$$E_c(N)_{(CFL_X \to 0)} = \frac{180}{N^2} = \frac{180}{\left(\frac{\lambda}{L}\right)^2} \qquad (4\cdot11)$$

This expression gives the value of the velocity error within 0.15% in a conservative manner based on the results in this work.

So far we have only considered the error along the element side (at 0 degrees). In a mesh of square elements such as the one in Figure 4.3, the mesh density is not constant for all angles of propagation of a wave. In particular, at element level, $L0$=$L90$ but $L45$=$\sqrt{2}\,L0$. In order to study this, the longitudinal and shear velocities were monitored from 0 to 90 degrees for various mesh densities N defined at zero degrees. As seen above, the error varies quite strongly for CFL close to 1 whereas it is almost constant at low CFL. For this series of models, a low CFL value of 0.05 is taken in order to avoid a variation of the error due to this parameter.

Figure 4.7 shows the variation of the error against the angle for both wave types and a mesh density varying from 6 to 30. The expected symmetry exists at 45 degrees. The curves for both wave types and all mesh densities follow a similar pattern. The minimum error is located at 0 degrees and increases as the angle increases towards 45 degrees where it reaches its maximum. There is a good match between shear and longitudinal errors which indicates that the same mechanism determines the error variation against the angle.

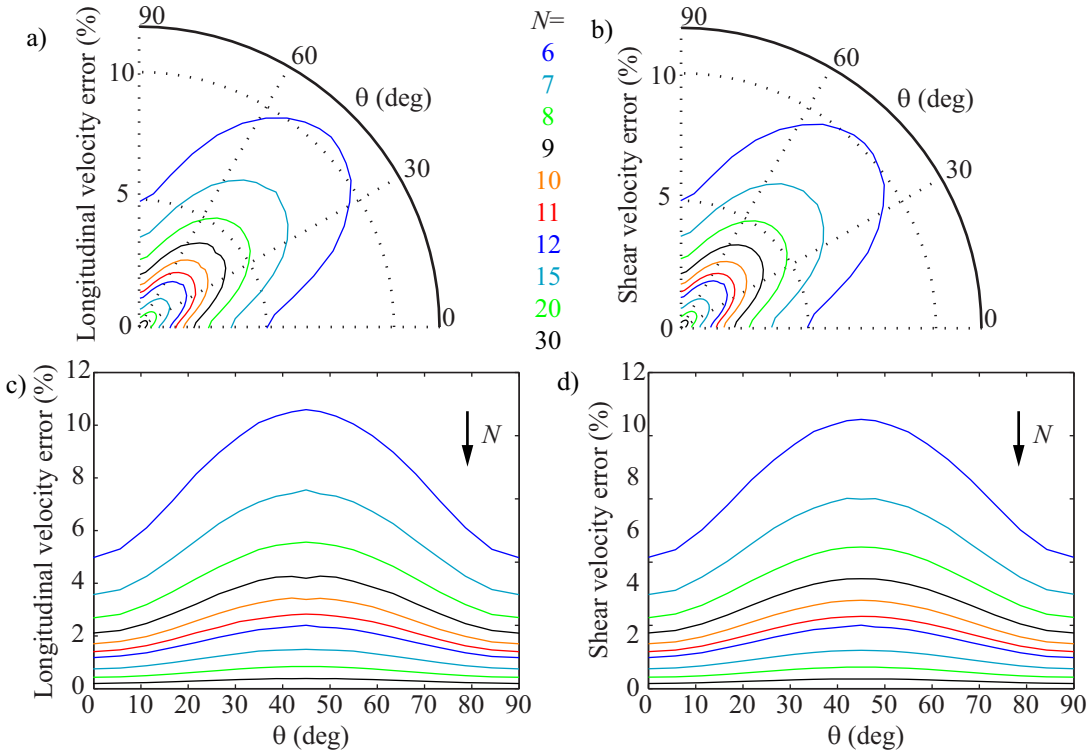

Figure 4.7. Variation of the longitudinal (a and c) and shear (b and d) velocity error against the angle of incidence for various values of mesh density plotted in polar (a and b) and linear (c and d) plots.

On Figure 4.8, it is very interesting to note that the actual error at 0, 45 and 90 degrees matches the value given closely by the analytical expression of equation 4·11 when it is calculated using L as $L0$, $L45$ and $L90$.

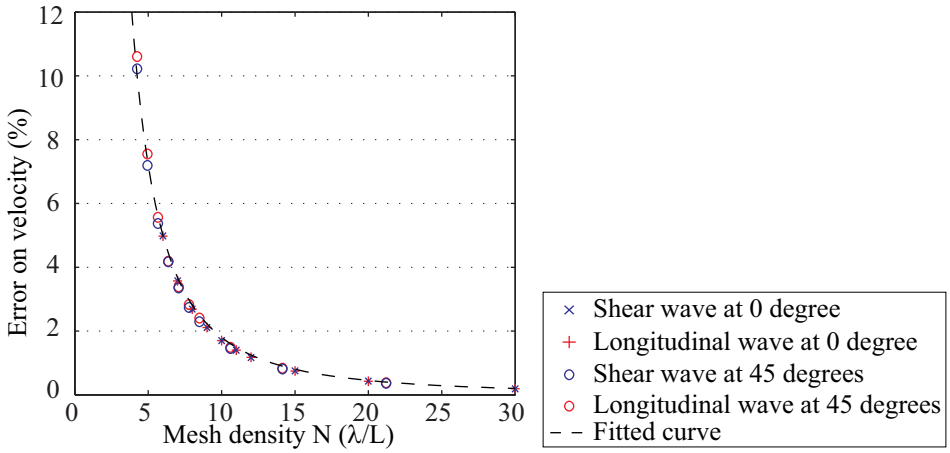

Figure 4.8. Velocity error against mesh density for shear and longitudinal waves at 0 and 45 degree.

The agreement is relatively good for all values of N. The maximum difference between the predicted values and the actual value is 0.6% for N=4.24 (mesh of density 6 at 45 degrees). The analytical expression used for the prediction gives a conservative estimate for all cases apart from extremely low mesh densities (N<6). This should not

be a cause for concern. Such low mesh densities are only rarely used as the wave phenomenon is likely to be incorrectly represented.

The agreement between predicted and measured values does not exist at other angles than 0, 45 and 90 degrees if we were to use $L\theta$ to calculate the mesh density N but it can be precisely predicted using another expression. The variation of the error between these values calculated with the analytical expression can be fitted to the following expression:

$$E(\theta) = E(0) + (E(45) - E(0))\left(\sin\left(2\theta\frac{\pi}{180}\right)\right)^2 \qquad (4\cdot12)$$

with $E(0)$ and $E(45)$ the errors at 0 and 45 degrees calculated using equation 4·11 and θ in degrees. Therefore, we are able to predict the error for any direction of the mesh by using the fitted analytical expressions.

As discussed previously, the value of CFL_X influences the value of the error. At 45 degrees, the value of Δt_{L45} and Δt_{S45} is higher than Δt_{L0} and Δt_{S0} and is the highest in the model. This restricts the range of CFL_X as illustrated on Figure 4.9 and implies that the maximum error due to the CFL occurs at 45 degrees.

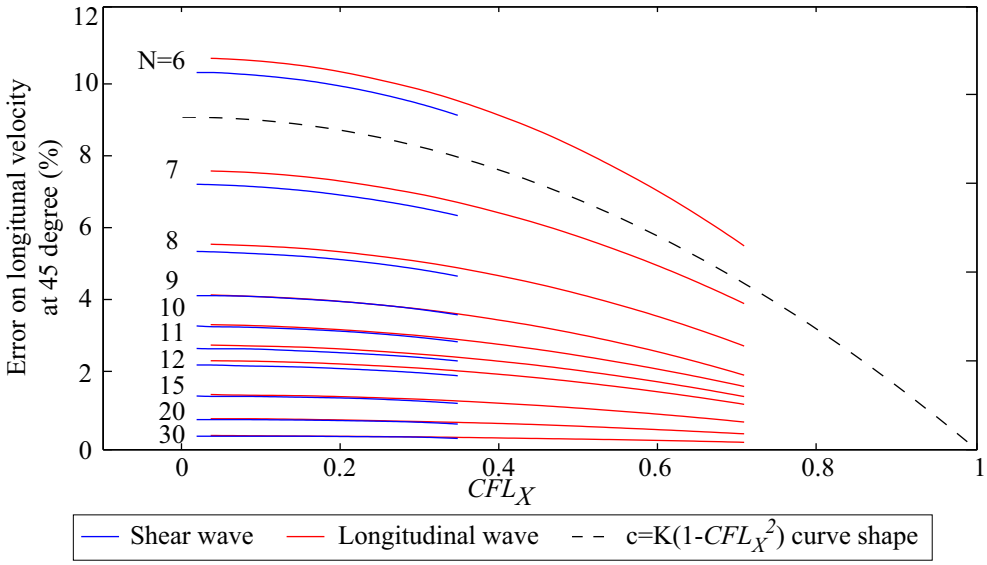

Figure 4.9. Velocity errors against CFL_X for various mesh densities at 45 degrees.

Figure 4.10 presents the results of Figure 4.5 over a surface that shows the variation of the velocity error against the scaled Courant number CFL_X and mesh density N. This

surface can be used to predict the error on the velocity in the principal directions of the mesh (0, 45, 90 degrees) for any mesh density and stability factor.

A close fit to this surface is given by the analytical expression:

$$E_c = 180\frac{(1 - CFLX^2)}{N^2} \tag{4·13}$$

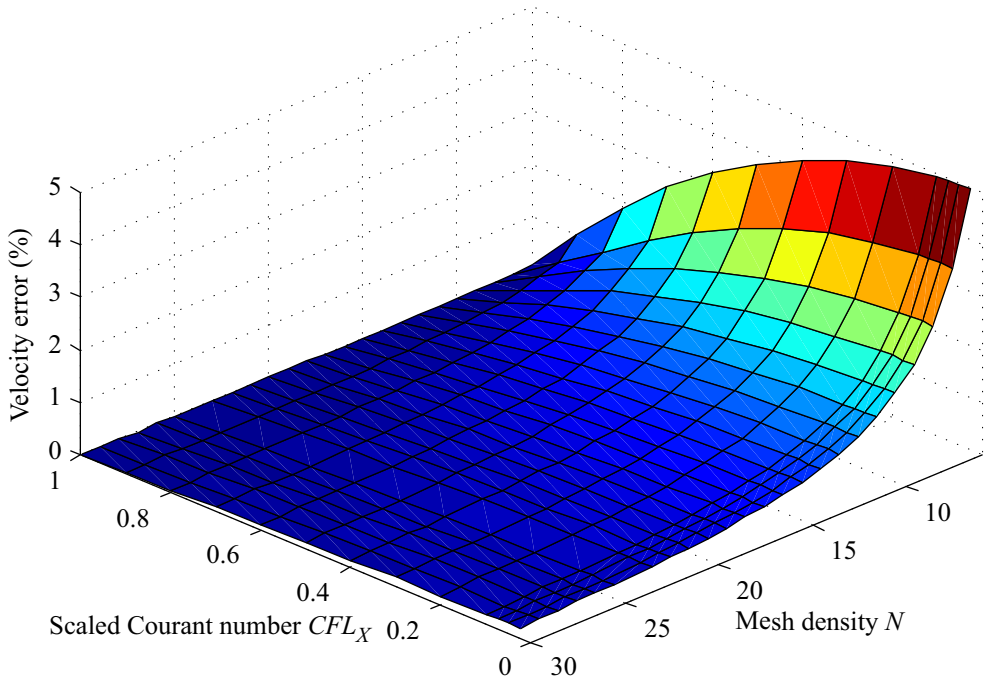

Figure 4.10. Velocity error against the scaled Courant number CFL_X and mesh density N

For a given model, as shear waves have shorter wavelength than longitudinal waves, the mesh density is lower for shear waves than longitudinal waves. Also, as shown in this section, CFL_X will be lower than for longitudinal waves. As the mesh density is lowest at 45 degrees, the overall maximum error will be indicated by equation 4·13 for a shear wave travelling at 45 degrees with the lowest CFL_X.

4.2.2.2 Rectangle elements

The models studied in this part are similar to those used in the previous part apart from the fact that the elements are “stretched” in one direction to become rectangular. The element size in the vertical direction y is kept the same for all models so that the mesh density N in this direction is 15. The element size in the horizontal direction x is varied so that the mesh density N varies from 7.5 to 30. The ratio between the element side $R=Lx/Ly$ is hence varied from 0.5 to 2 as illustrated on Figure 4.11.a. The error on the

velocity is measured over a range of angles from 0 to 90 degrees and plotted on Figure 4.11.b,c,d,e. Small circles are plotted on the linear plots. These represent the amplitude of the error predicted using the expression given in equation 4·13.

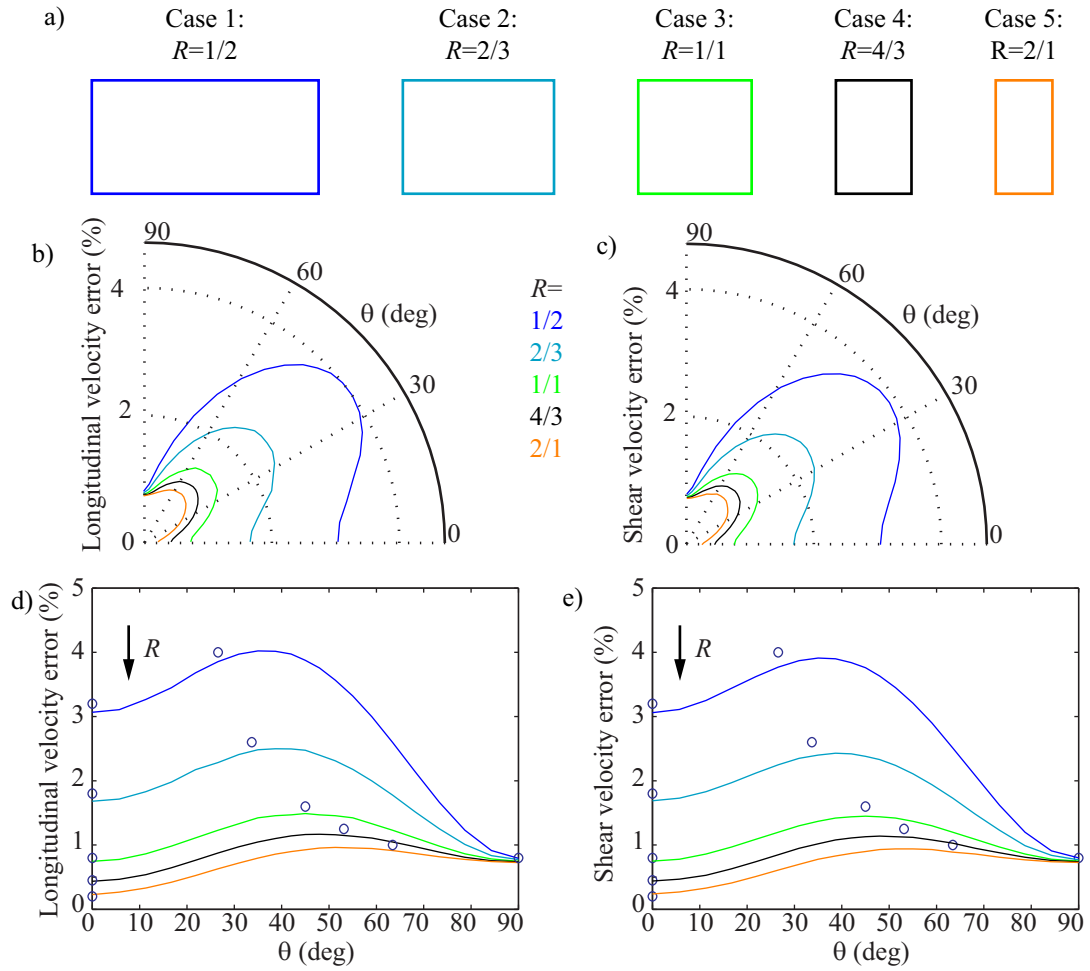

Figure 4.11. a) Shape of the different rectangular elements used in the mesh; Variation of the longitudinal (b and d) and shear (c and e) velocity error against the angle of incidence for various *R* plotted in a polar (b and c) and linear (d and e) fashion. The coloured circles indicate the error prediction along the element side and diagonal.

It can be noted that, as seen in the case of square elements, longitudinal and shear waves react in a similar way to the element distortion. At 90 degrees, the mesh density is constant for all models. At this angle, the error is almost the same for all models and matches the prediction of equation 4.13 very closely, within 0.08%. As the angle θ is decreased, it can be seen that the error increases smoothly - in a similar way to that observed for square elements - until it reaches its maximum. As would be expected, the maxima are reached at different angles depending on *R,* but it is interesting to note that the angle at which the maximum is reached matches the angle of the element diagonal only for *R* equals 1. In other cases, an angle difference exists and increases non linearly

as *R* moves away from 1. Interestingly, despite the drift of the position of the maximum error, the actual value of the maximum very closely matches the predicted error given using the diagonal of the element to evaluate the mesh density. The maximum predicted error is within 0.2% of the actual error. Following the maximum value, the error decreases smoothly to reach a minimum at 0 degrees. As expected, at this angle, the error varies as the mesh density differs. The error prediction at this angle agrees well with the actual result. It is therefore clear that the analytical predictions match the results obtained at 0 and 90 degrees extremely well.

The study of square elements showed that the prediction on the diagonal of a square element could be used. For the other cases, it is also noticed that the analytical prediction of the velocity error on the diagonal closely matches the actual maximum, despite the fact that the diagonal angle does not match the angle at which the maximum occurs. Over the cases studied, the difference between predicted errors and actual maximum errors is 0.2%. It is therefore justified to apply the model devised for square elements to rectangular elements.

4.2.2.3 Rhombus elements

In this case, the model used for the square elements study is sheared so that all elements are deformed from a square to a rhombus. The models studied have a mesh density of 15 along the sides of the elements. A low *CFL* of 0.05 is used. The shearing angle γ is varied from 0 to 45 degrees by 15 degrees increments. The error on the velocity is monitored from -90 to +90 degrees, as in this case there is no symmetry in the horizontal direction. Results for longitudinal and shear waves are plotted on Figure 4·7. Small circles are plotted on the linear plots. These represent the amplitude of the error predicted using the expression given in equation 4·13.

All cases for both longitudinal and shear waves exhibit two maxima and two minima. Contrary to the case with a mesh of rectangular elements, the minima occur at the same angle as the diagonals. This corresponds with the minima and maxima for Lθ. As shown on Figure 4.12.b and c, the values of the maxima and minima are well predicted in a conservative manner. It can be noted that the difference between the prediction and the measured error increases for maxima on the longest diagonal and decreases for maxima on the shortest diagonal. This is more pronounced for shear waves than

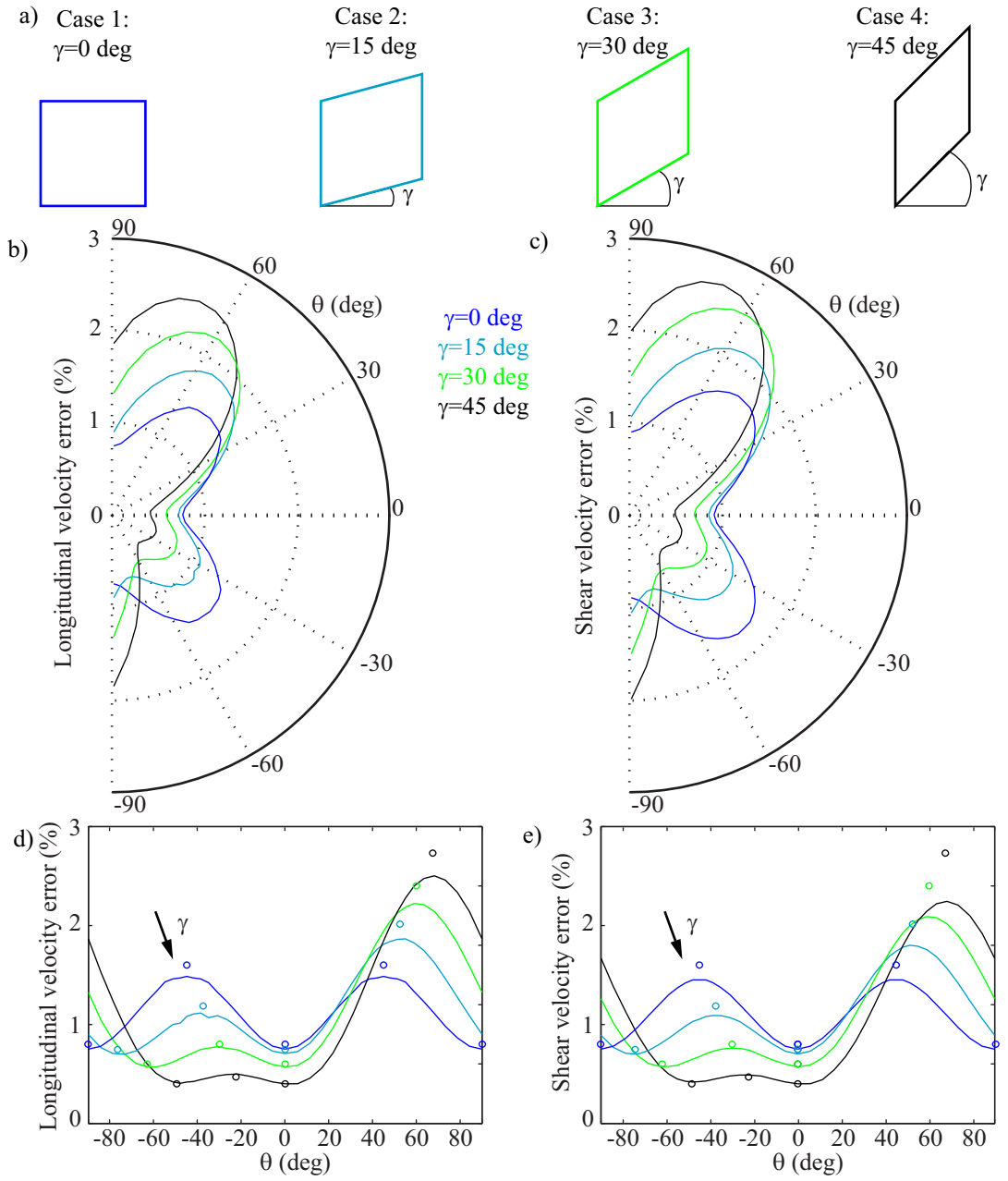

Figure 4.12. a) Shape of the different rhombic elements used in the mesh; Variation of the longitudinal (b and d) and shear (c and e) velocity error against the angle of incidence for various shearing angle γ plotted in a polar (b and c) and linear (d and e) fashion. The coloured circles indicate the error prediction along the element side and diagonal.

longitudinal waves. This phenomenon can be described as a stiffening of the element along the longest diagonal and a softening of the element along the shortest diagonal. As mentioned in the previous section, the critical factor determining the maximum velocity error is the error on the longest diagonal for shear waves. The stiffening occurring in this case is therefore beneficial to the modeller as it makes the predictions more conservative and thus safe to use.

4.2.2.4 Parallelogram elements

The mesh in this case is sheared and stretched. This means that the elements are transformed from a square to a parallelogram shape. The mesh density is kept constant in both the horizontal and the vertical directions. Contrary to the rhombus case, the element sides are not of equal length.

The models studied have a mesh density of 15 at 0 and 90 degrees. A low *CFL* of 0.05 is used. The shearing angle γ is varied from 0 to 45 degrees by 15 degree increments. The error on the velocity is monitored from -90 to +90 degrees as in this case there is no symmetry in the horizontal direction. Results for longitudinal and shear waves are plotted on Figure 4.13. Small circles are plotted on the linear plots. These represent the amplitude of the error predicted using the expression given in equation 4·13.

The general evolution of the error agrees with the rhombus case. The error is the same for all cases at 0 degrees and agrees well with the prediction. Contrary to the rhombus case, but as for the rectangle case, there is a shift between the actual position of the maximum and the diagonal where it would be expected. This confirms that the shift is likely to be due to the difference in length of the two pairs of opposite edges. Despite this shift, the actual value of the error and the predicted value on the diagonal agree closely. As seen before, the maximum value for the shear wave error is increasingly overestimated as the shearing angle increases. This is interpreted as a stiffening of the element along its longest diagonal as it is deformed. The longitudinal wave does not seem to suffer from this effect as strongly as the shear wave.

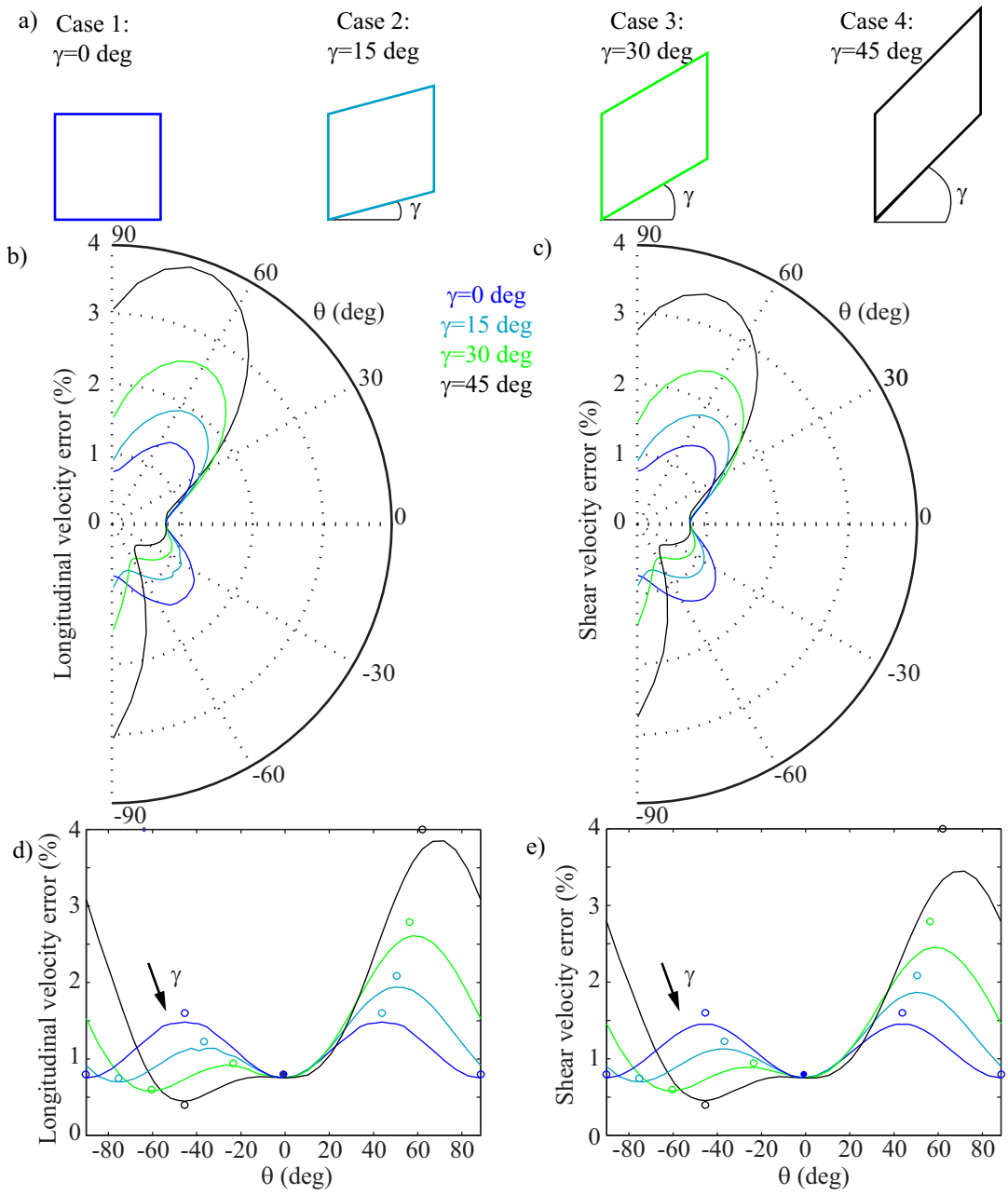

Figure 4.13. a) Shape of the different parallelogramatic elements used in the mesh; Variation of the longitudinal (b and d) and shear (c and e) velocity error against the angle of incidence for various shearing angle γ plotted in a polar (b and c) and linear (d and e) fashion. The coloured circles indicate the error prediction along the element side and diagonal.

4.2.2.5 Conclusion

The study of square element meshes has shown that the error along the element sides and diagonals can be predicted by the expression:

$$E_c = 180\frac{(1 - CFLX^2)}{N^2} \tag{4·14}$$

where CFL_X is the scaled Courant number and N is the mesh density.

Studies of deformed meshes made of rectangles, rhombi and parallelograms show that this expression also enables the obtention of a correct conservative approximation of the velocity error along the element sides and diagonals. This study looks at element deformation where square elements are stretched with element side ratios up to 2 and sheared up to 45 degrees. The main consequence of this point is that it indicates that as square elements are deformed in such a way, they do not lose their precision dramatically. Therefore, it is acceptable to apply such deformation to square elements in practical models.

4.2.3 Linear triangular elements

This section investigates models made of linear triangular elements. In ABAQUS/ Explicit, the only element of this type is a 3 node linear triangular element called CPE3 [14]. Meshes made of equilateral, isosceles and scalene triangles are investigated.

4.2.3.1 Equilateral triangle elements

In this part, the influence of *CFL* and *N* on wave propagation in a regular mesh made of linear equilateral triangular elements is investigated. A typical mesh is shown in Figure 4.14.

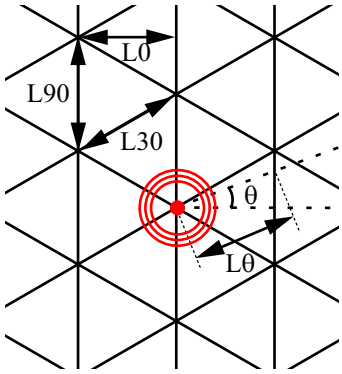

Figure 4.14. Schematic defining $L0$, $L90$, $L30$ and $L\theta$ in a mesh of equilateral-triangular elements.

The critical time step for this case is determined by the value $L0$ and not the element side length $L30$ or $L90$ as in the square element case, as explained in Section 2.3.1. The Courant number *CFL* is varied from 1 to 0.05 and the mesh density *N* ranges from 6 to 30 along the element side.

A first series of models is run. The error on both shear and longitudinal velocities is monitored over a range of angles from 0 to 90 degrees for a range of mesh densities using a low *CFL* of 0.05. Results are presented in Figure 4.15.

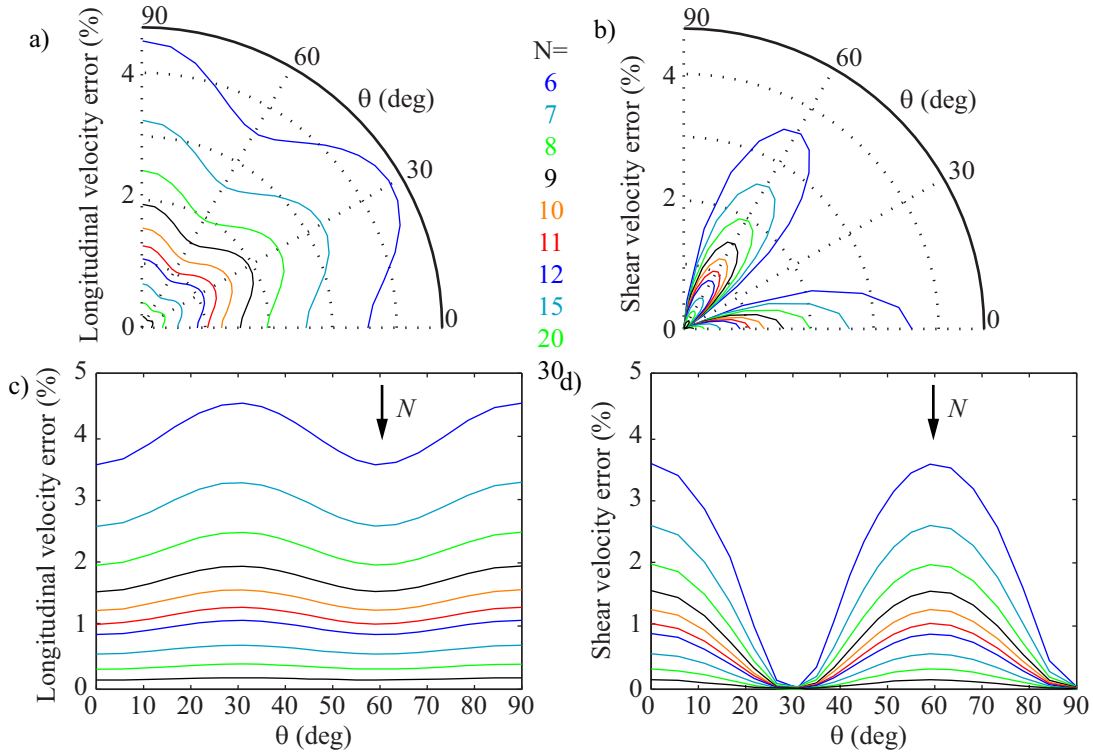

Figure 4.15. Variation of the longitudinal (a and c) and shear (b and d) velocity error against the angle of incidence for various mesh densities plotted in a linear (a and b) and polar (c and d) fashion.

As expected there are symmetries at 0, 30, 60 and 90 degrees in both cases. The longitudinal error is maximum at 30 and 90 degrees in the direction aligned with the mesh where $L\theta$ is maximum, and the error is minimum at 0 and 60 degrees where $L\theta$ is minimum. Between these points, the longitudinal error varies smoothly in a similar fashion to the phenomena observed for quadrilateral elements. On the other hand, the shear wave velocity error reaches its maximum at 0 and 60 degrees where $L\theta$ reaches its minimum and is unexpectedly close to zero at 30 and 90 degrees in the direction aligned with the mesh. Between these extremes, the variation is smooth but, unlike in previous cases, this variation cannot be described by a squared sine relation.

It is interesting to note that the value of maxima (at 30 and 90 degrees) and minima (at 0 and 60 degrees) of the error for the longitudinal wave and the maxima (at 0 and 60 degrees) of the error for the shear wave can be predicted accurately using the equation defined previously for quadrilateral elements:

$$E_c = \frac{180}{N^2} = \frac{180}{\left(\frac{\lambda}{L}\right)^2} \tag{4·15}$$

with L the element size defined as in Figure 4.14. This is clearly shown in Figure 4.16. This expression gives a general conservative value of the maximum error for a regular mesh of linear equilateral triangular elements. Given that the minimum shear error is zero at 30 and 90 degrees, all minima and maxima can be precisely predicted.

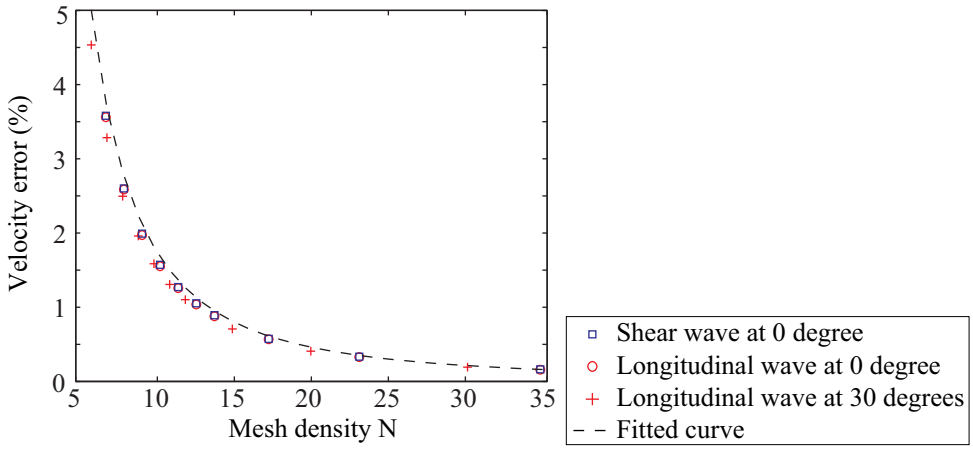

Figure 4.16. Velocity error against mesh density for shear and longitudinal waves at 0 and 30 degrees.

For longitudinal waves, it can be noted that the variation of the longitudinal wave error is precisely described by the following fitted expression:

$$E(\theta) = E(0) + (E(30) - E(0))\left(\sin\left(3\theta\frac{\pi}{180}\right)\right)^2 \tag{4·16}$$

with $E(0)$ and $E(30)$ the error at 0 and 30 degrees and θ the angle in degrees.

Figure 4.17 shows the influence of CFL_X on the value of the error on the longitudinal velocity at 0 and 90 degrees and the shear velocity at 0 degrees. The error tends towards zero as CFL_X tends to 1. This confirms that the stability limit is not defined by the smallest gap between nodes but by the transit time of a dilatational wave through the

smallest element in the model as described in Section 2.3.1. Once again, it can be seen that the errors can be fitted to the analytical expression:

$$E_c(N, CFL_X) = E_c(N)_{(CFL_X \to 0)} \cdot (1 - CFL_X^2) \tag{4·17}$$

where $E_c(N)_{(CFL_X \to 0)}$ is value of the velocity error when CFL_X tends to zero.

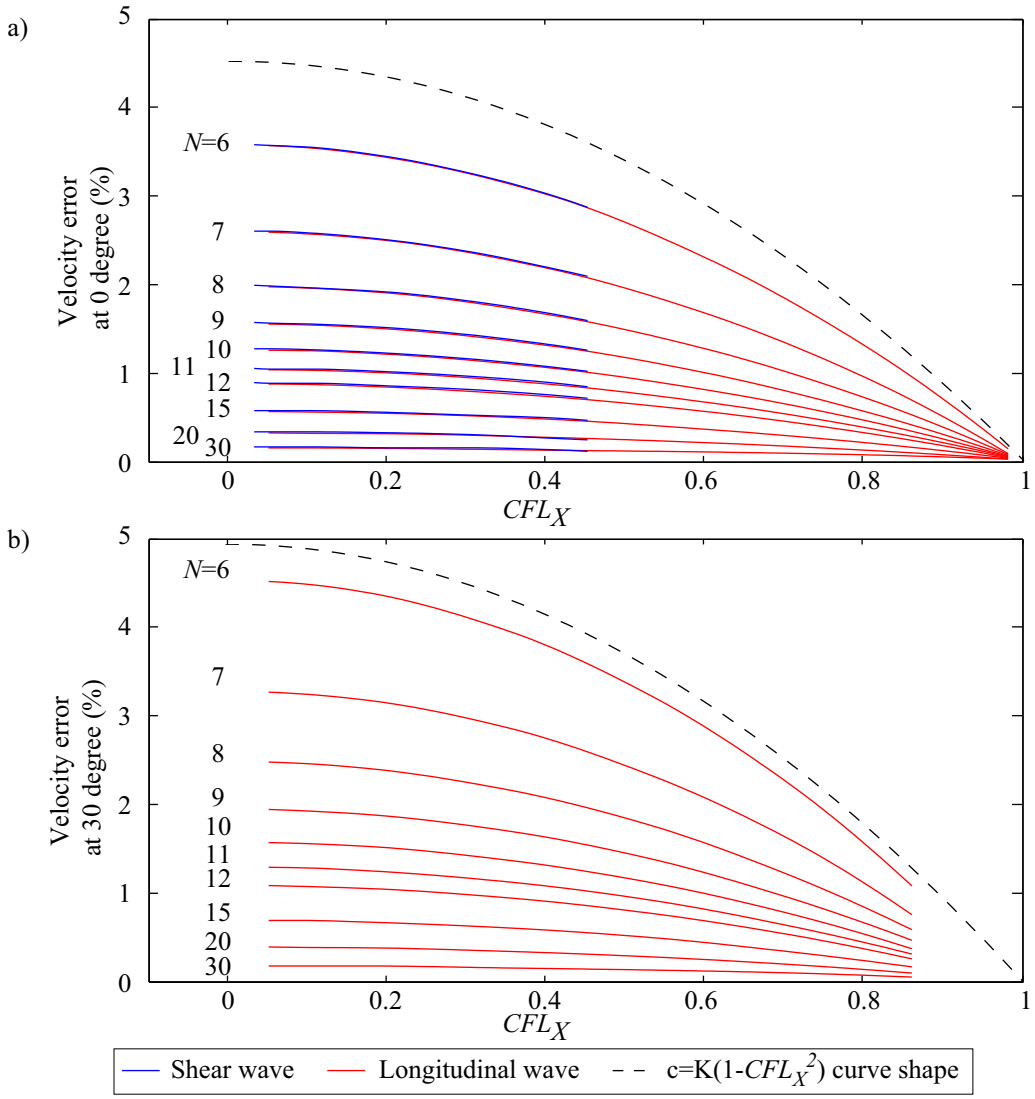

Figure 4.17. Velocity errors against CFL_X for various mesh densities at a) 0 and b) 30 degrees.

It is therefore possible to predict the maximum longitudinal error along the element side, the minimum longitudinal error along the altitude of the element and the maximum shear error along the altitudes of the triangular element for any mesh density N and relative Courant number CFL_X by using the following expression:

$$E_c = 180\frac{(1 - CFLX^2)}{N^2} \tag{4·18}$$

4.2.3.2 Isosceles triangle elements

This section looks into the influence of having a mesh of isosceles triangular elements rather than equilateral ones. It is essential to be able to evaluate the impact of deforming elements from the equilateral form as automatic meshing algorithms used by standard FE package will commonly contain non-equilateral triangular elements. In this study, we used a mesh similar to the one used previously but the mesh density is kept the same in the y (vertical) direction whereas it is varied in the x (horizontal) direction. This leads to a mesh constituted of same-size isosceles triangles in a similar way to the equilateral case considered previously. The 7 isosceles triangles shapes used for this study are shown in Figure 4.18.a. For each triangle, one angle is varied from 30 to 90 degrees while the two other angles are equal. It can be seen that the mesh density will be constant in the vertical direction and is taken as 10 elements per wavelength whereas the density in the horizontal direction is varied from 5.35 to 20. The mesh is stretched in the horizontal direction and the mesh density is kept the same in the vertical direction. The equal angles are varied from 75 degrees to 45 degrees leading to a variation of the other angle ϕ from 30 to 90 degrees. Results of the variation of the velocity error against the angle are shown on Figure 4.18.

Looking at the longitudinal wave error, it can be seen that the constant mesh density at 90 degrees leads to the error being between 1.35% and 1.70% and relatively close to the estimate of 1.8% predicted by equation 4·18. Despite the constant mesh density in this direction, one can see that the error drops systematically as ϕ is increased at this angle. At 0 degrees, a much greater difference exists between cases. This is justified by the fact that the mesh density varies strongly in this direction. Once again, the prediction agrees closely with the actual values. Between these values, a cycle similar to that for equilateral linear elements is observed. The maximum and minimum occurs close to - but not exactly at - the location of the local maximum and minimum of $L\theta$. These occur when $L\theta$ is aligned with the mesh and when $L\theta$ is perpendicular to the opposite face of an element. Although the angular position of the maximum is slightly incorrect, the predicted value of the error proves to be close to the actual minimum and maximum. It is therefore possible for the modeller to predict the longitudinal velocity error quite precisely using equation 4·18.

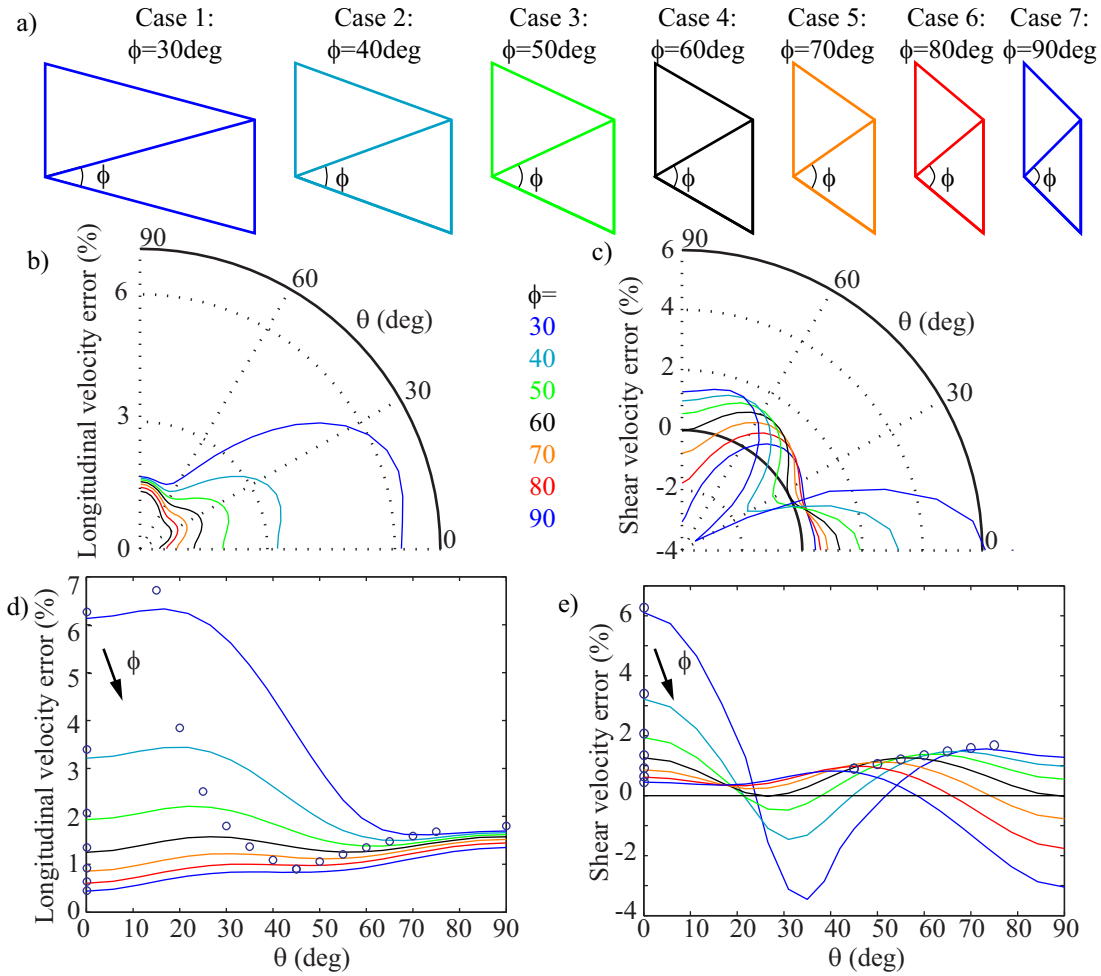

Figure 4.18. a) Shape of the different isosceles-triangular elements used in the mesh; Variation of the longitudinal (b and d) and shear (c and e) velocity error against the angle of incidence for various values of ϕ plotted in a polar (b and c) and linear (d and e) fashion. The coloured circles indicate the error prediction along the element side and diagonal.

For shear waves, a maximum (local for cases 5 to 7) occurs at 0 degrees. The value of this maximum matches the prediction closely as represented on the Figure 4.18. For all cases, another maximum (local for cases 1 to 3) occurs at an angle close to the direction of the median of the upper triangle. The value of this maximum is also closely predicted. Between these maximum values, the error varies smoothly toward minimum values located at angles where Lθ is aligned with the mesh. For case 4 where ϕ is 60 degrees the triangle is equilateral, this minimum occurs at θ equals 30 degrees and is close to zero. As ϕ is increased, the value of the minimum increases despite the fact that $L\theta$ is reduced. When ϕ is decreased from 60 degrees, the minimum error becomes negative, meaning that the actual velocity is higher than the theoretical one. This phenomenon occurs despite the fact that $L\theta$ is increased and indicates a stiffening effect along the longest edge of the element. The same effect occurs at 90 degrees when minima (local for cases 1 to 3) occur. At this angle, a decrease of ϕ leads to an increase

in the minimum despite $L\theta$ being constant whereas an increase of ϕ leads to a decrease in the error. This decrease from ϕ equals 60 degrees means cases 5 to 6 have negative errors at 90 degrees. The essential point is that, for case 7, the maximum absolute error is 3% due to the measured negative error whereas the measured positive and predicted maximum error is 0.8%. The deformation of the element leads to a strong increase of the shear velocity along the longer edge of the element. This is critical when the longest edge of the triangle faces a large angle as is the case for cases 5, 6 and 7.

These results strongly highlight that using two triangular linear elements to create a "composite quadrilateral element" leads to results which will not match those of a real quadrilateral linear element and should therefore be avoided.

4.2.3.3 Scalene triangle elements

This part looks into the influence of having a mesh of scalene triangular elements. The mesh used for the equilateral case is sheared in a similar way to the parallelogram study for quadrilateral elements. The mesh density is kept the same in the *y* (vertical) and *x* (horizontal) direction at 10 and 11.55 elements per wavelength respectively while the element is sheared in the *y* direction. The shearing angle varies from 0 to 45 degrees. The 4 scalene triangular shapes used for this study are shown in Figure 4.19.a. Case 1 is the equilateral case while case 3 uses right (but not isosceles) triangles. Results of the variation of the velocity error against the angle are shown on Figure 4.19.

For longitudinal waves, the variation of the error for cases 1, 2 and 3 is similar to what was experienced in previous studies. For case 4, an unexpected minimum occurs at 22 degrees and an unexpected maximum occurs at -63 degrees. These could be explained by the cumulation of the effects of mesh density variation and a stiffening and softening of the element along the longest edge and the altitude from the longest edge respectively. The effect explains why the overall maximum for case 4 is strongly underestimated and the overall minimum slightly overestimated. A similar milder effect is occurring for case 3 where the difference between the predicted and actual maximum is 0.75%.

For shear waves, the variation of the error highlights the same issue observed with isosceles triangles with large angle opposite long edges as the error becomes negative.

Case 4 is the most critical case studied for triangle elements so far as the ratio of the longest to the shortest edge is 1.62 and the long edge is opposite to an angle of 107 degrees. The stiffening effect is the most pronounced as the error reaches a maximum negative value of 16.4% which is more than 10 times the maximum predicted error for this case. This emphasizes that using highly deformed triangular linear elements for wave propagation should be avoided.

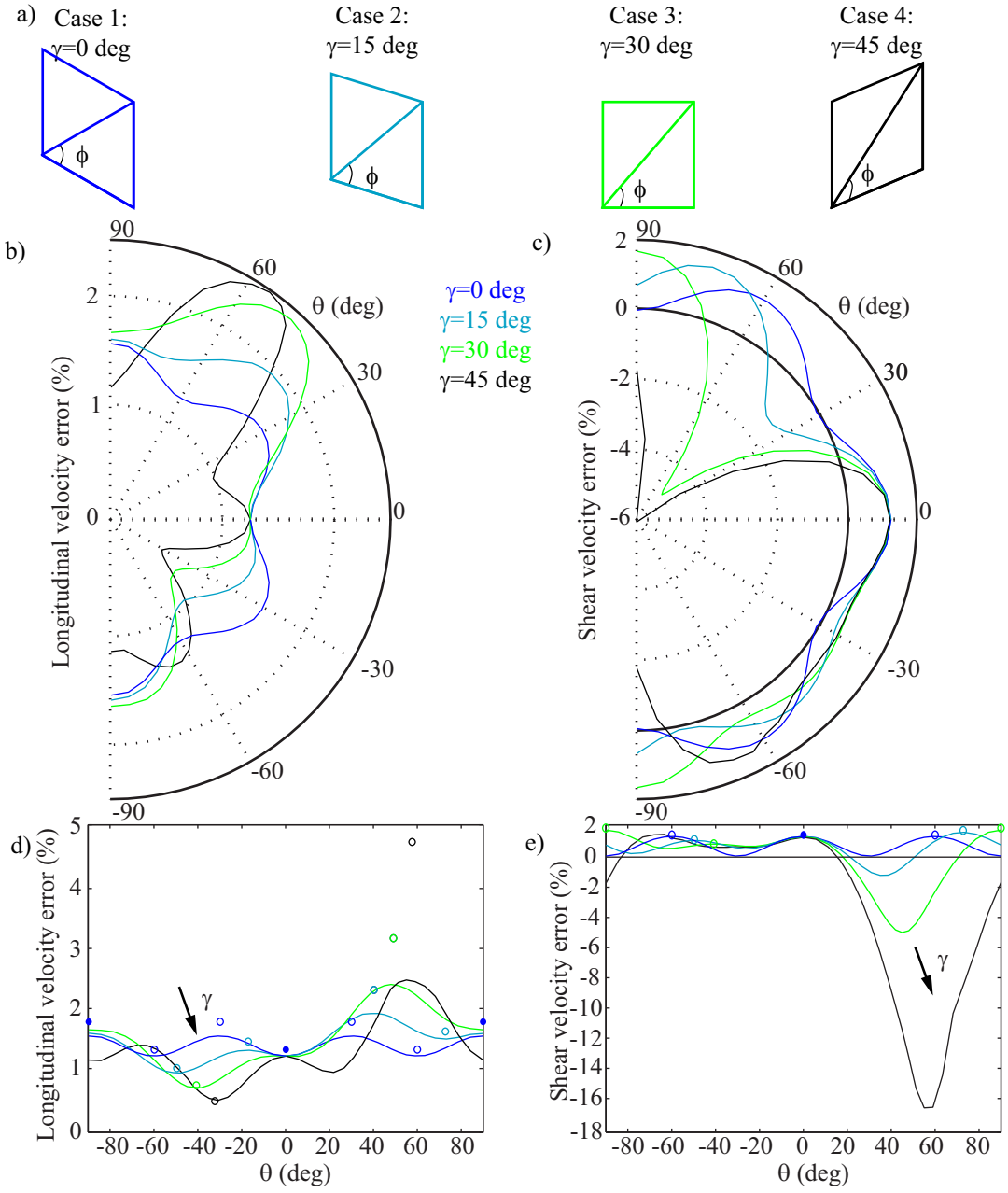

Figure 4.19. a) Shape of the different scalene-triangular elements used in the mesh; Variation of the longitudinal (b and d) and shear (c and e) velocity error against the angle of incidence for various values of γ plotted in a polar (b and c) and linear (d and e) fashion. The coloured circles indicate the error prediction along the element side and diagonal.

4.2.3.4 Conclusion

The study of equilateral triangular element meshes has shown that the error along the element sides and altitudes could be accurately predicted. The influence of the Courant number on the error is confirmed to be similar to the one observed with quadrilateral elements.

Studies of deformed meshes made of isosceles and scalene triangles shows that it is possible to use predicted errors to conservatively evaluate the maximum error for longitudinal waves. The situation with shear waves is rather different as it is observed that an apparent stiffening of the deformed elements leads to a large increase in the propagation velocity leading to a large velocity error that cannot be predicted in the same way as was done in previous cases. This effect is a noticeable concern regarding the use of linear triangular elements with automatic meshing algorithms.

4.2.4 Modified quadratic triangular elements

This section investigates models made of quadratic triangular elements. In ABAQUS/ Explicit, the only element of this type is a 6 node modified quadratic triangular element called CPE6M [14]. Meshes made of equilateral, isosceles and scalene triangles are investigated.

4.2.4.1 Equilateral triangle elements

In this part, we investigate the influence of *CFL* and *N* on wave propagation in a regular mesh made of quadratic equilateral-triangular elements as shown in Figure 4.20. The mesh density *N* and *CFL* is expressed in terms of the node grid and not the actual element size as it will be shown that this is what actually matters with this element type.

As for linear elements, the critical time step is determined by the value $L0$ and not the element side length $L30$ or $L90$. The Courant number *CFL* is varied from 0.9 to 0.05 and the mesh density *N* ranges from 6 to 30 along the element side.

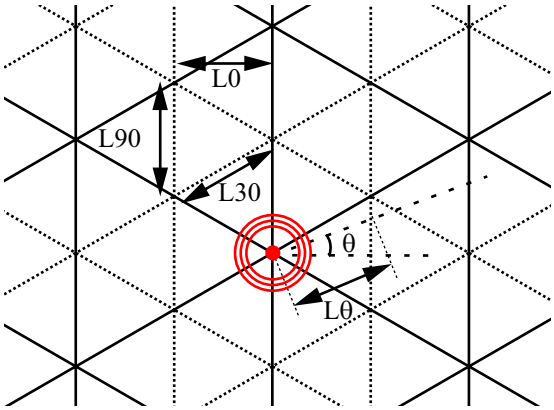

Figure 4.20. Schematic defining $L0$, $L90$, $L30$ and $L\theta$ in a mesh of quadratic equilateral-triangular elements.

A first series of models is run. The error on both shear and longitudinal velocity is monitored over a range of angle from 0 to 90 degrees for a range of mesh densities using a low *CFL* of 0.05. Results are presented in Figure 4.21.

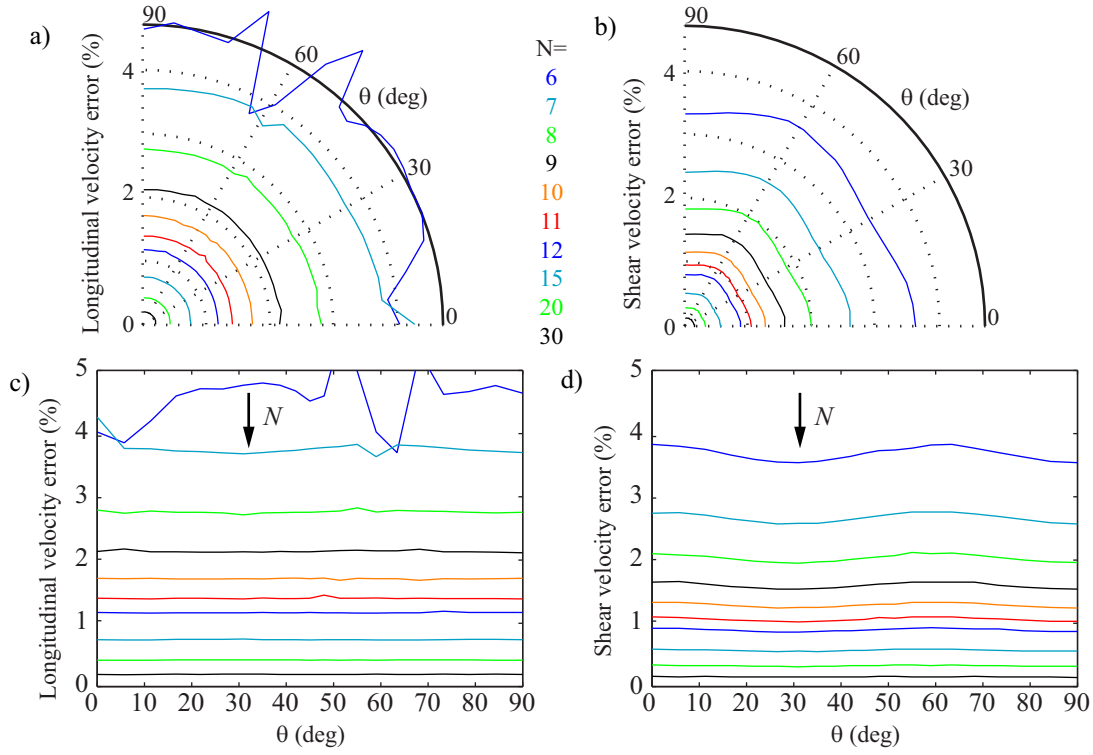

Figure 4.21. Variation of the longitudinal (a and c) and shear (b and d) velocity error against the angle of incidence for various mesh densities plotted in a polar (a and b) and linear (c and d) fashion.

The results for longitudinal waves indicate that for any mesh density higher than 7 the error remains close to constant at any angle. This is an interesting feature as it means that the wave propagates in all directions at a constant velocity as one would expect in an isotropic material. For a mesh density of 6 nodes per wavelength, the number of elements per wavelength is 3. The inconsistency of the results in this particular case

indicates that this is not sufficient to correctly represent longitudinal wave propagation. As the mesh density is increased, the strength of these inconsistencies decreases indicating that the wave propagation is correctly represented. This point raises the issue of the minimum number of elements necessary to represent the wave propagation correctly and will be discussed further.

For shear waves, the pattern observed for all mesh densities is similar to the one observed for linear quadrilateral elements as the maxima occur at 0 and 60 degrees and the minima at 30 and 90 degrees with a squared sine variation between them.

The improvement in the consistency of the velocity for both longitudinal and shear waves against the angle of propagation is an interesting feature. The fact that the mesh density needs to be at least equal to 7 to correctly represent the wave propagation is of limited importance. It indicates that the use of quadratic elements increases the minimum computational needs, but this only affects a limited range of models. The influence of the mesh density on the error is represented in Figure 4.22.

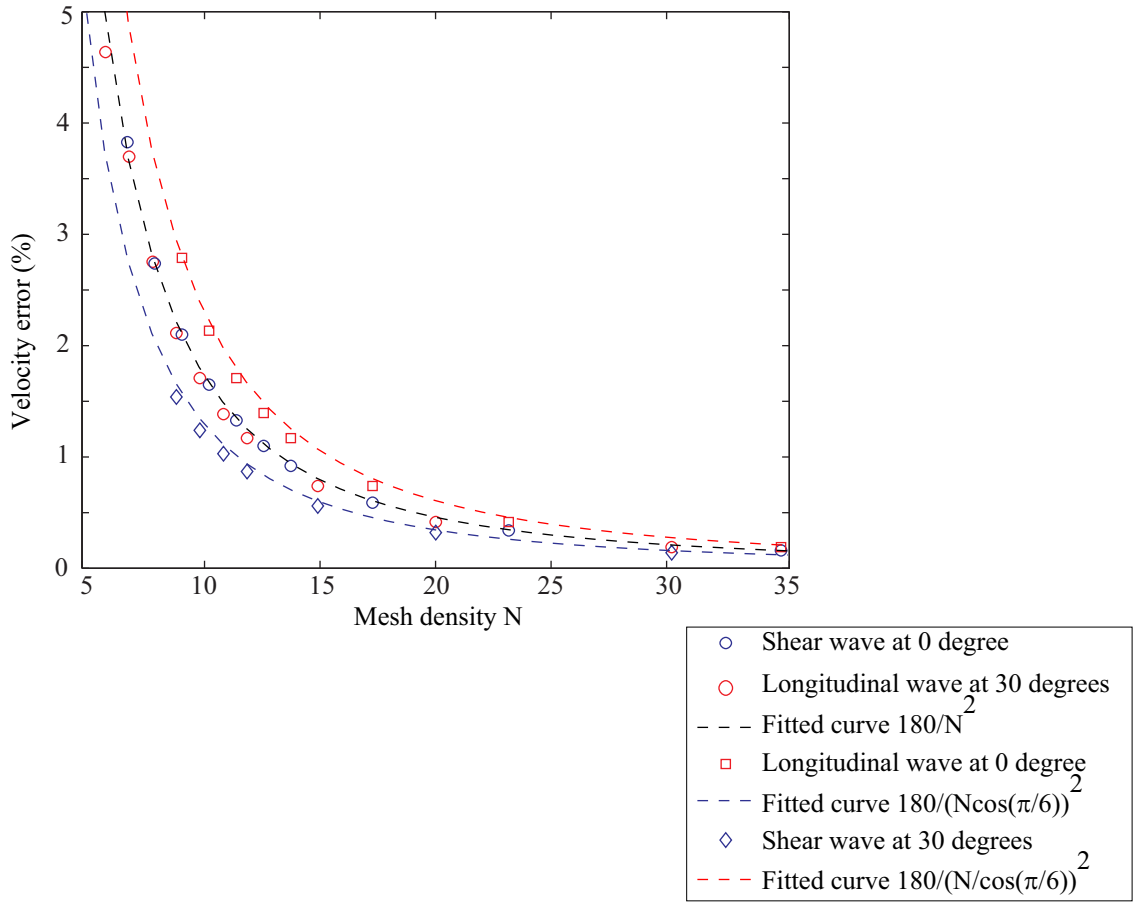

Figure 4.22. Velocity error against mesh density for shear and longitudinal waves at 0 and 30 degrees.

As the longitudinal velocity is constant against the angle, the error is plotted against the mesh density defined by the node spacing on the edge of the elements. Plotting the error for both longitudinal and shear waves at 0 and 30 degrees, it can be seen that the errors for shear waves at 0 degrees and for longitudinal waves at 30 degrees agree well with the prediction given for linear elements:

$$E_c = \frac{180}{N^2} = \frac{180}{\left(\frac{\lambda}{L_\theta}\right)^2} \tag{4·19}$$

where N is defined using $L\theta$ as defined on Figure 4.20.

The plot also indicates the trend followed by the longitudinal error at 0 degrees as:

$$E_c = \frac{180}{N^2 \cos\left(\frac{\pi}{6}\right)^2} = \frac{180}{\left(\frac{\lambda}{L_\theta}\right)^2 \cos\left(\frac{\pi}{6}\right)^2} \tag{4·20}$$

The shear error at 30 degrees can also be predicted by:

$$E_c = \frac{180\cos\left(\frac{\pi}{6}\right)^2}{N^2} = \frac{180\cos\left(\frac{\pi}{6}\right)^2}{\left(\frac{\lambda}{L_\theta}\right)^2} \tag{4·21}$$

This validates that the maximum errors for quadratic and linear elements vary in the same way and with the same amplitude as the mesh density varies but that the minimum error follows different rules.

The next point to look into is the influence of the Courant number CFL on the error. It is varied from 0.9 to 0.05. The scaled Courant number CFL_X varies from 0.78 to 0.043 for a longitudinal wave at 30 degrees and from 0.45 to 0.025 for a shear wave at 0 degrees. The errors for longitudinal waves at 90 degrees and shear waves at 0 degrees are plotted against CFL_X over the range of mesh density studied. Results are shown on Figure 4.23. The variation of the error against CFL_X is similar to the one experienced for linear elements.

The maximum error for both wave types is defined as:

$$E_c = 180\frac{(1-CFLX^2)}{N^2} \tag{4·22}$$

where N is the mesh density calculated using $L\theta$.

As a conclusion, quadratic elements have the advantage of an improved consistency of the propagation velocity against the angle of incidence for both shear and longitudinal waves. On the other hand, it was noted that the smallest mesh density to correctly model wave propagation is 8 nodes per wave length (against 6 for linear elements). The fact that the element size is doubled compared to linear elements reduces the capability to represent small model features with a regular mesh but the quadratic variation of the edge means less elements are required to represent features such as holes.

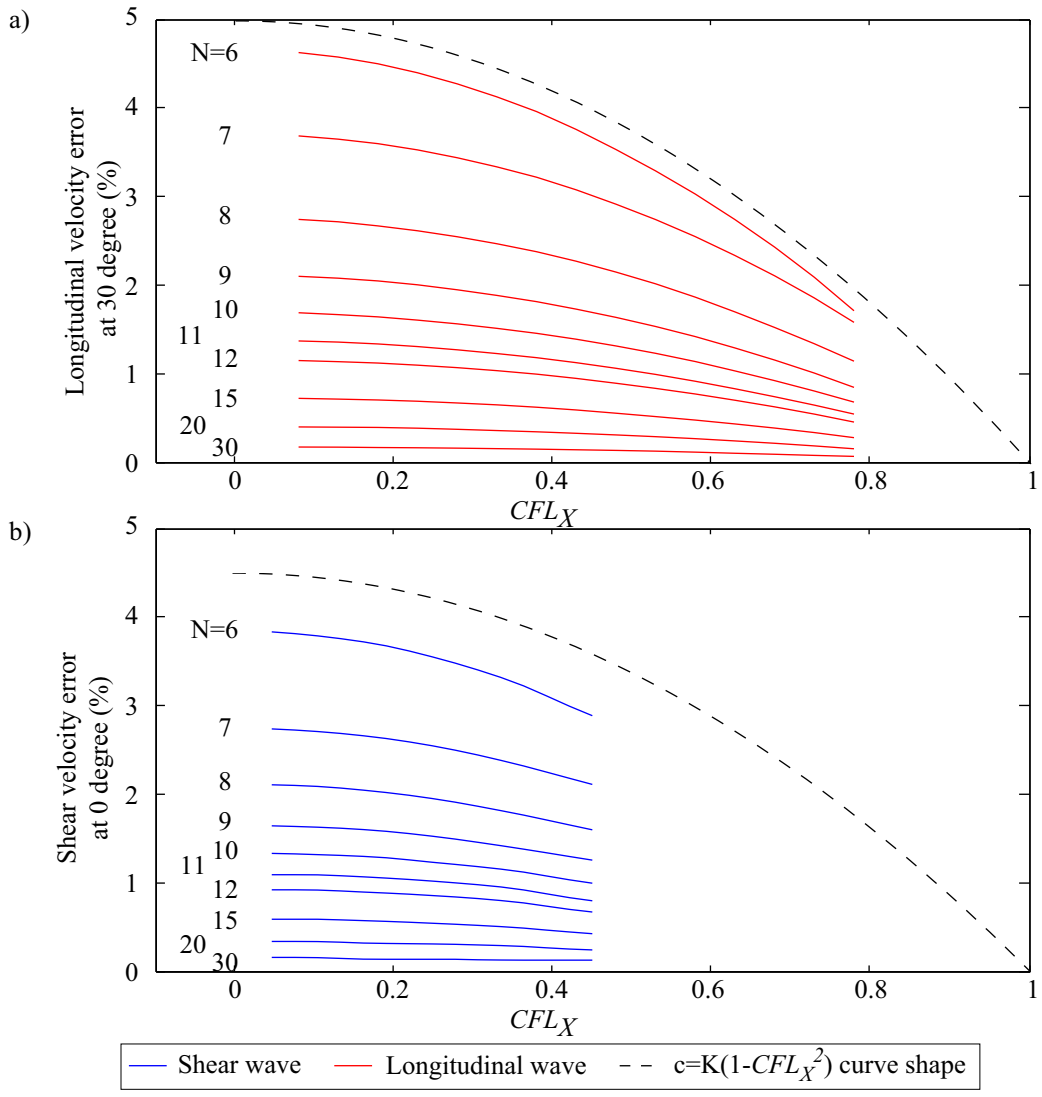

Figure 4.23. Velocity errors against CFL_X for various mesh densities at a) 0 and b) 30 degrees.

4.2.4.2 Isosceles triangle elements

This study is similar to that done for linear isosceles triangular elements. The same node grid is used but is filled with quadratic rather than linear elements. This means that the mesh density is the same and the element size is doubled. The mesh density is kept at 10 nodes per wavelength in the *y* (vertical) direction whereas it is varied in the *x* (horizontal) direction from 5.35 to 20. The mesh is hence constituted of same-size isosceles triangles. The 7 isosceles triangle shapes used for this study are shown in Figure 4.24.a. For each triangle, one angle is varied from 30 to 90 degrees while the two other angles are kept equal. The equal angles are varied from 75 degrees to 45 degrees leading to a variation of the other angle ϕ from 30 to 90 degrees. Results of the variation of the velocity error against the angle are shown on Figure 4.24.

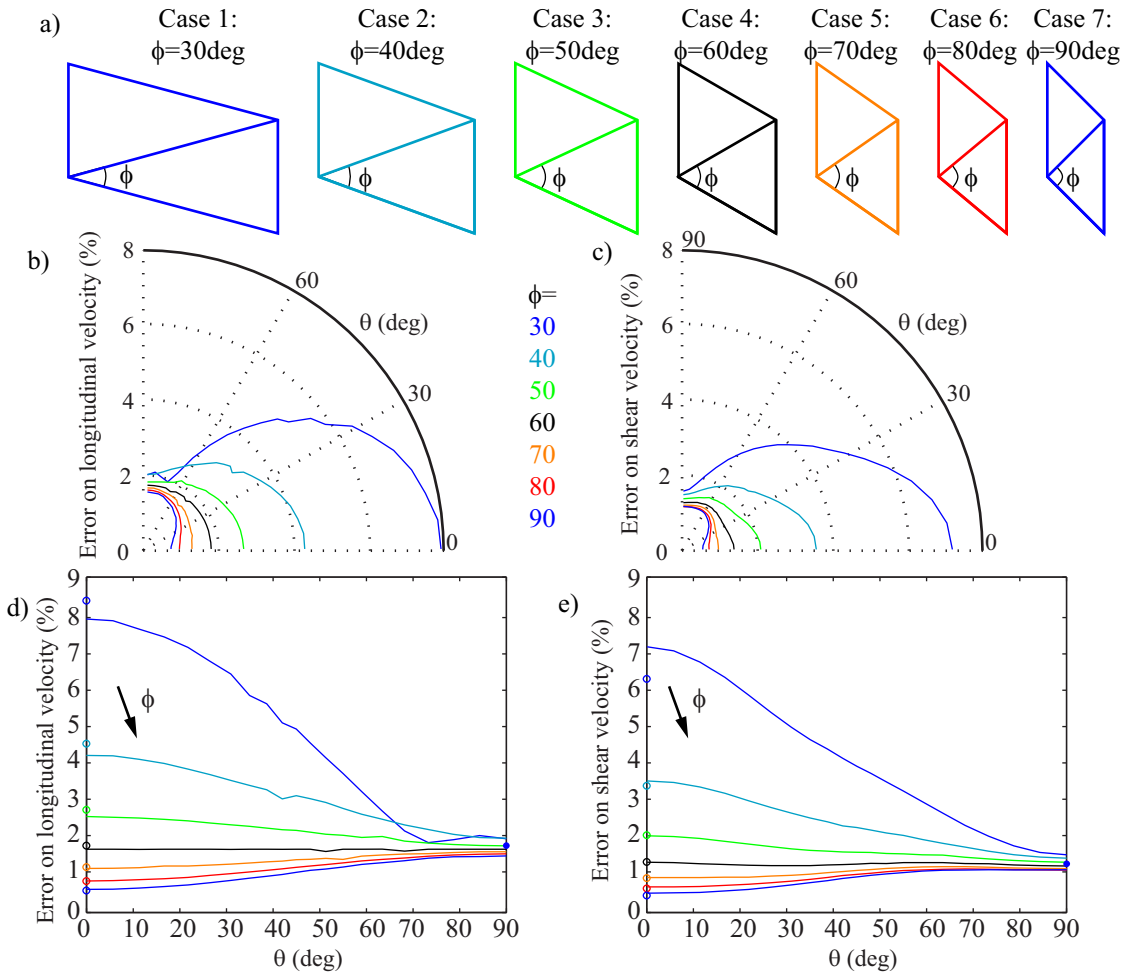

Figure 4.24. a) Shape of the different quadratic isosceles-triangular elements used in the mesh; Variation of the longitudinal (b and d) and shear (c and e) velocity error against the angle of incidence for various values of ϕ plotted in a polar (b and c) and linear (d and e) fashion. The coloured circles indicate the error prediction along the element side and diagonal.

For longitudinal waves, as seen previously, the error for the equilateral case is constant. For other cases, the maximum and minimum are located at 0 and 90 degrees and a smooth variation occurs between these 2 points. As the angle ϕ is reduced, the maximum error is located at 0 degrees and the minimum at 90 degrees. For ϕ greater than 60 degrees, the maximum is at 90 degrees and the minimum at 0 degrees. The predictions given by equation 4·18 agree well with the actual minima and maxima and are conservative for the maxima.

For shear waves, the variation follows a similar pattern to the one observed for bulk waves although the undulation occurring for the equilateral case is visible on the other cases but does not seem to influence the overall results. The prediction of the maxima is accurate for all cases apart for case 1 for which the prediction is 0.9% below the actual value. It is also noted that the prediction is not conservative for case 2 being 0.1% below the correct value. For all other cases, the estimate is conservative and within 0.2%. It is therefore correct to use the estimates as outlined previously for equilateral triangles.

It is very interesting to note the significant improvement observed for shear waves compared to linear elements. The shear error does not deteriorate dramatically as the element is deformed. Quadratic elements can be used without any fear of a small deformed element giving a larger than expected error for shear waves. This allows the modeller to use automatic meshing algorithms more confidently.

4.2.4.3 Scalene triangle elements

This part looks into the influence of having a mesh of quadratic scalene triangular elements. The node mesh is the same as used previously for the linear case. The mesh density is kept the same in the *y* (vertical) and *x* (horizontal) direction at 10 and 11.55 elements per wavelength respectively while the element is sheared in the *y* direction. The shearing angle varies from 0 to 45 degrees. The 4 scalene triangular shapes used for this study are shown in Figure 4.25.a. Case 1 is the equilateral case while case 3 uses right (but not isosceles) triangles. Results of the variation of the velocity error against the angle are shown on Figure 4.25.

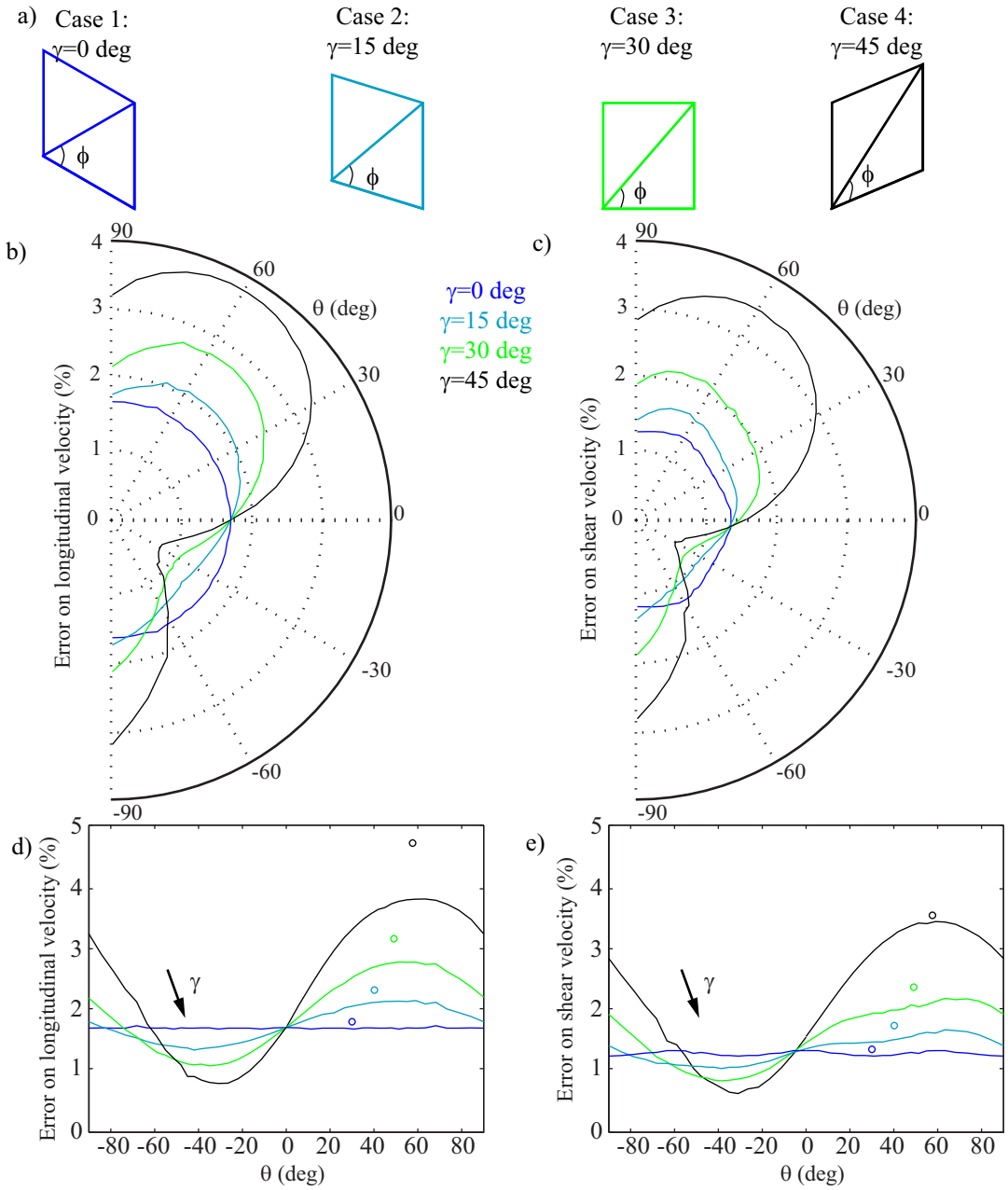

Figure 4.25. a) Shape of the different quadratic scalene-triangular elements used in the mesh; Variation of the longitudinal (b and d) and shear (c and e) velocity error against the angle of incidence for various values of γ plotted in a polar (b and c) and linear (d and e) fashion. The coloured circles indicate the error prediction along the element side and diagonal.

For longitudinal waves and all cases apart from case 1, the error varies smoothly and describes a full sine like cycle. Maxima are reached between 0 and 90 degrees and a minimum between -90 and 0 degrees. The prediction for the maxima is calculated along the longest edge of the element. The estimation is relatively accurate although, as γ is increased, the margin grows larger. This is in line with the relative error that was observed at 90 degrees for isosceles triangles.

For shear waves, a similar pattern is observed although the undulation occurring for case 1 (equilateral triangle), exists for all cases and modifies slightly the overall shape of the curves. The predictions for the maximum error are calculated along the longest element side and agree well with the actual results in a conservative way. Again, using modified quadratic elements instead of linear ones dramatically improves the precision of the shear wave propagation velocity.

4.2.4.4 Conclusion

The study of equilateral triangular meshes made of modified quadratic elements has shown that the longitudinal velocity error is very close to constant for N superior to 7. For shear waves, a velocity error variation exists but is limited. This variation is closer to the one observed with square elements than with equilateral triangular elements. The maximum error for both wave types is identified and an expression can be used to predict its amplitude. The influence of the Courant number on the error is confirmed to be similar to the one observed previously in this chapter.

Studies of deformed meshes made of isosceles and scalene triangles show that the error predictions derived from equation 4.26 are quite accurate although not always conservative in cases where deformation is high. The most important point of this study is that, contrary to linear triangular elements, no dramatic degradation of the error is noted for any wave type and deformation level. Therefore, it can be said that this element type can be used deformed without concern. It can be noted that the modified quadratic elements react to deformation in a similar fashion as linear quadrilateral elements. In the same way, the velocity error for a mesh of linear square elements and modified quadratic equilateral triangle elements is relatively close. Based on these two facts, it can be said that modified quadratic triangular elements behave in a similar way to linear quadrilateral elements.

4.3. Implicit solving

4.3.1 Introduction

In this section, the influence of the mesh density and angle of incidence are investigated for a range of element types.

The geometry and properties of the models are the same as in the explicit cases. The excitation is applied in the same way apart from the fact that it is applied as a real harmonic signal of unit frequency. Models are solved in the frequency domain by the implicit direct-solution steady state scheme of ABAQUS/Standard [14]. As the model is solved in the frequency domain, no time increment is used and no Courant number applies to these models. The monitored displacements are processed in the same way in order to measure the propagation velocity.

As ABAQUS/Standard offers a wider range of elements than ABAQUS/Explicit, the following elements [14] are investigated: linear quadrilateral element (CPE4), quadratic quadrilateral element (CPE8), linear triangular element (CPE3), modified quadratic triangular element (CPE6M) and quadratic triangular element (CPE6). CPE4 and CPE8 elements are full integration elements and are not available in ABAQUS/ Explicit (which only has reduced integration linear quadrilateral elements available).

All studies start with a mesh made of square or equilateral elements. Following this, the meshes are deformed in order to understand how the deformation impacts the velocity error. The mesh density is varied from 6 to 30 and is defined in the same way as in Section 2.3.1.

4.3.2 Linear quadrilateral elements

4.3.2.1 Square elements

The velocity errors for both shear and longitudinal velocities monitored over a range of angles from 0 to 90 degrees for a range of mesh densities are plotted on Figure 4.26.

It can be noted that the general variation of the error is the same as the one observed with reduced integration linear square elements in Section 4.2.2.1. The amplitude of the error for the longitudinal wave superimposes almost perfectly with the results from

Section 4.2.2.1. For shear waves, the agreement is similar at 0 and 90 degrees but the increase in error with reduced integration elements in the explicit case is stronger than the full integration ones in the implicit case. This discrepancy is likely to be due to the change in integration technique rather than the change in solving process.

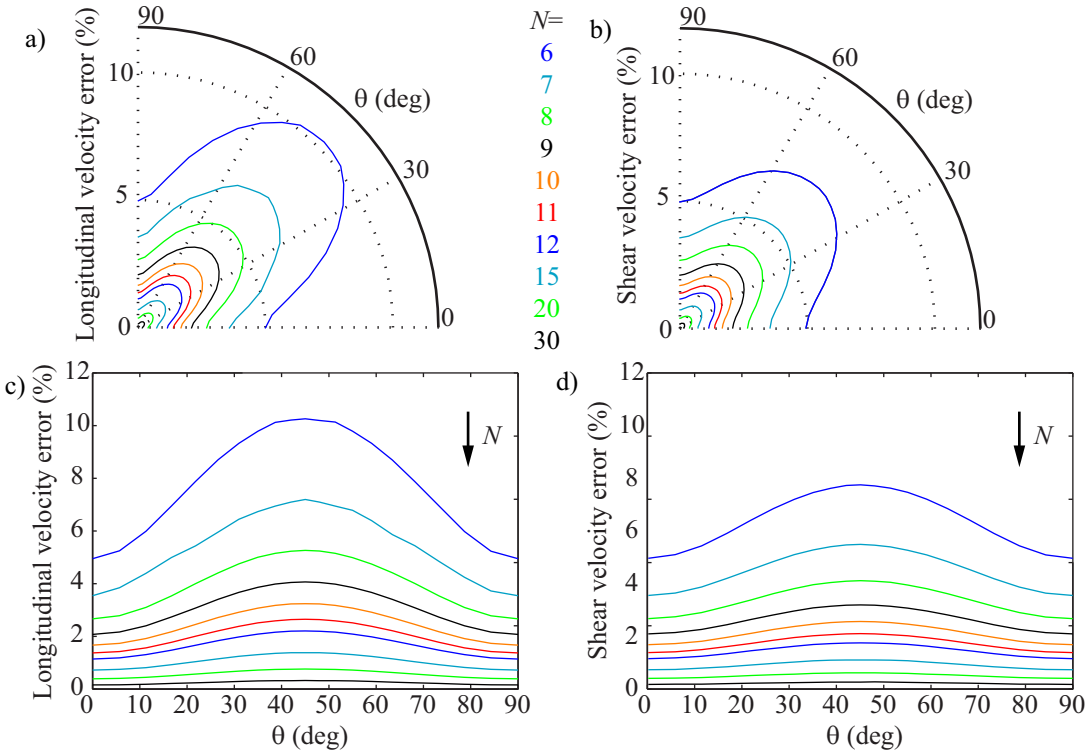

Figure 4.26. Variation of the longitudinal (a and c) and shear (b and d) velocity error against the angle of incidence for various values of mesh density plotted in linear (a and b) and polar (c and d) plots.

4.3.2.2 Rectangle elements

The meshes studied in this part are "stretched" in one direction to create rectangular elements. The element size in the vertical direction *y* is kept the same for all models so that the mesh density *N* in this direction is 15. The element size in the horizontal direction *x* is varied so that the mesh density *N* varies from 7.5 to 30. The ratio between the element side *R=Lx/Ly* is hence varied from 0.5 to 2 as illustrated on Figure 4.27.a. The error on the velocity is measured over a range of angles from 0 to 90 degrees and plotted on Figure 4.27.b,c,d,e.

As seen with square elements, the longitudinal wave case matches the explicit case almost perfectly and the shear wave case matches it at 0 and 90 degrees, but the increase in error between these points is smaller than in the explicit case.

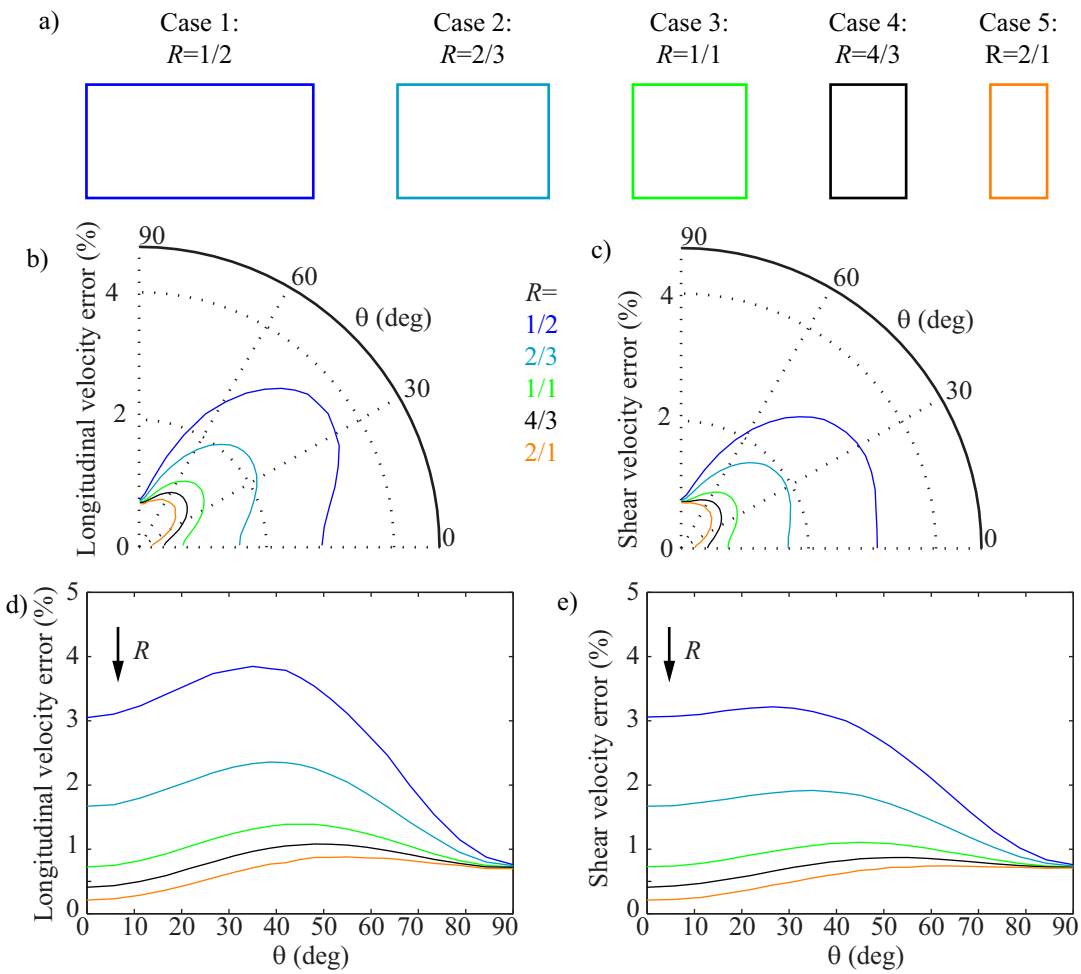

Figure 4.27. a) Shape of the different rectangular elements used in the mesh; Variation of the longitudinal (b and d) and shear (c and e) velocity error against the angle of incidence for various values of *R* plotted in a polar (b and c) and linear (d and e) fashion.

4.3.2.3 Rhombus elements

Meshes in this case are sheared so elements are deformed from a square to a rhombus. The models studied have a mesh density of 15 along the element sides. The shearing angle γ is varied from 0 to 60 degrees by 15 degree increments. The error on the velocity is monitored from -90 to +90 degrees and is plotted on Figure 4.28.

In these cases, the amplitude of the error is similar to the explicit case for low deformation. It diverges quite strongly (in particular for shear waves) as the mesh is deformed but stays smaller than the explicit case error.

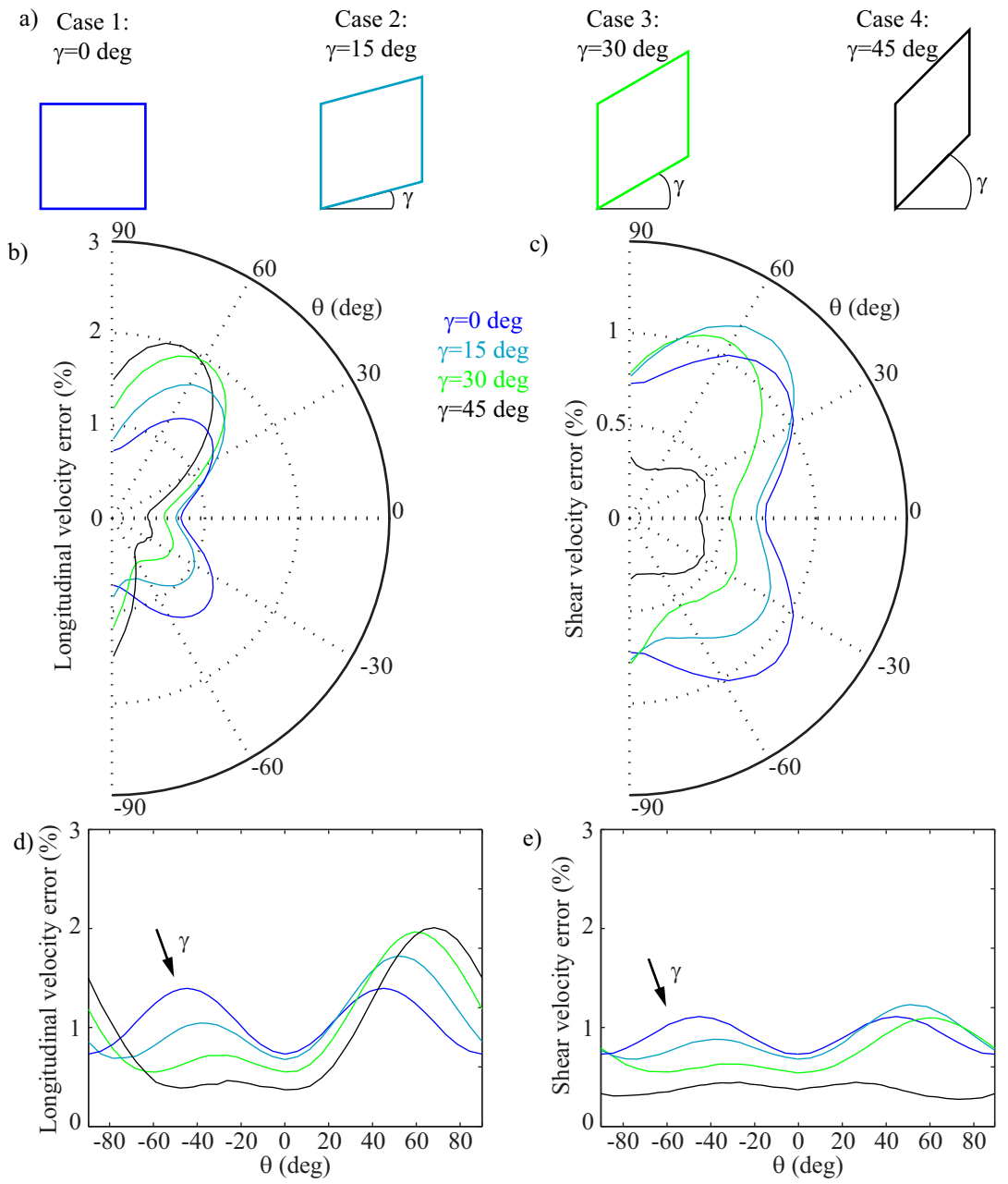

Figure 4.28. a) Shape of the different rhombic elements used in the mesh; Variation of the longitudinal (b and d) and shear (c and e) velocity error against the angle of incidence for various values of γ plotted in a polar (b and c) and linear (d and e) fashion.

4.3.2.4 Parallelogram elements

The mesh in this case is sheared and stretched with a mesh density of 15 at 0 and 90 degrees. The shearing angle γ is varied from 0 to 45 degrees by 15 degree increments as shown on Figure 4.29.a. Results are plotted on Figure 4.29.

The findings for the parallelogram case are in line with those of the rhombus cases.

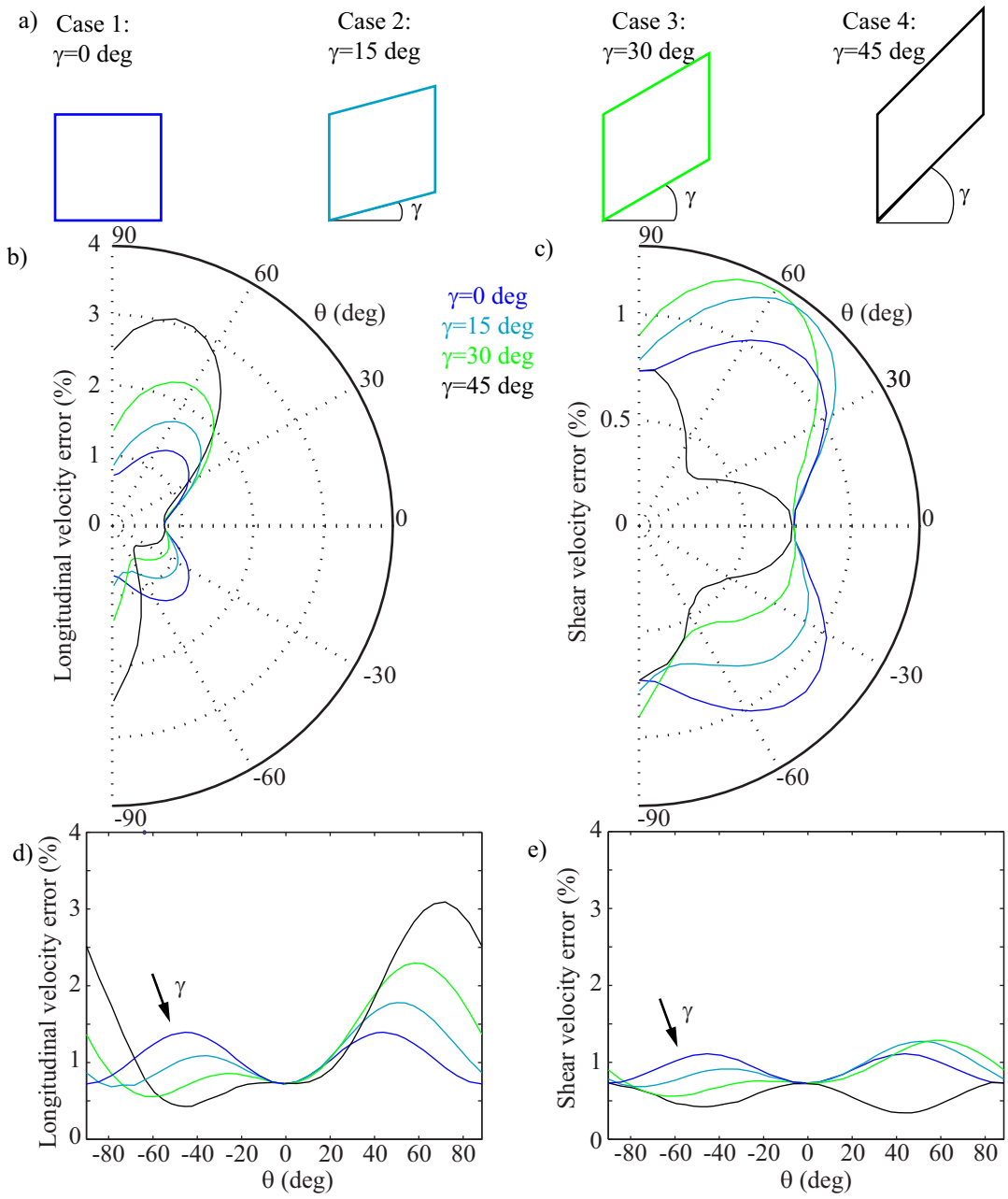

Figure 4.29. a) Shape of the different parallelogramatic elements used in the mesh; Variation of the longitudinal (b and d) and shear (c and e) velocity error against the angle of incidence for various values of γ plotted in a polar (b and c) and linear (d and e) fashion.

4.3.2.5 Conclusion

The study of the implicit cases with fully integrated elements shows that results for these cases are similar to the ones obtained for the reduced integration cases solved with the explicit solver. Two differences are noticed: the amplitude of the error tends to be lower for fully integrated elements than reduced integration elements with shear waves for all element shapes; deformation of elements leads to a reduction in error compared to the explicit cases. Although not optimum, the general rule to determine

the maximum velocity error established for explicit quadrilateral elements can be adapted to implicit cases as:

$$E_{cmax} = \frac{180}{N_{min}^2} \tag{4·23}$$

with N_{min}, the mesh density along the longest diagonal.

4.3.3 Quadratic quadrilateral elements

It is important to mention that, in this case, as in Section 4.2.4.1, the mesh density is determined in terms of node spacing not element side size.

4.3.3.1 Square elements

The velocity errors for both shear and longitudinal velocities monitored over a range of angles from 0 to 90 degrees for a range of mesh densities are plotted on Figure 4.26.

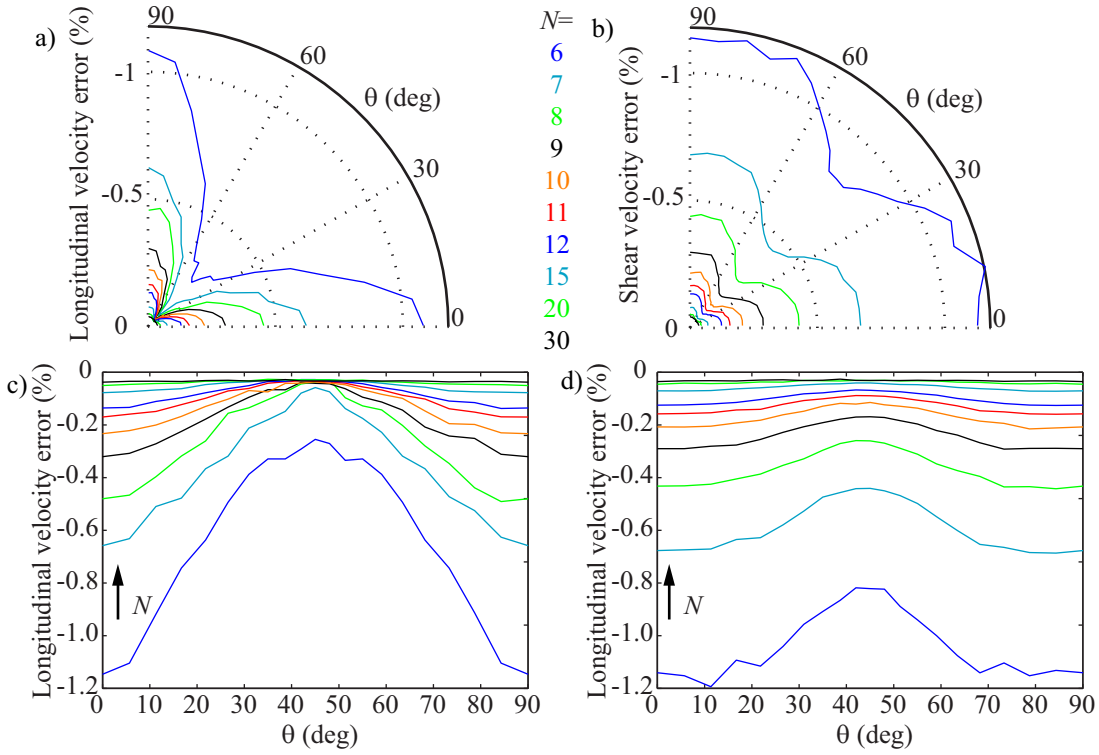

Figure 4.30. Variation of the longitudinal (a and c) and shear (b and d) velocity error against the angle of incidence for various values of mesh density plotted in polar (a and b) and linear (c and d) plots.

Looking at the results for quadratic square elements, it can be seen that the absolute value of the error is much lower than for linear elements as it is smaller than 0.5% for a mesh density superior to 8. Unlike all cases seen previously, the velocity is higher than the theoretical value which explains why a negative error is plotted. As seen in previous cases, there is a variation in the error but here the smallest error occurs at 45 degrees where the mesh density is at its lowest. This indicates that the approach to predict the velocity error that was used for linear and modified quadratic elements cannot be applied to this case.

4.3.3.2 Rectangle elements

The meshes studied in this part are "stretched" in one direction to create rectangular elements. The element size in the vertical direction *y* is kept the same for all models so that the mesh density *N* in this direction is 15. The element size in the horizontal direction *x* is varied so that the mesh density *N* varies from 7.5 to 30. The ratio between the element side *R=Lx/Ly* is hence varied from 0.5 to 2 as illustrated on Figure 4.31.a. The error on the velocity is measured over a range of angles from 0 to 90 degrees and plotted on Figure 4.31.b,c,d,e.

Looking at the results for both longitudinal and shear waves, it can be seen that the amplitude of the reflection is impacted by the deformation of the elements. The general shape of the curves is similar to what was seen for linear quadrilateral elements although the amplitude of the error stays in line with quadratic quadrilateral results. It can be noted that the error is positive along the shortest edge of case 5. This indicates a softening of the element in this direction and the error is higher than what would have been expected at the mesh density in this direction.

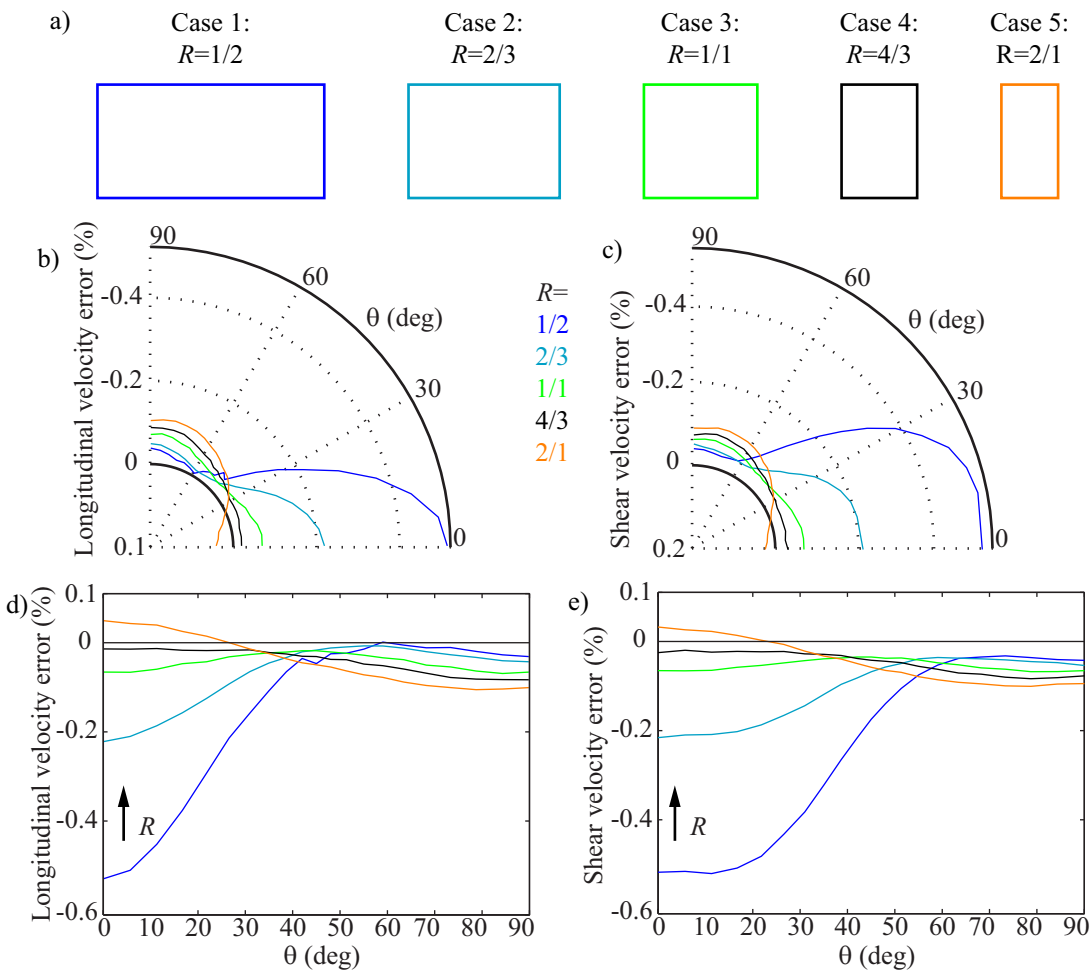

Figure 4.31. a) Shape of the different rectangular elements used in the mesh; Variation of the longitudinal (b and d) and shear (c and e) velocity error against the angle of incidence for various values of *R* plotted in a polar (b and c) and linear (d and e) fashion.

4.3.3.3 Rhombus elements

Meshes in this case are sheared so that all elements are deformed from a square to a rhombus. The models studied have a mesh density of 15 along the element sides. The shearing angle γ is varied from 0 to 60 degrees by 15 degree increments as seen in Figure 4.32.a. The error on the velocity is monitored from -90 to +90 degrees and is plotted on Figure 4.32.

The deformation of the element from a square to a rhombus does not lead to a dramatic deterioration of the error and is in line with amplitudes experienced before with quadratic elements.

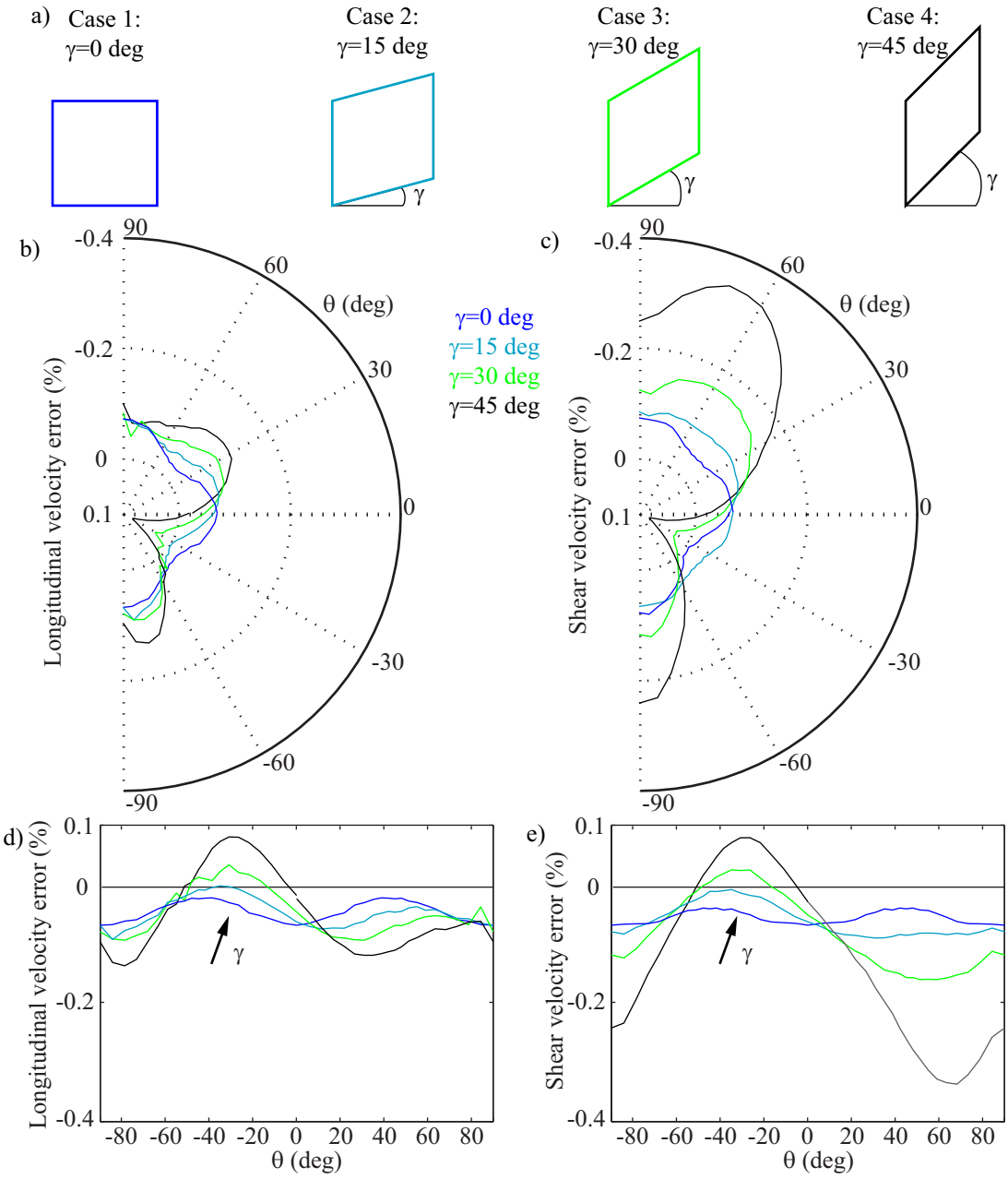

Figure 4.32. a) Shape of the different rhombic elements used in the mesh; Variation of the longitudinal (b and d) and shear (c and e) velocity error against the angle of incidence for various values of γ plotted in a polar (b and c) and linear (d and e) fashion.

4.3.3.4 Parallelogram elements

The mesh in this case is sheared and stretched with a mesh density of 15 at 0 and 90 degrees. The shearing angle γ is varied from 0 to 45 degrees by 15 degree increments as shown on Figure 4.33.a. Results are plotted on Figure 4.33.

Results are relatively similar to the rhombus results except that the velocity error has a higher amplitude. This can be explained by the fact that the mesh density in this case is more strongly modified than in the rhombus one.

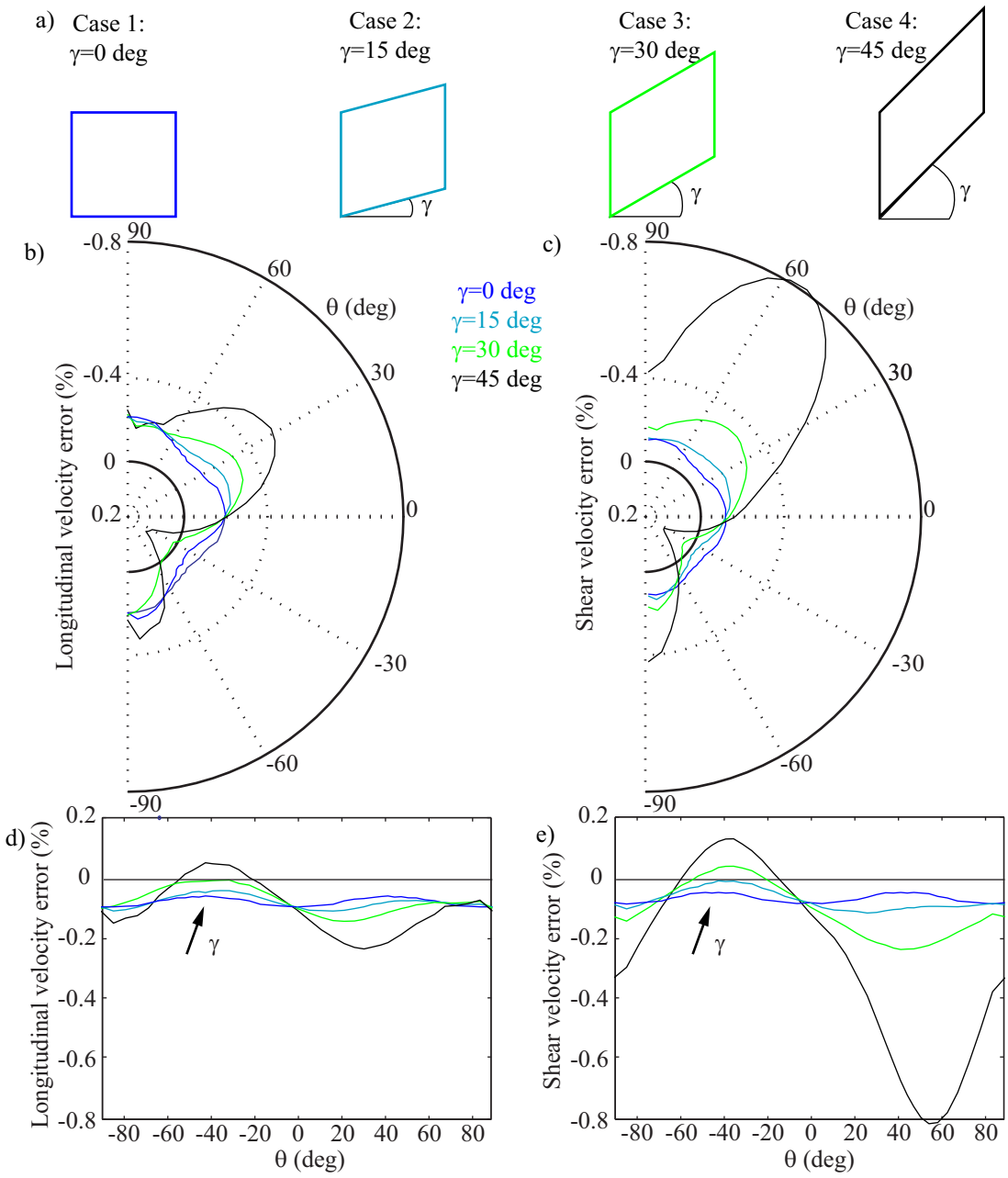

Figure 4.33. a) Shape of the different parallelogramatic elements used in the mesh; Variation of the longitudinal (b and d) and shear (c and e) velocity error against the angle of incidence for various values of γ plotted in a polar (b and c) and linear (d and e) fashion.

4.3.3.5 Conclusion

At a particular mesh density, quadratic quadrilateral elements have a much smaller velocity error than linear quadrilateral elements. For square elements, the error is less than 0.5% for a mesh density of 8. The velocities with this type of element are superior to the theoretical value except for some angles with strongly deformed elements. This element type copes generally well with small deformations.

4.3.4 Linear triangular elements

4.3.4.1 Equilateral triangle elements

The error on both shear and longitudinal velocity is monitored over a range of angles from 0 to 90 degrees for a range of mesh densities. Results are presented in Figure 4.34.

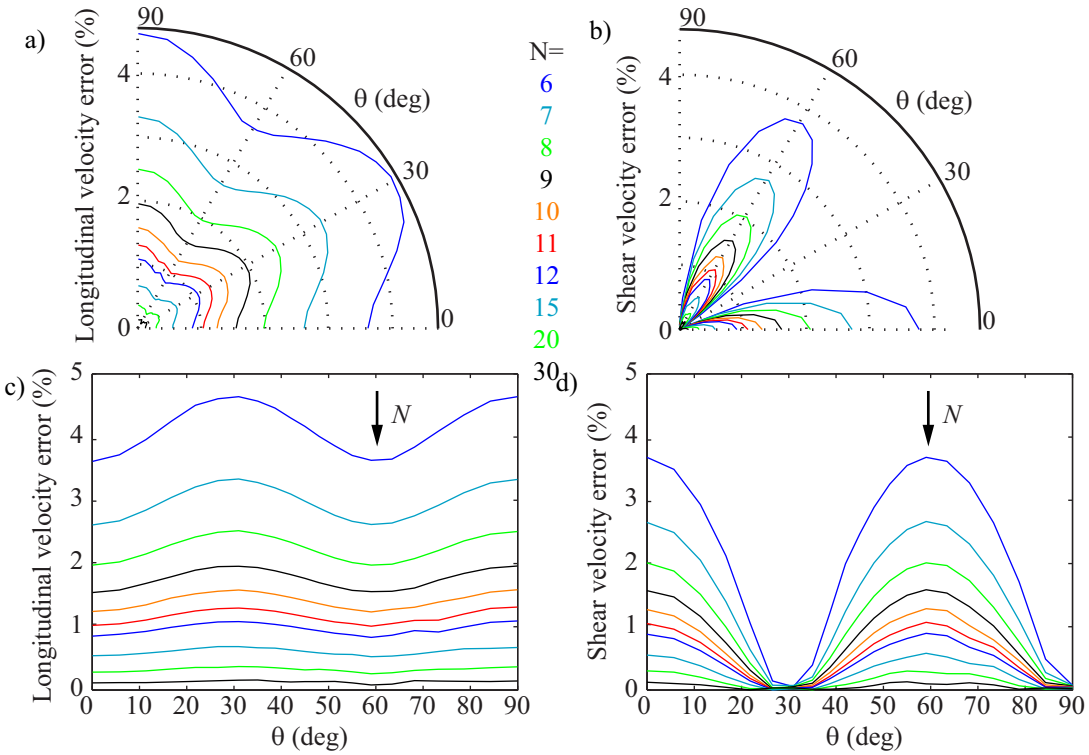

Figure 4.34. Variation of the longitudinal (a and c) and shear (b and d) velocity error against the angle of incidence for various mesh densities plotted in a linear (a and b) and polar (c and d) fashion.

Results for this case superimpose almost perfectly with those of the explicit case with linear equilateral triangle meshes. It is interesting to note that the implicit results match the explicit ones obtained with a low CFL_X. Findings from the explicit case can therefore be applied to the implicit case, in which case, the CFL_X in the former should be replaced by zero in the latter.

4.3.4.2 Isosceles triangle elements

The meshes studied in this part are "stretched" in one direction to have isosceles triangle elements. The element size in the vertical direction y is kept the same for all models so that the mesh density N in this direction is 10. The element size in the horizontal direction x is varied so that the mesh density N varies from 5.35 to 20. Results plotted on Figure 4.35 show an excellent agreement with the explicit case.

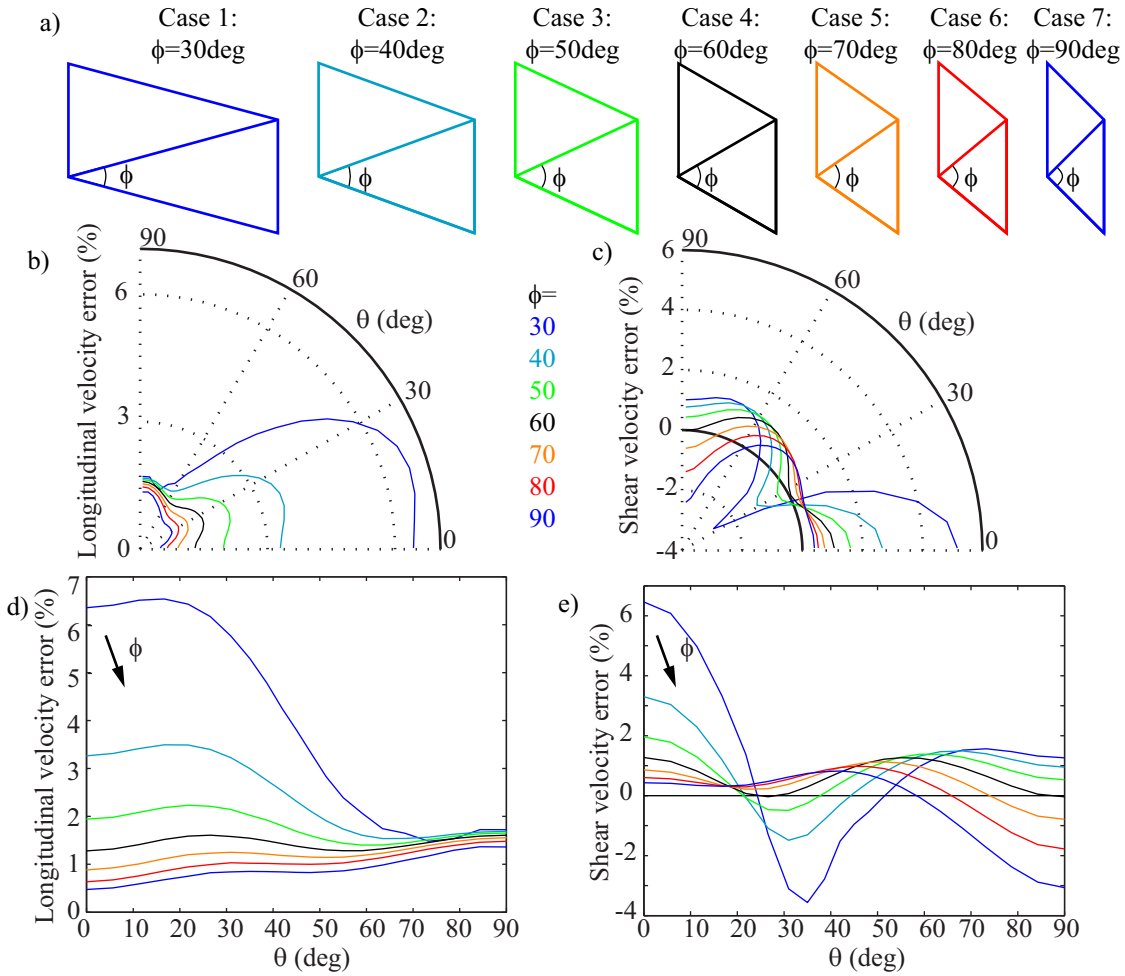

Figure 4.35. a) Shape of the different quadratic isosceles-triangular elements used in the mesh; Variation of the longitudinal (b and d) and shear (c and e) velocity error against the angle of incidence for various value of ϕ plotted in a polar (b and c) and linear (d and e) fashion.

4.3.4.3 Scalene triangle elements

In this case, the mesh density is kept the same in the *y* (vertical) and *x* (horizontal) direction at 10 and 11.55 elements per wavelength respectively while the element is sheared in the *y* direction. The shearing angle varies from 0 to 45 degrees. Results of the variation of the velocity error against the angle for a range of mesh density are shown on Figure 4.36 and agree extremely well with results obtained in the explicit case.

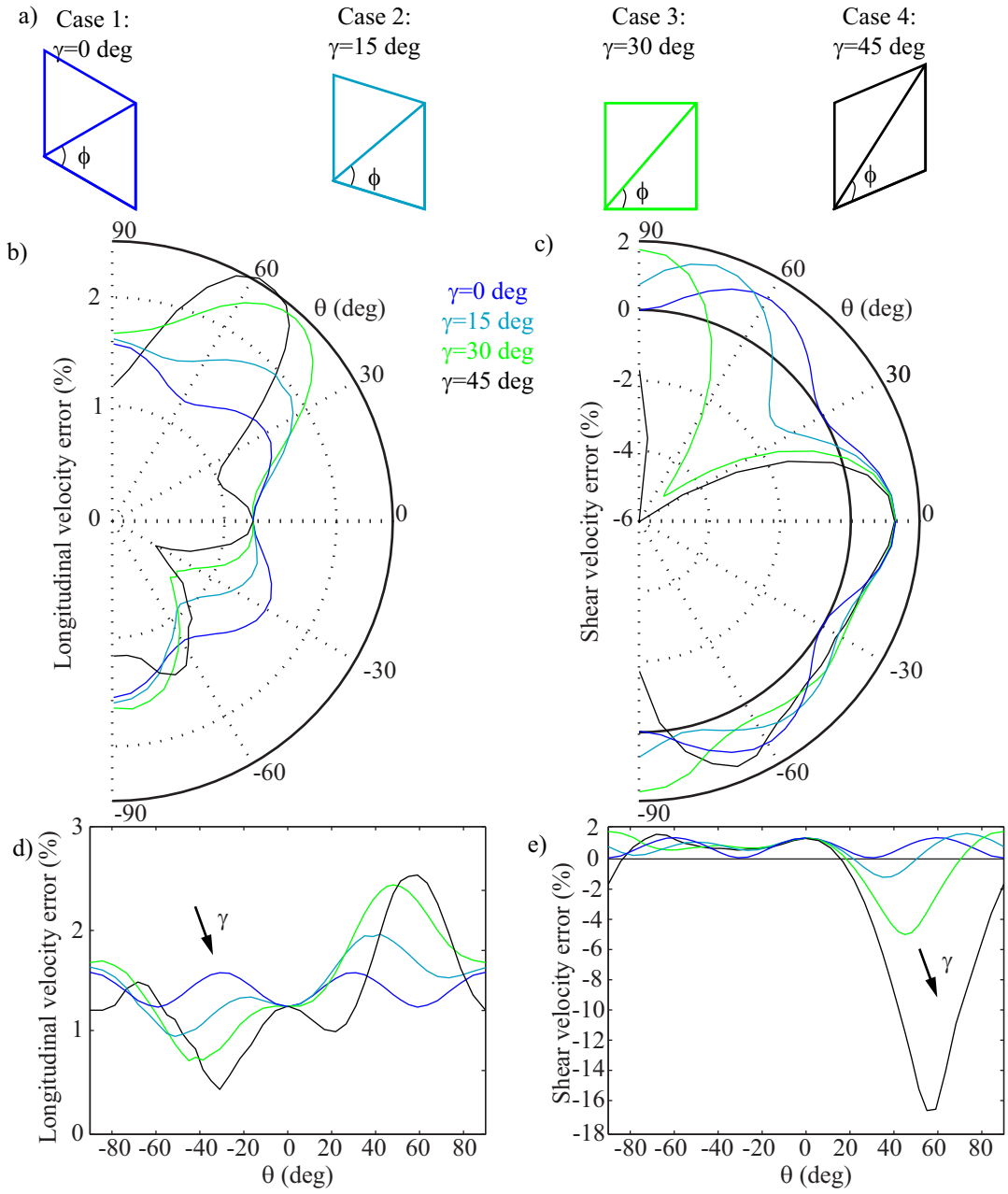

Figure 4.36. a) Shape of the different scalene-triangular elements used in the mesh; Variation of the longitudinal (b and d) and shear (c and e) velocity error against the angle of incidence for various values of γ plotted in a polar (b and c) and linear (d and e) fashion.

4.3.4.4 Conclusion

Results obtained with all shapes of linear triangular elements in the implicit case match almost perfectly those obtained with the explicit case with low CFL_X. This highlights that the solving scheme has a limited influence compared to the element type used.

4.3.5 Quadratic triangular elements

4.3.5.1 Equilateral triangle elements

The error on both shear and longitudinal velocities is monitored over a range of angles from 0 to 90 degrees for a range of mesh densities. Results are presented in Figure 4.37.

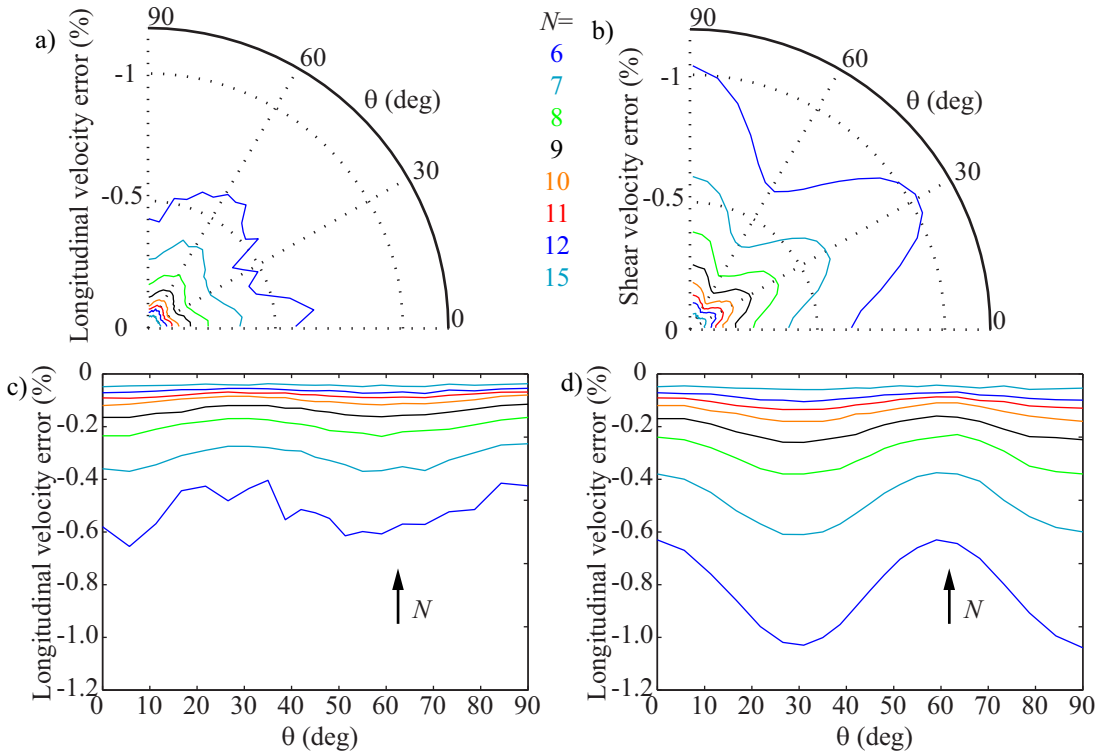

Figure 4.37. Variation of the longitudinal (a and c) and shear (b and d) velocity error against the angle of incidence for various mesh density plotted in a linear (a and b) and polar (c and d) fashion.

The error on velocity measured in this case is much lower than that observed with linear triangular elements. The absolute value of the error on velocity is lower than 0.4% for a mesh density greater than 8. As for the case of quadratic quadrilateral elements, the measured velocity is higher than the theoretical one. The error is the same for both wave types at 0 and 60 degrees. The velocity variation is not the same between these two points as it increases for shear waves but decreases for longitudinal waves.

As for the quadratic quadrilateral elements, the prediction of the error devised for linear and modified quadratic elements cannot be applied. The fact that the error is so low means that the error is practically negligible.

4.3.5.2 Isosceles triangle elements

The meshes studied in this part are "stretched" in one direction to create isosceles triangle elements. The element size in the vertical direction y is kept the same for all models so that the mesh density N in this direction is 10. The element size in the horizontal direction x is varied so that the mesh density N varies from 5.35 to 20. Results are plotted on Figure 4.38.

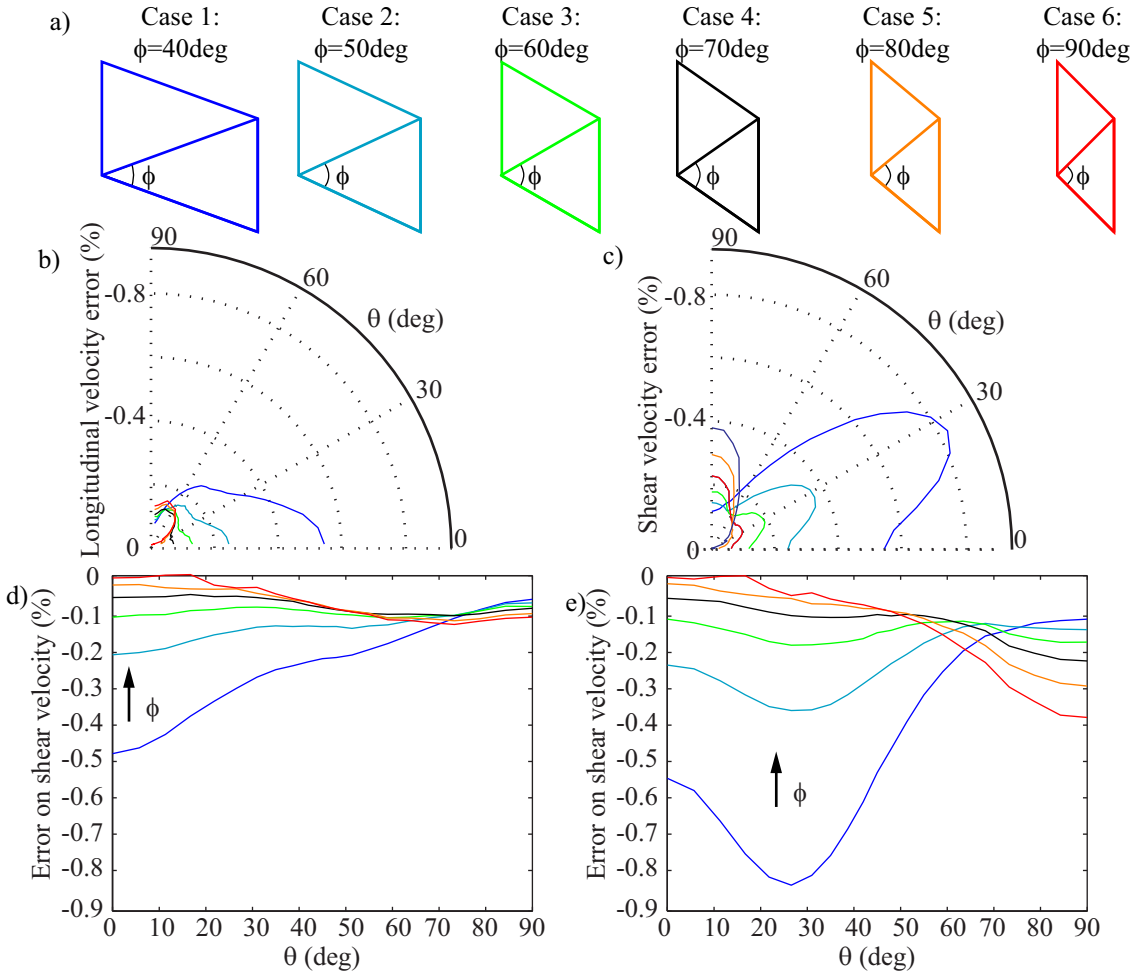

Figure 4.38. a) Shape of the different quadratic isosceles-triangular elements used in the mesh; Variation of the longitudinal (b and d) and shear (c and e) velocity error against the angle of incidence for various values of ϕ plotted in a polar (b and c) and linear (d and e) fashion.

Deformation of the elements leads to a modification of the error curves. The maximum error is in line with what is expected and no loss of precision seems to occur in this case.

4.3.5.3 Scalene triangle elements

In this case, the mesh density is kept the same in the *y* (vertical) and *x* (horizontal) direction at 10 and 11.55 elements per wavelength respectively while the element is sheared in the *y* direction. The shearing angle varies from 0 to 45 degrees. Results of the variation of the velocity error against the angle for a range of mesh density are shown on Figure 4.39.

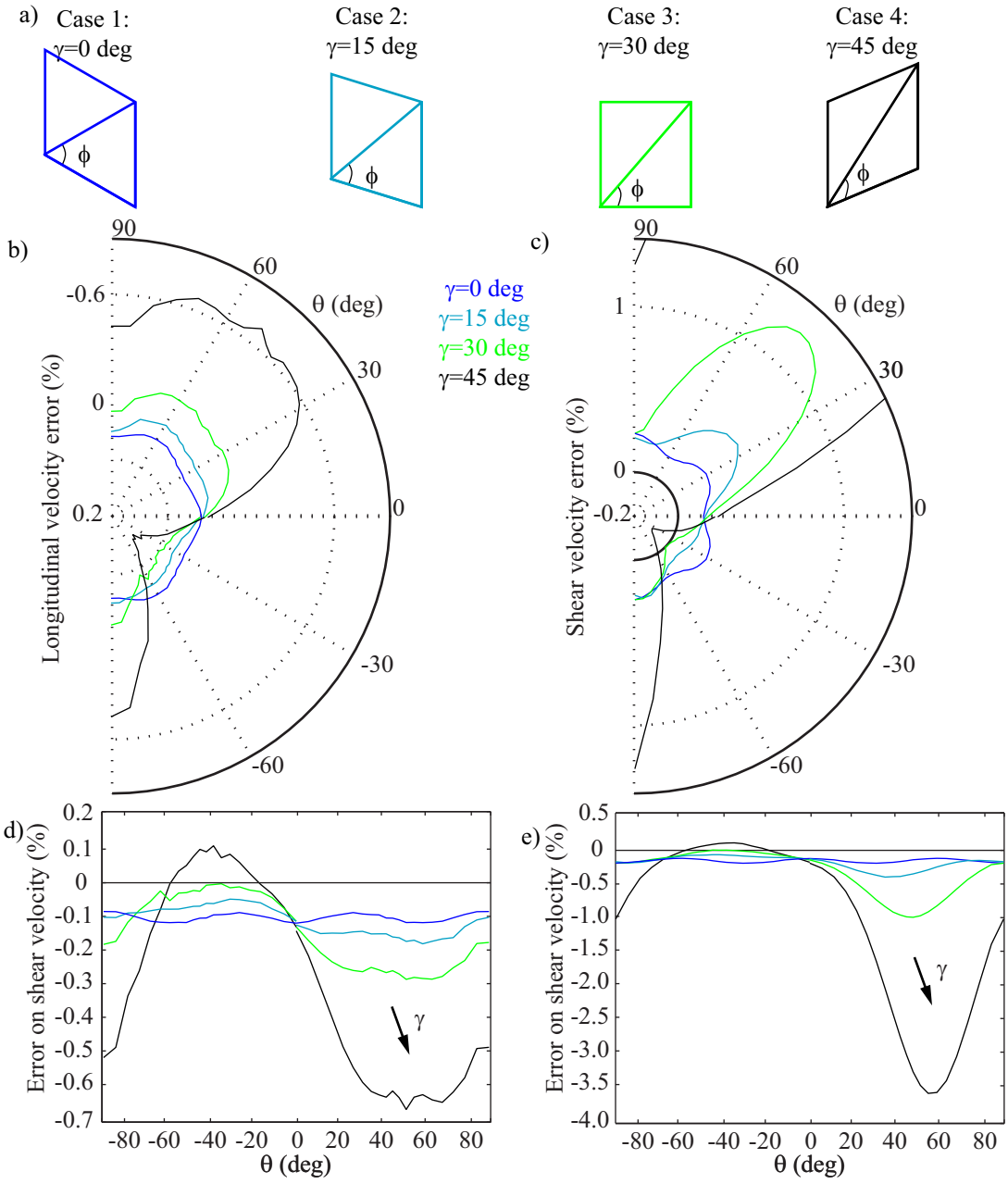

Figure 4.39. a) Shape of the different scalene-triangular elements used in the mesh; Variation of the longitudinal (b and d) and shear (c and e) velocity error against the angle of incidence for various values of γ plotted in a polar (b and c) and linear (d and e) fashion.

Results for both wave types up to case 3 show a relatively good behaviour but results for case 4 clearly show a great increase in the velocity error along the longest triangle edge. The absolute error reaches a value of 3.5% which is much higher than expected.

4.3.5.4 Conclusion

Quadratic triangular elements (CPE6 [14]) have been shown to provide good results for equilateral and isosceles triangle shapes. Velocity error in these cases is very low and is close to the amplitudes observed with quadratic quadrilateral elements. The shearing of the element did not prove problematic up to the case of the right angle triangle. For larger shearing, the velocity error dramatically increased along the longest edge of the triangles. This phenomenon is similar to what was observed for linear triangular elements. Element deformation is acceptable but should be limited.

4.3.6 Modified quadratic equilateral triangular elements

4.3.6.1 Equilateral triangle elements

The error on both shear and longitudinal velocity is monitored over a range of angles from 0 to 90 degrees for a range of mesh densities. Results are presented in Figure 4.40.

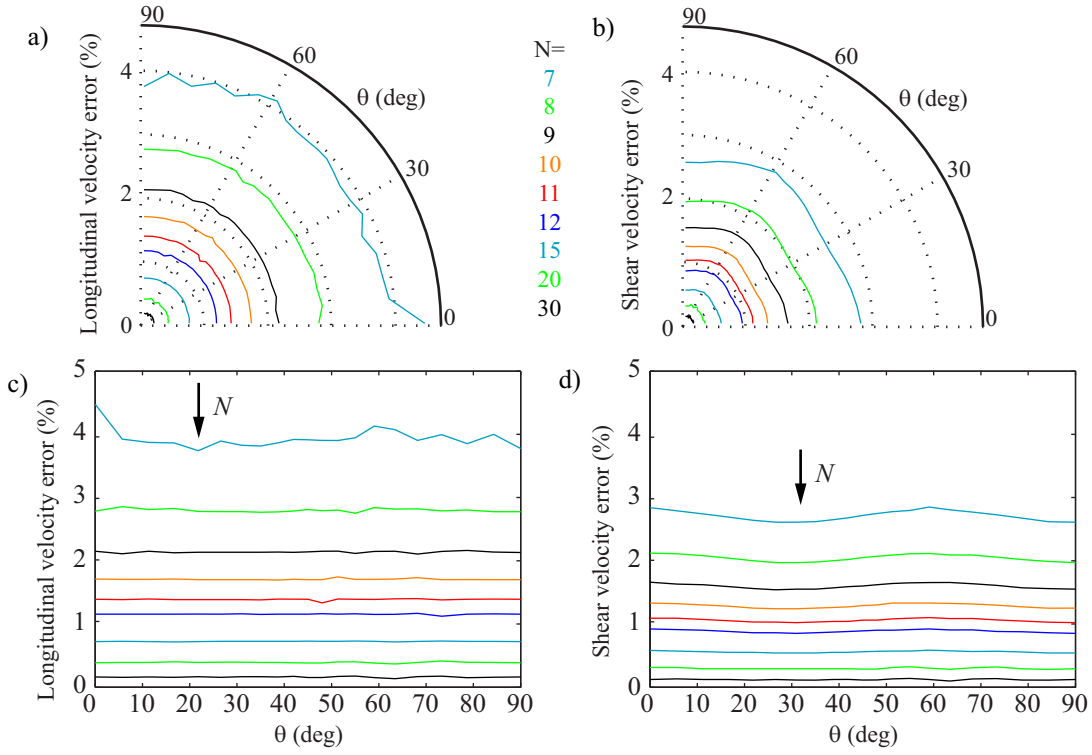

Figure 4.40. Variation of the longitudinal (a and c) and shear (b and d) velocity error against the angle of incidence for various mesh densities plotted in a linear (a and b) and polar (c and d) fashion.

It is interesting to note that the results agree very well with the ones obtained with the same element type solved with an explicit scheme. The amplitude of the error for the modified quadratic triangle elements is much higher than the quadratic triangle or quadrilateral elements and is generally in line with the amplitude observed for linear elements. Velocity error prediction as defined in Section 4.2.4 is valid in this case.

4.3.6.2 Isosceles triangle elements

The meshes studied in this part are "stretched" in one direction to have isosceles triangle elements. The element size in the vertical direction y is kept the same for all models so that the mesh density N in this direction is 10. The element size in the horizontal direction x is varied so that the mesh density N varies from 5.35 to 20. Results are plotted on Figure 4.42. As for the equilateral case, an excellent agreement exists between the explicit and implicit cases.

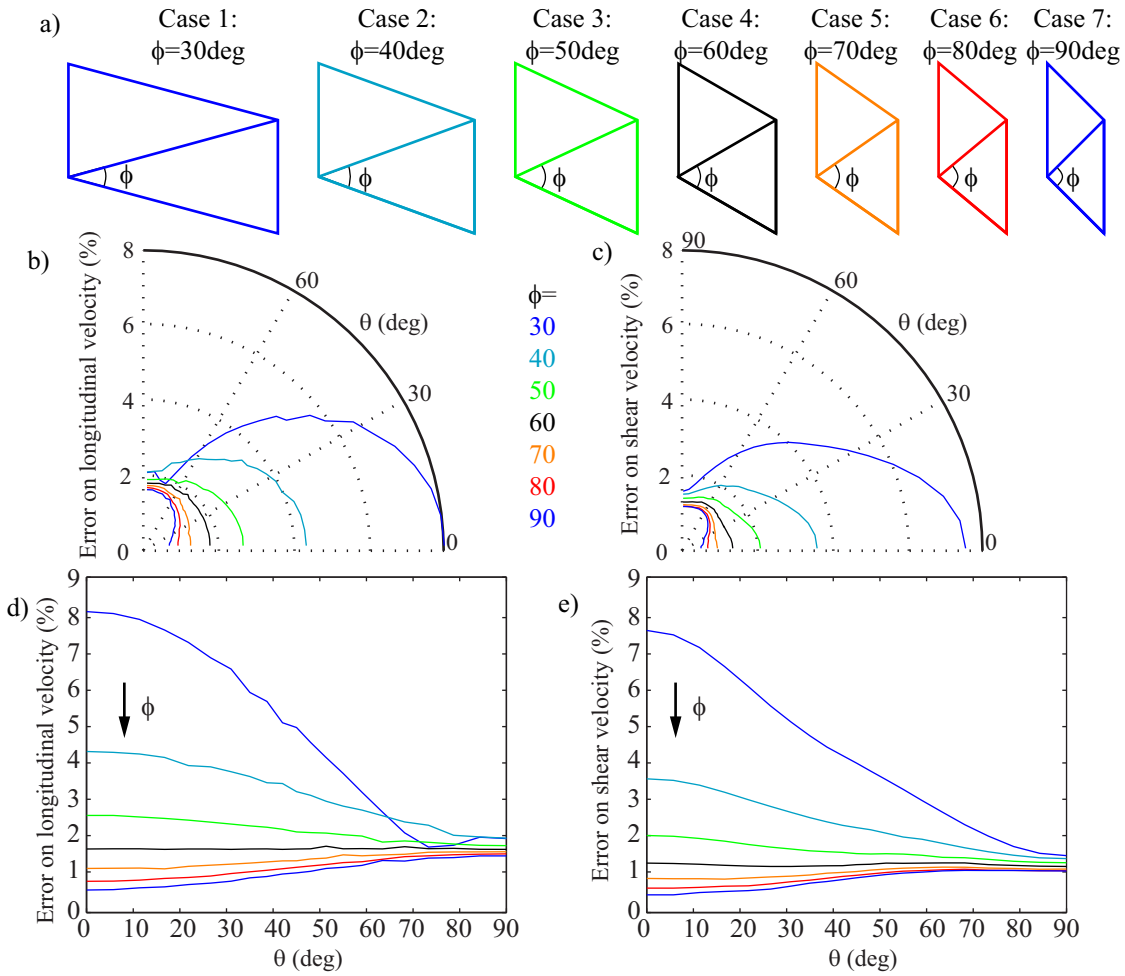

Figure 4.41. a) Shape of the different quadratic isosceles-triangular elements used in the mesh; Variation of the longitudinal (b and d) and shear (c and e) velocity error against the angle of incidence for various values of ϕ plotted in a polar (b and c) and linear (d and e) fashion.

4.3.6.3 Scalene triangle elements

In this case, the mesh density is kept the same in the *y* (vertical) and *x* (horizontal) direction at 10 and 11.55 elements per wavelength respectively while the element is sheared in the *y* direction. The shearing angle varies from 0 to 45 degrees. Results are plotted on Figure 4.42. Comparing implicit and explicit results shows an almost perfect superimposition of results.

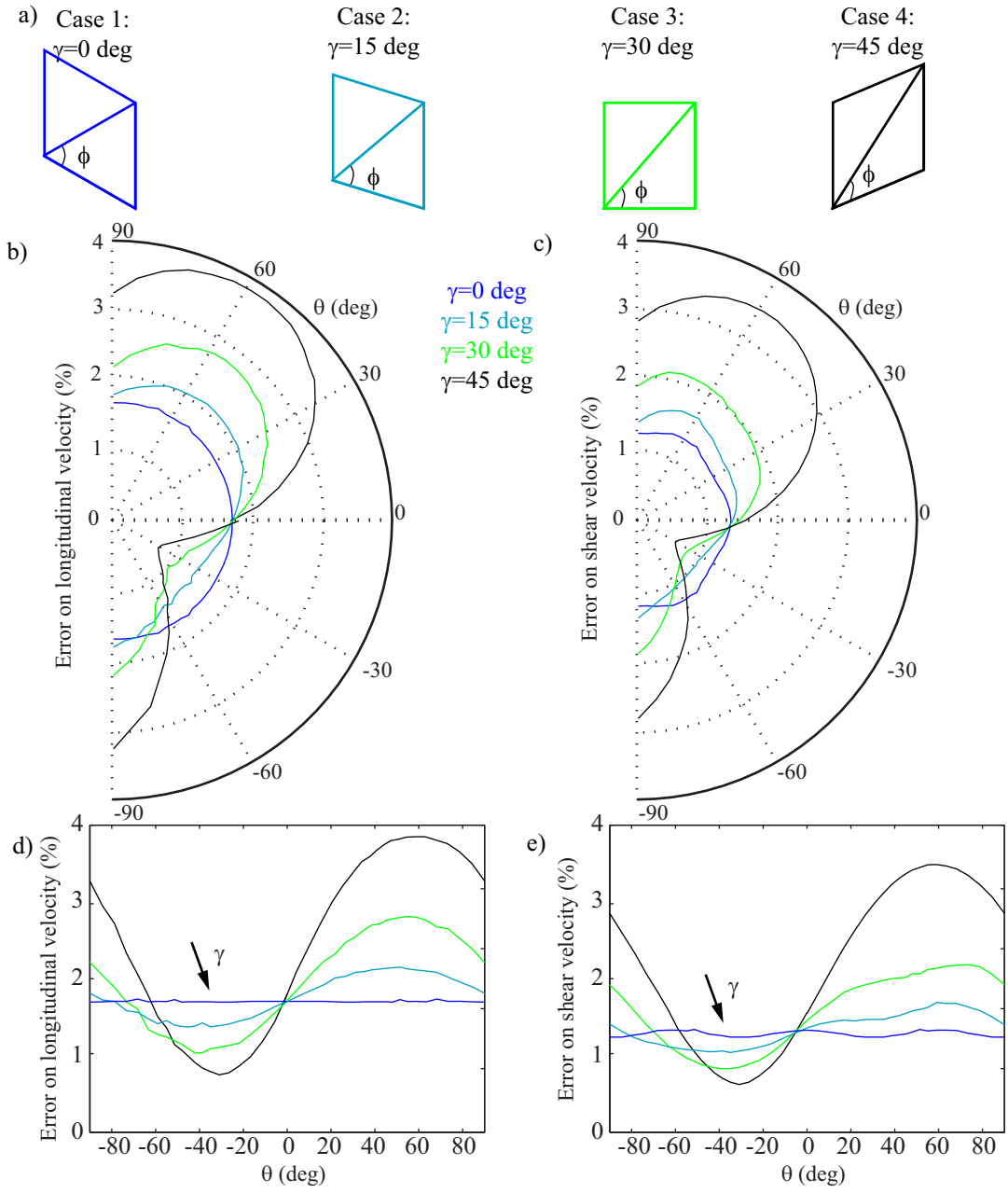

Figure 4.42. a) Shape of the different scalene-triangular elements used in the mesh; Variation of the longitudinal (b and d) and shear (c and e) velocity error against the angle of incidence for various values of γ plotted in a polar (b and c) and linear (d and e) fashion.

4.3.6.4 Conclusion

As for the linear triangular elements, results for modified quadratic triangular elements show an excellent agreement between explicit and implicit results. It is interesting to note that this element type does not suffer from a great loss of precision due to the deformation of the element. Modified triangular elements behave in a way closer to linear quadrilateral elements than linear or quadratic triangular ones.

4.4. Conclusions

The study of reduced integration linear quadrilateral elements solved with an explicit solver showed the influence of the scaled Courant number CFL_X and mesh density N on the velocity. Patterns were identified and permitted to define a fitted analytical expression to evaluate with high accuracy the amplitude of the velocity error E_c at any angle, any scaled Courant number and for a mesh density higher than 6:

$$E_c = 180\frac{(1 - CFLX^2)}{N^2} \tag{4·24}$$

Following this, the study of deformed elements highlighted that the maximum error in a mesh could be predicted using the fitted analytical expression defined for square elements (see Equation 4·24). This indicates that this element type is not the subject of dramatic loss of performance when deformed. Therefore using deformed quadrilateral elements in a model is not an issue on its own but other factors should also be considered. As quadrilateral elements are deformed, the maximum error will consequently increase with the longest diagonal. Therefore, for a given maximum acceptable error, the overall node density of a model will increase with the level of element deformation. In other words, the number of degrees of freedom necessary to cover the geometry of a model with deformed elements will be greater than with square ones. On top of this, the reduction in the length of the shortest diagonal leads to a reduction in the stable increment meaning that, for the same number of degrees of freedom, a model with deformed elements can not be solved as quickly as one made of square elements.

With linear equilateral triangular elements, it was demonstrated that the error could be correctly predicted using rules established for quadrilateral elements (see Equation 4·24) along the altitudes and element sides for longitudinal waves and along the element sides for shear waves. The influence of the scaled Courant number CFL_X and mesh density N was confirmed at these positions and wave types. An error of zero was measured for shear waves along the altitudes of the triangular elements. Deformed mesh cases showed that this element type is sensitive to high levels of deformations as the predicted error was more than tripled in one case (16.4% instead of 4.8%). Using highly deformed linear triangular elements is therefore not advised. The author of this work recommends that linear triangular element internal angles should all have values higher than 50 degrees and lower than 70 degrees in order not to experience significant loss of precision.

Modified quadratic equilateral triangular elements proved to have a close to constant error against the angle for a given N when being solved with a low CFL. The maximum amplitude of the error was in line with the one observed with linear elements and defined using equation 4·24. The influence of CFL_X and N was demonstrated to be similar to previous cases. Modified quadratic triangular elements were shown to cope well with being deformed like linear quadrilateral elements and unlike linear triangular elements. Large deformation of modified triangular elements is therefore not an issue and the author is confident that using linear triangular elements whose internal angles are between 30 and 90 degrees will not cause a large loss of precision in the model.

For implicit solving, full integration linear square element results for longitudinal waves showed very good agreement with the ones obtained with reduced integration elements and the explicit solver. For shear waves, the plot had the same shape but the error was marginally smaller (factor of 0.75). In a similar way to the explicit case, the following fitted analytical expression can be used to define the velocity error:

$$E_c = \frac{180}{N^2} \tag{4·25}$$

Deformation of elements showed similar (although marginally better) results when compared to the reduced integration explicit case. Fully integrated quadrilateral

elements cope well with being deformed and the use of deformed ones in a model is not a problem.

For a given mesh density, quadratic quadrilateral elements proved to strongly reduce the velocity error to less than 0.5% for a node density higher than 8. Therefore, the velocity error with this type of element is not a cause for concern compared to other cases. Deformation of elements did not prove to be a problem. The two weaknesses of this element type are that in ABAQUS it can only be used with an implicit solver and that, as it is a quadratic element, geometric resolution (defined by the smallest geometric size of an element) is halved compared to linear elements for a given node density.

Linear and modified quadratic elements results for the implicit case matched almost exactly results obtained with the explicit solver and therefore the findings are the same.

Quadratic equilateral triangular elements were shown to lead to low velocity error as were quadratic square elements, but proved to be sensitive to high levels of deformation in the same way as linear triangular elements. Therefore the author recommends limiting the internal angle range to 50 and 70 degrees.

Overall, the influence of the solver is ruled out, as element type and shapes are the factor determining the velocity error. Unlike quadrilateral elements, all triangular elements apart from modified quadratic ones were shown to be sensitive to element deformation. This justifies why automatic meshing algorithms seek to minimize the deformation and why modellers need to exercise caution when using linear and quadratic triangular elements.

The angle of propagation in a regular mesh was shown to play an important part in the amplitude of the velocity error as it leads to a non-negligible variation.

The mesh density was shown to be the driving factor influencing the velocity error for all element types. The influence is not so noticeable for quadratic elements as the velocity is highly accurate for any mesh density. For linear and modified quadratic elements, its influence is much stronger.

An interesting point is that the difference in velocity between 2 meshes causes a difference in acoustic impedance that may be partly responsible for possible reflection occurring at their interface. The knowledge gained in this section regarding the velocity error will be used in Chapter 6 which investigates local mesh refinement.

Chapter 5

Accurate modelling of defects using Finite Elements

5.1. Introduction

In the same way as a stress analysis engineer studying the stresses in a mechanical component, an NDT engineer developing an ultrasonic inspection technique has to make assumptions and simplifications in order to be able to numerically model the interaction of a wave with a structural defect. In the past, the vast majority of wave propagation work focused on strongly simplified defects. One reason for this is that initial work is bound to focus on the simplest cases, but many modellers are ready to go on to more complex problems. As computer power has developed exponentially, new opportunities have arisen and have highlighted the fact that only a limited amount of information is available regarding how to accurately model the interaction of elastic waves with complex defects using FE.

One specific issue related to modelling wave propagation using FE is that a change in element shape or size leads to a change of acoustic impedance that generates unwanted reflections. As these reflections pollute the signal of interest, most NDT modellers favour the use of regular meshes usually constituted of linear square elements. In this context, it is well known that the correct representation of the wave propagation phenomenon requires the mesh density to be at least 7 nodes per shortest wavelength.

When using a regular square mesh, defects and features are represented by adding or removing elements. This can be thought of as a "LEGO" approach where the elements are LEGO bricks. Clearly, the down side to this is that the geometric definition of features and defects is dependent on the mesh size and orientation. As a consequence, theoretical geometric edges not aligned with the mesh are approximated and sometimes represented in a jagged fashion. This leads to discrepancies between the theoretical and modelled geometries.

It is generally accepted - although not thoroughly verified - that refinement of the mesh leads to a convergence of the FE results towards the exact results. In some cases, mesh refinement is applied in order to correctly model defects. The direct consequence of this is an increase in the number of degrees of freedom solved and hence the computational requirements of the model. Keeping the classic regular square mesh approach, this raises the question of how fine a mesh needs to be refined - if at all - for a particular defect or feature to be realistically represented from a wave propagation perspective.

Another approach which has been less popular in the past is to use automatic meshing algorithms using triangular elements. These are now widely available in commercial FE packages. Aside from the lack of availability in the past, one reason why these algorithms have not been commonly used in NDT wave modelling is that, in most cases, elements are deformed when automatically generated. As deformation of elements leads to a change of acoustic impedance and consequently reflections, the mesh structure is key to appropriate modelling of wave propagation. On the positive side, when using an automatic meshing algorithm, the geometry is represented more closely than with the regular mesh approach presented above as the edges of the elements follow the edges of the geometry. It would be beneficial to perform a meticulous study to verify whether this approach is well adapted for the modelling of the interaction of elastic waves with complex defects.

In this chapter, the two meshing approaches described above are tested for a range of defects, element types and solving methods with both elastic wave types. The general approach is to refine the mesh size for all these cases until an acceptable reference is obtained in order to evaluate the evolution of the error as the mesh is refined. The defects modelled included straight edges, circular defects of various sizes and cracks of various sizes. These cases are chosen as they are commonly modelled in NDT and should provide the foundations to more complex defect modelling.

5.2. Model definition

As in the previous chapter, models are non-dimensional and the elastic material is chosen so that the longitudinal and shear wavelengths are 2 and 1 units respectively: Young's modulus is 8/3, Poisson's ratio is 1/3 and density is 1.The cases investigated here are the reflection of bulk waves from:

- straight edges
- straight cracks at an angle of 80 degrees and of length 0.25, 1 and 4 units
- circular holes of diameter 0.25, 1 and 4 units

Models are 2D plane strain. Both shear and longitudinal wave generations are considered, as models are excited by body forces being applied on four elements as shown on Figure 5.1. Body forces rather than point forces are used in this Chapter as they offer better mode purity. This generates an almost pure wave - shear or longitudinal - and as the size of the source is only a fraction of a wavelength is a close representation of a point source. The point located at the centre of the four elements is referred to as the excitation point. As the body force load is dependent on the area of the elements excited, the load is normalised so that the amplitude of the incident wave is the same in all cases studied in this chapter.

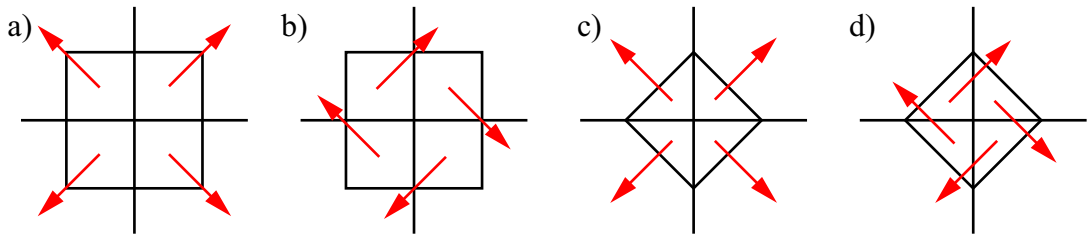

Figure 5.1. (a) Longitudinal and (b) shear wave excitation for a square element mesh and (c) longitudinal and (d) shear excitation for a triangular element mesh.

Models are run with ABAQUS 6.6-1 in both the time domain (explicit) and the frequency domain (implicit). For the latter, the excitation is applied as a real harmonic excitation whose frequency is 1; the complex displacement field is obtained directly and used later to plot the absolute displacement field. For the explicit case, in order to obtain an absolute displacement field similar to the frequency domain one, it is decided to run two separate models: one with cosine and one with sine excitation of unit frequency . The complex displacement field is obtained by adding the result of the

cosine case to the result of the sine case multiplied by i. The first half of a Hanning window is used over the first 5 cycles in order to ramp up the amplitude of the sine and cosine to a constant value in order to avoid exciting a broad range of frequencies. The model is run sufficiently long so that the steady state is reached at all locations where the displacements are monitored.

Implicit models are run using linear square elements with full (CPE4) and reduced (CPE4R) integration, linear triangular elements (CPE3), quadratic triangular elements (CPE6) and modified quadratic triangular elements (CPE6M). Explicit models are only run using CPE4R, CPE3 and CPE6M as they are the only elements available for this type of solver.

Appropriately dimensioned ALID are used for all models. In the case of square meshes, the width of each sub layer in the ALID is one element. For triangular mesh cases, as the model is generated using the interactive user interface of ABAQUS CAE 6.6-1, a fixed number of sub layers of width 0.25 are defined. Free meshing of these layers is then performed.

In order to evaluate the influence of the mesh density on the accuracy of the results, the following numbers of nodes per shortest wavelength are investigated: 6, 10, 15, 20, 25 and 30. This parameter is identified as the mesh density and is assigned the letter N. In the case of regular square meshes, N is exact over the whole model. For triangular element meshes generated by the free meshing algorithm of ABAQUS CAE 6.6-1, the node spacing is specified on the internal and external boundaries of the model. A variation in node spacing over the model exists but is limited overall. This leads to a limited variation in the mesh density. There are two cases of interest where significant local deviations can exist between the prescribed and actual node spacing: small linear edges and small circular holes. When a linear edge is smaller than the node spacing, it is defined by a single element. The node spacing on the edge is directly dependent on the edge length and locally over-rules the prescribed node spacing condition. All circular holes receive a special treatment that guarantees that they are not incorrectly represented. The default setting of the free meshing algorithm of ABAQUS CAE 6.6.1 [14] means that a circular hole is defined by at least 8 nodes. This condition is used in this work and locally over-rules the prescribed node spacing condition for small holes.

5.3. Reflection from a straight edge

The first case investigated is that of the reflection from a straight edge. The geometry of the model is presented in Figure 5.2.a.

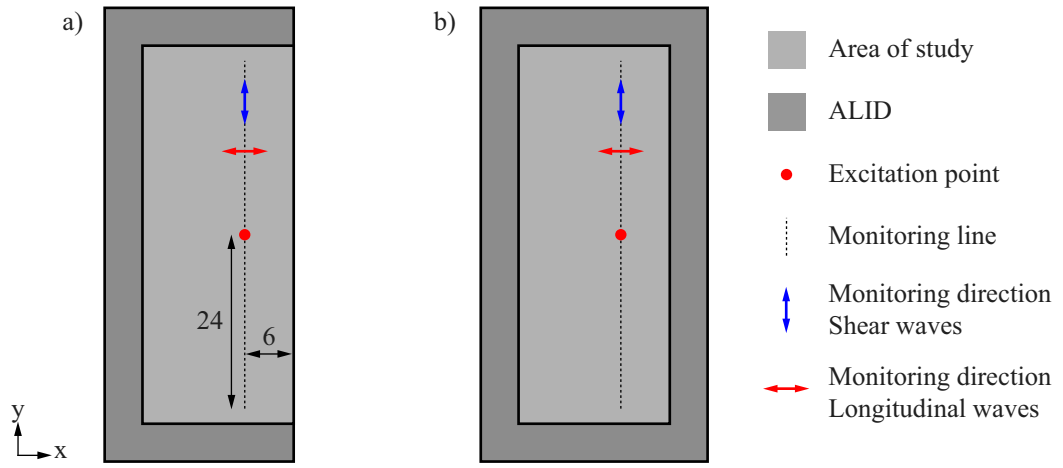

Figure 5.2. Straight edge model: a) with edge, b) without edge.

Three mesh cases are considered:

- square mesh at 0 degrees aligned with the edge
- square mesh at 45degrees to the edge resulting in a stair-cased edge
- triangular mesh generated with automatic meshing algorithm

These are shown on Figure 5.3.

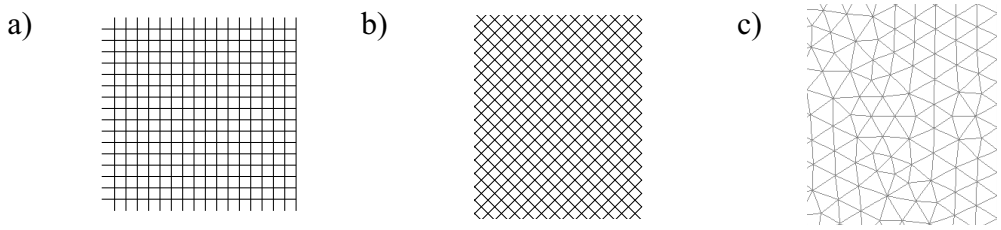

Figure 5.3. a) square mesh at 0 degrees aligned with the edge, b) square mesh at 45 degrees, c) triangular free mesh

As shown on Figure 5.2.a, the excitation point is located 6 units away from the edge (6 shear wavelengths or 3 longitudinal ones). As the edge is jagged when the mesh is at 45 degrees, an error on the exact position of the edge exists. In this study, the outside limit is used as the reference. The complex displacement field is monitored up to 24 units away from the excitation point along a line coincident with the excitation point and parallel to the edge (see Figure 5.2). For a longitudinal wave excitation, the displacements are monitored in the x direction and for a shear wave excitation, the

displacements are monitored in the y direction. In theory, the incident displacement field is zero in these directions and only the reflection from the edge is present. In practice, some slight numerical issues (low amplitude noise, oscillation close to the excitation point) exist on this line. In order to achieve high quality reflection fields, each case was run with (Figure 5.2.a) and without (Figure 5.2.b) the edge being modelled. For the models without the edge, models are extended behind the edge and ALID are used to absorb incident waves. The complex displacement field of the case without the edge is substracted from the one with the edge. Thus the slight coherent numerical noise is removed. The absolute displacement along the monitoring line measured in the direction described above is then plotted. The horizontal axis represents the position of the monitoring point relative to the reference which is excitation point as shown on Figure 5.2. The vertical axis indicates the amplitude of the displacement. It should be mentioned that the general shape of the amplitude of the displacement plots is the result of the interaction of shear and longitudinal reflection resulting from the incident wave being reflected by the edge. As these two waves have different properties, this causes interference patterns which result in the presence of a central main lobe and side lobes.

Results obtained for the implicit models for longitudinal and shear wave excitation are presented in Figure 5.4 and 5.5 respectively. Results for the explicit models for longitudinal and shear waves are presented in Figure 5.6 and 5.7. This represents a very large amount of data. In order to simplify the identification of cases, each plot is associated with a letter and a number (e.g. D15). The number is the mesh density of the case (row) and the letter identify the excitation, mesh and element types as indicated on the column of the figures. A letter on its own (e.g. D) indicates the whole column.

The first point to be noted is that the results for all cases with a density of 30 agree very well with each other and that, in most cases, the difference between the 25 and 30 cases is negligible. These plots can therefore be confidently taken as references. In order to highlight the discrepancies between these cases (i.e. the reference) and all other cases where the density is lower than 30, the reference curves are plotted in red for each case modelled.

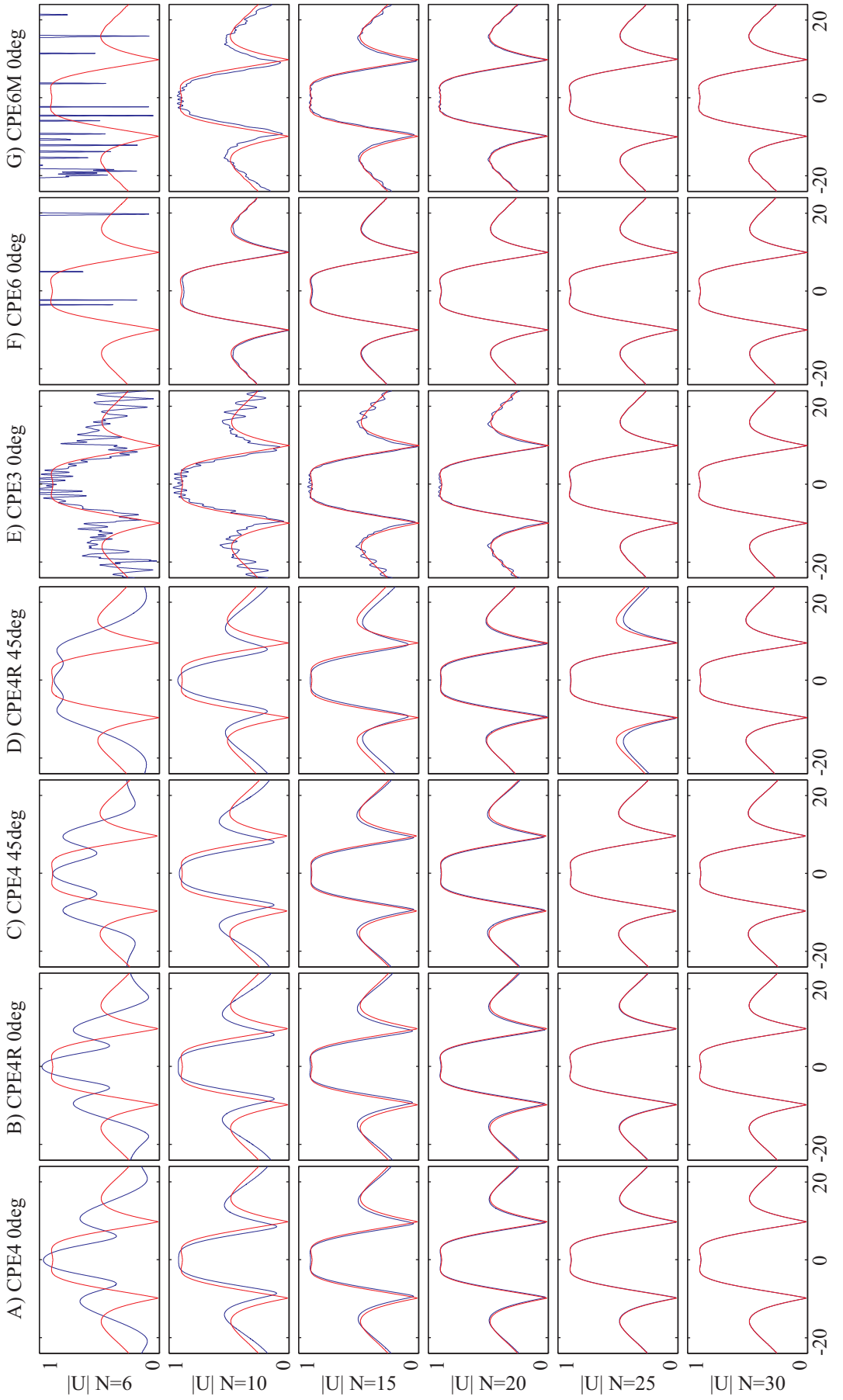

Figure 5.4. Implicit models for straight edge: Monitored absolute displacement for a longitudinal wave excitation using CPE4 and CPE4R meshes at 0 degrees, CPE4 and CPE4R meshes at 45 degrees and CPE3, CPE6 and CPE6M triangular elements. Thin red line is reference for N=30 for each case.

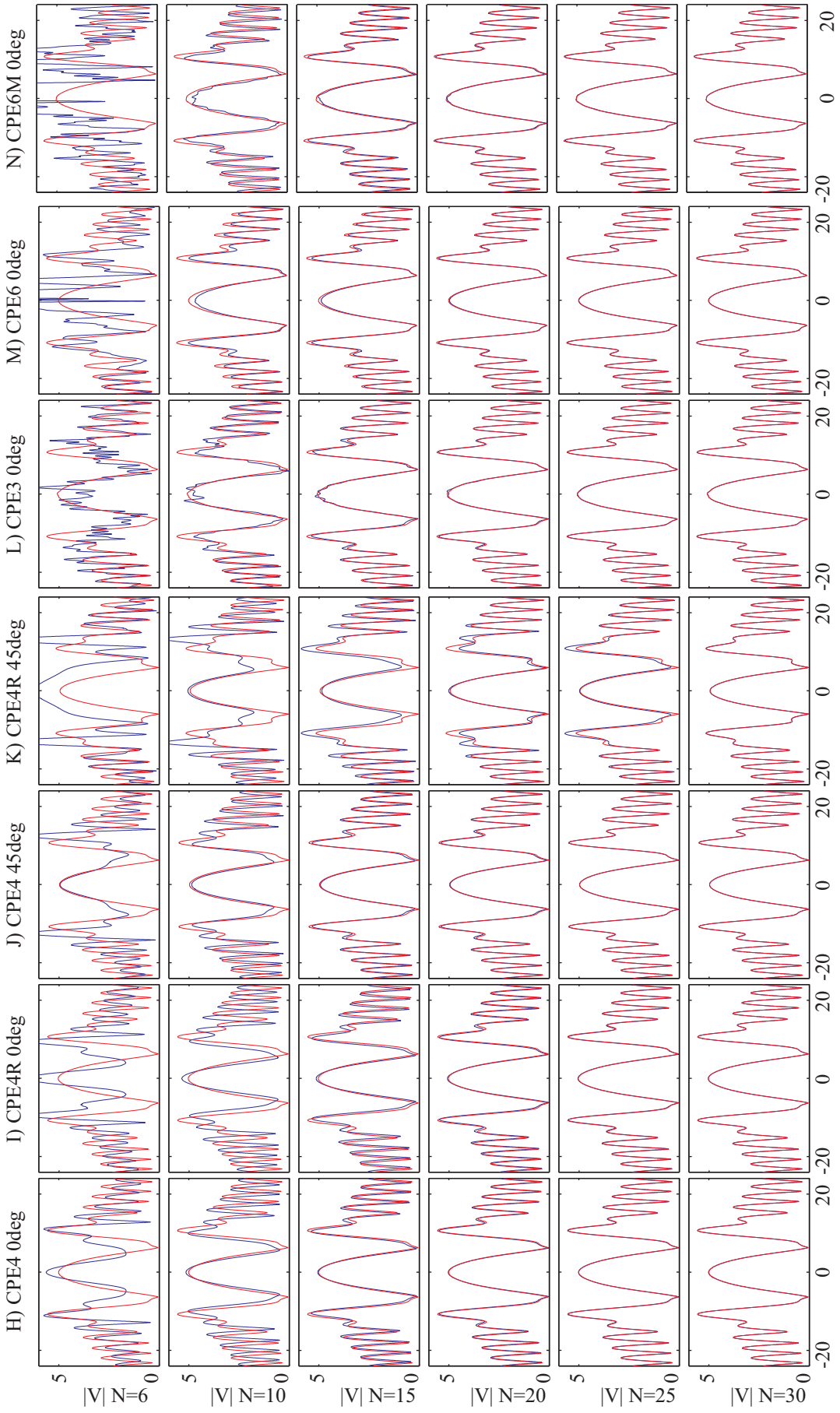

Figure 5.5. Implicit models for a straight edge: Monitored absolute displacement for a shear wave excitation using CPE4 and CPE4R meshes at 0 degrees, CPE4 and CPE4R meshes at 45 degrees and CPE3, CPE6 and CPE6M triangular elements. Thin red line is reference for N=30 for each case.

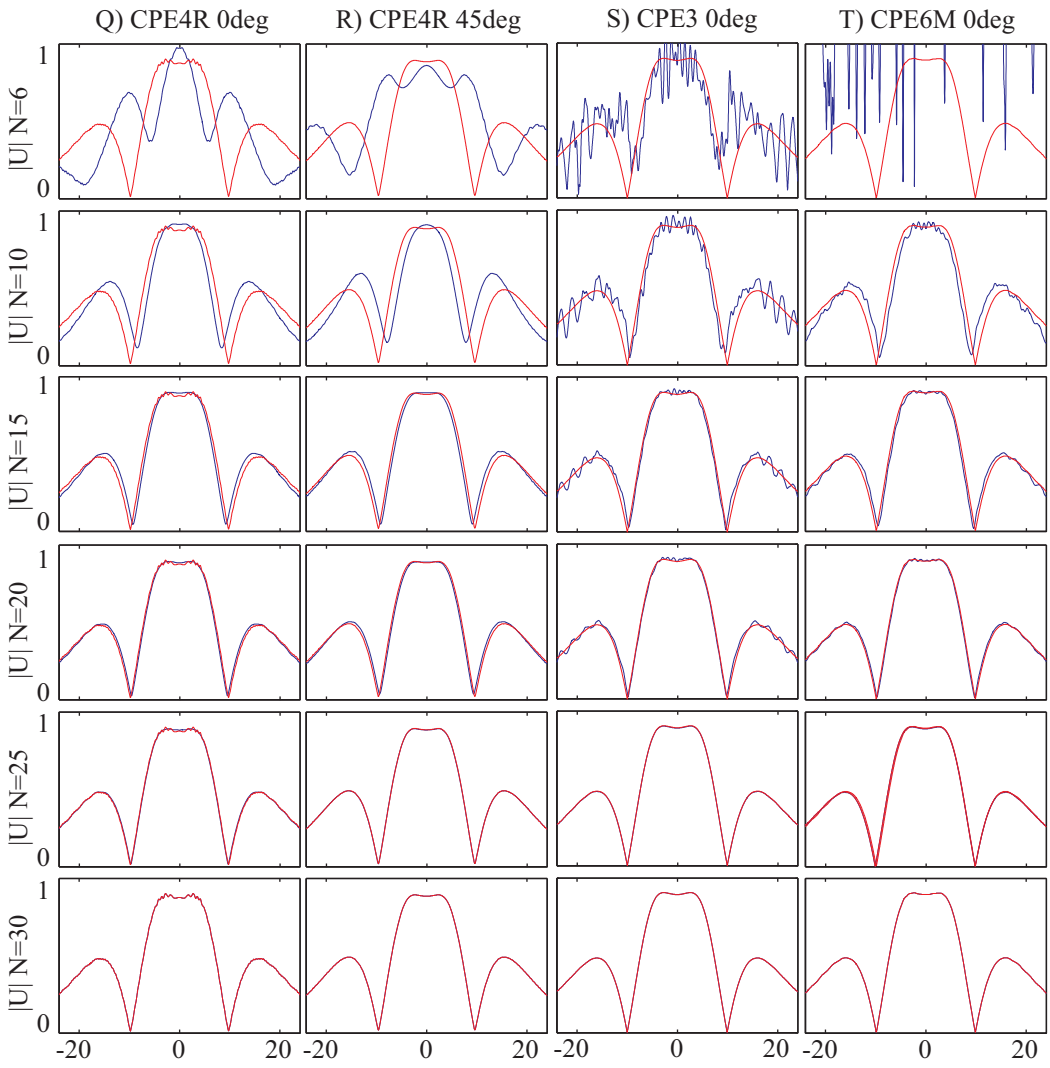

Figure 5.6. Explicit models for a straight edge: Monitored absolute displacement for a longitudinal wave excitation using CPE4R meshes at 0 degrees, CPE4R meshes at 45 degrees and CPE3 and CPE6M triangular elements. Thin red line is reference for N=30 for each case.

A and B show the results obtained with square element meshes at 0 degrees. The difference between using full (A) or reduced (B) integration elements is negligible for all mesh densities and they are therefore assessed jointly. It can be seen that there is a good convergence towards the reference case (30) with an error of less than 3% for a density of 20. A mesh of density 6 gives inaccurate results but increasing this value to 10 leads to a relatively correct representation of the phenomena occurring despite a large amplitude error.

C and D show the results obtained with square element meshes at 45 degrees. Results for fully integrated elements (C) are very similar to the results obtained with a mesh at 0 degrees (A) whereas reduced integration element ones (D) differ noticeably. In this case, one can see that the amplitude of side lobes oscillates on each side of the

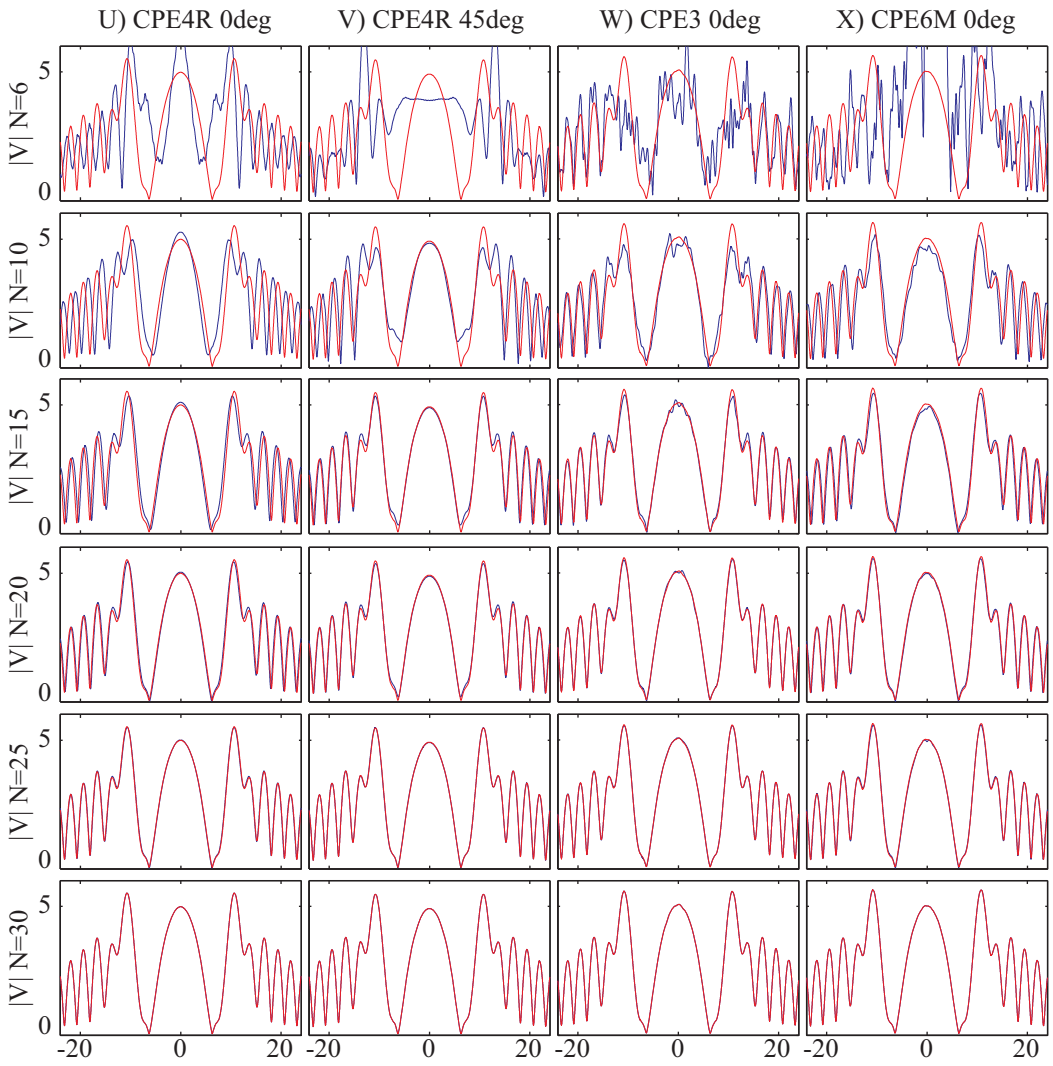

Figure 5.7. Explicit models for a straight edge: Monitored absolute displacement for a shear wave excitation using CPE4R meshes at 0 degrees, CPE4R meshes at 45 degrees and CPE3 and CPE6M triangular elements. Thin red line is reference for N=30 for each case.

reference ones as the mesh is refined. This indicates that, despite a fine mesh (D25), the stair-cased edge interferes with the correct representation of the reflection.

E, F and G show the results obtained with automatically generated triangular element meshes. A convergence towards the reference occurs in the same way as for square elements results (A). Quadratic elements (F) offer the best results with a good agreement achieved for a mesh density of 15. Linear triangular elements (E) cause an oscillation to occur on the side lobes and a mesh density of 25 (E25) is required to have acceptable results. A similar, although milder, phenomenon occurs with modified quadratic elements (G).

Results for shear wave excitation are presented in Figure 5.5 and show a similar behaviour to longitudinal waves except from the lack of oscillation (observed in E and G but absent in L and M).

Explicit results presented in Figure 5.6 and 5.7 agree very well with the results from the implicit solver with their respective element type. In other words, the results of the CPE4R element type are the same when solved with an implicit (B) or an explicit method (Q). Consequently the findings obtained for the implicit solver are also valid for the explicit one.

Overall, based on the plots for square element meshes at 0 degrees, it can be said that this case provides superior results to square element meshes at 45 degrees and triangular element meshes for the modelling of the reflection from a straight edge. The use of square element meshes at an angle gives acceptable results but the oscillation of the side lobes is a concern and could be explained by diffraction occurring due to the jagged nature of the edge. Quadratic triangular elements give results close to square elements with a mesh at 0 degrees. Linear triangular elements need a finer mesh than the other triangular element types in order to provide accurate results and the noticeable undulation on the side lobes is a concern. Modified quadratic element meshes seem to offer a compromise between linear and quadratic triangular elements.

5.4. Reflection from a straight crack at an angle

In this part, the longitudinal and shear wave reflection from a crack at an angle are studied. It should be noted that the angle and length of the modelled cracks have not particular significance and are just sensibly chosen examples. The geometry of the models is presented in Figure 5.8.a. The mid-point of the crack is located 10 units away from the excitation point and the crack is at an angle of 10 degrees relative to the vertical. Three crack lengths are used: 0.25, 1, 4. This permits a wide range of reflection regimes for both wave types.

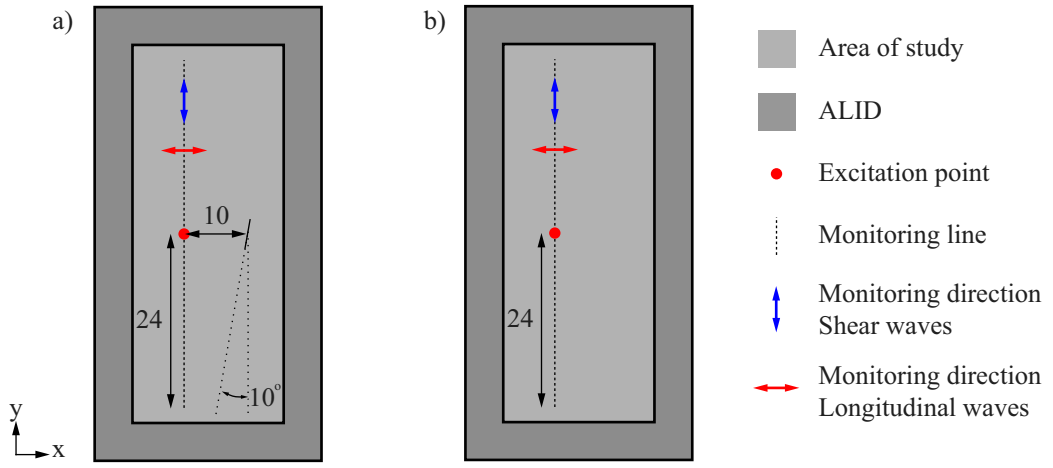

Figure 5.8. Straight crack model: a) with crack, b) without crack.

Two meshing strategies are used. On one side, a regular square mesh is used and nodes are disconnected in order to create a crack following the edges of the elements in the mesh. It can be seen as creating a free edge following the lines of the regular square grid. This is achieved by using a MATLAB routine created by a summer placement student, Sumeet Kale, under the guidance of the author. It defines a crack as close as possible to the exact crack within the particular regular square mesh. On the other side, a triangular element mesh generated by the free meshing algorithm from ABAQUS CAE 6.6-1 is used. In this situation, the geometry of the crack is determined first and then free meshing of the geometry is performed. The particular shape and mesh of each crack generated with both methods is shown in each section where the particular straight crack geometry is studied.

As shown on Figure 5.8, the displacement field is monitored on a line perpendicular to the line joining the crack mid-point to the excitation point and over a length of 24 units on each side of the excitation point. For a longitudinal wave excitation, the displacements are monitored in the x direction and for a shear wave excitation, the displacements are monitored in the y direction. In theory, the incident displacement field is zero in these directions and only the reflection from the edge is present. In practice, some slight numerical issues (low amplitude noise, oscillation close to the excitation point) exist on this line. In order to achieve high quality reflection fields, each case was run with (see Figure 5.8.a) and without (see Figure 5.8.b) the crack being modelled. The complex displacement field of the case without the crack is substracted from the one with the crack. The absolute displacement in the direction specified above is then plotted.

5.4.1 Crack of unit length

The first case studied is the case of a crack of unit length. The actual cracks used for these models are represented in Figure 5.9. When using a triangular mesh, the crack geometry is exactly defined whereas the crack obtained with the square mesh differs from the exact crack. This is highlighted in Figure 5.9 where the theoretical crack as defined in Figure 5.8 is shown in red and the actual modelled crack in blue. Both lines superimpose for triangular element meshes but do not for the regular square element meshes. In both cases, as the mesh is refined, the number of elements defining the crack increases. This should increase the accuracy of the reflection.

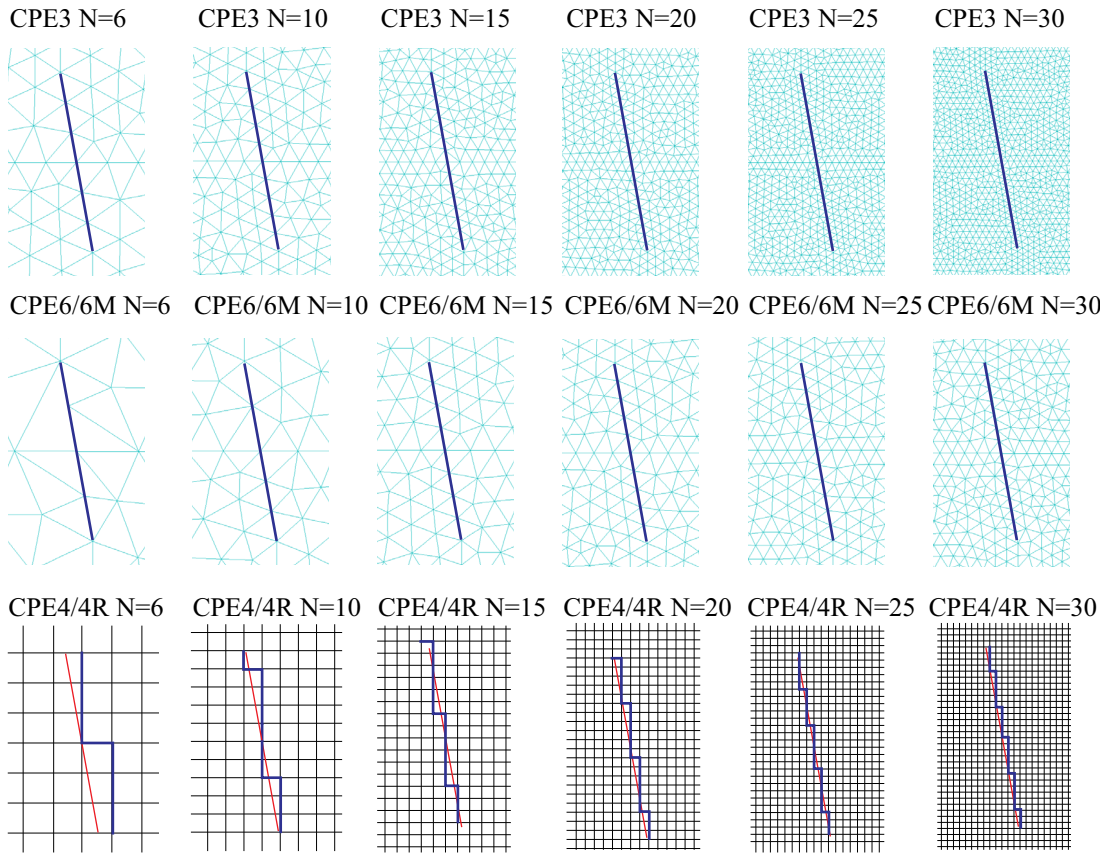

Figure 5.9. Definition of unit long cracks with triangular and square meshes. Blue line shows modelled crack and red line theoretical crack (which is the same line with triangular element meshes but not with regular square element meshes).

Results obtained for the implicit models are presented in Figure 5.10 and 5.11. Results for the explicit models for longitudinal and shear waves are presented in Figure 5.12. In order to simplify the identification of cases, each plot is associated with a letter and a number as in the previous sections.

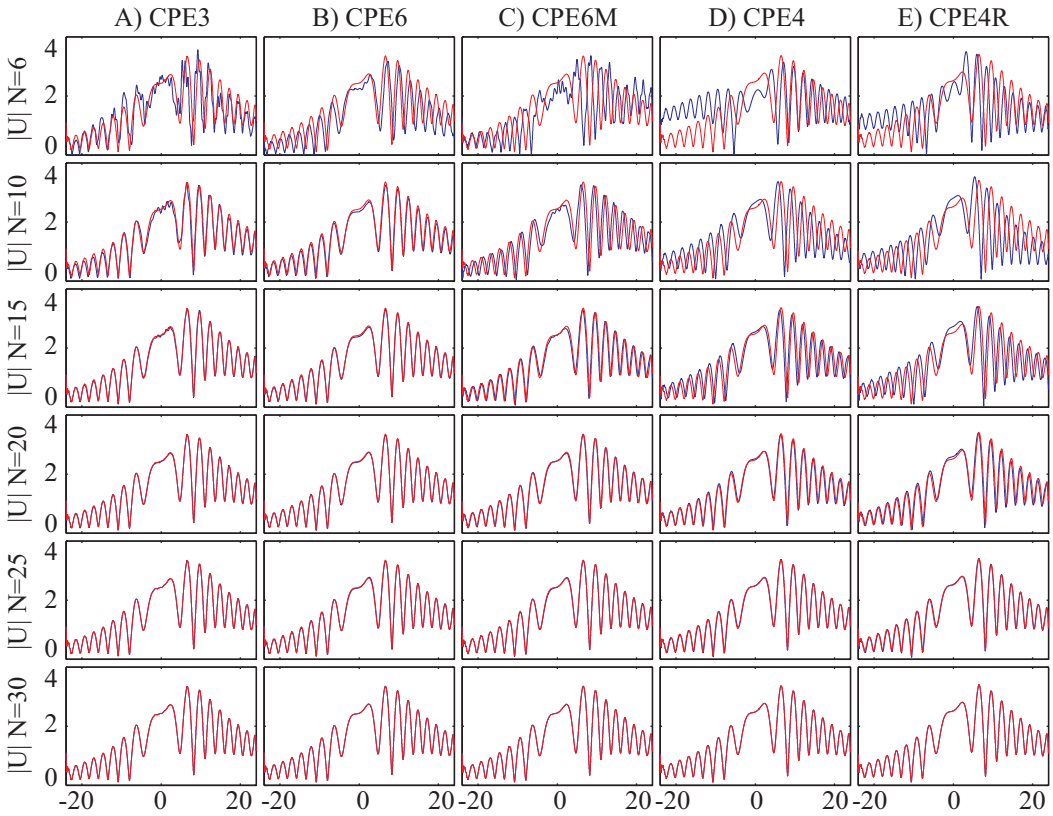

Figure 5.10. Implicit models for a crack of unit length: Monitored absolute displacement for a longitudinal wave excitation using mesh made of CPE3, CPE6, CPE6M, CPE4 and CPE4R elements. Thin red line is reference for N=30 for each case.

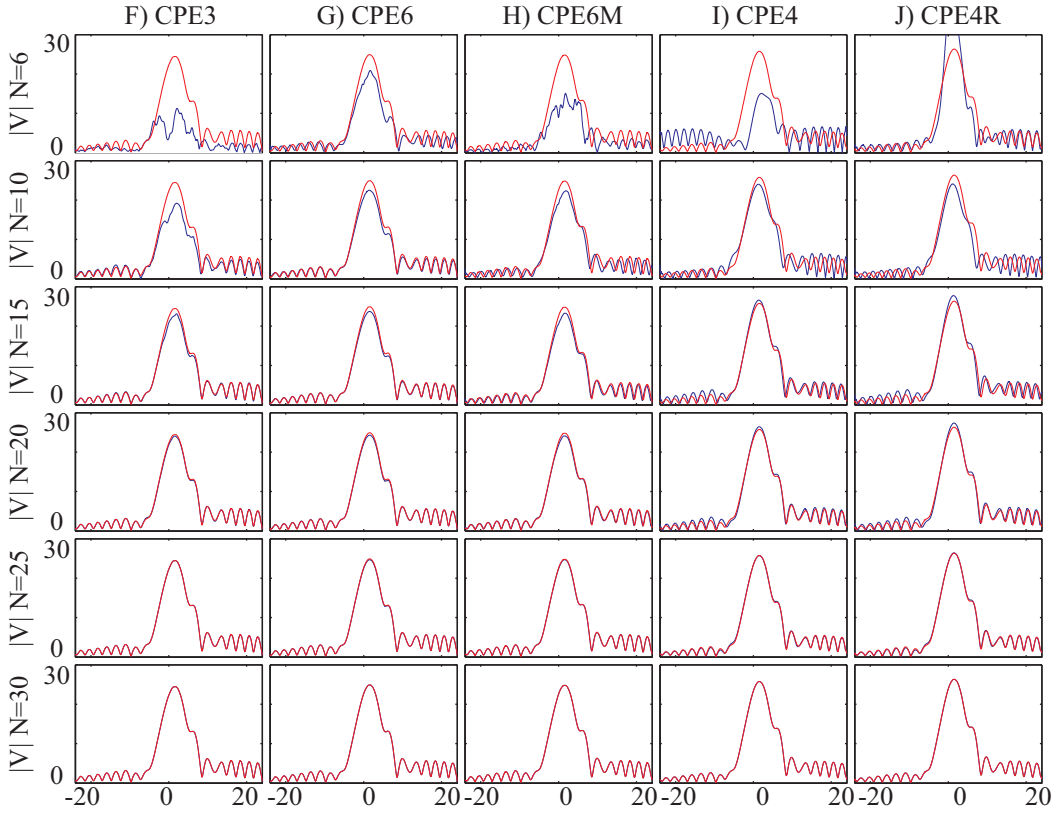

Figure 5.11. Implicit models for a crack of unit length: Monitored absolute displacement for a shear wave excitation using mesh made of CPE3, CPE6, CPE6M, CPE4 and CPE4R elements. Thin red line is reference for N=30 for each case.

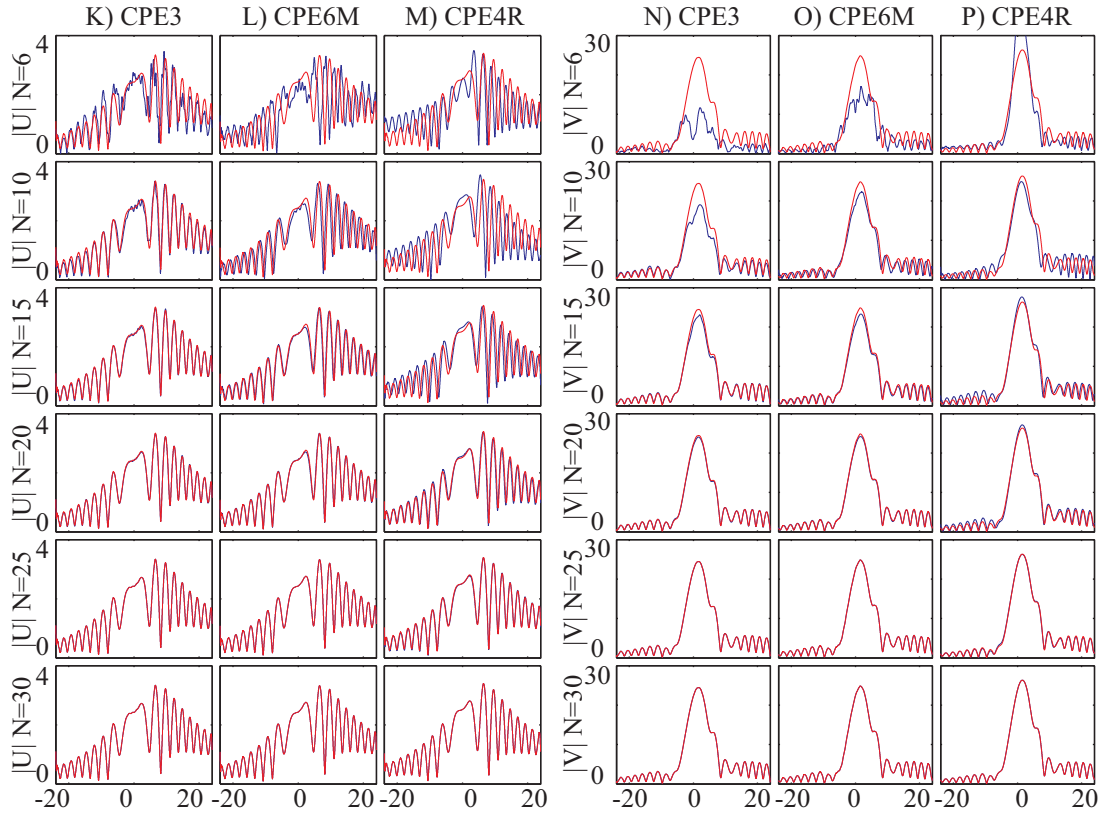

Figure 5.12. Explicit models for a crack of unit length: Monitored absolute displacement for a shear and longitudinal wave excitation using mesh made of CPE3, CPE6M and CPE4R elements. Thin red line is reference for N=30 for each case.

Looking at the implicit results for a longitudinal wave excitation presented in Figure 5.10, it can be seen that, for all element types, there is a good convergence towards the models with 30 elements per wavelength. In this case, the displacement fields are almost perfectly matching for all element types. For all triangular elements, a mesh density of 20 gives results very close to the reference. CPE6 elements (B) provide higher quality than CPE3 (A) and CPE6M (C), with acceptable results being obtained for N=10. Square elements (D-E) - in particular the reduced type (E) - have a slower convergence. For shear wave excitation, the results in Figure 5.11 show a similar pattern, although the rate of convergence for all element types is slower. A mesh density of 25 is necessary for the error on the displacement amplitude to be negligible. This can be explained by the fact that, for a given mesh density, the shear wave velocity error is higher than the longitudinal one but also that the shear wavelength is shorter than the longitudinal one making it more sensitive to numerical “defects” (changes in element size in triangular meshes, steps in square meshes).

For all mesh densities, explicit results shown in Figure 5.12 (K-P) superimpose almost perfectly with the results obtained for the implicit ones with the same element type. These are presented separately for completeness.

Overall, representing an average size straight crack at an angle of 80 degrees does not seem to be challenging for either meshing strategy. The physics are modelled quite accurately for any mesh density over 10. The main source of error is likely to be the actual velocity error and its consequences on the reflection angles. Indeed, as angle of reflection of a wave depends on the wave propagation velocity, an error on the propagation velocity leads to an error on the angle of reflection. In the regular mesh approach, the actual geometric difference between the theoretical crack and the actual crack accounts for another source of error which can explain the slower convergence. Once again, it is interesting to note that the use of free meshing with triangular elements of various sizes does not harm the accuracy of the results.

5.4.2 Crack of length 0.25

The second crack case studied is the case of a crack of length 0.25. The actual cracks used for these models are represented in Figure 5.13. This defect is more challenging than the previous one as the number of nodes defining the defect is very limited in all cases with only 9 nodes for the highest density. As in the previous case, when using a triangular mesh, the crack geometry is exactly defined whereas the crack obtained with the square mesh differs from the exact crack. As the defect is smaller than in the previous case, the definition of the crack using a square mesh differs more strongly in terms of shape but also in terms of length from the theoretical crack. When a square mesh of density 6 is used, the algorithm does not generate any crack and therefore the results for this case are of no interest as no reflection occurs.

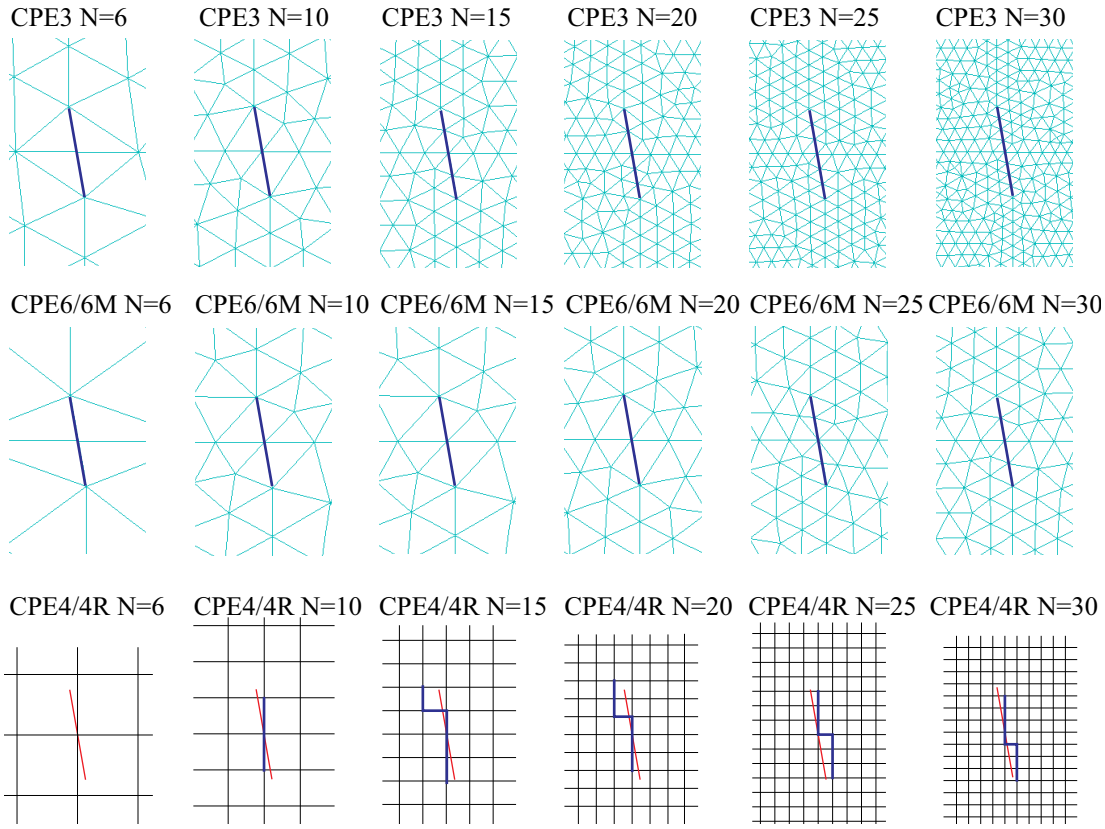

Figure 5.13. 0.25 unit long crack definition with triangular and square meshes. Blue line shows modelled crack and red line theoretical crack (which is the same line with triangular element meshes but not with regular square element meshes).

Results obtained for the implicit models are presented in Figure 5.14 and 5.15. Results for the explicit models for longitudinal and shear waves are presented in Figure 5.16. In order to simplify the identification of cases, each plot is associated with a letter and a number as in the previous section.

Looking at the results for the longitudinal cases presented in Figure 5.14, it is interesting to see that there is a convergence towards the results obtained with the finest mesh for both triangular and square meshes, but this convergence is much slower than the one observed for the crack of unit length. For quadratic triangular meshes of density 20, the error on the amplitude relative to the reference varies between 6 and 8%, but for a density of 25 this error is almost negligible. The most likely explanation for this is that independently of the mesh density the improvement in the quality of results is caused by the increase in the number of nodes defining the crack. Using the free meshing algorithm, the number of nodes on the crack is 5, 5, 9 and 9 for densities of 15, 20, 25 and 30. It can therefore be said that it is necessary to have at least 7 nodes over the length of a crack to have an error smaller than 5% relative to the case with a mesh of density 30. As mentioned previously, the agreement is very good between

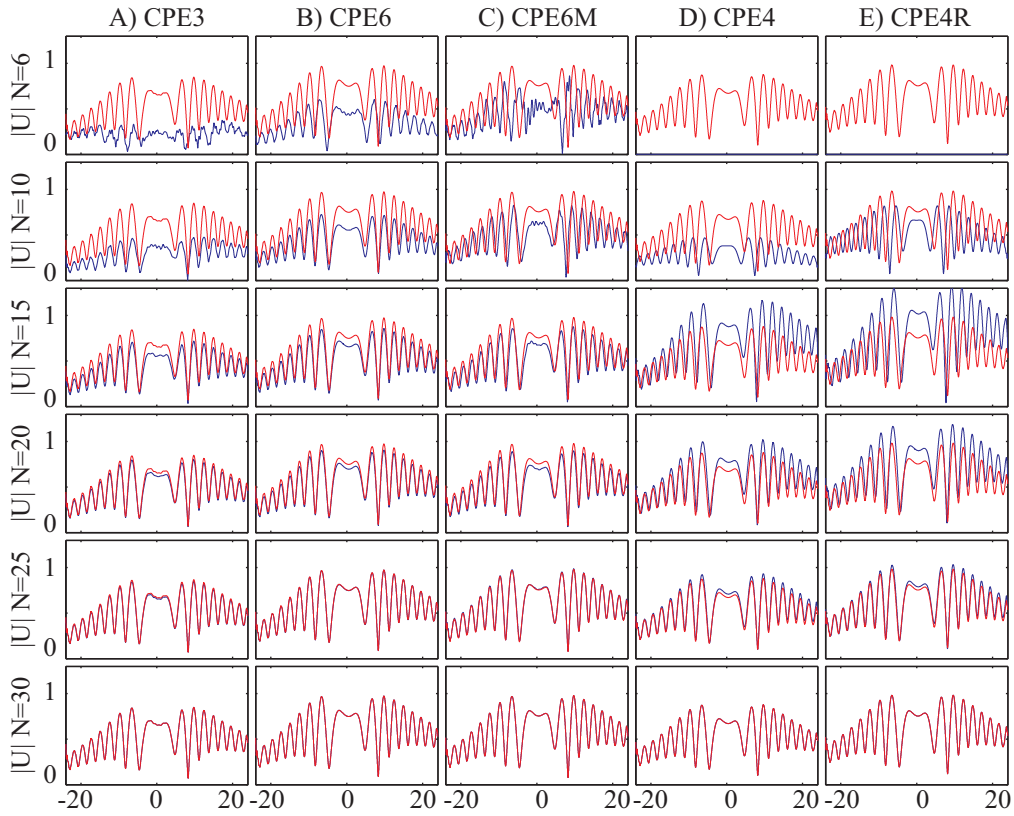

Figure 5.14. Implicit models for a crack of length 0.25: Monitored absolute displacement for a longitudinal wave excitation using mesh made of CPE3, CPE6, CPE6M, CPE4 and CPE4R elements. Thin red line is reference for N=30 for each case.

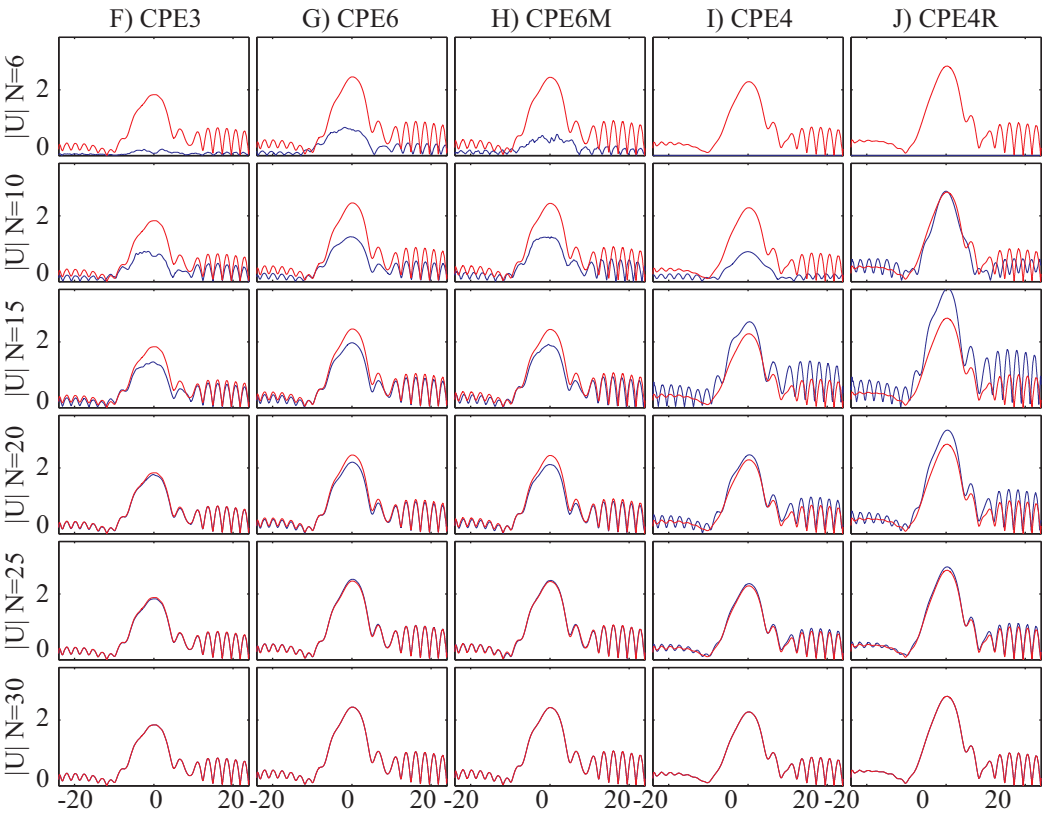

Figure 5.15. Implicit models for a crack of length 0.25: Monitored absolute displacement for a shear wave excitation using mesh made of CPE3, CPE6, CPE6M, CPE4 and CPE4R elements. Thin red line is reference for N=30 for each case.

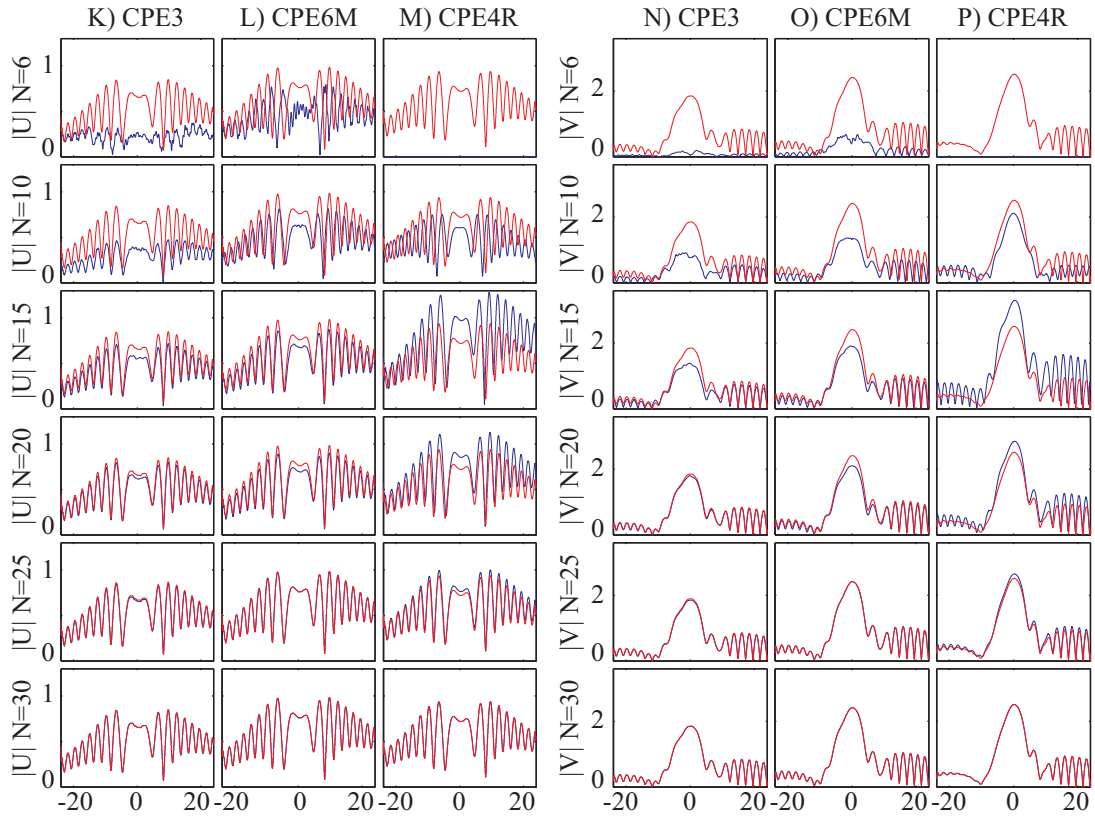

Figure 5.16. Explicit models for a crack of length 0.25: Monitored absolute displacement for a shear and longitudinal wave excitation using mesh made of CPE3, CPE6M and CPE4R elements. Thin red line is reference for N=30 for each case.

results for N=25 and N=30 for quadratic (B) and modified (C) triangular element types indicating that the physical phenomena are very accurately represented. The fact that the convergence is not as good with linear triangular elements (A) and that there is an error of 13% between the linear and quadratic element cases for N=30 means that with linear triangular elements the mesh needs to be refined further in order to model the physical phenomena very accurately. Therefore, one can say that quadratic triangular elements offer superior results to linear ones when modelling small defects.

For square elements (D-E), cases for density 6 (no crack) and 10 (short vertical crack) are ruled out. Convergence towards the reference occurs for both square element types. Unexpectedly, the reference for the reduced integration elements (E) matches more closely our best reference (for triangular quadratic elements) than the full integration ones. No strong convergence has been reached for N=30; it is therefore difficult to draw definite conclusions on the quality of the representation using square elements. It can nevertheless be noted that, despite the coarse geometry of the crack and the inaccuracy on the exact length of the crack, the reflection is relatively well modelled.

The findings from shear wave excitation for all element types are in line with the longitudinal ones.

For all mesh densities, explicit results in Figure 5.16 superimpose closely with the results obtained from the implicit ones with the same element type and are presented separately for completeness.

Overall, it is clear that not only the mesh density but also the number of nodes used to define a short straight crack at an angle is crucial to accurately represent its reflections from both longitudinal and shear waves. Quadratic triangular meshes offer a quick convergence towards accurate results. The use of square meshes leading to only roughly represented cracks give acceptable results. These are not as accurate as the ones obtained with quadratic triangular elements. Linear triangular meshes would need to be refined over 30 nodes per shortest wavelength to obtain the same result quality as with quadratic triangular elements. The use of quadratic triangular elements is therefore preferable to linear triangular and square ones in this case.

5.4.3 Crack of length 4

The last crack case studied is the case of a crack of length 4. The actual cracks used for these models are represented in Figure 5.17. This defect is not as challenging as the two previous ones in terms of correctly defining the geometry of the crack. With a square mesh approach even with a mesh density of 6, the crack is well represented geometrically.

Results obtained for the implicit models for longitudinal and shear wave excitation are presented in Figure 5.18 and 5.19 respectively. Results for the explicit models for longitudinal and shear waves are presented in Figure 5.20.

For both longitudinal and shear wave excitation, all element types show a quick convergence towards their reference. The references are very closely matched for all element types. For triangular elements, a mesh density of 10 gives acceptable results and a mesh density of 15 limits the error on the amplitude to 2%. The error is negligible for N superior or equal to 20. For square elements, the criterion is slightly more stringent, with results for a mesh density of 20 being acceptable.

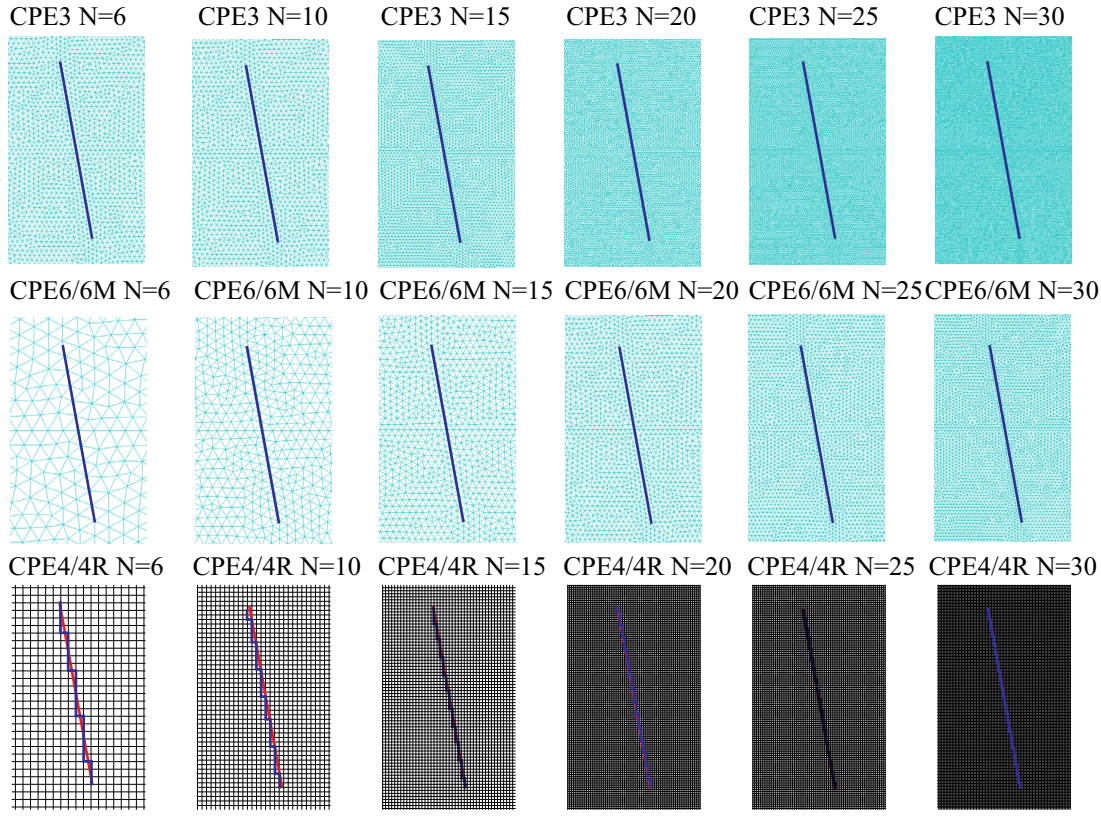

Figure 5.17. 4 unit long crack definition with triangular and square meshes. Blue line shows modelled crack and red line theoretical crack (which is the same line with triangular element meshes but not with regular square element meshes).

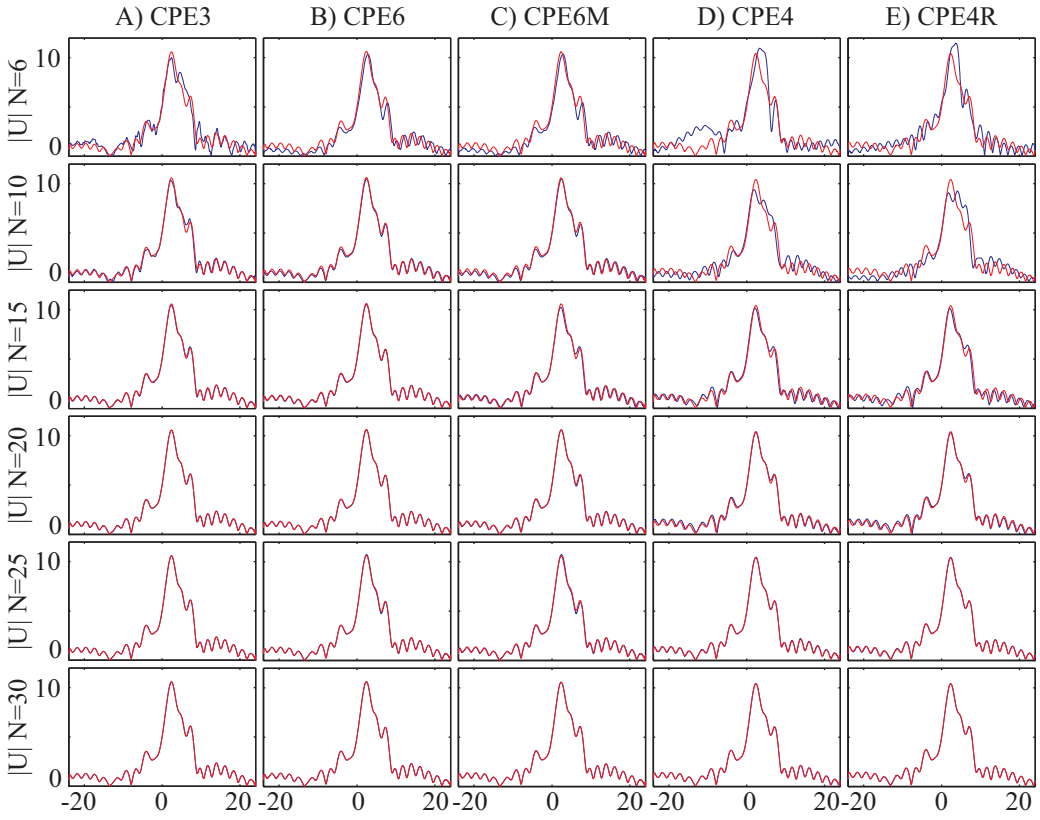

Figure 5.18. Implicit models for a crack of length 4: Monitored absolute displacement for a longitudinal wave excitation using mesh made of CPE3, CPE6, CPE6M, CPE4 and CPE4R elements. Thin red line is reference for N=30 for each case.

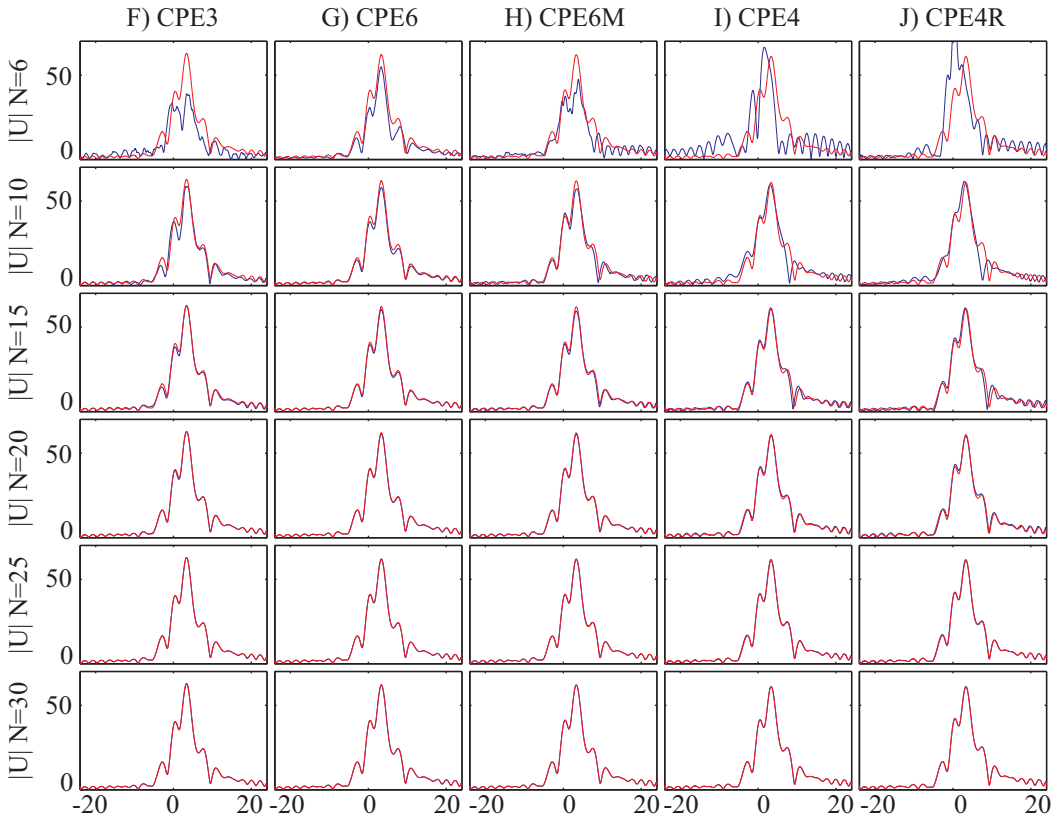

Figure 5.19. Implicit models for a crack of length 4: Monitored absolute displacement for a shear wave excitation using mesh made of CPE3, CPE6, CPE6M, CPE4 and CPE4R elements. Thin red line is reference for N=30 for each case.

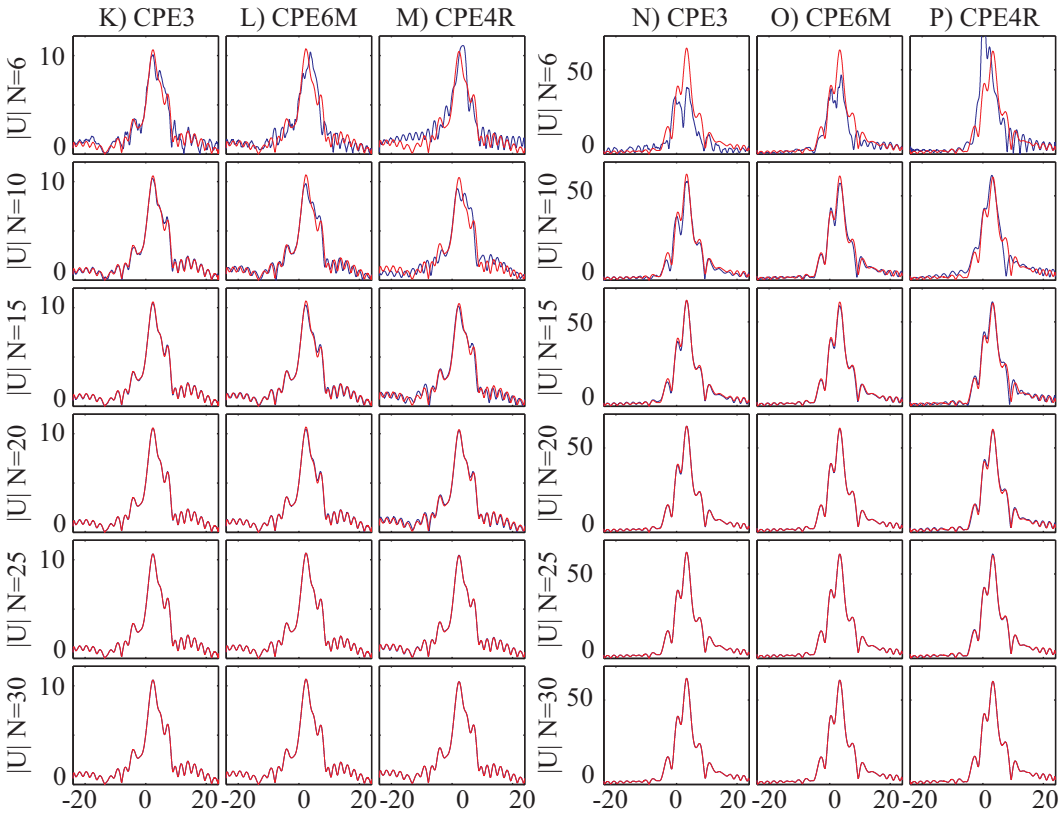

Figure 5.20. Explicit models for a crack of length 4: Monitored absolute displacement for a shear and longitudinal wave excitation using mesh made of CPE3, CPE6M and CPE4R elements. Thin red line is reference for N=30 for each case.

Explicit results for all mesh densities superimpose closely with the results obtained from the implicit ones with the same element type and are presented separately on Figure 5.20 for completeness.

In this case, the relaxation of constraints regarding the number of nodes defining the crack leads to a faster convergence of results for all techniques and element types.

5.4.4 Conclusion

The influence of the mesh density on the accuracy of results is confirmed by the present study but most significantly the importance of the number of elements defining a defect is demonstrated. The fact that it is much more difficult to obtain acceptable results for a short crack than for a long one is easily understandable. It is interesting to note that a large improvement in result quality was achieved when a limited refinement of the triangular mesh caused a large increase in the number of nodes defining the smallest crack (from 5 to 9). It shows that the number of nodes defining a crack has a strong impact on the accuracy of the reflection. It is also worth noting that the regular square mesh approach is more adapted to the long crack case than the shorter ones. However, even with long cracks, a square mesh needs to be finer than a triangular one in order to achieve the same accuracy. Local mesh refinement would be advantageous in models where short defects are present if there are no issues with the mesh density transition. This last point will be examined in the next chapter.

5.5. Reflection from circular defects

The reflection of longitudinal and shear waves from circular defects is studied. In each case, a hole is located 10 units away from the excitation point. Three hole diameters are used: 0.25, 1 and 4 units. This permits to have a wide range of reflection regimes for both wave types. The general geometry of the models is shown in Figure 5.21.a.

Two meshing strategies are used. On one side, a regular square mesh is used and elements are removed in order to create a hole. This is achieved by using a MATLAB routine created by a summer placement student, Sumeet Kale, under the guidance of the author. It defines a hole as close as possible to the exact hole within the particular regular square mesh. The criterion used to determine whether to generate an element or not is the distance between the centre point of a potential square element in the node

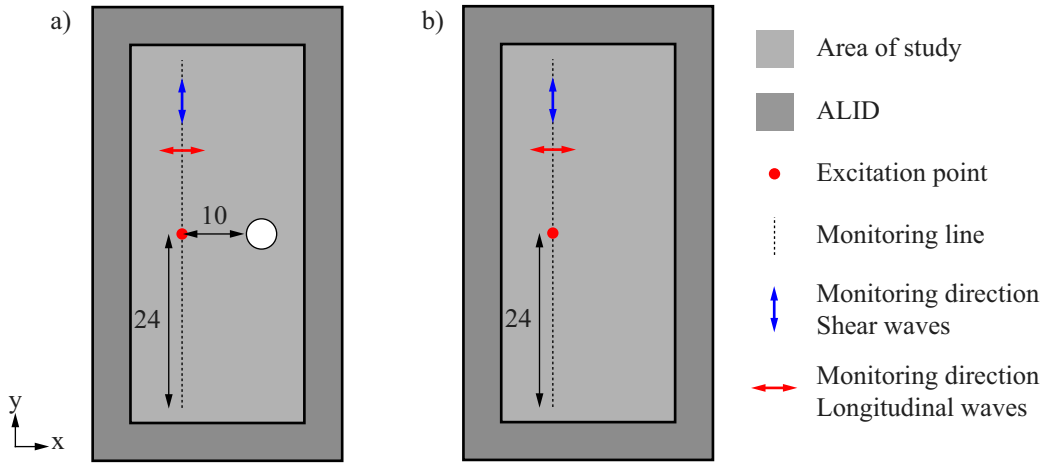

Figure 5.21. Circular defect model: a) with circular defect, b) without circular defect.

grid to the centre of the exact hole. If this distance is lower than the radius, no element is created. This leads to a hole whose edge is jagged. On the other side, a triangular mesh generated by the free meshing algorithm from ABAQUS CAE 6.6-1 is used. In this situation, the geometry of the hole is determined first and then free meshing of the geometry is performed. When using a triangular mesh, nodes are placed on the edge of the exact hole and are then used to create elements. The number of elements on the hole depends on the diameter of the hole. It is never lower than 8 as the curvature control is set to the default setting of 0.1. It is important to note that with linear triangular elements, the hole will be made of straight segments whose end points are located on the exact circle whereas, with quadratic triangular elements, the hole is represented almost exactly with curved segments.

The displacement field is monitored on a line perpendicular to the line joining the hole centre point to the excitation point and over a length of 24 units on each side of the excitation point as shown on Figure 5.21. For a longitudinal wave excitation, the displacements are monitored in the x direction and for a shear wave excitation, the displacements are monitored in the y direction. In theory, the incident displacement field is zero in these directions and only the reflection from the edge is present. In practice, each case was run with (see Figure 5.21.a) and without (see Figure 5.21.b) the crack being modelled in order to achieve high quality reflection fields as this resolved some slight numerical issues (low amplitude noise, oscillation close to the excitation point). The complex displacement field of the case without the edge is substracted from the one with the edge. The absolute displacement in the direction specified above is then plotted.

5.5.1 Hole of unit diameter

The first case studied is the case of a hole of unit diameter. The actual holes used for these models are represented in Figure 5.22. The hole definition is very good with triangular meshes whereas, with square elements, a noticeable difference exists for coarse meshes. For a regular square mesh of density 15, two models are run: one using a diameter of 1 and one with a slightly larger diameter of 1.01. The consequence of this change in diameter is that an extra 8 elements are not generated in the second case. These elements are shown in Figure 5.22 and are crossed in order to identify them.

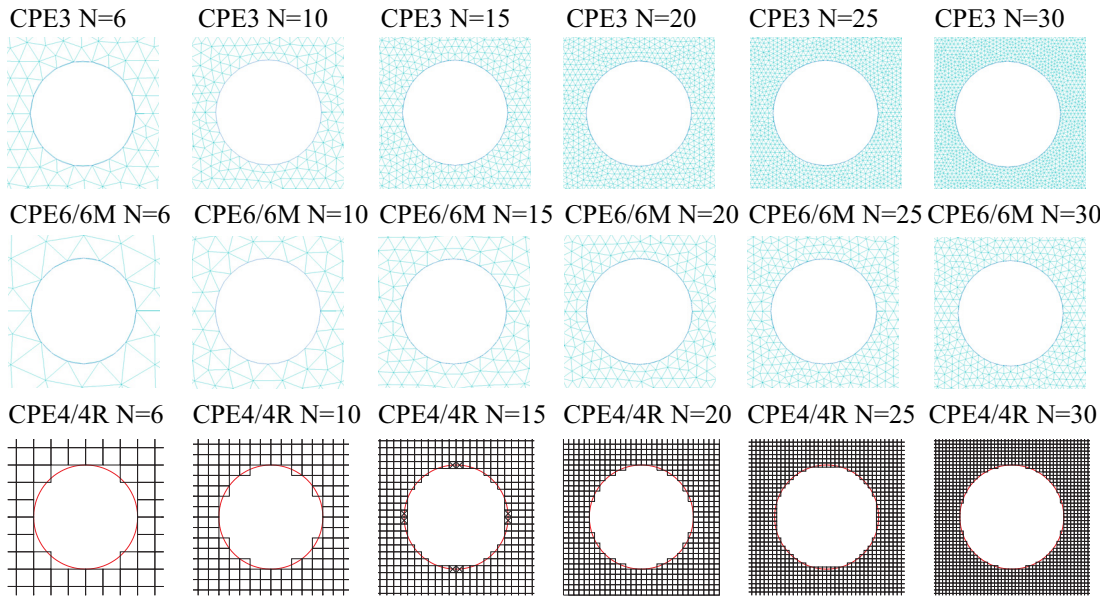

Figure 5.22. Unit diameter hole definition with triangular and square meshes

Results obtained for the implicit models for longitudinal and shear wave excitation are presented in Figures 5.23 and 5.24 respectively. Results for the explicit models for longitudinal and shear waves are presented in Figure 5.25.

Results for the triangular meshes indicate a good convergence of the solution for both longitudinal and shear wave excitation towards a common reference. Acceptable displacement fields are obtained with 15 nodes per wavelength. A negligible error is achieved with a mesh density of 20, although some unwanted low amplitude oscillations are still present for linear and modified quadratic elements.

Looking at the results given by square meshes using the standard algorithm (blue and red lines), one can see that the general physical phenomena are correctly represented for N superior to 10 and 15 with longitudinal and shear wave excitation respectively.

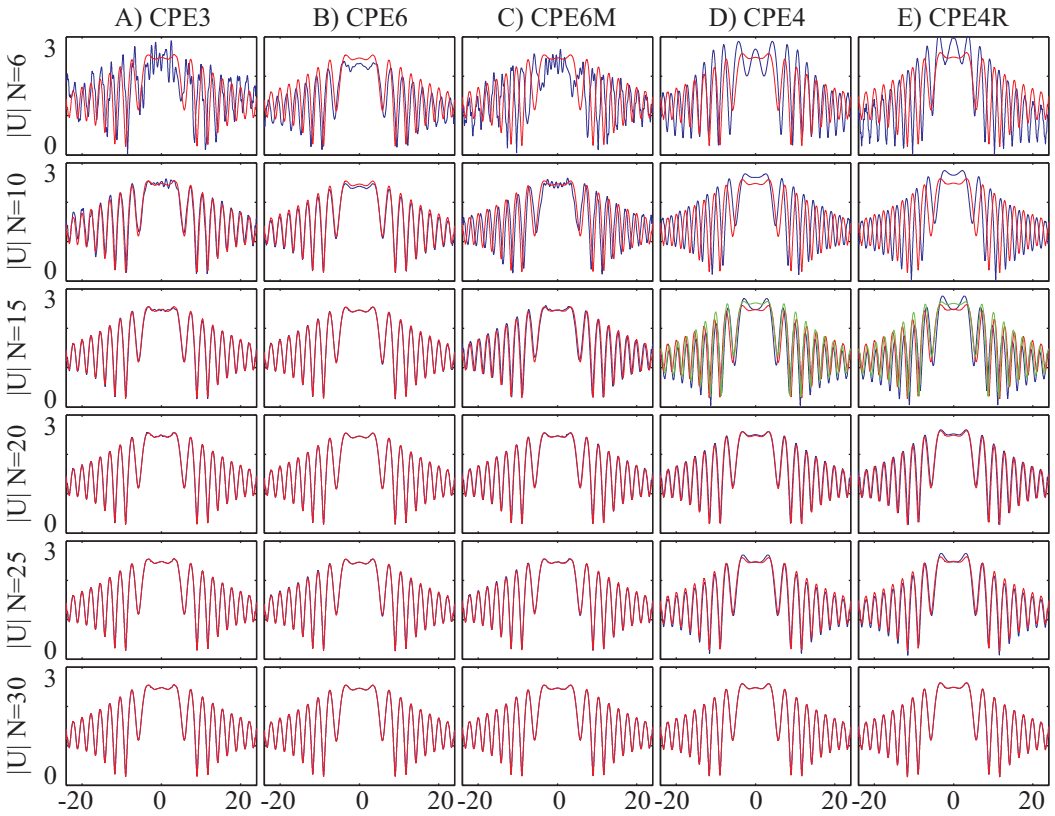

Figure 5.23. Implicit models for a hole of unit diameter: Monitored absolute displacement for a longitudinal wave excitation using mesh made of CPE3, CPE6, CPE6M, CPE4 and CPE4R elements. Thin red line is reference for N=30 for each case.

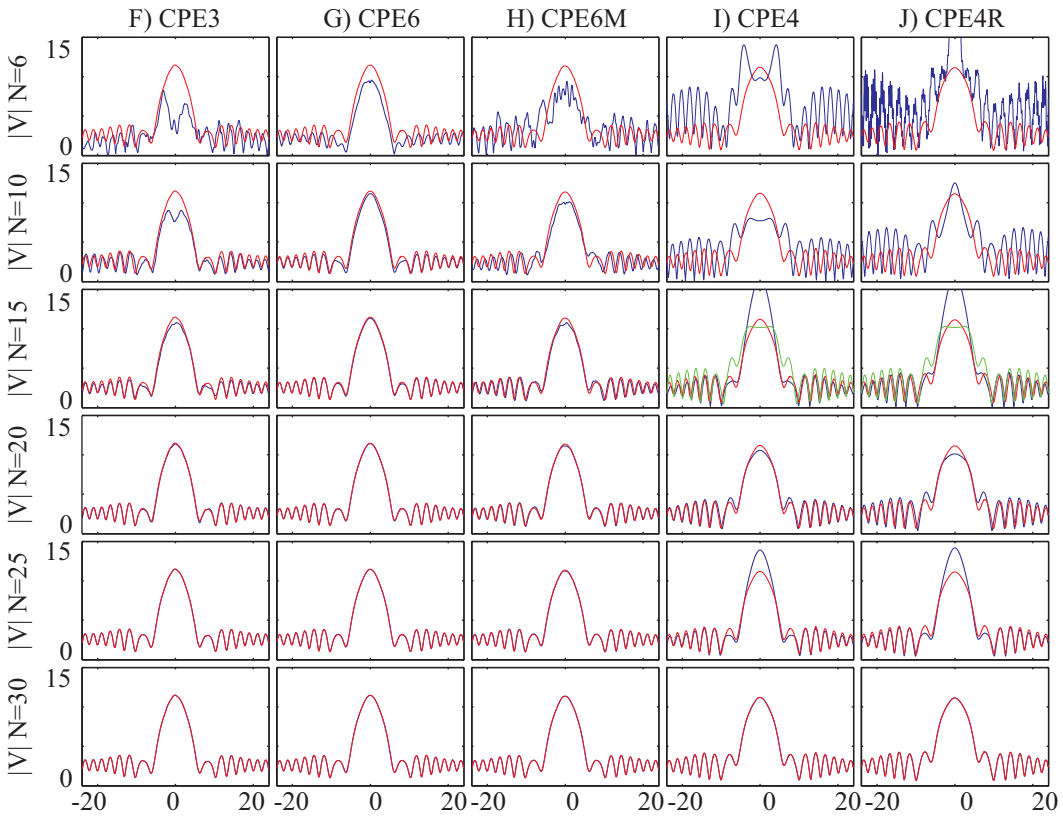

Figure 5.24. Implicit models for a hole of unit diameter: Monitored absolute displacement for a shear wave excitation using mesh made of CPE3, CPE6, CPE6M, CPE4 and CPE4R elements. Thin red line is reference for N=30 for each case.

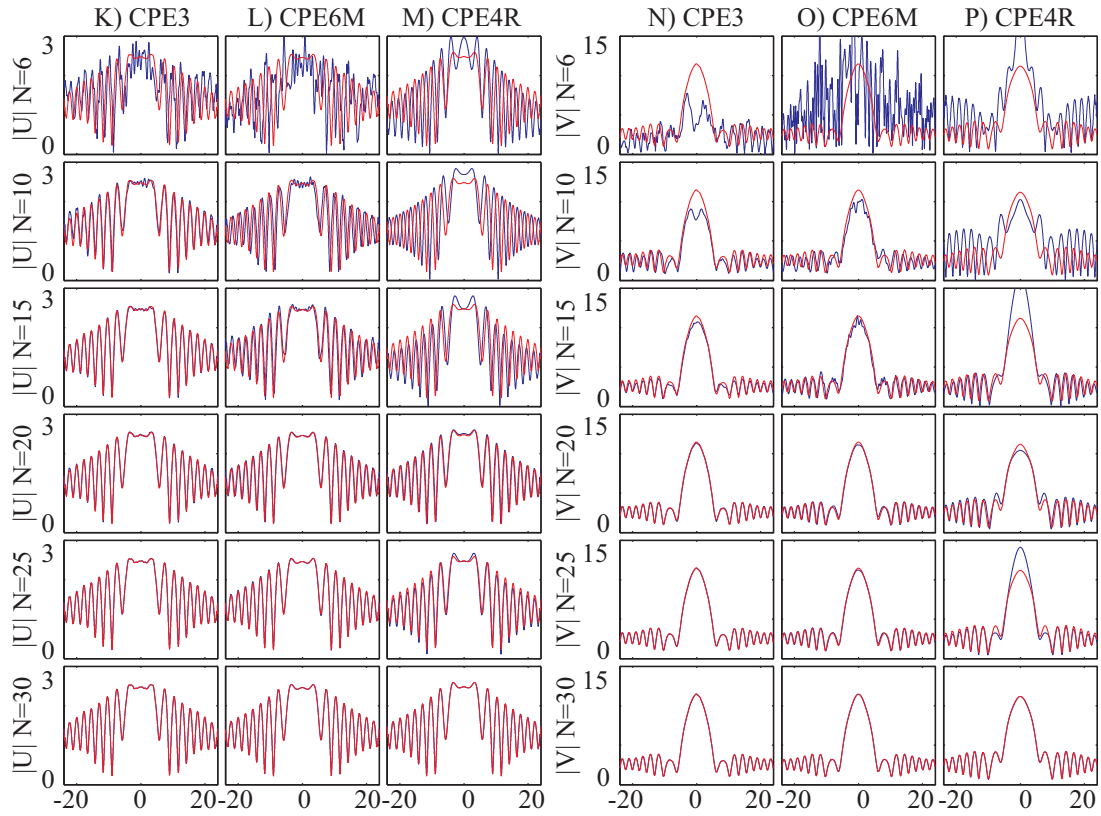

Figure 5.25. Explicit models for a hole of unit diameter: Monitored absolute displacement for a shear and longitudinal wave excitation using mesh made of CPE3, CPE6M and CPE4R elements. Thin red line is reference for N=30 for each case.

The reference matches the one for triangular elements indicating that the displacement field is accurate at this density. There is an issue with the amplitude of the signal for N up to 25. The convergence is not constant as the amplitude error is higher for a density of 25 and 15 than for one of 20. This is much stronger with shear wave cases than with longitudinal ones. Two possible sources of error combine to explain this. The first is that the diameter at 0 and 90 degrees is smaller than the exact ones for densities of 15 (diameter of 0.88) and 25 (diameter of 0.96). This should give lower displacement amplitude which is not the case here. Against this, with a shear wave excitation, a density of 20 and an exact diameter at 0 and 90 degrees, the amplitude is lower than the reference. This shows that the error on the diameter is not the major contributor to the amplitude error. The low slope of the front face of the hole can not be resolved accurately by the square mesh and a small variation on the density or diameter leads to very different shape. At a density of 15, the front face of the hole is made of a flat area of 8 elements out of the 14 on the diameter (57%) and in the same way, for a density of 25, a flat area of 10 out of 24 elements (42%) whereas for a density of 20, it is only 6 out of 20 (30%).

In order to look at the influence of this, a hole of diameter 1.01 is generated. The small change in the exact diameter means that the shape of the front face changes as the crossed elements in Figure 5.22 are omitted. The flat central part of 8 elements changes into 2 central elements bordered by 2 flat parts of 3 elements each. The results for this modified hole are plotted with a green line on Figures 5.23 and 5.24. The change causes the reflected amplitude at the excitation point to drop by 40% for the shear wave despite the change in the actual diameter at 0 and 90 degrees from 0.88 to 1.12 units.

It is likely that this dramatic change can be explained by the fact that the front face of the hole does not behave as a flat reflector in the new configuration. This may also be the consequence of a change in the reflection interference pattern of the various steps of the edge of the hole. The shear wave case is far more sensitive to this than the longitudinal case. This shows that the way the jagged edge of the hole is defined strongly influences the reflection from a hole in particular in the case of shear wave excitation.

5.5.2 Hole of diameter 0.25

The second case studied is the case of a hole of diameter 0.25. The actual holes used for these models are represented in Figure 5.26. The effect of the curvature control is clearly seen for linear and quadratic triangular meshes up to a density of 15 and 20 respectively. It is worth mentioning that using the default setting, the number of elements is at least 8 on the edge of the hole. This means that at least 8 and 16 nodes are used for linear and quadratic elements respectively. The definition of holes using a square mesh is much approximated. Given the findings of the previous part, this should be reflected in the results.

Results obtained for the implicit models for longitudinal and shear wave excitation are presented in Figures 5.27 and 5.28 respectively. Results for the explicit models for longitudinal and shear waves are presented in Figure 5.29.

The results obtained with quadratic and modified quadratic triangular meshes for both type of excitation show a good convergence with a negligible difference between N=25 and N=30. Convergence is slower with linear elements and errors still exist between N=25 and N=30. An error of 4% exists between the reference for quadratic and linear

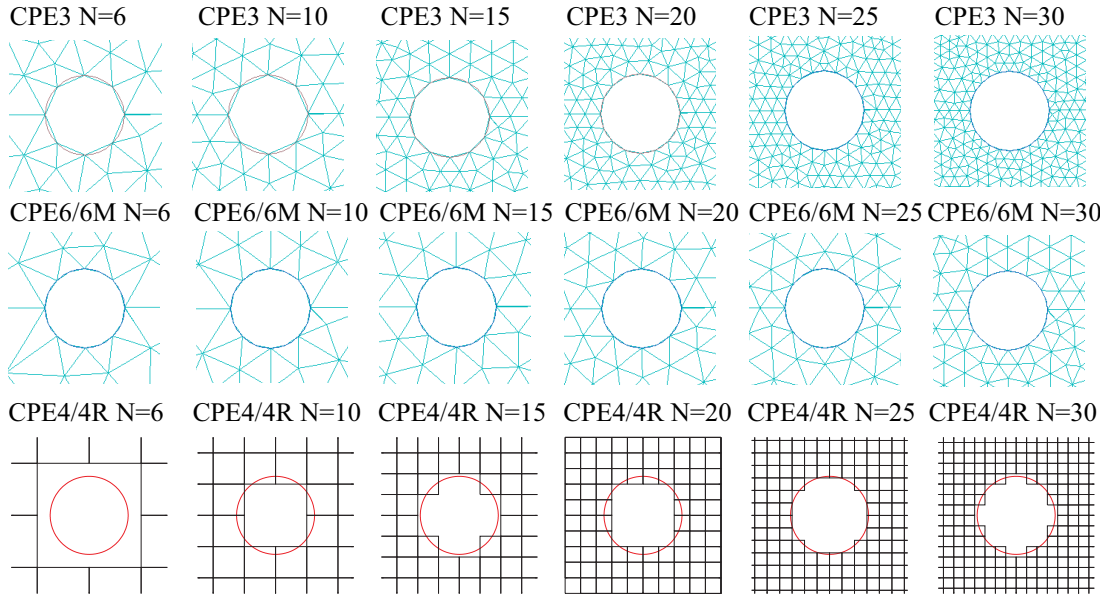

Figure 5.26. 0.25 unit diameter hole definition with triangular and square meshes

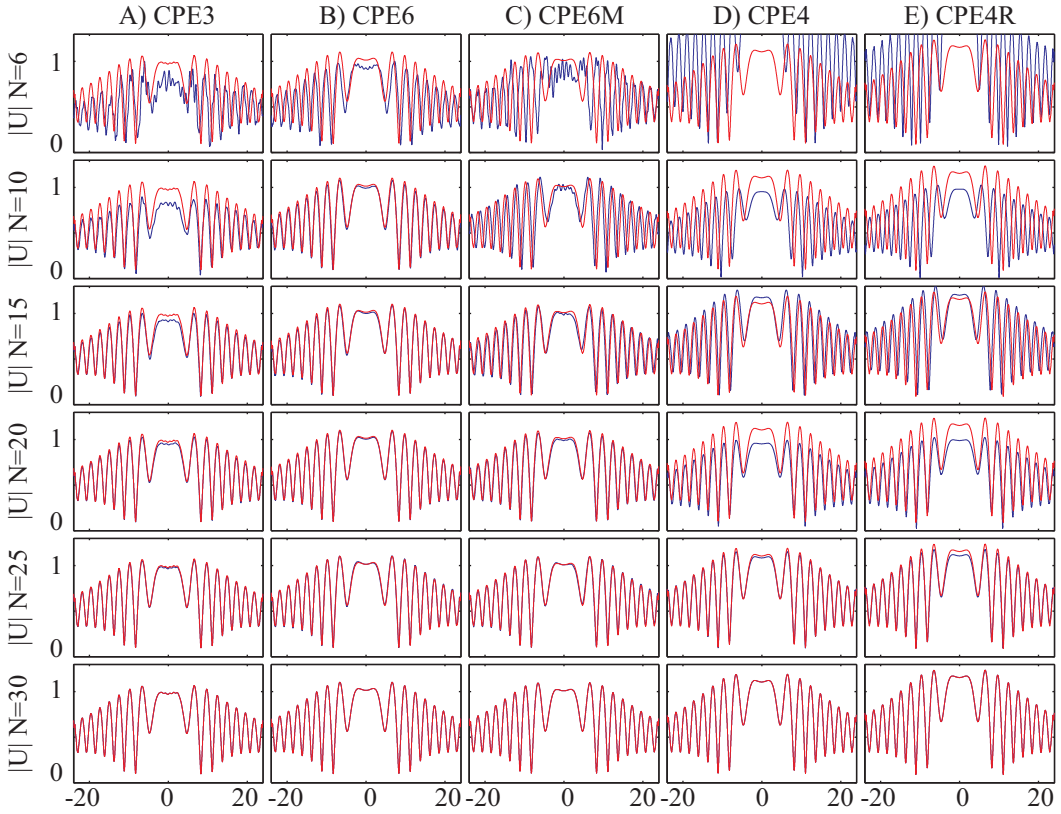

Figure 5.27. Implicit models for a hole of diameter 0.25: Monitored absolute displacement for a longitudinal wave excitation using mesh made of CPE3, CPE6, CPE6M, CPE4 and CPE4R elements. Thin red line is reference for N=30 for each case.

elements. This indicates that an even finer mesh is required for the linear elements in order to represent the reflection very accurately. For square meshes, the reflection pattern is correctly represented for all mesh densities but, as seen previously, a variation on the amplitude is caused by the actual diameter of the hole and the shape

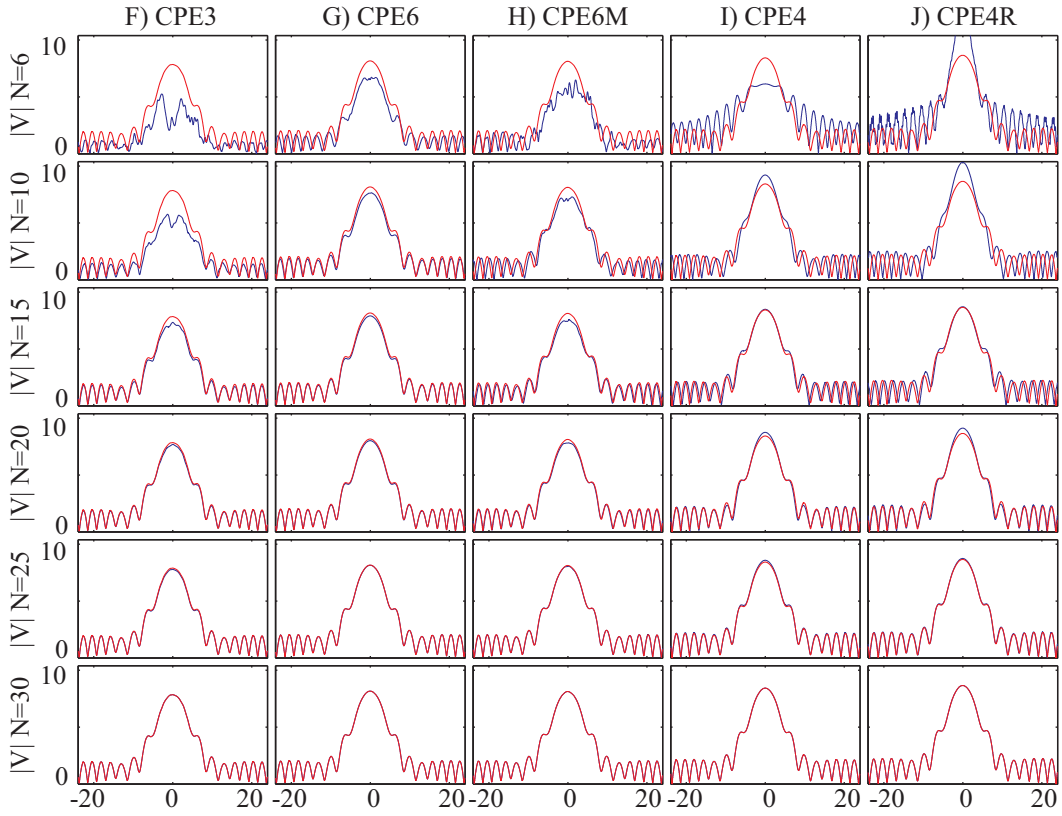

Figure 5.28. Implicit models for a hole of diameter 0.25: Monitored absolute displacement for a shear wave excitation using mesh made of CPE3, CPE6, CPE6M, CPE4 and CPE4R elements. Thin red line is reference for N=30 for each case.

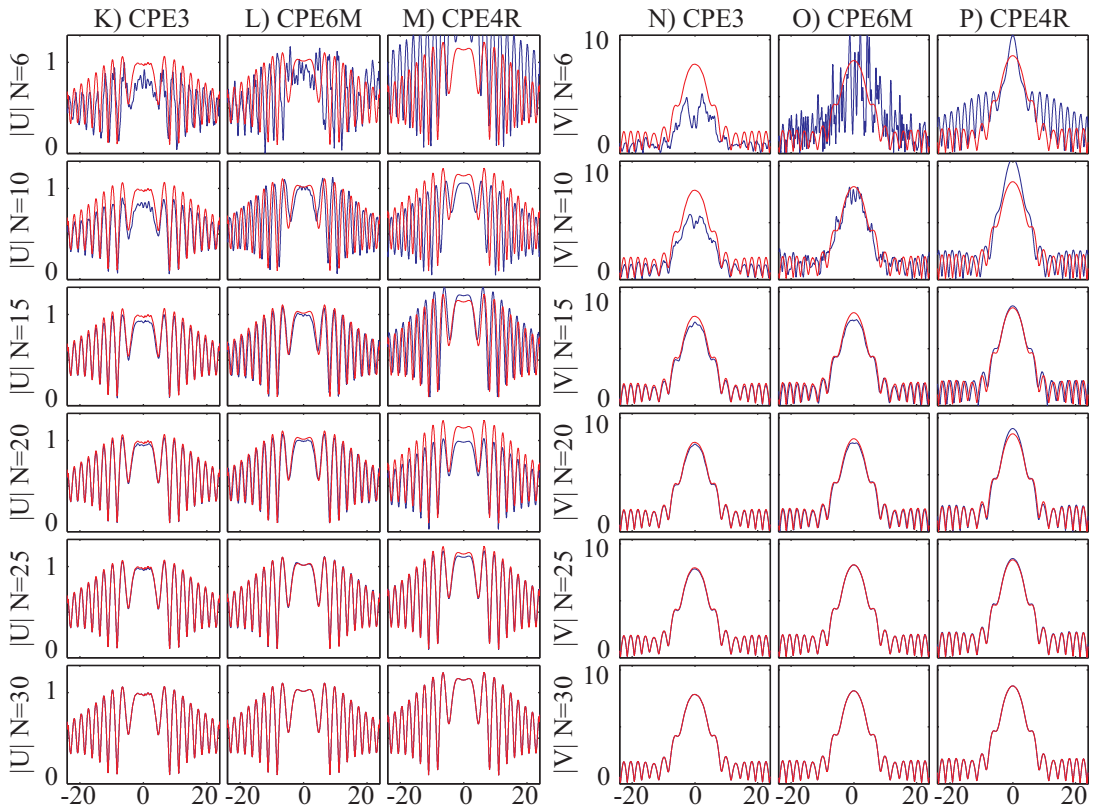

Figure 5.29. Explicit models for a hole of diameter 0.25: Monitored absolute displacement for a shear and longitudinal wave excitation using mesh made of CPE3, CPE6M and CPE4R elements. Thin red line is reference for N=30 for each case.

of the jagged edge. This variation is far from being as strong as in the previous case. This is likely to be due to the fact that the curvature of the hole is higher relative to the element size and that the behaviour of the hole is closer to a point scatterer.

5.5.3 Hole of diameter 4

The last case studied is the case of a hole of diameter 4. The actual holes used for these models are represented in Figure 5.30. The curvature control has no effect even for the coarsest of mesh. The definition of the holes using the square mesh approach provides a jagged edge which seems to be geometrically close to the exact hole.

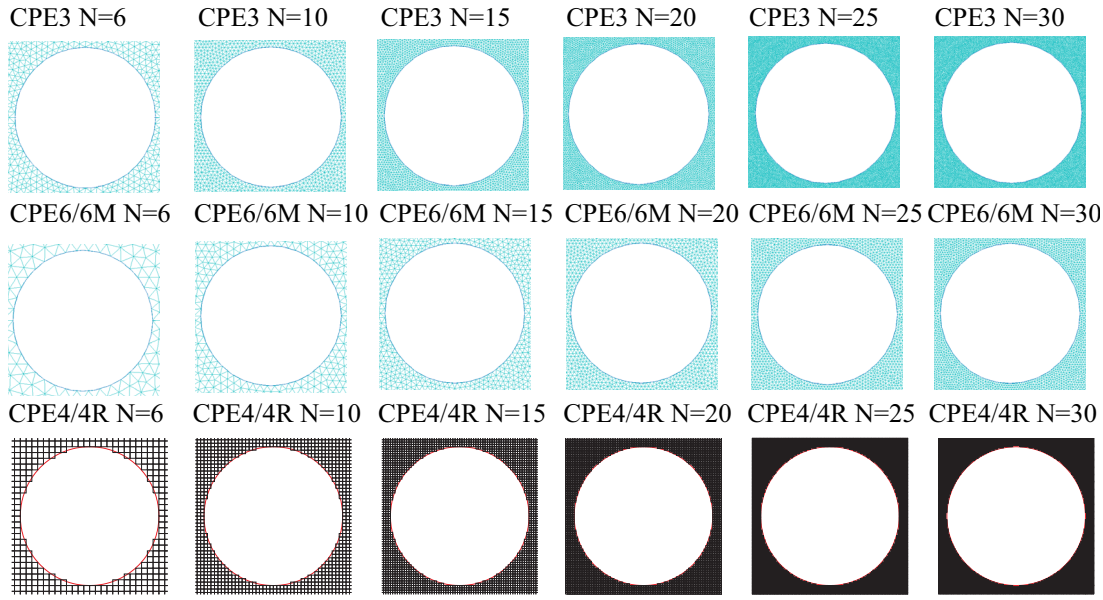

Figure 5.30. 4 units diameter hole definition with triangular and square meshes

Results obtained for the implicit models for longitudinal and shear wave excitation are presented in Figures 5.31 and 5.32 respectively. Results for the explicit models for longitudinal and shear waves are presented in Figure 5.33.

Results for the triangular meshes show a good convergence for both longitudinal and shear wave excitation towards a common reference. The error is negligible with a mesh density of 20, although some unwanted low amplitude oscillation is still present for linear and modified quadratic elements. For N=15, acceptable results are obtained.

With square elements, longitudinal wave excitation results converge towards the reference of the triangular elements, but results for shear wave excitation are only acceptable for N=30. For mesh densities lower than this, the expected single peak at

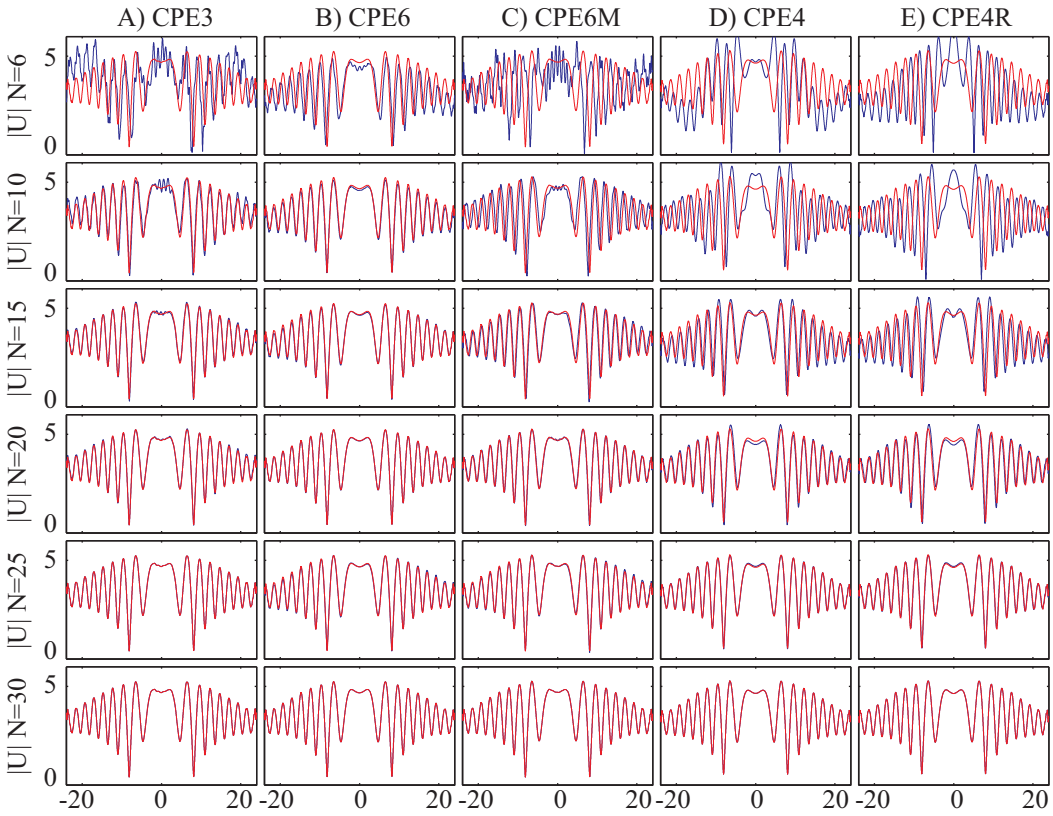

Figure 5.31. Implicit models for a hole of diameter 4: Monitored absolute displacement for a longitudinal wave excitation using mesh made of CPE3, CPE6, CPE6M, CPE4 and CPE4R elements. Thin red line is reference for N=30 for each case.

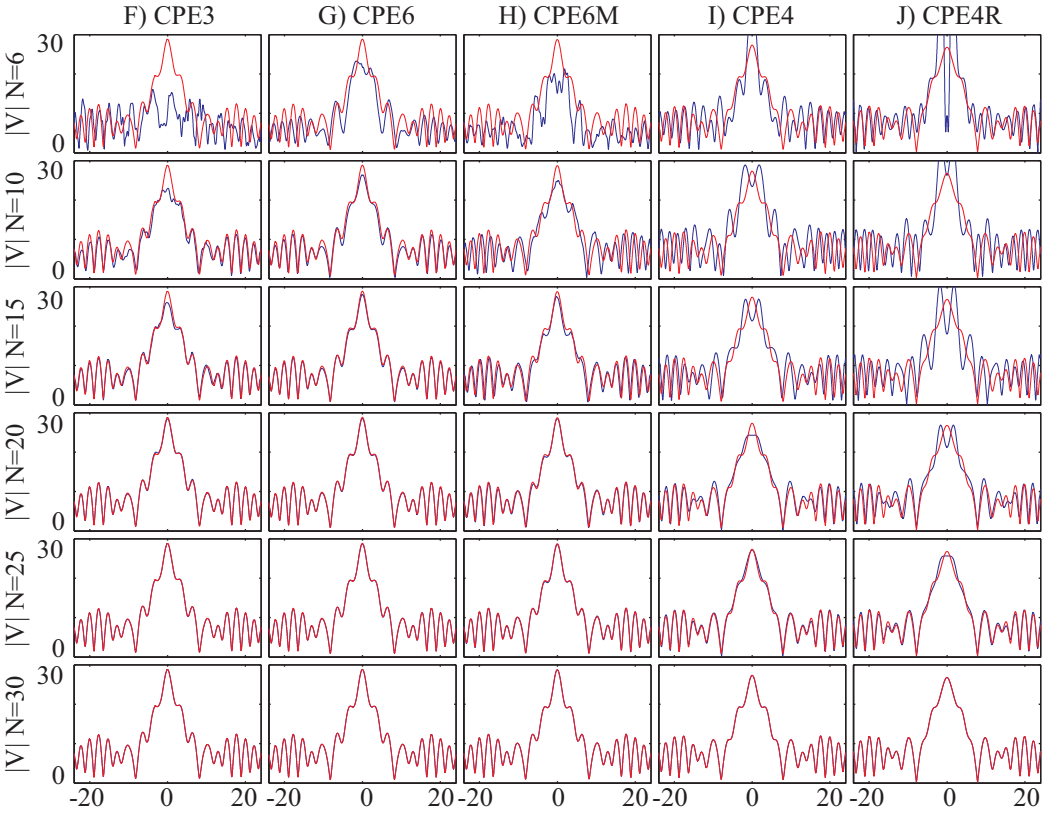

Figure 5.32. Implicit models for a hole of diameter 4: Monitored absolute displacement for a shear wave excitation using mesh made of CPE3, CPE6, CPE6M, CPE4 and CPE4R elements. Thin red line is reference for N=30 for each case.

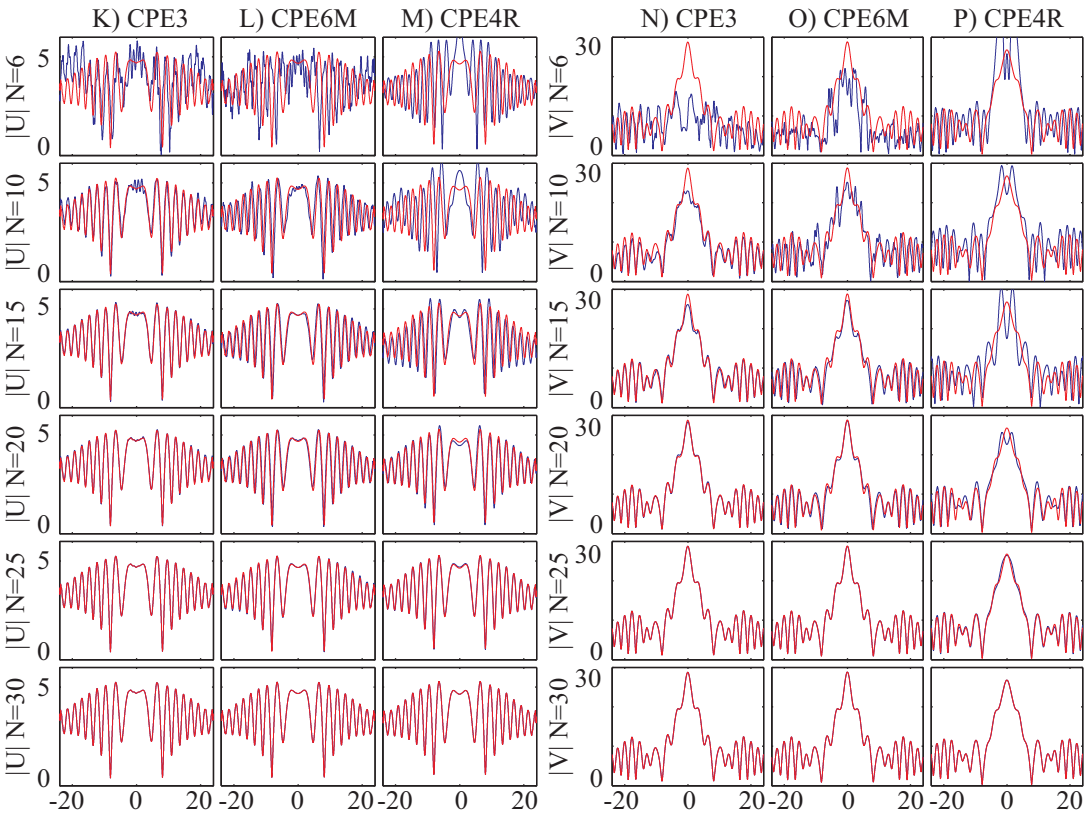

Figure 5.33. Explicit models for a hole of diameter 4: Monitored absolute displacement for a shear and longitudinal wave excitation using mesh made of CPE3, CPE6M and CPE4R elements. Thin red line is reference for N=30 for each case.

the excitation point is replaced by twin peaks that gradually disappear as the mesh is refined. This confirms that shear waves are particularly sensitive to the jagged edge that occurs when modelling a hole with a regular square mesh.

5.5.4 Conclusion

The study of the modelling of the reflection of waves from circular defects showed that the use of triangular element meshes gives accurate results for small, average and large holes. The strength of the method was demonstrated when modelling a small hole of diameter 0.25 (a quarter of the shortest wavelength). The curvature control provided by the free meshing algorithm set at the default setting (0.1) refined the mesh around the location of the hole allowing a precise representation of the feature despite the overall coarseness of the mesh. In this case, excellent results were obtained with quadratic and modified quadratic elements for a mesh density of 20. A finer mesh is required to achieve similar quality using linear elements. For other cases, all triangular elements performed in a similar way providing high quality results for a mesh density of 20.

It was demonstrated that the use of a regular square mesh to model circular defects is not appropriate unless a very fine mesh of density superior to 30 is used. Although the method performed well with longitudinal excitation, shear wave excitation cases were shown to be particularly sensitive to the way the edge of the hole is defined. Performance was in fact better for the small hole case than for the average and large hole cases.

5.6. Conclusions

This study has highlighted the challenges of modelling a range of defects using finite elements. The use of a regular mesh was shown to perform very well to model a straight edge when aligned with the mesh, but its inefficiency was demonstrated when modelling features whose geometries do not follow the grid exactly. The issue of correctly dimensioning a feature in a fixed grid (e.g exact crack length) length was highlighted but can be easily resolved by adjusting the mesh density to fit the size of the defect. It was demonstrated that this is not the main issue influencing the quality of results. The stair-cased definition of the edges of defects proved to be the crucial parameter influencing the quality of results. Even with large defects, relatively fine meshes (N=25) performed poorly in cases dominated by shear waves. Therefore, the regular mesh approach can only be confidently used to model defects not aligned with the mesh when the mesh density is extremely fine (N>=30).

Local mesh refinement where only a small area around the defect is extremely finely meshed would be advantageous in this situation. The use of two meshes of different densities tied together, which would enable such a refinement to be achieved economically, is investigated in the next chapter.

Triangular meshes generated by the free meshing algorithm have proved to perform well in most cases. The fact that the element size is not exactly constant did not cause a deterioration of results. Dimensioning of the defect was better than with the regular square mesh approach. As the geometry was defined using the interactive tools of ABAQUS/CAE before meshing, straight defects were defined exactly. Circular defects were well defined in all cases; this was helped by the curvature control which in fact provided a local mesh refinement in the case where a small hole was modelled.

Quadratic and modified quadratic elements proved to perform better in situations where only a limited number of nodes defined a defect.

Overall, the author recommends using meshes of regular linear square elements for models where features can be aligned with the node grid. Automatically generated meshes made of modified quadratic triangular elements should be used in cases where this can not be done or where features include curved edges.

The number of nodes that defines a small feature plays an important role in the quality of the modelling of the interaction of a wave with the feature. In this situation, the author would recommend using at least 8 nodes to define a feature in order to be confident that the physical phenomenon is correctly represented.

With regards to the mesh density, it is difficult to provide a general rule. Nevertheless, it can be said that a mesh density of 10 generally provides good qualitative results and that a mesh density of 30 generally provides excellent qualitative and quantitative results. It is therefore down to the modeller to decide what mesh density to use for a particular model based on what is required from the model.

Chapter 6

Local mesh refinement

6.1. Introduction

As seen in the previous chapter, when using a mesh made of regular square elements, it is challenging to accurately model defects whose geometry is not aligned with the node grid. One technique targeted at correctly modelling the interaction of waves with complex defects is known as the fictitious domain method. This technique is presented in Section 6.2. Research is still active in this topic and has successfully shown to improve modelling of complex defects but, to the best of our knowledge, the implementation of the technique cannot be achieved in commercially available FE packages and requires the use of specialist FE codes.

Let us consider a complex defect in a regular square mesh. As seen in Chapter 5, a mesh density superior or equal to 30 nodes per shortest wavelength is necessary to accurately define the defect whereas a mesh density of 10 or 15 would be suitable for the rest of the mesh. Using an extremely fine mesh over the whole model would provide satisfactory results but would also drastically limit modelling potential for large components. A way of improving this would be to use a relatively coarse mesh for the majority of the model but use a refined mesh in the local area surrounding the defect. This would allow a precise representation of the interaction of the wave with a defect while significantly reducing the number of degrees of freedom in the model.

The work in this chapter solely focuses on local mesh refinement of a regular square mesh using conventional tools available in the commercial FE package ABAQUS. The advantage of opting for a commercially available solution is that it removes the need to create and maintain a specialist code and strongly facilitates the transfer of the capability to industry. The method investigated in this part consists in creating two separate areas having a different mesh density and tieing them together.

There are two main issues which have not allowed this to be implemented straightforwardly in FE models in the past. The first one is the fact that changing the element size in a regular mesh of elements changes the acoustic impedance of the mesh. This fact is confirmed by the findings of chapter 4 as it was demonstrated that wave velocities depend on the type of element and the density of the mesh. The other issue is related to the way meshes of different size are tied together. At the interface between meshes of different densities, the displacements of both meshes on each side of this boundary are matched closely. As this is not done perfectly, it causes reflections.

In this chapter, a range of FE models are created and studied in order to better understand and quantify the influence of these sources of error.

6.2. Fictitious domain technique

6.2.1 Review

A recent review by Dr Elizabeth Skelton [28] offers a good overview of the technique. The development of the fictitious domain method started in the early 1960s but only gained momentum in the 1990s through the work performed at the INRIA research centre in France. Early developments and a portion of the research that followed concentrated on the implementation of the technique for elliptic equations [75, 76, 77]. Since our focus is on wave propagation problems, it is noted that developments of the technique for the Helmholtz problem were performed in several papers [78, 79, 80]. Time domain methods were also developed for time dependent acoustic [29] and elastodynamic [30] problems.

6.2.2 Presentation

Without getting into a detailed description of various mathematical implementations and their implications, the general philosophy of the methods is to describe the area of study and the defect separately and then to link them. A generally coarse (e.g. density of 10 elements per shortest wavelength) regular square mesh describes the whole area of study. The defect is created independently using a set of new variables. The equation defining the boundary condition at the edge of the defect is coupled with the wave

equation in order to solve the problem. The technique proved to work well for a variety of cases and is still the subject of active research.

6.2.3 Conclusion

Despite the success of the technique, it requires the modification of the way the solver computes the results. This unfortunately makes this technique not adapted to an implementation into a commercial FE package. Although the technique seems promising, as the implementation in commercial FE packages is not possible, it is not investigated further in this work.

6.3. Abrupt mesh density variation

In this section, the reflection from an abrupt change in mesh density is investigated.

6.3.1 1D wave propagation models

6.3.1.1 Model definition

As in the previous chapter, models are non-dimensional and the elastic material is defined so that the longitudinal and shear wavelengths are 2 and 1 units respectively: Young's modulus is 8/3, Poisson's ratio is 1/3 and density is 1. The general geometry of the models is presented in Figure 6.1. Models are 2D plane strain, 100 units long and 1 unit thick but are constrained (i.e. displacement equal to zero) in order to have 1D plane wave propagation. For 1D longitudinal wave propagation, the vertical displacement is set to zero on the top and bottom surfaces of the model. In the case of shear wave propagation, the horizontal displacement is constrained.

A regular square mesh is used over the whole model but it is split halfway (50 units from excitation) into two parts. The density of the mesh is different between the left and right hand sides. Both parts are tied together using the TIE function of ABAQUS 6.6-1 [14]. This function applies a rule that links the displacement of the nodes of the boundaries of the two parts.

The excitation is applied using a uniform force of unit amplitude over the whole thickness at the left hand extremity of the geometry. An ALID is used on the right hand

extremity of the model to absorb incoming waves. Figure 6.1 shows a schematic of the model geometry.

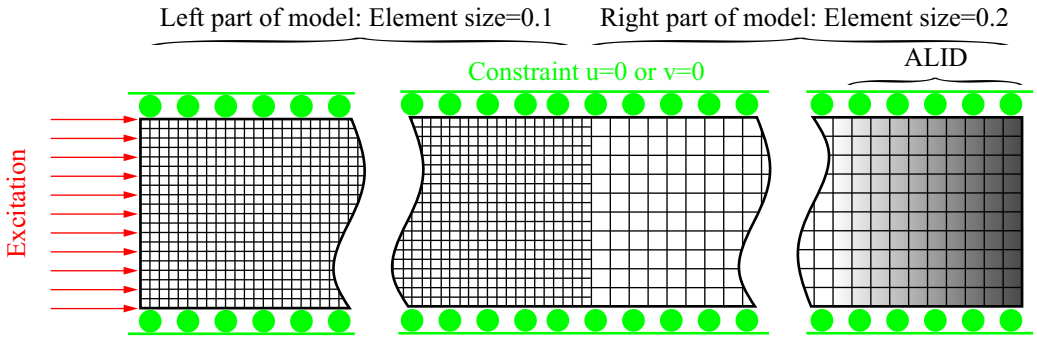

Figure 6.1. Definition of 1D model

Models are run with ABAQUS 6.6-1 in both the time domain (explicit) and the frequency domain (implicit). For the latter, the excitation is applied as a real harmonic excitation whose frequency is 1; the complex displacement field is obtained directly and used later to plot the absolute displacement field. For the explicit case, in order to obtain an absolute displacement field similar to the frequency domain one, two separate models are run: one with cosine and one with sine excitation of unit frequency. The complex displacement field is obtained by adding the result of the cosine case to the result of the sine case multiplied by i. The first half of a Hanning window is used over the first 5 cycles in order to ramp up the amplitude of the sine and cosine to a constant value in order to avoid exciting a broad range of frequencies. The model is run sufficiently long so that the steady state is reached at all locations where the displacements are monitored.

For longitudinal waves, the horizontal displacement is monitored at the half thickness line from 10 to 40 units away from the excitation. For shear waves, the vertical displacement is monitored. A spatial FFT [61] is applied to the complex displacement field in a similar way to the example presented in Section 3.5.3.1. As shown in Figure 3.25, the positive peak gives the amplitude of the incident wave generated by the excitation and the negative one the amplitude of the wave travelling in the opposite direction caused by the interface between the two parts of the model. The ratio of these two amplitudes gives the reflection coefficient of the waves from the interface. As explained in Section 3.5.3.1, the propagation velocity is given by the x-position of the

peak on the spatial FFT graph. In this case, padding is applied to the FFT to have a precise value of the velocity.

Implicit models are run using linear square elements with full (CPE4) and reduced (CPE4R) integration. Explicit models are only run using reduced integration linear square elements (CPE4R) as they are the only linear square elements available for this type of solver. The tie function is used with its default settings for implicit (TYPE=SURFACE TO SURFACE) and explicit (TYPE=NODE TO SURFACE) solvers with no adjustment on the position of the nodes as the two tied surfaces superimpose perfectly. Element based surfaces are used with explicit and implicit models. In both cases, following the user manual instructions, the surface with coarsest mesh is set as the master surface. Details about the TIE function can be found in [14].

6.3.1.2 L wave 1D model using theoretical material properties

In the first model, only longitudinal waves are generated. The element size is 0.1 on the left part and 0.2 on the right part. This corresponds to a mesh density of 20 and 10 elements per longitudinal wavelength. The theoretical material properties given above are used.

The results obtained from the model give a reflection of 1.972% (-34.1dB) of the incident wave in all cases. The fact that the same reflection is obtained for all solvers and element types means that the integration type (full or reduced) and solver type (explicit or implicit) do not influence the amplitude of the reflection at the interface between the two meshes. This also confirms that implicit and explicit implementation of the tie are correct. The following models are therefore run just with the implicit solver and reduced integration elements. The propagation velocities measured on each side of the interface are 1.992 and 1.966. This agrees very well with results obtained in Chapter 4, as the predicted velocities at 0 degrees are 1.991 and 1.964 for a regular mesh of 20 and 10 elements per longitudinal wavelength respectively.

As presented in [34], the reflection at 0 degrees based on the impedance is given by:

$$RC = \frac{Z_{20} - Z_{10}}{Z_{20} + Z_{10}} = \frac{\rho_{20} c_{20} - \rho_{10} c_{10}}{\rho_{20} c_{20} + \rho_{10} c_{10}} \quad (6{\cdot}1)$$

where Z is the impedance, ρ the density and c the velocity. The subscript indicates the density of the mesh.

Using the velocities measured in the model, the theoretically predicted reflection due to the change in impedance is 0.657%. As the amplitude of the reflection is higher than this value, the remaining part of the reflection may be due to the way the interface is implemented.

6.3.1.3 L wave 1D model with matched acoustic impedance

The second model is similar to the first model but in order to separate the contribution of the velocity error and the tie of the mesh, the acoustic impedances of both meshes at 0 degrees are matched by adjusting the longitudinal velocities in both parts of the FE model to be equal to the theoretical one (c_{Lth}=2) The velocity in the original FE model c_{Lor} is defined by the theoretical velocity c_{Lth} multiplied by a ratio R_L:

$$c_{Lor} = \frac{1}{R_L} c_{Lth} = \frac{1}{R_L} \sqrt{\frac{E_{th}}{\rho_{th}} \frac{(1 - \nu_{th})}{(1 + \nu_{th})(1 - 2\nu_{th})}} \quad (6{\cdot}2)$$

$$\text{with } R_L = \frac{c_{Lth}}{c_{Lor}} \quad (6{\cdot}3)$$

The original velocity in the FE model c_{Lor} necessary to define R_L is either measured by spatial FFT in the model or derived by using the estimate given in Chapter 5.

As the error between c_{Lor} and c_{Lth} is small, the adjusted velocity c_{Ladj} is defined as:

$$c_{Ladj} = R_L c_{Lth} = R_L \sqrt{\frac{E_{th}}{\rho_{th}} \frac{(1 - \nu_{th})}{(1 + \nu_{th})(1 - 2\nu_{th})}} = \sqrt{\frac{E_{adj}}{\rho_{adj}} \frac{(1 - \nu_{adj})}{(1 + \nu_{adj})(1 - 2\nu_{adj})}} \quad (6{\cdot}4)$$

The density and Poisson's ratio are kept the same but the Young's moduli are changed:

$$\nu_{adj} = \nu_{th}, \rho_{adj} = \rho_{th} \text{ and } E_{adj} = R_L^2 E_{th} \quad (6{\cdot}5)$$

The adjusted Young's moduli for mesh densities of 20 and 10 are 2.765 and 2.688. The adjusted velocities measured with the spatial FFT are 2.000 and 2.000 for densities of 10 and 20 elements. Therefore the theoretical reflection due to the change of impedance should be 0%. The reflection coefficient given by the spatial FFT is 1.240% (-38.134dB). As expected, matching the impedance has reduced the reflection coefficient. Interestingly, the difference in the reflection coefficient of the first and second models is 0.732% which is close to the predicted contribution of the change of impedance in the first model (0.657%). It indicates that the total reflection from the interface is equal to the sum of the change of impedance and the error due to the tie of the 2 meshes.

6.3.1.4 L and S wave 1D model with matched acoustic impedance

In this model, both shear and longitudinal waves are modelled in separate runs. The element size is 0.05 and 0.1 on the left and right part of the model respectively. The mesh density is therefore 20 and 10 elements per shear wavelength and 40 and 20 elements per longitudinal wavelength.

Theoretical material properties are used to start with. The measured reflection coefficients in this case are 0.470% (-46.56dB) and 1.971% (-34.108dB) for longitudinal and shear waves. The measured velocities are: c_{Lleft}=1.998, c_{Sleft}=0.996, c_{Lright}=1.9918 and c_{Sright}=0.983. The reflection caused by the change of impedance is predicted to be 0.155% and 0.657% of the incident signal. The reflection coefficient for shear waves in this case is the same as the longitudinal one in the first 1D model. The number of elements per considered wavelength is the same in both cases. This leads to the error on velocities being the same and therefore the change of impedance being the same. It indicates that both shear and longitudinal waves interact in the same way with the interface at equivalent number of elements per wavelength.

The material properties are adjusted in order to match the longitudinal wave acoustic impedance on both sides of the model. The velocities then are: c_{Lleft}=2.000, c_{Sleft}=0.997, c_{Lright}=2.000 and c_{Sright}=0.983. The reflection caused by the change of impedance is predicted to be 0% and 0.484% of the incident signal. The measured reflection coefficient for the longitudinal wave is 0.309% (-50.19dB) and for the shear wave is 1.795% (-34.92dB). In both cases, the drop in reflection coefficient matches the change in the contribution of the change of impedance. This confirms the findings of the previous model.

Following this, the material properties are adjusted in order to match the shear wave acoustic impedance in both sides of the model. The velocities then are: c_{Lleft}=2.006, c_{Sleft}=1.000, c_{Lright}=2.026 and c_{Sright}=1.001. In this case, the velocities in the right hand side of the model are higher than in the left one. This leads to a negative reflection contribution due to the impedance change which indicates a phase shift of 180 degrees. It is predicted to be -0.496% and -0.050% of the incident wave. The reflection coefficient for the shear wave is 1.240% and for the longitudinal wave is -0.197%. The negative sign indicates a phase shift. The results for the shear wave are in line with the previous cases. For the longitudinal wave, it is very interesting to note that the reflection coefficient (-0.197%) is also very close to be the sum of the contribution due to the change of impedance (-0.496%) and the interface (0.309%). This indicates that it should be possible to completely remove the reflection by matching the reflection due to the interface with a reflection due to an impedance change of equal amplitude and opposite phase.

Finally, the material properties are adjusted in order to match both the shear and longitudinal wave acoustic impedance in both sides of the model.

It is necessary to adjust the Young's modulus and the Poisson's ratio to do this.

$$c_{Lor} = \frac{1}{R_L} c_{Lth} = \frac{1}{R_L} \sqrt{\frac{E_{th}}{\rho_{th}} \frac{(1-\nu_{th})}{(1+\nu_{th})(1-2\nu_{th})}} \tag{6·6}$$

$$\text{with } R_L = \frac{c_{Lth}}{c_{Lor}} \tag{6·7}$$

$$c_{Sor} = \frac{1}{R_S} c_{Sth} = \frac{1}{R_S} \sqrt{\frac{E_{th}}{\rho_{th}} \frac{1}{2(1+\nu_{th})}} \tag{6·8}$$

$$\text{with } R_S = \frac{c_{Sth}}{c_{Sor}} \tag{6·9}$$

As the error between the FE and theoretical velocities is small, the adjusted velocities c_{Ladj} and c_{Sadj} are defined as:

$$c_{Ladj} = R_L c_{Lth} = R_L \sqrt{\frac{E_{th}}{\rho_{th}} \frac{(1-\nu_{th})}{(1+\nu_{th})(1-2\nu_{th})}} = \sqrt{\frac{E_{adj}}{\rho_{adj}} \frac{(1-\nu_{adj})}{(1+\nu_{adj})(1-2\nu_{adj})}} \tag{6·10}$$

$$c_{Sadj} = R_S c_{Sth} = R_S \sqrt{\frac{E_{th}}{\rho_{th}} \frac{1}{2(1+\nu_{th})}} = \sqrt{\frac{E_{adj}}{\rho_{adj}} \frac{1}{2(1+\nu_{adj})}} \tag{6·11}$$

As we want these velocities to match the theoretical ones, we have:

$$c_{Ladj} = 2 c_{Sadj} \tag{6·12}$$

The density is kept equal to 1 but the Young's moduli and Poisson's ratios are changed. Replacing c_{Ladj} and c_{Sadj} in 6·12 with 6·10 and 6·11 and doing some algebra, we have:

$$\nu_{adj} = \frac{2R_L^2 - R_S^2}{4R_L^2 - R_S^2}, \ \rho_{adj} = \rho_{th} \text{ and } E_{adj} = {R_S}^2 \frac{2(1+\nu_{adj})}{\rho_{adj}} \tag{6·13}$$

In this model, we therefore take: E_{left}=2.686, ν_{left}=0.3319, E_{right}=2.747 and ν_{right}=0.327. This gives: c_{Lleft}=2.000, c_{Sleft}=1.000, c_{Lright}=2.000 and c_{Sright}=1.001. The reflection caused by the change of impedance is predicted to be 0% and -0.050%

of the incident signal with longitudinal and shear waves respectively. The measured reflection coefficient for the longitudinal wave is 0.309% (-50.19dB) and for the shear wave is 1.240% (-38.13dB). In both cases, the drop in reflection coefficient matches the change in the contribution of the change of impedance compared to the non adjusted case. In this situation, the reflection is only due to the interface between the 2 parts.

6.3.1.5 L and S wave 1D model with varying acoustic impedance

This model is similar to the previous one except that in this case, the Young's modulus and Poisson's ratio are kept at their theoretical values in the left part of the model where the element size is 0.05 whereas the ones for the right part where the element size is 0.1 are varied parametrically.

To start with, the Poisson's ratio is kept constant and the Young's modulus is varied from 2.65 to 2.8 for the longitudinal wave and 2.65 to 2.95 for the shear wave. The reflection coefficient is measured as the Young's modulus is varied. The results are plotted in Figure 6.2. The reflection coefficient due to the impedance mismatch between the 2 parts of the model is calculated using Equation 6·1 and is plotted against the Young's modulus of the right part of the model. The difference between this and the total reflection is also plotted.

The first point of interest is that with both wave types the variation of the reflection from the FE model is linear against the Young's modulus. The impedance part of the reflection also varies linearly and with a slope close to the one of the total reflection. This is confirmed by the fact that the difference between these 2 curves, although not constant, varies linearly with a low slope. As mentioned in the previous part, it can be considered that the total reflection is made of the sum of the contribution due to the impedance mismatch and the one from the tie. In the previous plot, the difference between the FE and impedance related reflection is plotted as the reflection due to the tie. The assumption is made that the calculated and actual reflection due to the impedance mismatch are equal. As it is likely that a small discrepancy between these 2 exists, the plot for the tie reflection therefore includes this source of error. It is

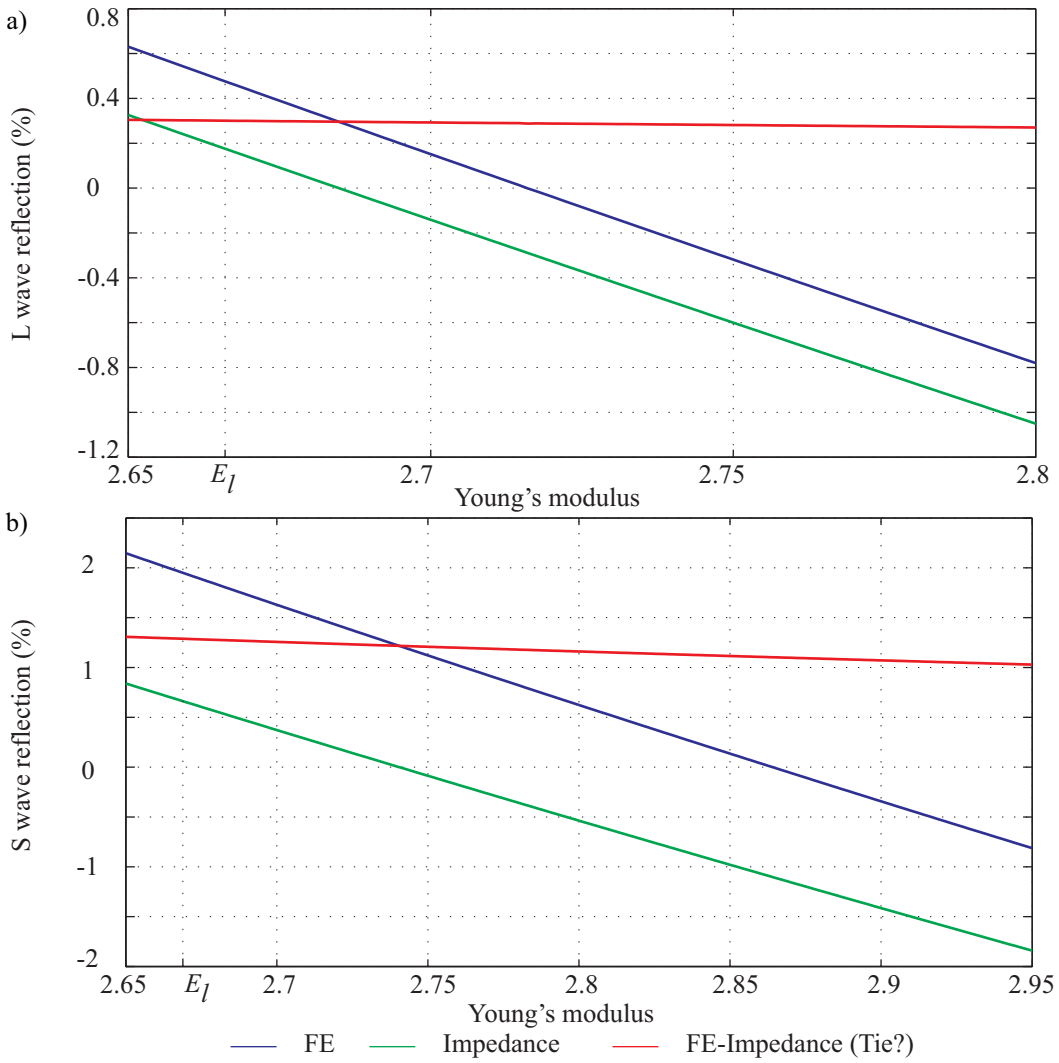

Figure 6.2. Reflection coefficient for longitudinal and shear waves against Young's modulus.

possible that this discrepancy is the reason for the reflection due to the tie not being constant but given the results from the previous model, this is unlikely. It can be said with a fair degree of confidence that the variation in the reflection due to the tie is mainly due to the variation of the Young's modulus rather than a change in the difference between the calculated and actual reflection due to the impedance mismatch.

The variation in Young's modulus leads to a variation in the overall reflection which is largely driven by the change in the impedance. It can be seen that the reflection due to the interface is higher for the shear wave case than the longitudinal one. Using results from 6.3.1.2, it is clear that this is not related to the wave type but to the mesh density and indicates that the interface reflection varies with the mesh density and that

it is dependent on the number of elements per wavelength of the considered wave. This point is investigated in detail further in this chapter.

Following this, the Poisson's ratio is varied from 0.32 to 0.335 and the Young's modulus from 2.6 to 2.9. The reflection coefficient is measured as the Young's modulus and Poisson's ratio are varied. The results are plotted in Figure 6.3. The reflection coefficient due to the impedance mismatch between the 2 parts of the model is calculated using equation 6·1 and is plotted against the Young's modulus in the right part of the model. The difference between this and the total reflection is also plotted in Figure 6.3.

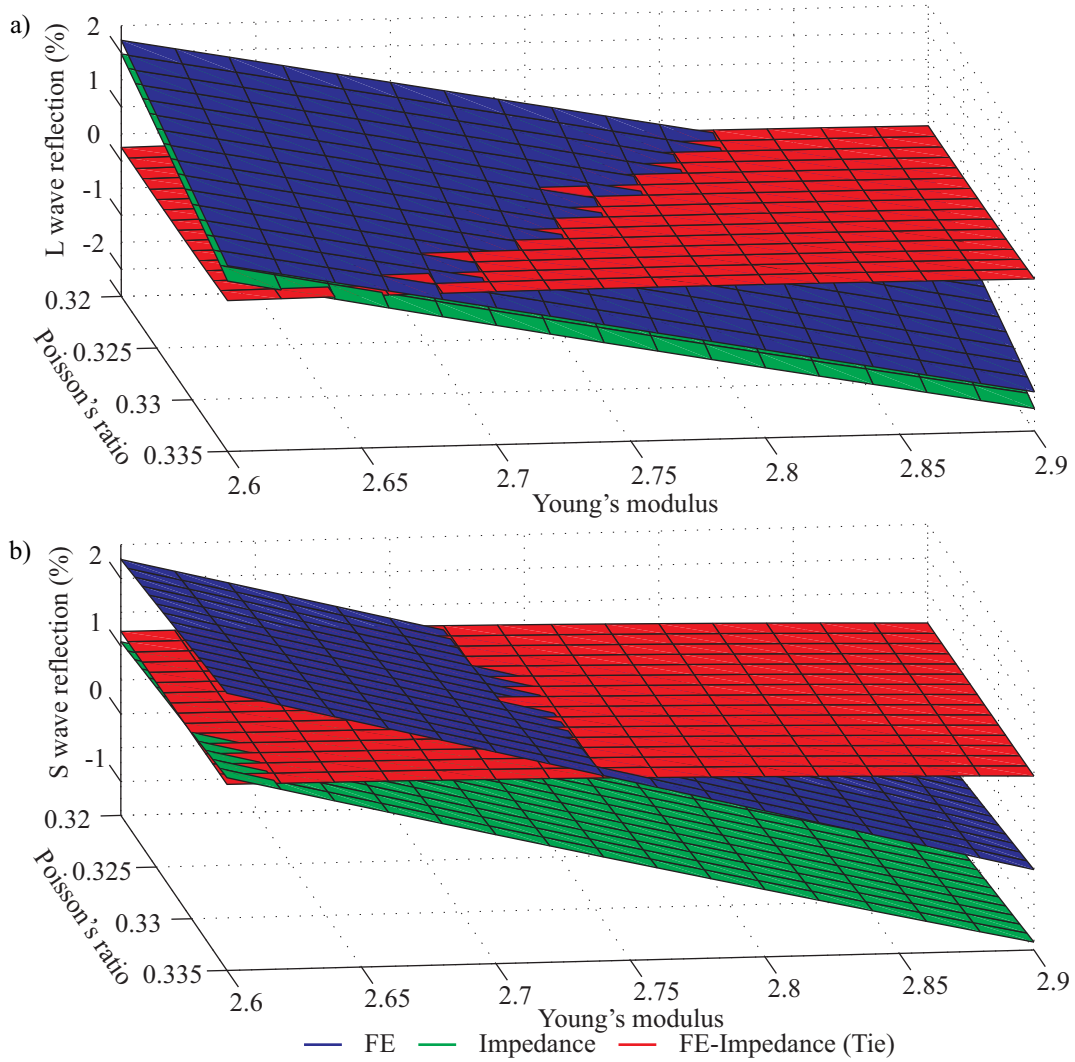

Figure 6.3. Reflection coefficient for longitudinal and shear waves against Young's modulus and Poisson's ratio.

The variation of the reflection coefficient against the Young's modulus and Poisson's ratio is close to linear for both parameters and wave types. The reflection due to the

impedance changes varies in a similar fashion. This means that, as can be seen on the figure, the reflection due to the interface is relatively stable over the whole range of parameters. As seen in the previous case, the amplitude of the reflection due to the interface is not the same for both wave types and depends on the mesh density.

Given the shape of the total reflection surfaces, it should be possible to find a point where there is no reflection for both wave types. Making the assumption that the surfaces are flat ones, the equations for the reflection coefficient for longitudinal and shear wave are found to be:

$$RC_L = -9.02E - 86.8\nu + 53.44 \quad (6{\cdot}14)$$

$$RC_S = -9.69E + 20.8\nu + 20.82 \quad (6{\cdot}15)$$

The total reflection is therefore zero for both waves when the elastic properties in the right part of the model are: Young's modulus=2.8372 and Poisson's ratio=0.3208.

A FE model is run for these parameters. The reflection is 0.006% (-84.52dB) and 0.005% (-85.75dB) for longitudinal and shear waves respectively. These values are negligible and confirm that it is possible to remove the reflection from both wave types at a given angle by adjusting the Poisson's ratio and Young's modulus.

6.3.1.6 L wave 1D model with different mesh ratio

As seen previously, the reflection due to the interface is close to constant when the acoustic impedance in one side of the model is changed but it varies noticeably with the mesh density. In this model, only longitudinal waves are studied as it was demonstrated that the reflection from the interface is independent of the wave type. The theoretical material properties as defined in Section 6.3.1 are used. The mesh density of both parts of the model is varied from 6 to 40 elements per longitudinal wavelength. The reflection coefficient is measured over this range of values and is plotted in Figure 6.4.a. The reflection due to the change in impedance calculated by using the measured velocities in each part of the model with equation 6·1 is plotted in Figure 6.4.b. The difference between these 2 reflections is considered to be the reflection due to the tie. This is plotted on a linear and log scale in Figure 6.4.c and d.

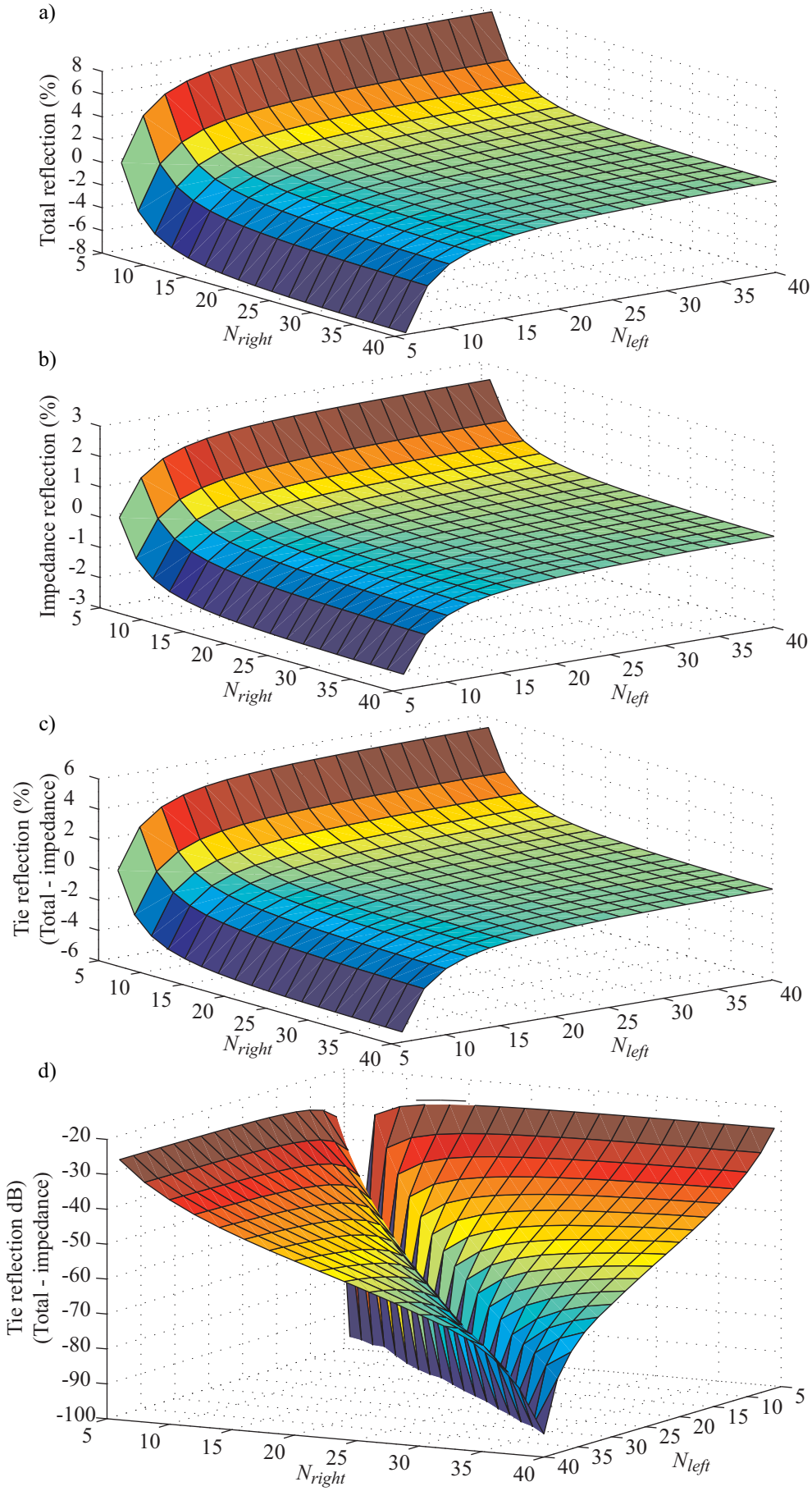

Figure 6.4. a) Total reflection, b) Reflection due to the impedance change, c) and d) Reflection due to the tie (linear scale and log scale).

The total reflection varies smoothly as the mesh densities are varied. As expected, central to all graphics in Figure 6.4 is a line of symmetry of zero reflection. Figure 6.4.d highlights that the reflection due to the tie is largely dependent on the mesh densities of both parts of the model. The reflection coefficient due to the tie and the impedance for a range of combinations of meshes in the situation where material properties are the same are presented in Table 6.1 and 6.2. It is interesting to note that the reflection caused by the tie contributes about twice as much as the one due to the impedance.

Table 6.1. Table of reflection coefficients due to the tie between two meshes in %

N	15	20	25	30	35	40
10	0.995%	1.325%	1.478%	1.561%	1.608%	1.639%
15		0.329%	0.482%	0.565%	0.612%	0.643%
20			0.152%	0.235%	0.281%	0.312%
25				0.082%	0.128%	0.159%
30					0.045%	0.076%
35						0.030%

Table 6.2. Table of reflection coefficients due to the impedance difference between two meshes in %

N	15	20	25	30	35	40
10	0.481%	0.646%	0.720%	0.759%	0.786%	0.802%
15		0.165%	0.238%	0.278%	0.304%	0.321%
20			0.073%	0.113%	0.1393%	0.156%
25				0.039%	0.066%	0.082%
30					0.026%	0.043%
35						0.016%

6.3.2 2D wave propagation models

As seen in the previous part, the reflection from the interface between 2 meshes can be made equal to zero at normal incidence. In this part, the effect of removing the reflection at one angle is investigated over the full angle range of 2D models.

6.3.2.1 Model definition

The 2D model is similar to the models used for the study of Chapter 4. At the centre of the model is a 70 unit square made of a fine mesh of density 20 elements per shortest wavelength. This square is bordered by a 9 unit thick layer made of a coarser mesh of

density 10 elements per shortest wavelength which is bordered by a 6 unit thick ALID of the same mesh density. This is shown in Figure 6.5.

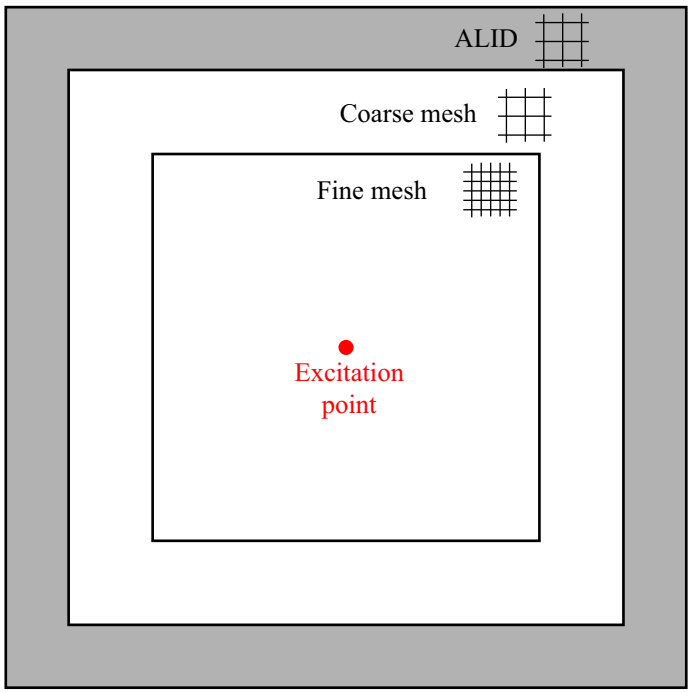

Figure 6.5. 2D model geometry

Both shear and longitudinal wave generations are considered. Models are excited by body forces being applied on four elements as in Chapter 5. This generates an almost pure wave - shear or longitudinal - and, as the size of the source is only a fraction of a wavelength, is close to a point source. The point located at the centre of the four elements is referred to as the excitation point. This point is located at the centre of the model. A 10 cycle Hanning windowed tone burst of centre frequency 1Hz is used.

The model is run for two cases. In one case, it is run using the reference material properties defined in Section 6.3.1.1 in both the coarse and fine mesh parts. In the other case, the material properties are the theoretical ones in the fine mesh part and the adjusted ones in the coarse mesh part in order to have zero reflection for both wave types at 0 degrees as defined in Section 6.3.1.5. The displacement fields in the top right corner at t=30 and t=60 for longitudinal and shear waves respectively are plotted in Figure 6.6.

Unlike in the 1D model, the waves decay as they propagate, due to beam spreading. The colour scale is adjusted so that the colour range covers the range of amplitude from

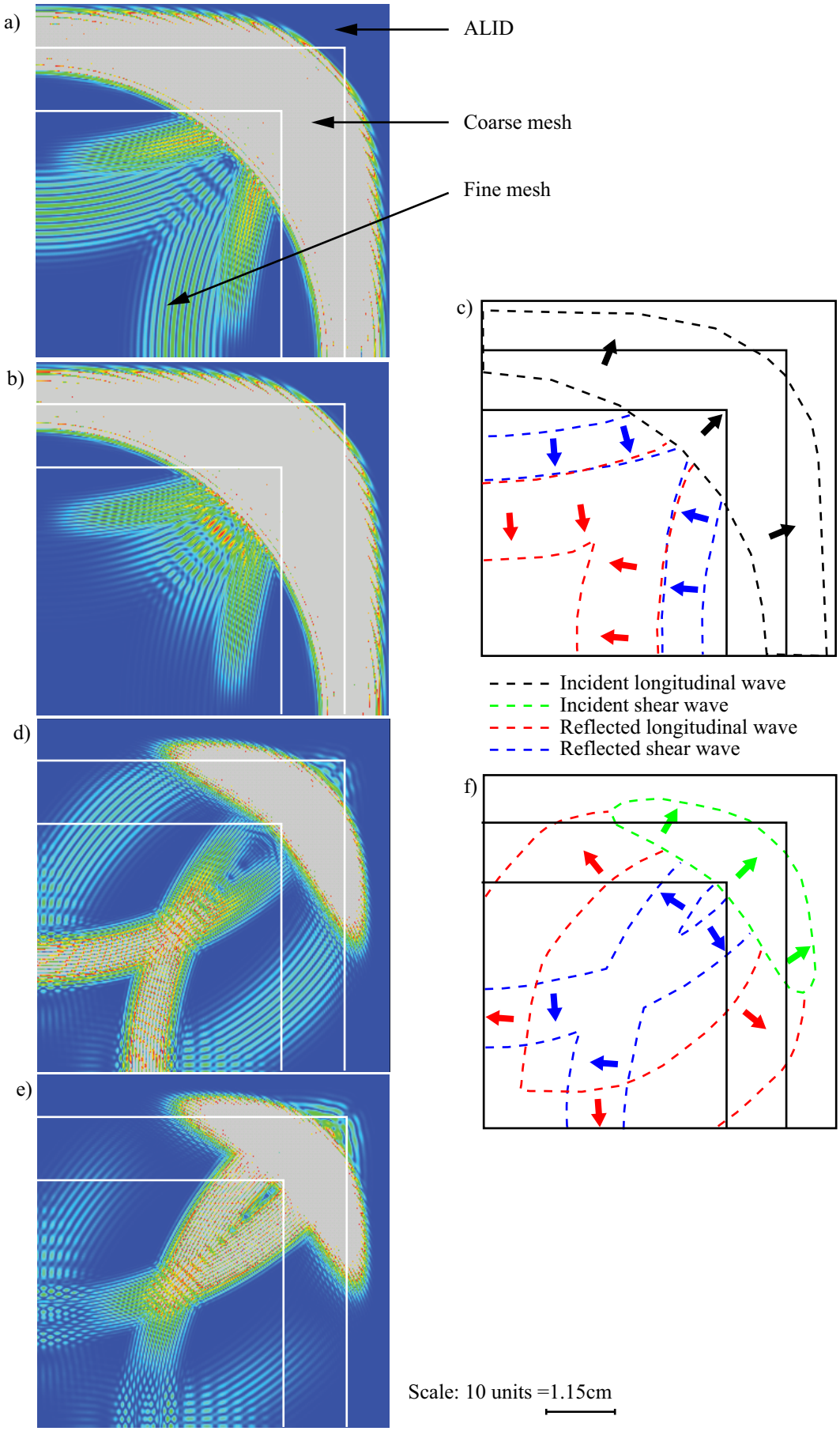

Figure 6.6. Absolute displacement field in the top right corner of the 2D models. Longitudinal wave excitation with a) theoretical and b) adjusted material properties. c) Definition of wave packet positions. d), e), f) same with shear wave excitation

0 to 1% of the desired incident wave when it hits the interface between coarse and fine meshes. All data above 1% is coloured in grey. The position and propagation direction of the different wave packets are schematically represented in order to simplify understanding.

Looking at the results for longitudinal wave excitation, it can be seen that there is a noticeable longitudinal wave reflection occurring at 0 degrees in the case using the theoretical material properties everywhere. The amplitude of this wave at 0 degrees is about 0.5%. It confirms that in the case of an abrupt change in mesh density the implicit and explicit cases give similar results. The use of adjusted properties significantly reduces the amplitude of the reflection for low angles of incidence but the amplitude of this reflection seems to increase with the angle of incidence. The shear wave reflection is reduced by the change in properties but has a similar amplitude variation.

Shear wave results carry similar findings. The shear wave reflection is not seen at 0 degrees but can be clearly identified at higher angles of incidence.

It can be concluded that the use of adjusted material properties based on the 1D model does not provide a significant gain in 2D compared to the non adjusted case. The explanation for this is two fold. First, as the angle of incidence varies, the visible acoustic impedance of the meshes changes because the mesh density is altered. Therefore the exact opposition of the reflections due to the tie and the impedance change does not exist anymore. Secondly, as mode conversion exists for angles different to zero, the reflection characteristics at each angle changes. Unique combinations of waves exist for each angle of incidence and means that there is a strong increase in the complexity of the problem.

Minimising the reflection due to the change of impedance over the full range of angle of incidence is an achievable target. Significantly reducing the reflection due to the tie below its original value is unlikely to be easily achievable if at all possible.

6.4. Gradual mesh density variation

As discussed previously, in a model where 2 meshes using the same material properties but having different mesh densities are tied together, a reflection occurs at the interface; this reflection is caused by the change of impedance and the error in the tying of the meshes. This latter contributes twice as much as the former. It would be beneficial if the reflection due to the tie could be reduced significantly. A solution which is investigated in this part is to have a gradual change in mesh density rather than an abrupt one.

6.4.1 1D wave propagation model

The 1D model is similar to the 1D models used in the previous part in all aspects apart from the way the mesh density change is achieved. In this case, the change in mesh density is achieved over a number of layers so that the mesh density is varied by 1 unit per layer. The layers are made of square elements whose dimension vary as the mesh density is varied. This is shown in Figure 6.7.

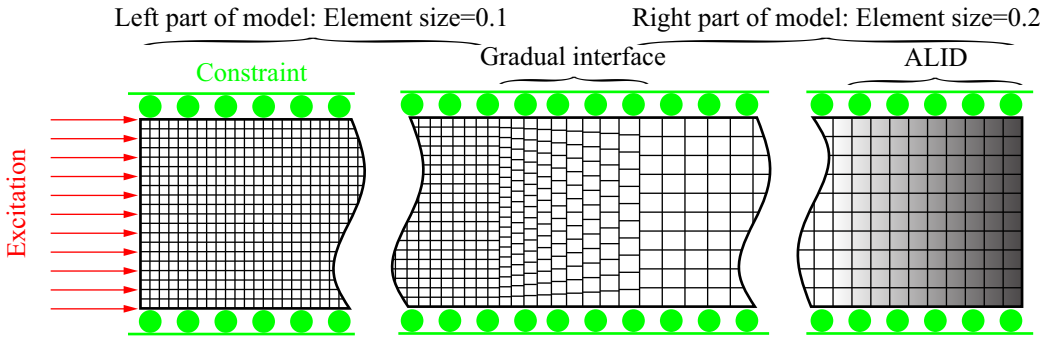

Figure 6.7. Definition of 1D model with gradual mesh density change.

The effect of the impedance change is removed by matching the acoustic impedance for both wave types at 0 degrees in every part of the model as described in Section 6·13. The impedances are adjusted to 2 for longitudinal waves and 1 for shear waves in all parts of the model. It is run in the time domain with the explicit solver. The excitation consists of a 10 cycles tone burst of unit centre frequency. The thickness is 1 unit. The left and right parts are 75 and 100 units long respectively. The central part where the gradual change of mesh density occurs is 0.62 units long.

The absolute displacement fields obtained at times 64 and 128 for longitudinal and shear waves are plotted in Figure 6.8. At these times, the incident wave packets have travelled through the interface. As previously, the colour scale is adjusted so that the colour range covers the amplitude from 0 to 1% of the incident wave. This is done to highlight low amplitude signals. All data above 1% is coloured in grey.

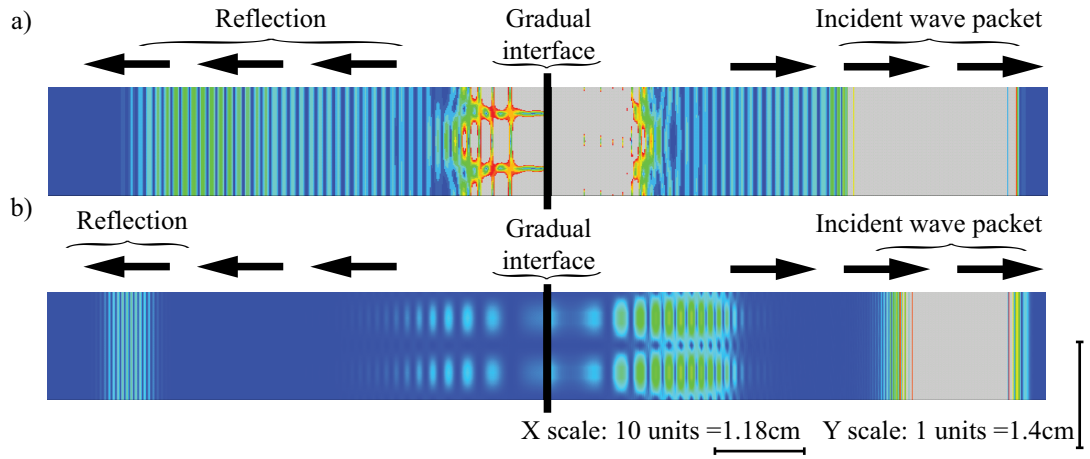

Figure 6.8. Absolute displacement field for a) longitudinal and b) shear wave excitation models with a gradual change of mesh density at t=34 (longitudinal) and t=68 (shear).

In both cases, the incident wave packet goes through the interface with almost no change to its amplitude but it can be seen that reflection from the interface occurs in both cases. Their amplitude is 0.52% and 0.32% of the longitudinal and shear incident wave packet. In the longitudinal wave case, it can be noted that the reflection is more spatially spread than the incident signal. This does not appear to be the same in the shear wave case. After the interface, the longitudinal wave packet is followed by a trail of waves similar to the reflection one. The striking feature in both cases is the presence of unexpectedly high displacements localized around the interface. For the fields plotted above, the maximum displacement is 10.5% and 0.65% of the incident longitudinal and shear wave packets. Given that boundary conditions are set such that the model should behave as a 1D one, the fact that these displacements are not constant in the vertical direction indicates numerical problems caused by the gradual interface.

This shows that the use of a gradual change of mesh density does not significantly reduce the reflection from the interface. It also causes numerical issues in the model.

6.4.2 2D wave propagation model

The 2D model is similar to the 2D models used in Section 6.3.2 apart from the way the mesh density change is treated. In this case, the mesh density change occurs over a range of layers as in the 1D study of this section. Figure 6.9 shows the way this is achieved in the 2D model. The mesh density is varied by 1 unit for each layer to gradually change the mesh density from 10 to 20. The Young's modulus and Poisson's ratio are adjusted to minimize the reflection due to the impedance change at 0 degrees.

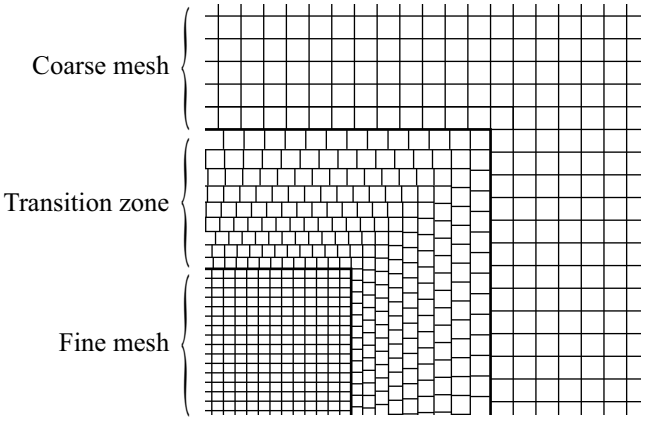

Figure 6.9. Gradual mesh density change for the 2D model.

The displacement fields in the top right corner of the model at t=35 and t=70 for longitudinal and shear wave respectively are plotted in Figure 6.10. The colour scale is adjusted so that the colour range covers the amplitude from 0 to 1% of the incident wave when it hits the gradual interface. All data above 1% is coloured in grey.

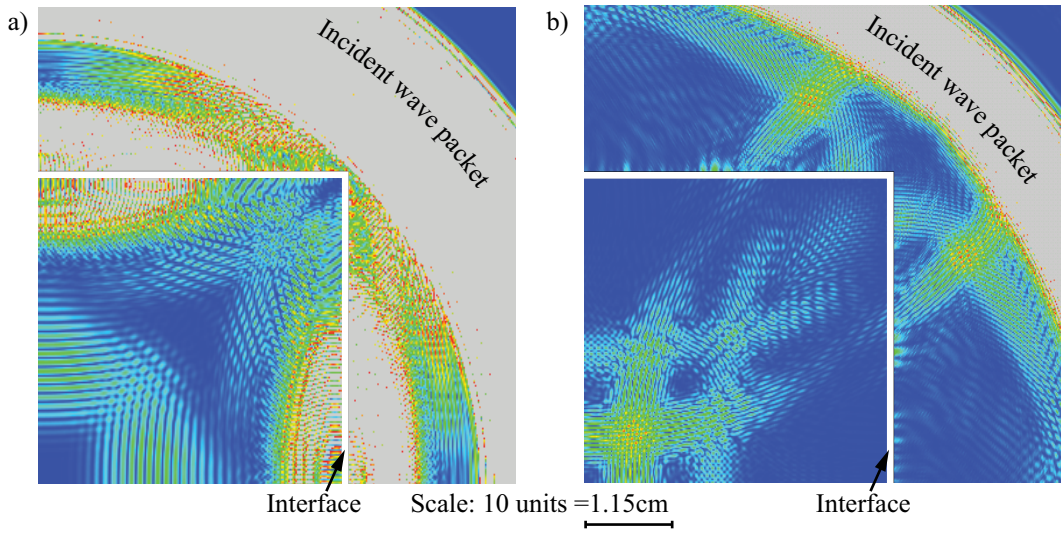

Figure 6.10. Absolute displacement field in the top right corner of the 2D model with a) theoretical and b) adjusted material properties.

As for the 1D model, it can be seen that gradual mesh density change as implemented in this case leads to a deterioration of the displacement field. This confirms that gradual change of mesh density with ties is not a viable option to achieve local mesh refinement.

6.5. Conclusions

The study of 1D models with abrupt change in density shows that the reflection is due to the change in impedance and the tie of the meshes. It is shown that the reflection due to the impedance change can be predicted using results from Chapter 5. This part of the reflection can be adjusted so that the overall reflection is zero for both wave types in the 1D model. In such case, it has the same amplitude but opposite phase as the part due to the tie of the meshes. 2D models show that this adjustment of the impedance leads to a significant reduction in the reflection at 0 and 90 degrees of incidence but that it is still noticeable at other angles of propagation different to the ones simulated in the 1D model (0 and 90 degrees). It is unlikely that it is possible to remove the reflection for all angles using this method. The contribution of the impedance change and tie at 0 degrees for a range of combination of mesh density in cases where theoretical material properties are used are presented in Tables 6.1 and 6.2. It gives modellers an estimate of the amplitude of reflection to expect if the technique is used and shows that the amplitude, although not negligible, is limited.

As the impedance reflection can be made equal to zero at a given angle and as the tie is the main contributor to the reflection, the idea of reducing the reflection due to the tie by using a gradual change in mesh density is investigated. The gradual change in mesh density is achieved by using a series of layers of varying mesh densities between the 2 meshes. Results from the 1D and 2D models show that this technique does not reduce the reflection significantly and causes localized numerical problems close to the interface although there is room for more detailed parametric studies.

Overall, local mesh refinement of a square mesh as implemented in this chapter with an abrupt change in mesh density has shown to work correctly but generates reflection at the interface. This can be an acceptable configuration in some cases. In other cases,

the use of an automatically generated modified quadratic triangular mesh (which does not use ties) is likely to be the best option. This is discussed in Chapter 7.

Chapter 7

Conclusions

7.1. Review of thesis

The work in this thesis investigates ways of improving elastic wave modelling in isotropic solids using commercially available FE packages. The focus is on developing new techniques as well as gaining a better understanding of the existing techniques.

Knowledge of the interaction of waves with defects and structural features is crucial in order to develop satisfactory ultrasonic NDT applications. As applications are developed for increasingly challenging situations, the use of numerical modelling has proved in many cases to be the most effective and cost efficient way of assessing potential problems early in the development process. Despite the exponential increase in computational capacities in recent years, there are many cases which remain out of reach.

The choice of commercially available FE packages is motivated by the fact that they enable new techniques to be quickly transferred to industry where these products are already or could easily be available and where a specific unsupported research code would be difficult to maintain.

Chapter 2 presents the theoretical basis of the bulk and guided wave propagation phenomena modelled in this work. Details of the numerical scheme used in this work are provided.

The implementation of the radiation of waves outside the area of study is studied in Chapter 3. Following the assessment of the available techniques, 2 types of absorbing layers are selected: Perfectly Matched Layers (PML) and Absorbing Layers Using Increasing Damping (ALID). The implementation of both methods is discussed. It is shown that the correct definition of layers parameters is crucial to the achievement of numerical efficiency. Analytical models are developed in order to facilitate the determination of these parameters for bulk wave and 2D plate guided wave problems. Analytical model results are validated against FE validation cases results.

Demonstrator cases for bulk and guided waves are developed to demonstrate gains achieved by the use of the techniques. The procedure of time domain reconstruction of frequency domain results is explained and validated. The ease of use of the frequency domain method to obtain reflection coefficient curves is presented and results are compared with published results.

In Chapter 4, the influence of meshing parameters on the wave propagation velocities in an elastic isotropic medium is investigated. Longitudinal and shear wave propagation are considered. The impact of the time step, mesh density and angle of propagation is studied for a range of element types with time domain models solved with an explicit scheme. The impact of the mesh density and angle of propagation is studied in a similar way for a range of element types with frequency domain models solved with an implicit scheme. Steady state is modelled in both cases using a time domain explicit solver and a frequency domain implicit solver. The consequence of element deformation is looked into.

In Chapter 5, a range of defects is modelled: straight edges, straight cracks at an angle of 80 degrees of various lengths and circular holes of various diameters. Longitudinal and shear wave propagations are considered. For each case, the mesh density is gradually refined to a very fine level in order to obtain a reference. Steady state for explicit and implicit solvers is achieved in the same way as in the previous chapter. Two meshing methods are compared. Automatically generated meshes made of triangular elements and regular meshes made of square elements are assessed.

The use of local mesh refinement techniques in regular square meshes is investigated in Chapter 6. One method investigated consists in tying together 2 meshes of different mesh densities. 1D and 2D models are used to evaluate the technique. Results obtained in Chapter 4 are used to improve the performance of the technique. The second method investigated achieves the mesh density change gradually through the use of a series of tied layers. The performance of this method is measured using 1D and 2D models.

7.2. Summary of findings

7.2.1 Absorbing layers

The study of PML and ALID in wave propagation models has shown that a significant reduction in a model's geometric size can be achieved through their use. Analytical

models provide a fast and efficient way of defining the layer's parameters and therefore offer a significant improvement over trial and error methods. Demonstrator cases have highlighted the gains obtained by using ALID or PML and have also shown that PML achieves smaller model sizes than ALID. This can be explained by the fact that with PML the layer matches the impedance of the area of study perfectly whereas for the ALID the strength of the decay is limited by the impedance change it causes. As a consequence, for a given case, ALID is generally thicker than PML. It is also more sensitive to waves incident at high angles, leading to a necessary increase of the area of study in order to minimize the model size. As the aim is to stretch modelling capabilities, this gives an advantage to the PML technique but it has to be balanced by the fact that, to our knowledge at the time of writing, COMSOL is the only mainstream FE package that allows implementation of PML. The implementation is limited to frequency domain solving with implicit solvers whereas ALID can be implemented to be used with any FE package which allows Rayleigh damping. The actual performance comparison depends on the type of result required.

A user wishing to obtain frequency domain results such as the reflection coefficient from a defect has a choice of directly using either PML or ALID. The two best combinations investigated are ABAQUS with ALID and COMSOL with PML. ABAQUS models were solved using the "Direct-solution steady-state dynamic analysis" procedure of ABAQUS/Standard which uses a direct implicit solver. COMSOL offers a range of direct and iterative implicit solvers. Direct solvers have proved to be robust and efficient but limited in term of the number of degrees of freedom that can be solved. Iterative solvers showed improvement in terms of speed and memory but convergence proved difficult. Overall, in our experience, using COMSOL 3.2 and ABAQUS 6.6, COMSOL did not match the performance of ABAQUS for a given number of degrees of freedom. Given these two combinations it is therefore not possible to clearly recommend one of them, as the best solution depends on the specific details of the model considered.

For time domain results, the most straightforward approach is to use ABAQUS/ Explicit with ALID. The explicit solver of ABAQUS uses the central difference algorithm. It is particularly attractive for large models as it is faster and more memory efficient than an implicit solver. This technique is recommended for most cases where time domain results are required. One alternative is to solve the model in the frequency

domain and reconstruct the time domain results by performing an inverse Fourier transform.

7.2.2 Influence of mesh parameters on the elastic bulk wave velocities

The study of reduced integration linear quadrilateral elements solved with an explicit solver showed the influence of the scaled Courant number CFL_X and mesh density N on the velocity. Patterns were identified. These permitted rules to be defined to evaluate with high accuracy the amplitude of the velocity error at any angle, any scaled Courant number and for a mesh density higher than 6. Following this, the study of deformed elements highlighted that the maximum error in a mesh could be predicted using the rules defined for square elements. This indicates that this element type can cope well with being deformed.

With linear equilateral triangular elements, it was demonstrated that the error could be correctly predicted using rules established for quadrilateral elements along the altitudes and element sides for longitudinal waves and along the element sides for shear waves. The influence of the scaled Courant number CFL_X and mesh density N was confirmed at these positions and wave types. A zero error was measured for shear waves along the altitudes of the triangular elements. Deformed mesh cases showed that this element type is sensitive to high levels of deformation as the predicted error was more than tripled in one case (16.4% instead of 4.8%).

Modified quadratic equilateral triangular elements proved to have a close to constant error against the angle for a given N when being solved with a low CFL. The amplitude of the error was in line with the one observed with linear elements. The influence of CFL_X and N was demonstrated to be similar to previous cases. Modified quadratic triangular elements were shown to cope well with being deformed like linear quadrilateral elements and unlike linear triangular elements. For implicit solving, full integration linear square element results for longitudinal waves showed very good agreement with those obtained with reduced integration elements and the explicit solver. For shear waves, the plot had the same shape but the error was marginally smaller (factor of 0.75). Deformation of elements showed similar results to the reduced integration explicit case except that the reduction in error compared to the prediction was more pronounced with fully integrated elements. Therefore, fully integrated quadrilateral elements cope well with being deformed. For a given mesh density,

quadratic quadrilateral elements proved to strongly reduce the velocity error. Rules established in previous cases could not be applied to this case but given that the velocity error is less than 0.5% for a mesh density higher than 8, it can be understood that the velocity error with this type of element is not a cause for concern. Deformation of elements did not prove to be a problem.

Linear and modified quadratic elements results for the implicit case matched almost exactly results obtained with the explicit solver. Quadratic equilateral triangular elements were shown to lead to low velocity error as were quadratic square elements, but proved to be sensitive to high levels of deformation in the same way as linear triangular elements.

Overall, the influence of the solver is ruled out as element type is the factor determining the velocity error. Unlike quadrilateral elements, all triangular elements apart from modified quadratic ones were shown to be sensitive to element deformation. This justifies why automatic meshing algorithms seek to minimize the deformation and why modellers need to exercise caution when using triangular elements.

The angle of propagation in a regular mesh was shown to play an important part in the amplitude of the velocity error as it leads to a non-negligible variation.

The mesh density was shown to be the driving factor influencing the velocity error for all element types. The influence is not so remarkable for quadratic elements as the velocity is highly accurate for any mesh density. For linear and modified quadratic elements, its influence is much stronger.

7.2.3 Accurate modelling of complex defects using Finite Elements

This study has highlighted the challenges of modelling a range of defects. The use of a regular mesh was shown to perform very well to model a straight edge when aligned with the mesh, but its limitations were demonstrated when modelling features whose geometry does not follow the grid exactly. The issue of correctly dimensioning a feature in a fixed grid was highlighted and can be easily resolved by adjusting the mesh density to fit the size of the defect. It was demonstrated that this is not the main issue influencing the quality of results. The stair-cased definition of the edges of defects proved to be the crucial parameter influencing the quality of results. Even with large defects, relatively fine meshes (N=25) performed poorly in cases dominated by shear

waves. Therefore, the regular mesh approach can only be used with extremely fine meshes (N>=30).

Triangular meshes generated by the free meshing algorithm have proved to perform well in most cases. The fact that the element size is not exactly constant did not cause a deterioration of results. Dimensioning of the defect was better than with the regular square mesh approach. Straight defects were defined exactly. Circular defects were well defined in all cases; this was helped by the curvature control which in fact provided a local mesh refinement in the case where a small hole was modelled. Quadratic and modified quadratic elements proved to perform better in situations where only a limited number of nodes defined a defect.

7.2.4 Local mesh refinement

The study of 1D models with an abrupt change in density shows that the reflection is due to the change in impedance and the tie of the meshes. It is shown that the reflection due to the impedance change can be predicted using results from Chapter 4. This part of the reflection can be adjusted so that the overall reflection is zero for both wave types in the 1D model. In such case, it has the same amplitude but opposite phase as the part due to the tie of the meshes. 2D models show that this adjustment of the impedance leads to a significant reduction in the reflection at 0 and 90 degrees of incidence but that it is still noticeable at other angles of propagation different to the ones simulated in the 1D model (0 and 90 degrees). It is unlikely that it is possible to remove the reflection for all angles using this method. The contribution of the impedance change and tie at 0 degrees for a range of combination of mesh densities in cases where theoretical material properties are used are presented for reference in Chapter 6. It gives modellers an estimate of the amplitude of reflection to expect if the technique is used and shows that the amplitude, although not negligible, is limited.

As the impedance reflection can be made equal to zero at a given angle and as the tie is the main contributor to the reflection, the idea of reducing the reflection due to the tie by using a gradual change in mesh density is investigated. The gradual change in mesh density is achieved by using a series of layers of varying mesh densities between the two meshes. Results from the 1D and 2D models show that this technique does not reduce the reflection significantly and causes numerical problems localized close to the interface.

Overall, local mesh refinement of a square mesh as implemented in this chapter with an abrupt change in mesh density has shown to work correctly but generates reflection at the interface. This can be an acceptable configuration in some cases. In other cases, the use of an automatically generated modified quadratic triangular mesh (without ties) is likely to be the best option.

7.3. Future work

7.3.1 Absorbing layers

It is mentioned that mass and stiffness proportional damping can be used in ALID. As stiffness proportional damping can lead to a dramatic reduction in the time increment in an explicit scheme, only mass proportional damping is used. For the implicit scheme, this is not the case and the simultaneous use of both damping types may lead to increased performance and could be investigated.

The bulk wave analytical models are valid for all cases (up to 3D) but the guided wave model is only valid for 2D plates. It would be beneficial to develop similar models for other guiding structures. In particular, in the field of Structural Health Monitoring (SHM), the development of a model for 3D plates would be of particular interest. In a similar way, a pipe analytical model would enable the creation of absorbing layers for this type of system.

Models using PML with viscoelastic materials will need to be investigated as PML proved to perform poorly when evanescent waves are present.

7.3.2 Influence of mesh parameters on the elastic bulk wave velocities

The work presented in this thesis is limited to a range of 2D plane strain elements. The study of other element types would increase the scope of the current study. It would be of particular interest to perform 3D elements studies.

As there are subtle differences in the way packages are implemented, small differences may exist between packages. Reproducing some of the models presented in this thesis with other FE packages should show that the results presented here can be used for other packages. It should be noted that despite this, it is expected that the principles developed here apply to all programs.

Another aspect that would require additional work is the investigation of irregular triangular element meshes such as those generated by automatic algorithms. Regarding this, it would be beneficial to evaluate whether the irregularity of the mesh causes some noise. If this occurs, the level of noise should be quantified.

7.3.3 Accurate modelling of complex defects using Finite Elements

It would be interesting to continue the present study by investigating more complex defects, as it was noted that automatic triangular element meshing of high curvature surfaces or short linear segments by free meshing algorithms leads to an increase in mesh density in their vicinity. The investigation of this phenomenon for critical cases may enable advances in the modelling of complex defects.

7.3.4 Local mesh refinement

The local mesh refinement technique of regular quadrilateral meshes presented in this work did not lead to the achievement of extremely low amplitude reflection at the interface and it seems unlikely that it would be possible to achieve it. The use of automatically generated meshes made of triangular elements seems to be the most promising technique for the achievement of local mesh refinement. Indeed, based on results obtained in Chapter 5, no numerical problem was noticed when mesh refinement in a triangular mesh was applied by the free meshing algorithm to define small circular defects. As it is expected that numerical problems will occur in extreme cases of mesh refinement, it would be interesting to determine the limits of this particular refinement technique.

References

1. **B. Pavlakovic, M. J. S. Lowe, P. Cawley and D. Alleyne**, *Disperse: A general purpose program for creating dispersion curves*, Review of Progress in Quantitative NDE (1997), Vol. 16, pp. 185 - 192.
2. **D. N. Alleyne**, *The nondestructive testing of plates using ultrasonic Lamb waves*, PhD thesis, Imperial College of Science Technology and Medicine, London, 1991.
3. **M. J. S. Lowe, R. E. Challis and C. W. Chan**, *The transmission of Lamb waves across adhesively bonded lap joints*, J. Acoust. Soc. Am., vol. 107, pp. 1333-1345 (2000).
4. **D. Hesse and P. Cawley**, *Surface Wave modes in rails*, J. Acoust. Soc. Am., vol. 120, pp. 733-740 (2006).
5. **M. Castaings, C. Bacon, B. Hosten and M. V. Predoi**, *Finite element predictions for the dynamic response of thermo-viscoelastic material structures*, J. Acoust. Soc. Am., vol. 115, pp. 1125 (2004).
6. **L. Wei and J.L. Rose**, *Phased array focusing with guided waves in a viscoelastic coated hollow cylinder*, J. Acoust. Soc. Am., vol. 121, pp.1945 (2007).
7. **P. Fromme**, *Experimental and Finite Element Study of Guided Ultrasonic Wave Scattering at Structural Features in a Plate*, AIP Conf. Proc., vol 55, pp. 894 (2007).
8. **D.N. Alleyne and P. Cawley**, *The interaction of Lamb waves with defects*, IEEE Transactions on Ultrasonics, Ferroelectrics and Frequency control, vol. 39, pp. 381-397 (1992).
9. **M. J. S. Lowe, D. N. Alleyne and P. Cawley**, *Defect detection in pipes using guided waves*, Ultrasonics, vol. 36, pp. 147-154 (1998).
10. **T. Vogt, M. Lowe and P. Cawley**, *The scattering of guided waves in partly embedded cylindrical structures*, J. Acoust. Soc. Am., vol. 113, pp. 1258-1272 (2003).
11. **B. Hosten and M. Castaings**, *Finite elements methods for modelling the guided waves propagation in structures with weak interfaces*, J. Acoust. Soc. Am., vol. 117, pp. 1108-1113 (2005).

12. **O. Diligent, T. Grahn, A. Bostrom, P. Cawley and M. J. S. Lowe**, *The low-frequency reflection and scattering of the S0 Lamb mode from a circular through-thickness hole in a plate: finite element, analytical and experimental studies*, J. Acoust. Soc. Am., vol. 112, pp. 2589-2601 (2001).
13. **M. J. S. Lowe and O. Diligent**, *Low-frequency reflection characteristics of the S0 Lamb wave froma rectangular notch in a plate*, J. Acoust. Soc. Am., vol. 111, pp. 64-74 (2002).
14. *ABAQUS v6.6 Analysis User's Manual*. (2006), www.simulia.com.
15. *COMSOL User's Guide version 3.2*. (2006), www.femlab.com.
16. **M.Drozdz, M.J.S. Lowe, E. Skelton, R.V. Craster**, *Modeling bulk and guided wave propagation in unbounded elastic media using absorbing layers in commercial FE packages*, Review of Progress in Quantitative NDE (2007), Vol. 26, pp. 87 - 94.
17. **D. Givoli**, *High-order local non-reflecting boundary conditions: a review*, Wave Motion, vol. 39, pp. 319-326 (2004).
18. **P. Bettess**, *Infinite Elements*, Penshaw Press, 1992.
19. **A.J. Burton and G.F. Miller**, *The application of integral equation methods to the numerical solution of some exterior boundary-value problems*, Proc. R. Soc. Lond. A, vol. 323, pp. 201-210 (1971).
20. **D. Givoli and J.B. Keller**, *Non-reflecting boundary conditions for elastic waves*, Wave Motion, **12**, 261-279 (1990).
21. **G.R. Liu and Jerry S.S. Quek**, *A Non-Reflecting Boundary for Analysing Wave Propagation Using the Finite Element Method*, Finite Elements in Analysis and Design, vol. 39, pp. 403-417 (2003).
22. **M. Israeli and S.A. Orszag**, *Approximation of radiation boundary conditions*, Journal of Computational Physics, vol. 41, pp. 115-135 (1981).
23. **J. Sochacki, R. Kubichek, J. George, W.R. Fletcher and S. Smithson**, *Absorbing boundary condition and surface waves*, Geophysics, vol. 52, pp. 60-71 (1987).
24. **J.P. Berenger**, *A Perfectly Matched Layer for the Absorption of Electromagnetic Waves*, Journal of Computational Physics, vol. 114, pp. 185-200 (1994).
25. **J. Davies and P. Cawley**, *The Application of Synthetically Focused Imaging Techniques for High Resolution Guided Wave Pipe Inspection*, Review of Progress in Quantitative NDE, vol. 27, pp. 681-688 (2007).

26. **F. Simonetti**, *Multiple scattering: The key to unravel the subwavelength world from the far-field pattern of a scattered wave*, Phys. Rev. E, vol. 73, 036619 (2006).
27. **M. Fleming, M. J. S. Lowe, F. Simonetti and P. Cawley**, *Super Resolution Imaging: Performance Studies*, Review of Progress in Quantitative NDE, vol. 26, pp. 820 (2006)
28. **E.A. Skelton**, *An Overview of the Fictitious Domain Method*, internal report, Imperial College of Science Technology and Medicine, London, 2007.
29. **F. Collino, P. Joly and F. Millot**, *Fictitious domain method for unsteady problems: application to electromagnetic scattering*, Journal of Computational Physics, vol. 138, pp. 907–938 (1997).
30. **E. Becache, P. Joly and C.Tsogka**, *Fictitious domains, mixed finite elements and perfectly matched layers for 2D elastic wave propagation*, I.N.R.I.A. report 3889, 2000.
31. **M. Drozdz, L. Moreau, M. Castaings, M.J.S. Lowe and P Cawley**, *Efficient numerical modelling of absorbing regions for boundaries of guided waves problems*, in Review of Progress in Quantitative NDE, vol. 25, pp. 126 (2005).
32. **M. Castaings and C. Bacon**, *Finite Element modeling of torsional wave modes along pipes with absorbing materials*, J. Acoust. Soc. Am., vol. 119, pp. 3741-3751 (2006).
33. **B. A. Auld**, *Acoustic fields and waves in solids*. (Krieger Publishing Company, Florida, 1990), 2nd edition.
34. **J.L. Rose**, *Ultrasonic Waves in Solid Media*, Cambridge University Press ed., 1999.
35. **J.D. Achenbach**, *Wave propagstion in elastic solids*. (North-Holland Publishing Compagny, Amsterdam, 1984).
36. **H. Lamb**, *On waves in an elastic plate*, Conference of the Royal Society, 1917, London.
37. **M.J.S. Lowe**, *Matrix techniques for modelling ultrasonic waves in multilayered media*, IEEE Transactions on Ultrasonics, Ferroelectrics and Frequency control, vol. 42, pp. 525-542 (1995).
38. **K.J. Bathe**, *Finite element procedures*, Ed. Prentice Hall, 1996.
39. **R. Courant, K. Friedrichs and H. Lewy**, *Über die partiellen Differenzengleichungen der mathematischen Physik*, Mathematische Annalen, vol. 100, no. 1, pages 32–74, 1928

40. **U. Basu and A. K. Chopra**, *Perfectly matched layers for time-harmonic elastodynamics of unbounded domains: theory and finite-element implementation*, Computer Methods in Applied Mechanics and Engineering, vol 192, pp. 1337-1375 (2003).
41. **F. Collino and C. Tsogka**, *Application of the PML Absorbing Layer model to the Linear Elastodynamic Problem in Anisotropic Heterogeneous Media*, Technical Report 3471, INRIA, 1998.
42. **A. Sommerfeld**, *Partial differencial equations in physics*, 1949, New York: Academic Press.
43. **J. Lysmer and R.L. Kuhlemeyer**, *Finite Dynamic Model for Infinite Media*, ASCE Journal of the Engineering Mechanics 1969. 95(August): p. 859-877.
44. **M. Cohen and P. C. Jennings**, *Silent Boundary Methods for Transient Analysis*, Computational Methods for Transient Analysis, Ed. T. Belytschko and T. R. J. Hughes, Elsevier, 1983.
45. **T. Dehoux**, *Finite Elements Modelling of Dissipative Materials*, internal report, Imperial College London, 2004.
46. **G. Liu and J.S. Quek**, *A Non-Reflecting Boundary for Analysing Wave Propagation Using the Finite Element Method,* Finite Elements in Analysis and Design, vol. 39, pp. 403-417 (2003).
47. **D. Givoli**, *Non-reflective boundary conditions: A review*, J. Comput. Phys., vol 94, pp. 1-29 (1991).
48. **B. Engquist and A. Madja**, *Radiation boundary conditions for acoustic and elastic calculation*, Commun. Pure Appl. Math., vol. 32, pp. 313-357 (1979).
49. **A. Bayliss and E. Turkel**, *Radiation boundary conditions for wave-like equations*, Commun. Pure Appl. Math., vol. 33, pp. 707-725 (1980).
50. **D. Givoli and J.B. Keller**, *Non-reflecting boundary conditions for elastic waves*, Wave Motion, vol. 12, pp. 261-279 (1990).
51. **J.B. Keller and D. Givoli**, *Exact non-reflecting boundary conditions*, J. Comput. Phys., vol. 82, pp. 172-192 (1989).
52. **D. Givoli**, *High-order local non-reflecting boundary conditions: a review,* Wave Motion, vol. 39, pp. 319-326 (2004).
53. **Q. Qi and T. L. Geers**, *Evaluation of the perfectly matched layer for computational acoustics*, J. Comput. Phys., vol. 139, pp. 166–183 (1994).

54. **E. Becache, A.-S. Bonnet Ben Dhia, and G. Legendre**, *Perfectly matched layers for the convected Helmholtz equation*, SIAM J. Numer. Anal. vol. 42, pp. 409–433 (2004).
55. **I. Singer and E. Turkel**, *A perfectly matched layer for the Helmholtz equation in a semi infinite strip*, J. Comput. Phys., vol. 201, pp. 439–465 (2004).
56. **F. D. Hastings, J. B. Schneider and S. L. Broschat**, *Application of the perfectly matched layer (PML) absorbing boundary conditions to elastic wave propagation*, J. Acoust. Soc. Am., vol. 100, pp. 3061–3069 (1996).
57. **F. Collino and C. Tsogka**, *Application of the perfectly matched absorbing layer to the linear elastodynamic problem in anisotropic heterogeneous media*, Geophysics, vol. 66, pp. 294–307 (2001).
58. **D. Komatitsch and J. Tromp**, *A perfectly matched layer absorbing boundary condition for the second-order seismic wave equation*, Geophysical Journal International, vol. 154, pp. 146–153 (2003).
59. **U. Basu and A. K. Chopra**, *Perfectly matched layers for transient elastodynamics of unbounded domains*, Int. J. Numer. Meth. Eng., vol. 59, pp. 1039–1074 (2004).
60. **E.A. Skelton**, *A perfectly matched layer (PML) for elastic wave propagation*, internal report, Imperial College of Science Technology and Medicine, London, 2007.
61. **D. Alleyne and P. Cawley**, *A two-dimensional Fourier transform method for the measurement of propagating multimode signals*, J Acoust Soc Am, vol. 89, pp. 1159-1168 (1991).
62. **T.P. Pialucha**, *The reflection coefficient from interface layers in NDT of adhesive joints*, PhD thesis, Imperial College of Science Technology and Medicine, London, 1992.
63. **J. De Moerloose and M.A. Stuchly**, *Behavior of Berenger's ABC for evanescent waves*, Microwave and Guided Wave Letters, IEEE [see also IEEE Microwave and Wireless Components Letters] , vol.5, no.10, pp.344-346, Oct 1995.
64. **J. P. Berenger**, *Evanescent waves in PML's: origin of the numerical reflection in wave-structure interaction problems*, Antennas and Propagation, IEEE Transactions on , vol.47, no.10, pp.1497-1503, Oct 1999.

65. **J. P. Berenger**, *Numerical reflection of evanescent waves from perfectly matched layers*, Antennas and Propagation Society International Symposium, vol.3, pp.1888-1891 (1997).
66. **J. Fang and Z. Wu**, *Generalized perfectly matched layer-an extension of Berenger's perfectly matched layer boundary condition* , Microwave and Guided Wave Letters, IEEE **5** (12), 451-453 (1995).
67. **J.P. Berenger**, *An effective PML for the absorption of evanescent waves in waveguides*, IEEE Microwave and Guided Wave Letters **8** (5), 188-190 (1998).
68. **E.A. Skelton, S.D.M. Adams, and R.V. Craster**, *Guided Elastic Waves and Perfectly Matched Layers*, Wave motion (2007), in press.
69. **W.B. Fraser**, *Orthogonality relation for the Rayleigh–Lamb modes of vibration of a plate*, J. Acoust. Soc. Am., vol. 59, pp. 215-216 (1976).
70. **V. Pagneux and A. Maurel**, *Lamb waves in inhomogeneous elastic waveguides*, Proc. R. Soc. Lond. A **458**, 1913-1930 (2002).
71. **J.E. Murphy, G. Li, and S.A. Chin-Bing**, *Orthogonality relation for Rayleigh–Lamb modes of vibration of an arbitrarily layered elastic plate with and without fluid-loading*, J. Acoust. Soc. Am., vol. 96, pp. 2313-2317 (1994).
72. **M.J.S. Lowe, P. Cawley, J.Y. Kao, O. Diligent**, *The low-frequency reflection characteristics of the fundamental anti-symmetric Lamb wave a0 from a rectangular notch in a plate*, J. Acoust. Soc. Am., vol. 112, pp.2612-2622 (2002).
73. **D. Hitchings**, Fe77 user manual, 1994, Imperial College: London, UK.
74. **N. Gengembre, A. Lhemery, R. Omote, T. Fouquet and A. Schumm**, *A Semi-analytic-FEM hybrid model for simulating UT configurations involving complicated interactions of waves with defects*, Review of Progress in Quantitative NDE, American Institute of Physics, New York, vol 23, pp.74-80 (2002).
75. **G. P. Astrakhantsev**, *Method of fictitious domains for a second order elliptic equation with natural boundary conditions*, USSR Comput. Maths. Meth. Phys. 18, pages 114–121, 1978.
76. **R. Glowinski, T-W. Pan, J. Periaux**, *A fictitious domain method for Dirichlet problem and applications*, Comput. Methods Appl. Mech. Engrg., vol. 111, pp. 283–303 (1994).

77. **L. Tomas**, *Une estimation d'erreur pour une formulation par domaine fictif avec multiplicateurs de volume du probleme de Dirichlet*, C. R. Acad. Sci. Paris Ser. I325, pages 793–796, 1997.

78. **A. Yu, O. Kuznetsov, O. D. Trufanov**, *Two-stage fictitious components method for solving the wave Helmholtz equation*, Sov. J. Numer. Anal. Math. Modelling, 5, 1988.

79. **E. Heikkola, Y. A. Kuznetsov, P. Neittaanmaki, J. Toivanen**, *Fictitious domain methods for the numerical solution of two dimensional scattering problems*, Journal of Computational Physics, vol. 145, pp 89–109, 1998.

80. **A. Bespalov**, *Application of fictitious domain method to the Helmholtz equation in unbounded domain*, I.N.R.I.A. Report 1797, 1992.